



**UCGE Reports
Number 20164**

Department of Geomatics Engineering

Augmentation of DGPS for Marine Navigation

(URL: <http://www.geomatics.ucalgary.ca/links/GradTheses.html>)

by

Samuel J. Ryan

October 2002



**UNIVERSITY OF
CALGARY**

UNIVERSITY OF CALGARY

Augmentation of DGPS for Marine Navigation

by

Samuel Joseph Ryan

A THESIS

SUBMITTED TO THE FACULTY OF GRADUATE STUDIES

IN PARTIAL FULFILMENT OF THE REQUIREMENTS FOR THE

DEGREE OF DOCTOR OF PHILOSOPHY

DEPARTMENT OF GEOMATICS ENGINEERING

CALGARY, ALBERTA

October 10, 2002

© Samuel Joseph Ryan 2002

ABSTRACT

Marine navigation has been revolutionised with the advent of the Global Positioning System (GPS), and the deployment of differential GPS (DGPS) systems. While most of the precision requirements for marine navigation can now be met with DGPS, the reliability of the user's position is often ignored. The question that is usually unanswered when it comes to marine navigation is "What is the typical marine blunder behaviour?" This question is answered through marine multipath simulations. The wide correlator simulations had a 99.9% blunder limit of 43 m, while the narrow correlator was only 11 m. Double blunders also occurred during the simulations, however, the second blunder was less than 4 m (99.9% of the time). This suggests that significant blunders can occur.

Software simulations were conducted to evaluate the availability and reliability improvements when DGPS is augmented with the Global Navigation Satellite System (GLONASS), Galileo, geostationary satellites, and height, clock, and dynamic constraints under various masking environments. These simulations clearly demonstrated the advantage of augmenting DGPS with a second full constellation of satellites, especially under moderate to extreme masking conditions.

The augmentation improvements are irrelevant if the user's receiver does not employ a real time reliability algorithm. Thus the reliability performance of four representative marine user receivers were tested using a DGPS signal simulator. None of the receivers tested employed a reliability algorithm. Although the higher end receivers mitigated the multipath blunders, gross position errors still occurred. A simple reliability algorithm was run in post mission to demonstrate that the blunders could have been detected. It is not good enough to augment DGPS, the user's receiver must also employ a real time reliability algorithm.

The simulation and user receiver testing results were validated through a field campaign on a Canadian Coast Guard survey in Saanich Inlet, British Columbia.

ACKNOWLEDGEMENTS

There are so many people who helped me over the past seven years its hard to know where to start. While I have dedicated my dissertation to my wife and parents, I must thank them first. Without their love and support, I would not be writing this today. Beth was there every step of the way and supported every move, from Ottawa to Calgary (96) to Ottawa (98) to Calgary (98) to ~~Ottawa (99)~~ to Ottawa (00). Without her help, I'm not sure if I would have ever finished.

I can't thank my supervisor, Dr. Gérard Lachapelle, enough. He gave me the extra push I needed to start my masters. It was during a meeting at the Canadian Coast Guard (CCG) Headquarters in Ottawa when Dr. Lachapelle planted the graduate studies seed. His support and guidance throughout my time at the University of Calgary (UofC) is greatly appreciated. His call to my director at the eleventh hour gave me the extra year to transfer to the Ph.D. program.

I could not have taken time off from work to pursue my studies without the support of my CCG colleagues. I would like to mention my CCG supervisor Fred Forbes. Fred supported my goal of going back to school, championed my cause to senior management, and eventually made it happen. Then there is Sun Wee. Sun had to take on double duty when I left, and then triple duty when Fred left, thanks Sun. The director who Dr. Lachapelle called at the eleventh hour was Pieter Leenhouts. Without Pieter's support I could not have transferred to the Ph.D. program.

I want to thank my fellow graduate students, faculty, and staff of Geomatics Engineering. It was a joy to work with each and every one of you. I won't try to list everyone because invariably I'll miss someone. Suffice it to say your help was appreciated, and you have been missed.

DEDICATION

To my family, my loving wife Beth, and my parents Sam and Maureen.

TABLE OF CONTENTS

ABSTRACT	III
ACKNOWLEDGEMENTS	IV
DEDICATION	V
TABLE OF CONTENTS	VI
LIST OF TABLES	IX
LIST OF FIGURES	XI
LIST OF SYMBOLS	XX
LIST OF ABBREVIATIONS	XXVII
CHAPTER 1 INTRODUCTION	1
1.1 CCG DGPS SHORE SYSTEM RELIABILITY	5
1.2 SHORTCOMINGS OF MARINE DGPS.....	8
1.3 THESIS COMPONENTS	10
CHAPTER 2 THEORY	12
2.1 GPS OVERVIEW	12
2.2 GLONASS OVERVIEW	17
2.3 GEOSTATIONARY AUGMENTATION OVERVIEW	21
2.4 GALILEO OVERVIEW	25
2.5 GNSS ERROR SOURCES	33
2.5.1 <i>Orbital Error</i>	34
2.5.2 <i>Tropospheric Error</i>	39
2.5.3 <i>Ionospheric Error</i>	48
2.5.4 <i>Measurement Noise</i>	59
2.5.5 <i>Multipath Error</i>	64
2.5.6 <i>Frequency Dependent Error</i>	83
2.5.7 <i>Changes with the Removal of SA</i>	85
2.6 RELIABILITY THEORY	88
2.6.1 <i>Least Squares Single Blunder Detection</i>	88
2.6.2 <i>Least Squares Multiple Blunder Detection</i>	92
2.6.3 <i>Internal Reliability using Kalman Filtering</i>	95
2.6.4 <i>Kalman Filtering External Reliability</i>	96
2.7 RECEIVER AUTONOMOUS FAULT DETECTION AND EXCLUSION INTEGRITY MONITORING.....	97
2.8 KALMAN FILTERING THEORY.....	97
2.8.1 <i>GPS Receiver Clock Model</i>	99

2.8.2	<i>First Order Gauss Markov Acceleration Model</i>	101
2.9	STOCHASTIC DYNAMIC BEHAVIOUR OF SHIPS	105
CHAPTER 3 MULTIPATH SIMULATIONS		108
3.1	DESCRIPTION	108
3.2	MULTIPATH SIMULATION RESULTS	112
3.3	MULTIPATH PERIOD	119
CHAPTER 4 SIMULATION ANALYSIS		123
4.1	INTRODUCTION	123
4.2	ISOTROPIC MASK ANGLES	127
4.2.1	<i>Availability Results</i>	128
4.2.2	<i>Reliability Results: 1 m² Measurement Variance</i>	133
4.2.3	<i>Reliability Results: 9 m² Measurement Variance</i>	137
4.2.4	<i>Reliability Results: Limited and Multiple Blunders</i>	139
4.2.5	<i>Single Point GLONASS</i>	141
4.3	CONSTRICTED WATERWAY SIMULATION	143
4.3.1	<i>Software Simulation Description</i>	143
4.3.2	<i>Availability Results</i>	145
4.3.3	<i>Reliability Results</i>	148
4.4	HYDROGRAPHIC SURVEYING USING A KALMAN FILTER	150
4.4.1	<i>Simulation Description</i>	150
4.4.2	<i>Results</i>	153
CHAPTER 5 STATIC DATA ANALYSIS		157
5.1	INTRODUCTION	157
5.2	RESULTS	158
CHAPTER 6 GPS SIGNAL SIMULATOR DATA ANALYSIS		163
6.1	INTRODUCTION	163
6.2	LEAST SQUARES RESULTS	167
6.3	KALMAN FILTERING RELIABILITY RESULTS	172
CHAPTER 7 VICTORIA DATA ANALYSIS		177
7.1	FIELD TEST DESCRIPTION	177
7.2	FIELD TEST RESULTS	182
7.2.1	<i>Availability Results</i>	183
7.2.2	<i>Reliability Results</i>	184
CHAPTER 8 CONCLUSIONS AND RECOMMENDATIONS		187
8.1	CONCLUSIONS	187
8.2	RECOMMENDATIONS	190
APPENDIX A ADDITIONAL GALILEO CONSTELLATIONS		192
A.1	INTRODUCTION	192
A.2	WALKER CONSTELLATION	192

A.3 GLOBAL AVAILABILITY RESULTS	193
A.3.1 <i>C³NAV^{G2}TM Repeats the GGPLAN Analysis for 60° N, 120° W,</i>	<i>195</i>
APPENDIX B MULTIPATH SIMULATION ANALYSIS PROGRAM FILE	
DESCRIPTIONS.....	203
B.1 OPTION FILE DESCRIPTION.....	203
B.2 REFLECTOR INPUT FILENAME DESCRIPTION.....	205
B.3 OUTPUT SUMMARY FILE	206
B.4 OUTPUT RESULTS FILE.....	206
B.5 OUTPUT INDIVIDUAL SATELLITE FILE.....	206
APPENDIX C ADDITIONAL MULTIPATH SIMULATIONS	208
C.1 INTRODUCTION.....	208
C.2 SIMULATION RESULTS.....	208
C.3 SUMMARY	215
APPENDIX D ADDITIONAL IONOSPHERIC SIMULATIONS	216
D.1 INTRODUCTION.....	216
D.2 SIMULATION RESULTS.....	216
APPENDIX E ADDITIONAL KALMAN FILTER DYNAMIC MODELS	219
E.1 INTRODUCTION.....	219
E.2 CONSTANT POSITION MODEL.....	219
E.3 CONSTANT VELOCITY MODEL	220
E.4 CONSTANT ACCELERATION MODEL.....	222
APPENDIX F PICTURES OF THE CANADIAN COAST GUARD SHIPS.....	224
F.1 INTRODUCTION.....	224
F.2 THE CCGS MARTHA L. BLACK.....	224
F.3 THE CCGS F.C.G. SMITH.....	225
F.4 CCGS TOFINO.....	226
F.5 CCG SURVEY LAUNCH THE RAVEN.....	227
APPENDIX G ADDITIONAL RESULTS FROM THE DGPS SIGNAL	
SIMULATOR	228
G.1 INTRODUCTION.....	228
G.2 NOVATEL OEM3	228
G.3 CSI GBX-PRO	231
G.4 MX-9212	233
APPENDIX H ADDITIONAL PICTURES OF SAANICH INLET TEST	236
H.1 INTRODUCTION.....	236
REFERENCES.....	239

LIST OF TABLES

Table 1-1 Marine Accuracy Requirements	3
Table 1-2 Summary of Minimum Standards for Hydrographic Surveys (IHO, 1998)	4
Table 1-3 DGPS Site Reliability Calculation.....	7
Table 1-4 RS and IM Integrity Checks	8
Table 2-1 GPS Code Specifications.....	14
Table 2-2 GPS Modernisation Activities (Lachapelle and Ryan, 2001).....	15
Table 2-3 Comparison of GPS and GLONASS (U.S. Department of Defence, 1999 and Russian Federation Ministry of Defence, 1995)	18
Table 2-4 Galileo Navigation Services Mapping to Signals (Genesis Office, 2002b)	29
Table 2-5 Galileo Satellite Constellations.....	30
Table 2-6 Results for all of the Satellites	35
Table 2-7 Single Difference Misclosures for all 26 Satellites	36
Table 2-8 HPE and VPE Statistics due to Ephemeris Errors for a 556 km Baseline.....	38
Table 2-9 HPE and VPE due to the Tropospheric Misclosures	46
Table 2-10 HPE and VPE with the Misclosures Scaled by a Factor of 0.20	47
Table 2-11 Maximum Value for each Parameter (Latitude Simulation)	58
Table 2-12 Minimum Received RF Signal Strength.....	61
Table 2-13 Common DLL Discriminators (Ward, 1996)	73
Table 2-14 Non Centrality Parameter (Leick, 1995).....	91
Table 2-15 Allan Variance GPS Receiver Clock Parameters (Brown and Hwang, 1997)	101
Table 2-16 Kalman Filter Process Noise Parameters.....	107
Table 3-1 MDB Limits from the Multipath Simulations	119
Table 6-1 Maximum and RMS Errors (m) During the Multipath Periods.....	171

Table A-1 Different Satellite Constellations.....	192
Table C - 1 Reflection Parameters	211
Table C - 2 Narrow Correlator Errors for Various Loop Iterations	213

LIST OF FIGURES

Figure 1-1 World Wide Marine DGPS Stations (Lachapelle et al., 2002b).....	2
Figure 1-2 CCG DGPS Station Block Diagram.....	5
Figure 2-1 Orbital Locations for the GPS Constellation (YUMA Almanac 1167)	13
Figure 2-2 Number of Healthy GPS Satellites vs. Time	14
Figure 2-3 Number of Satellites with L2C and L5 signals (Fontana et al., 2001a).	16
Figure 2-4 Number of Healthy GLONASS Satellites vs. Time.....	20
Figure 2-5 Orbital Locations for the GLONASS Constellation (GLONASS Almanac for GPS Week 1167, in YUMA Format)	20
Figure 2-6 Geostationary Satellite Elevation Angle	23
Figure 2-7 Number of Visible Geostationary Satellites (Mask Angle of 5°).....	23
Figure 2-8 Number of Visible Geostationary Satellites (Mask Angle of 30°).....	24
Figure 2-9 Galileo Development Schedule (EUROPA, 2002a and Tytgat and Campagne 2001).....	26
Figure 2-10 GNSS Frequency Plan.....	28
Figure 2-11 Galileo Signals (Genesis Office, 2002b).....	28
Figure 2-12 Number of Visible Geostationary Satellites, Galileo #1, 30° Mask Angle...	31
Figure 2-13 Galileo Constellations	32
Figure 2-14 Galileo Satellite Ground Trace.....	32
Figure 2-15 GPS Broadcast Orbit Position Errors	35
Figure 2-16 GPS Broadcast Orbit Statistical Analysis for each Satellite	36
Figure 2-17 St. Lawrence Seaway CCG DGPS Stations and the Selected Baseline	37
Figure 2-18 Single Difference Satellite Misclosures	37
Figure 2-19 HPE and VPE due to Ephemeris Errors for a 556 km Baseline.....	38
Figure 2-20 Atmosphere Regions (Seeber, 1993).....	39

Figure 2-21 Tropospheric Attenuation vs. Elevation Angle	40
Figure 2-22 Zenith Hydrostatic Delay	43
Figure 2-23 Tropospheric Delay vs. Elevation Angle using Niell's Mapping Function ..	44
Figure 2-24 Derivative of the Tropospheric Delay vs. Satellite Elevation Angle	45
Figure 2-25 Tropospheric Simulation Single Difference Misclosures.....	45
Figure 2-26 HPE and VPE due to the Tropospheric Misclosures.....	46
Figure 2-27 HPE and VPE with the Misclosures Scaled by a Factor of 0.20.....	47
Figure 2-28 Ionospheric Layers and Electron Densities	48
Figure 2-29 Typical Ionospheric Mapping Function for Different Shell Heights	54
Figure 2-30 Ionospheric Profile (Foster, 2000).....	55
Figure 2-31 Differential Satellite Misclosures (95%).....	56
Figure 2-32 1 st , 2 nd , and 3 rd Simultaneous Differential Satellite Misclosures (95%).....	57
Figure 2-33 95% Position Errors.....	58
Figure 2-34 DLL Thermal Noise Performance	60
Figure 2-35 PLL Thermal Noise Errors for Various Bandwidths.....	62
Figure 2-36 Pseudorange and Carrier Phase Measurement Accuracy for the Ashtech GG24™ Integrated GPS / GLONASS Receiver.....	63
Figure 2-37 Multipath and Direct GNSS Signals.....	64
Figure 2-38 Reflected and Incident Plane Waves (Hecht, 1990).....	67
Figure 2-39 GPS Signal Maximum Axial Ratio	68
Figure 2-40 Reflection Coefficients for Seawater ($\kappa = 81$ and $\sigma = 4$ S).....	70
Figure 2-41 Reflection Coefficients for Dry Land ($\kappa = 4$ and $\sigma = 0.001$ S).....	70
Figure 2-42 Sensor Systems Antenna Gain Response	71
Figure 2-43 Autocorrelation Functions for various input GNSS Signal Bandwidths.....	75
Figure 2-44 Multipath Error Envelope, SMR = 6 dB	76

Figure 2-45 Multipath Signal Delayed by 1.5 Chips (Infinite Bandwidth)	77
Figure 2-46 Multipath Error Envelopes for the Wide and Narrow Correlators for Different SMRs	77
Figure 2-47 Short Delay Multipath Errors for the Wide and Narrow Correlators.....	78
Figure 2-48 Correlation Triangles and Resulting Multipath Error for one Multipath Signal with Delay of $200 \times \text{wavelength of L1}$ and Amplitude of 0.5.....	79
Figure 2-49 Multipath Induced Carrier Phase Tracking Error for Various Multipath Phase Offsets	80
Figure 2-50 Carrier Phase Multipath Error Envelopes for Various SMRs	81
Figure 2-51 GLONASS Code DD Bias for all Four Tests.....	84
Figure 2-52 HPE 95% Using Four Hours of Data Prior to SA's Removal.....	87
Figure 2-53 HPE 95% Using 44 Hours of Data After SA's Removal	87
Figure 2-54 HPE 95% and 99% Using 44 Hours of Data After SA's Removal.....	88
Figure 2-55 Type I/II Errors & Non Centrality Parameter.....	90
Figure 2-56 Local MDB Polygon and Global Ellipse.....	94
Figure 2-57 GPS Receiver Clock Model State Diagram.....	99
Figure 2-58 Autocorrelation Function for a First Order Gauss Markov Process.....	102
Figure 2-59 First Order Gauss Markov Acceleration State Diagram.....	102
Figure 2-60 North Acceleration Autocorrelation Function for CCGS F.C.G. Smith	106
Figure 3-1 Multipath Simulation Program Flowchart.....	109
Figure 3-2 Large Simulated Ship	110
Figure 3-3 Simulated Survey Launch.....	110
Figure 3-4 Largest Error for the Large Ship and Survey Launch for both the Wide and Narrow Correlators.....	113
Figure 3-5 Multipath Amplitude and Delay for all Satellites for both the Large Ship and the Survey Launch.....	114
Figure 3-6 The Simulation's Multipath Discrimination.....	115

Figure 3-7 Second Largest Error for the Large Ship and Survey Launch for both the Wide and Narrow Correlators	117
Figure 3-8 Multipath Simulation Results Summary	118
Figure 3-9 Multipath Reflection from a Smooth Horizontal Surface	119
Figure 3-10 Multipath Delay (τ) and Delay Rate ($d\tau/dt$) with $h = 1$ and $d\theta/dt = 1$	120
Figure 3-11 PRN 1's Elevation Angle and Elevation Angle Rate vs. Time	121
Figure 3-12 Multipath Period vs. Elevation Angle with $h = 1$ m	122
Figure 3-13 PRN 1's Elevation Angle, Multipath Delay and Multipath Period	122
Figure 4-1 Simulation Computation Points.....	126
Figure 4-2 95% HDOP, for the World, Isotropic Mask Angles.....	128
Figure 4-3 Percent HDOP ≤ 2.0 , for the World, Isotropic Mask Angles.....	129
Figure 4-4 95% HDOP, DGPS + Height, 30° Mask Angle	131
Figure 4-5 95% HDOP, DGPS +GAL24, 30° Mask Angle.....	131
Figure 4-6 Computation Points Statistics, 95% HDOP, 30° Mask Angle	132
Figure 4-7 95% MHE, for the World, Single Unlimited Blunder, $\sigma = 1$ m	133
Figure 4-8 Percent MHE ≤ 10 m, for the World, Single Unlimited Blunder, $\sigma = 1$ m ...	134
Figure 4-9 95% MHE, DGPS + Height, 20° Mask Angle	135
Figure 4-10 Computation Points Statistics, 95% MHE, 20° Mask Angle	136
Figure 4-11 Computation Points Statistics, 95% MHE, 30° Mask Angle	137
Figure 4-12 95% MHE, for the World, Single Unlimited Blunder, $\sigma^2 = 9$ m ²	138
Figure 4-13 95% MHE, for the World, Single Blunder, Mask Angle 30°	139
Figure 4-14 95% MHE, for the World, Double Blunder, Mask Angle 30°	141
Figure 4-15 95% HDOP, for the World, Isotropic Mask Angles, with GLOSP.....	142
Figure 4-16 95% MHE, for the World, Isotropic Mask Angles, with GLOSP.....	143

Figure 4-17 Simulated Constricted Waterway	144
Figure 4-18 Constricted Waterway Mask Angle Profile.....	144
Figure 4-19 95% HDOP, for the World, Constricted Waterway	146
Figure 4-20 Percent HDOP ≤ 2 , for the World, Constricted Waterway	146
Figure 4-21 Computation Points Statistics, 95% HDOP, Constricted Waterway.....	147
Figure 4-22 95% MHE, for the World, Constricted Waterway, $\sigma^2 = 1 \text{ m}^2$	148
Figure 4-23 Percent MHE $\leq 10 \text{ m}$, for the World, Constricted Waterway, $\sigma^2 = 1 \text{ m}^2$	149
Figure 4-24 Computation Points Statistics, 95% MHE, Constricted Waterway.....	150
Figure 4-25 Simulated Survey Line	152
Figure 4-26 East / West Survey Line Mask Profile	152
Figure 4-27 East / West Line - HDOP 95% - DGPS & All Kalman Filters	154
Figure 4-28 East / West Line - HDOP 95% - DGPS & Kalman Filter #4	155
Figure 4-29 East / West Line - MHE 95% - DGPS & Kalman Filter #4	156
Figure 5-1 Blunder Introduced on Each GPS Satellite	158
Figure 5-2 HPE - 15° Mask Angle - Ramp on PRN 1 Reliability Disabled	159
Figure 5-3 HPE - 15° Mask Angle - Ramp on PRN 1 Reliability Enabled	160
Figure 5-4 HPE - 15° Mask Angle - Ramp on PRN 1 Reliability Enabled	161
Figure 5-5 HPE - Four Mask Angles - Six Positioning Methods Reliability Enabled....	162
Figure 6-1 Ship Test Trajectory	164
Figure 6-2 Number of SVs, HDOP, and MHE for the Simulation	165
Figure 6-3 Multipath Signal Delay and Amplitude Added to PRN 8's Direct Signal	166
Figure 6-4 Multipath Range Error Added to PRN 8	166
Figure 6-5 NovAtel OEM3 HPE for the Three Positioning Cases	168
Figure 6-6 CSI GBX-Pro HPE for the Three Positioning Cases.....	169

Figure 6-7 Magnavox MX-9212 HPE for the Three Positioning Cases	170
Figure 6-8 Northstar 941 HPE for the Internally Generated Position.....	171
Figure 6-9 NovAtel OEM3 – 20° Mask Angle	173
Figure 6-10 CSI GBX-Pro – 20° Mask Angle	174
Figure 6-11 MX-9212 – 20° Mask Angle	175
Figure 6-12 Isolation Probabilities During the Multipath Periods.....	176
Figure 7-1 CCG Survey Launch the Raven	177
Figure 7-2 Field Test Trajectory in Saanich Inlet, Vancouver Island.....	178
Figure 7-3 Cliffs in Saanich Inlet Taken During the Test.....	179
Figure 7-4 GPS and GLONASS Satellite Visibility at the RS During the Test.....	180
Figure 7-5 Number of Satellites and DOP at the Reference Station During the Test.....	180
Figure 7-6 Blunder Added to GPS Satellites (PRN # 3, 17, 21, 23, 26, and 31)	182
Figure 7-7 Actual Terrain – HDOP.....	183
Figure 7-8 Simulated 600 m Cliffs – HDOP.....	184
Figure 7-9 Actual Terrain - HPE 6 SVs During Ramps.....	185
Figure 7-10 Simulated 600 m Cliffs - HPE 6 SVs During Ramps.....	185
Figure A-1 HDOP 95% for the World using the Constellation #1.	193
Figure A-2 HDOP 95% for the World using the Constellation #2.	194
Figure A-3 HDOP 95% for the World using the Constellation #3.	194
Figure A-4 HDOP 95% for the World using the Constellation #4.	195
Figure A-5 HDOP and Number of Satellites Tracked for the Entire Test from C ³ NAVIG ² ™	196
Figure A-6 HDOP and Number of Satellites Tracked for the Entire Test from GGPLAN	196
Figure A-7 Satellite Visibility for the First Poor Geometry Period from C ³ NAVIG ² ™ (4860-8040).....	197

Figure A-8 HDOP and Number of Satellites Tracked: First Poor Geometry Period from C ³ NAVIG ² ™ (4860 - 8040).....	198
Figure A-9 Satellite Visibility for the Beginning of the First Poor Geometry Period from C ³ NAVIG ² ™ (4910 - 5000).....	198
Figure A-10 HDOP and Number of Satellites Tracked for the Beginning of the First Poor Geometry Period from C ³ NAVIG ² ™ (4910 - 5000).....	199
Figure A-11 HDOP 95% for the World using the Constellation #1 with Westward Phasing.	200
Figure A-12 HDOP 95% for the World using the Constellation #2 with Westward Phasing.	200
Figure A-13 HDOP 95% for the World using the Constellation #3 with Westward Phasing.	201
Figure A-14 HDOP 95% for the World using the Constellation #4 with Westward Phasing.	201
Figure A-15 HDOP 95% for the World using Constellation #5 with Westward Phasing.	202
Figure A-16 Satellite Locations Within Their Orbital Planes for Different Orbital Plane Phasing of Constellation #4.....	202
Figure C - 1 Multipath Simulation Summary Results Without the 3 dB Attenuation	209
Figure C - 2 Large Ship, Largest Multipath Error, Ship Orientation 60°.....	210
Figure C - 3 Large Ship, PRN 3's Code Multipath Error, Ship Orientation 60°.....	210
Figure C - 4 DLL Discriminator Output for Epochs 44363 and 44364.....	212
Figure C - 5 Autocorrelation Functions for Epoch 44364.....	214
Figure C - 6 Power Loss due to Multipath Signals.....	214
Figure D - 1 Satellite Misclosures (95%).....	217
Figure D - 2 1 st , 2 nd , and 3 rd Simultaneous Differential Satellite Misclosures (95%).....	217
Figure D - 3 Position Errors.....	218
Figure E - 1 Constant Position State Diagram.....	219
Figure E - 2 Constant Velocity State Diagram.....	221

Figure E - 3 2 Constant Acceleration State Diagram	222
Figure F - 1 Picture of CCGS Martha L. Black (CCG, 2002).....	224
Figure F - 2 Picture of CCGS F.C.G. Smith (CCG, 2002).	225
Figure F - 3 Picture of CCGS Tofino (CCG, 2002).....	226
Figure F - 4 Engineering Drawings of the CCGS Tofino (CCG, 2002)	226
Figure F - 5 Picture of the CCG Survey Launch Raven.....	227
Figure G - 1 NovAtel OEM3, 5° Mask Angle, Carrier Smoothing	228
Figure G - 2 NovAtel OEM3, 10° Mask Angle, Carrier Smoothing	229
Figure G - 3 NovAtel OEM3, 15° Mask Angle, Carrier Smoothing	229
Figure G - 4 NovAtel OEM3, 20° Mask Angle, Carrier Smoothing	230
Figure G - 5 NovAtel OEM3, 25° Mask Angle, Carrier Smoothing	230
Figure G - 6 CSI GBX-Pro, 5° Mask Angle, Carrier Smoothing.....	231
Figure G - 7 CSI GBX-Pro, 10° Mask Angle, Carrier Smoothing.....	231
Figure G - 8 CSI GBX-Pro, 15° Mask Angle, Carrier Smoothing.....	232
Figure G - 9 CSI GBX-Pro, 20° Mask Angle, Carrier Smoothing.....	232
Figure G - 10 CSI GBX-Pro, 25° Mask Angle, Carrier Smoothing.....	233
Figure G - 11 MX-9212, 5° Mask Angle, Carrier Smoothing	233
Figure G - 12 MX-9212, 10° Mask Angle, Carrier Smoothing	234
Figure G - 13 MX-9212, 15° Mask Angle, Carrier Smoothing	234
Figure G - 14 MX-9212, 20° Mask Angle, Carrier Smoothing	235
Figure G - 15 MX-9212, 25° Mask Angle, Carrier Smoothing	235
Figure H - 1 GPS Antenna Set up on the Raven	236
Figure H - 2 The Bends in Saanich Inlet.....	237
Figure H - 3 Touching the Shoreline at the End of the Survey Line.....	237

Figure H - 4 Test Set up on the Raven 238

LIST OF SYMBOLS

ϵ	European Union currency also called Euros
\parallel	parallel component
$\hat{\parallel}$	unit vector in the parallel direction
\perp	perpendicular component
$\hat{\perp}$	unit vector in the perpendicular direction
∇	unknown blunder vector
$\nabla_{i\&j}$	column vector containing all zero's except the pair of MDBs
∇_o	column vector containing all zero's except for the MDB in the ith position
α_i	relative amplitude of the multipath
α	type I error
β	type II error
β	phase constant
χ^2	chi squared distribution
$\Delta\phi$	phase tracking error
$\Delta\phi_i$	error in latitude due to the ith blunder
$\Delta\lambda_i$	error in longitude due to the ith blunder
Δ_{HZ}	hydrostatic delay at zenith
Δ_{WZ}	wet component delay at zenith
δ	phase difference between the two components
$\hat{\delta}$	corrections to the parameters
$\hat{\delta}_k^-$	parameter corrections before measurement update, epoch k
$\hat{\delta}_k^+$	parameter corrections after measurement update, epoch k.
δ_o	non centrality parameter
δr	path length difference

δt	time difference
ϵ_0	permittivity of free space
$\epsilon(\Phi)$	carrier phase measurement noise
$\epsilon(p)$	pseudorange measurement noise
Φ	carrier phase
Φ_k	transition matrix
ϕ	state transition matrix
ϕ	grazing angle
κ	relative permittivity
λ	carrier phase wavelength
λ	non centrality parameter for the SSR
θ	satellite elevation angle
θ	angle between the RF signal and the earth's magnetic field
$\hat{\theta}$	receiver phase tracking point
θ_i	multipath phase delay
θ_o	direct signal's phase
θ_s	reflecting surface phase delay
ρ	reflection coefficient
ρ	total density
ρ	true geometric range
ρ_{\perp}	reflection coefficient in the perpendicular direction
ρ_{\parallel}	reflection coefficient in the parallel direction
ρ_d	dry density
ρ_w	wet density
σ	conductivity
σ	standard deviation
σ^2	variance
$\hat{\tau}$	receiver code tracking point

τ_i	multipath time delay
ν	electron collision frequency
ν	observation redundancy
ω	angular frequency
ω_g	gyro frequency
ω_p	plasma frequency
A	acceleration
A	design matrix
A_{\parallel}	direct signals parallel amplitude
A_{\perp}	direct signals perpendicular amplitude
A_k	Kalman design matrix for epoch k
A_x	x component amplitude
A_y	y component amplitude
A_{zenith}	tropospheric attenuation for a satellite at zenith
B	earth's magnetic field
B_n	carrier loop noise bandwidth
B_n	code loop noise bandwidth
C_i	innovation covariance matrix
C_l	observation covariance matrix
C_{lk}	observation covariance matrix, epoch k
$C_{\hat{r}}$	residuals covariance matrix
$C_{\hat{x}_k}^-$	parameter covariance matrix before measurement update, epoch k
$C_{\hat{x}_k}^+$	parameter covariance matrix after measurement update, epoch k
c	PRN code
c	speed of light
c	number of simultaneous blunders being tested
d	correlator spacing
d_{ion}	ionospheric error
d_{trop}	tropospheric error

dp	ephemeris error
df_{RX}	receiver frequency bias
dT_{SV}	satellite clock bias
dt_{RX}	receiver clock bias
E	early correlator
E	elevation angle
$E_{i\parallel}$	incident electric field in the parallel direction
$E_{i\perp}$	incident electric field in the perpendicular direction
E_l	LHCP gain
E_{max}	maximum value of the electric field
E_{min}	minimum value of the electric field
\vec{E}_{Mul}	incident multipath electric field
E_r	RHCP gain
$E_{r\parallel}$	reflected electric field in the parallel direction
$E_{r\perp}$	reflected electric field in the perpendicular direction
$E_{T\parallel}$	transmitted electric field in the parallel direction
$E_{T\perp}$	transmitted electric field in the perpendicular direction
e	electron charge
e	partial pressure of water vapour
e	measurement noise
F	state space parameter matrix
F	relative phasing between satellites in adjacent planes
F_1	DLL correlator factor
F_2	DLL type factor
f	frequency
f_0	GPS carrier frequency
G	state space noise matrix
h	height
h_m	equivalent height for oxygen

I	identity matrix
I	in-phase component
IE	in-phase early correlator
IL	in-phase late correlator
IP	in-phase prompt correlator
I_c	$n \times c$ matrix containing all zero's except for ones in the locations of the residuals being tested
i	inclination angle
i	innovation sequence
j	imaginary number $\sqrt{-1}$
K_k	Kalman gain, epoch k
K_1	tropospheric refractivity constant
K_2	tropospheric refractivity constant
K_3	tropospheric refractivity constant
L	late correlator
L^{-1}	inverse Laplace transform
M_d	molecular weight of dry air
M_w	molecular weight of wet air
m	electron mass
$m(\Phi)$	carrier phase multipath error
$m(E)$	elevation mapping function
$m(p)$	pseudorange multipath error
$m_H(E)$	hydrostatic mapping function
$m_W(E)$	wet component mapping function
N	carrier phase integer ambiguity
N	electron density
N	tropospheric refractivity
N	normal matrix
n	index of refraction
n	normal distribution

n	number of observations
n_g	group index of refraction
n_p	phase index of refraction
P	weight matrix
P	prompt correlator
P	number of orbital planes
P_d	partial pressure of dry air
p	pseudorange
Q	quadra-phase
QE	quadra -phase early correlator
QL	quadra -phase late correlator
QP	quadra -phase prompt correlator
Q_k	process noise covariance matrix, epoch k
Q_{k-1}	process noise covariance matrix, epoch $k-1$
q	noise covariance
R	redundancy matrix
R	universal gas constant
R	autocorrelation function
R_e	earth's radius
\hat{r}	least squares residuals
S	spectral amplitude for the white noise driving functions
T	predetection integration time
T	temperature
T	time constant
T	total number of satellites
t	time
td	correlator spacing
V_{oc}	open circuit voltage
W	observation weight matrix
w	white noise driving function

x	filter parameters
\dot{x}	time derivative of the parameters
\hat{x}_k^+	parameters after measurement update, epoch k
\hat{x}_k^-	parameters before measurement update, epoch k
z_k	linearized measurement vector, epoch k
Z_w	wet compressibility factor
Z_d	dry compressibility factor

LIST OF ABBREVIATIONS

3D	Three Dimensional
AOR-E	Atlantic Ocean Region East
AOR-W	Atlantic Ocean Region West
AR	Axial Ratio
AS	Anti Spoofing
BOC	Binary Offset Carrier
BPSK	Binary Phase Shift Keying
C/A	Clear Acquisition or Coarse Acquisition Code
c/n_0	Carrier to Noise Power as ratio
C/N_0	Carrier to Noise Power in dB
CCG	Canadian Coast Guard
CCGS	Canadian Coast Guard Ship
CDMA	Code Division Multiple Access
CGSIC	Civil GPS Service Interface Committee
CHS	Canadian Hydrographic Service
COSPAS-SARSAT	Soviet Search and Rescue Satellite System - Search and Rescue Satellite Aided Tracking
CS	Control Station
cm	centimetres
dB	decibels
DGEO	Differential GEO
DGLO	Differential GLONASS
DGNSS	Differential Global Navigation Satellite System
DGPS	Differential Global Positioning System
DLL	Delay Lock Loop
DLR	Institute for Communication and Navigation, Navigation and Guiding Systems, Neustrelitz
DOP	Dilution of Precision
ECDIS	Electronic Chart Display and Information Systems

EDOP	East Dilution of Precision
EGNOS	European Geostationary Navigation Overlay Service
ESA	European Space Agency
FDMA	Frequency Division Multiple Access
FOC	Full Operational Capability
GEO	Geosynchronous Earth Orbiting
GGPLAN	GPS GLONASS Pseudolite Analysis Program
GLONASS	Global Navigation Satellite System (Russian System)
GLOSP	GLONASS Single Point
GNSS	Global Navigation Satellite System (Generic name)
GPS	Global Positioning System
GSS	Global Simulation Systems
HDOP	Horizontal Dilution of Precision
HPE	Horizontal Position Error
HPL	Horizontal Protection Limit
IALA	International Association of Light House Authorities
IGS	International GPS Service
IHO	International Hydrographic Organisation
IM	Integrity Monitor
INMARSAT	International Marine/Maritime Satellite
IOC	Initial Operational Capability
ION AM	Institute of Navigation Annual Meeting
ION GPS	Institute of Navigation GPS Meeting
ION NTM	Institute of Navigation National Technical Meeting
IOR	Indian Ocean Region
IOS	Institute of Ocean Sciences
kHz	kilohertz
L1	GPS Link 1, carrier frequency = 1575.42 MHz
L2 C	GPS Civil signal on L2
L2	GPS Link 2, carrier frequency = 1227.6 MHz

L5	GPS Link 5, carrier frequency = 1176.45 MHz
LHCP	Left Hand Circular Polarisation
LHEP	Left Hand Elliptical Polarisation
LORAN	Long Range Navigation
m	metre
MDB	Marginally Detectable Blunder
MEO	Medium Earth Orbiting
MHE	Maximum Horizontal Error
MHz	Megahertz
mm	millimetre
MRA	Maximum Residual Algorithm
MSAS	MTSAT Satellite Augmentation System (Japan)
MTBF	Mean Time Between Failure
MTSAT	Multi-Function Transport Satellite (Japan)
MTTR	Mean Time to Repair
NDOP	North Dilution of Precision
OTF	On the Fly Positioning
P	Precise Code
PA	Power Amplifier
PLC	Programmable Logic Controller
PLL	Phase Lock Loop
POR	Pacific Ocean Region
ppm	parts per million
PRC	Pseudorange Corrections
PRN	Pseudorandom Noise
PRR	Pseudorange Residuals
PRS	Public Regulated Service
PZ	Parameters of the Earth (Russian)
RADAR	Radio Detecting and Ranging
RAIM	Receiver Autonomous Integrity Monitoring

RF	Radio Frequency
RHCP	Right Hand Circular Polarisation
RHEP	Right Hand Elliptical Polarisation
RMS	Root Mean Square
RRC	Range Rate Corrections
RRR	Range Rate Residuals
RS	Reference Station
RTCA	Radio Technical Commission for Aeronautics
RTCM	Radio Technical Committee for Maritime Services
RTK	Real Time Kinematic (Carrier Phase Positioning)
SA	Selective Availability
SBAS	Satellite Based Augmentation Systems
SED	Storm Enhanced Density
SIS	Signal in Space
SMR	Signal to Multipath Ratio
SOL	Safety of Life
SSI	Sum Squared Innovations
SSR	Sum Squared Residuals
SV	Space Vehicle
TCAR	Three Frequency Carrier Phase Ambiguity Resolution
TEC	Total Electron Content
TECU	Total Electron Content Units
TX	Transmitter
UERE	User Equivalent Range Error
UPS	Uninterruptible Power Supply
USCG	United States Coast Guard
UTC	Coordinated Universal Time
VDOP	Vertical Dilution of Precision
VPE	Vertical Position Error
WAAS	Wide-Area Augmentation System

WGS	World Geodetic System
Y	Code used in place of the P-code for anti-spoofing

CHAPTER 1

INTRODUCTION

Marine navigation and positioning have been dramatically changed with the advent of the Global Positioning System (GPS). With its worldwide coverage and absolute positioning accuracy of 100 m (95%) with selective availability (SA) on (U.S. Department of Defense, 1995), marine users quickly migrated from radiobeacon direction finding, long range navigation (LORAN-C) and Transit, to GPS as their primary electronic navigational aid. This trend was accelerated when differential GPS (DGPS) code based services became available, which improved the positioning accuracy to several metres (95%). With the deactivation of SA on May 1, 2000 (Office of the U.S. President's Press Secretary, 2000), even more users will migrate to GPS, since the single point positioning accuracy is now in the 8-20 m (95%) range (U.S. Department of Defense, 2001). Many in the marine industry would agree that the combination of electronic chart display and information systems (ECDIS) and DGPS technologies represents the greatest advancement in navigation since the introduction of RADAR to the bridge. The dynamic electronic chart, with DGPS positioning, continually displays where the vessel actually is and where it is headed with unprecedented accuracy. Alarms are automatically generated if the ship ventures into shallow water, crosses a user defined area (e.g. drags its anchor), et cetera. This allows ships to navigate safely in constricted and shallow channels as well as under reduced visibility. Commercial shipping companies are recognising the potential operational efficiencies of modern electronic navigation. Recent marine accidents have also focused attention on the safety and environmental protection value of electronic

navigation. There has been increasing demand from many quarters for DGPS service, particularly from those outfitting their ships and fleets with electronic charts.

World-wide marine DGPS systems are being implemented in increasing numbers of maritime countries by both private companies (i.e. Omnistar) and government agencies (i.e. members of the International Association of Lighthouse Authorities (IALA)). Figure 1-1 shows the location and coverage from the differential global navigation satellite system (DGNSS) reference and transmitting stations in the maritime radiobeacon band (IALA, 1999 and CSI Wireless Inc., 2000). The current operational stations are shown in red with green coverage contours and the planned stations are in blue with grey contours. Marine DGPS is a worldwide endeavour.

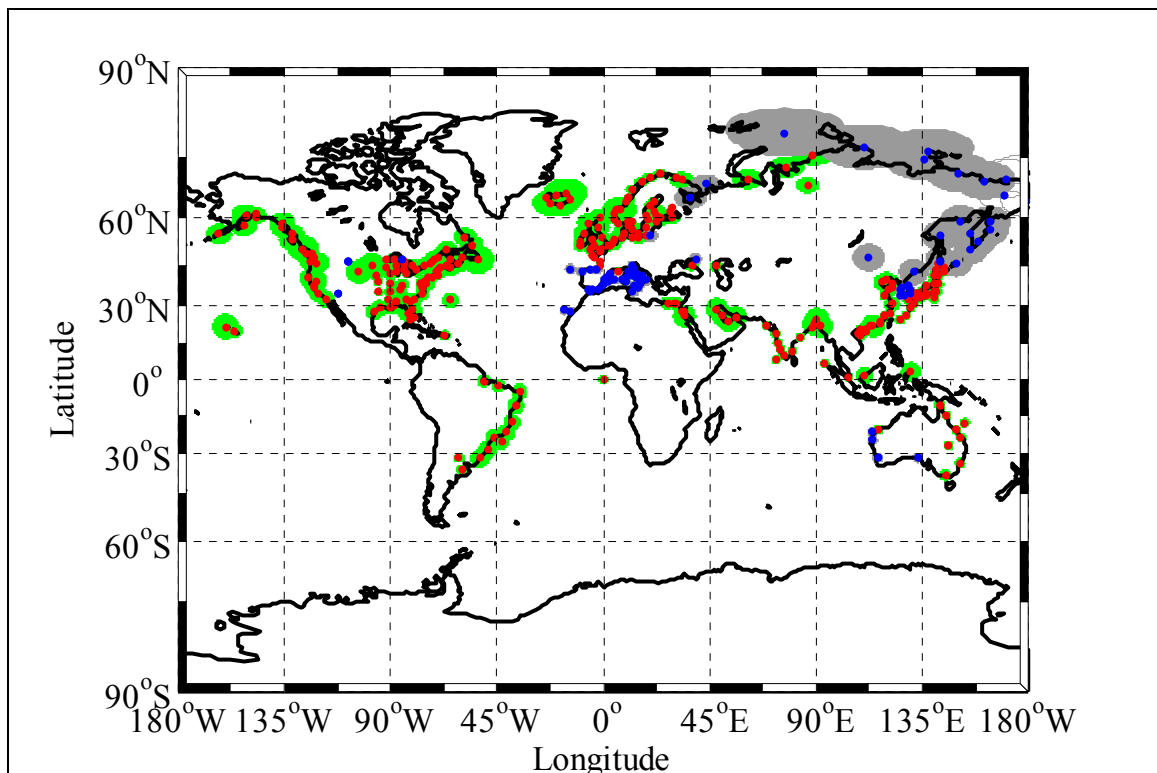


Figure 1-1 World Wide Marine DGPS Stations (Lachapelle et al., 2002b)

In North America, both the United States Coast Guard (USCG) and the Canadian Coast Guard (CCG) are providing free DGPS corrections via marine radiobeacons (285-325

kHz). The USCG and the CCG declared their DGPS systems to be fully operational on March 12, 1999 (Office of the Assistant Secretary of Transportation, 1999) and on May 25, 2000 (Fisheries and Oceans Canada, 2000) respectively. The levels of service being provided by the two Coast Guards are essentially identical (USCG, 1993 and CCG, 1996), with both systems using Ashtech reference stations (based on the Ashtech Z-12™ receiver). While the horizontal accuracy specification for both systems is 10 m (95%), metre level positioning is achievable if the user employs a high quality GPS receiver.

Marine navigation and positioning accuracy requirements vary greatly depending on the application, from hundreds of metres for oceanic navigation, to centimetres for three dimensional (3D) navigation in constricted waterways. Table 1-1 lists the major requirements.

Table 1-1 Marine Accuracy Requirements

Applications	95% Accuracy
Safety of Navigation (U.S. Department of Defense and U.S. Department of Transport, 1999)	
Ocean Phase	1.8 - 3.7 km
Coastal Phase	460 m
Harbour and Harbour Approach	8 – 20 m
Inland Waterways	2 – 5 m
Other Desirable Requirements (Lachapelle, 1998)	
Placing Aids to Navigation	< 5 m
Resource Exploration	1 - 5 m
3D Navigation in constricted Channels	< 10 cm

Thus the public marine DGPS systems can meet all of the requirements of Table 1-1, except the 10 cm requirement. This can only be met using an on-the-fly (OTF) carrier phase positioning system, which is outside the scope of the current marine DGPS systems and this research. However, OTF systems are being studied by other investigators (e.g. Raquet, 1998, Fortes et al., 1999, and Lachapelle et al., 2000).

The introduction of DGPS has also changed hydrographic surveying. In the past, specialised user-owned positioning systems would be installed on the hydrographic vessel as well as on the shore. The equipment was expensive and set-up very time consuming since line of site was required to the shore stations. Today, these expensive systems have been replaced with relatively inexpensive user-owned GPS receivers on the vessel, supplemented with DGPS corrections from either a private or public service. The horizontal positioning requirements for hydrographic surveying depend on the specific surveying environment, and are summarised in Table 1-2.

Table 1-2 Summary of Minimum Standards for Hydrographic Surveys (IHO, 1998)

Order	Examples of Typical Areas	Horizontal Accuracy (95% confidence level)
Special	Harbours, berthing areas, and associated critical channels with minimum under-keel clearance	2 m
1	Harbours, harbour approach channels, recommended tracks, and some coastal areas with depths up to 100 m	5 m + 5% of depth
2	Areas not described in Special Order and Order 1, or areas up to 200 m water depth	20 m + 5% of depth
3	Offshore areas not described in Special Order, Orders 1 and 2	150 m + 5 % of depth

All of these requirements can be met with the marine DGPS system assuming that survey grade receivers are employed.

Although the accuracy requirements of the systems can be achieved, questions remain as to the reliability of the DGPS corrections, and of the resulting positions. As the mariner begins to use DGPS and ECDIS as the sole means of navigation, ensuring the reliability of the position solution becomes paramount. The reliability of a marine DGPS system is composed of two parts, namely the shore based network of DGPS stations that generate and transmit the DGPS corrections, and marine users' equipment which applies the DGPS corrections. Although the methodology used by the IALA nations to generate and check the DGPS corrections is sound, hard numbers for the reliability of these corrections

are not available. The following section applies to the CCG DGPS System (Ryan et al., 1997), however, all of the other IALA nations that have implemented marine DGPS systems are using a similar configuration.

1.1 CCG DGPS Shore System Reliability

The reliability of the shore based network of DGPS stations can be sub-divided into equipment reliability and the reliability of the DGPS corrections (no blunders are contained in the DGPS corrections). The CCG's equipment reliability is addressed by installing redundant units for each of the major DGPS components, as shown in Figure 1-2.

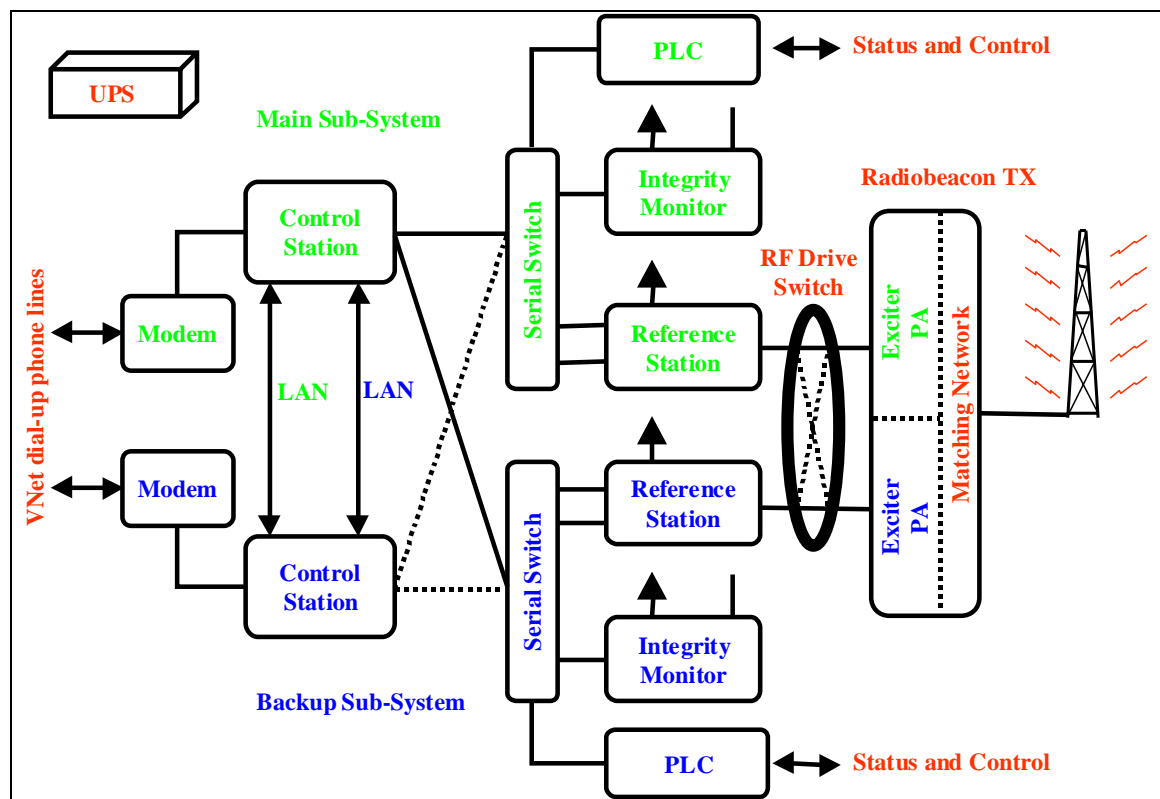


Figure 1-2 CCG DGPS Station Block Diagram

The reference station (RS), integrity monitor (IM), control station (CS), serial switch, programmable logic controller (PLC), radio frequency (RF) drive switch, radiobeacon

transmitter (TX) including the power amplifier (PA), and modems all have hot standby units. The only components that are not backed up are the radiobeacon transmitting antenna and the uninterruptible power supply (UPS). It would not be cost effective to have a redundant radiobeacon antenna, since such structures are very expensive and considered to be very robust and reliable. While the UPS is not a high cost device, its high reliability and soft failure modes obviate the need for a backup.

The required equipment reliability for each CCG DGPS station is 99.7% (CCG, 1996). Using the DGPS station configuration given in Figure 1-2 and the individual components mean time between failure (MTBF) and mean time to repair (MTTR) values, the resulting station reliability was calculated. The individual component reliabilities were computed via:

$$\text{Component Reliability} = \frac{\text{MTBF}}{\text{MTBF} + \text{MTTR}} \quad (1-1)$$

Since the DGPS stations are often sited in remote locations a large value of MTTR was used (60 hours). The MTBF values for all of the equipment except the radiobeacon were obtained from the manufacturers. The radiobeacon's reliability was calculated from an existing CCG database. Redundant devices were modelled as being in parallel and their protected reliability is given by

$$\text{Protected Reliability} = 1 - (1 - \text{Component Reliability})^2 \quad (1-2)$$

All of the other devices are modelled as being in series, thus their respective reliabilities are multiplied together to generate the overall DGPS site reliability. The results of the reliability calculation are shown in Table 1-3. The resulting DGPS station reliability was 99.745%, which met the requirement of 99.7%. The reliability analysis assumed that there was a spare available for every failure. A separate spares analysis was performed to determine the number of spares required for each piece of equipment. For more details on the reliability and spares analysis see Ryan et al. (1997).

Table 1-3 DGPS Site Reliability Calculation

Equipment	MTBF	MTTR	Reliability
RF Sub-System			
<i>IM</i>	<i>10,000</i>	<i>60</i>	<i>99.404%</i>
Protected IM			99.996%
<i>RS</i>	<i>10,000</i>	<i>60</i>	<i>99.404%</i>
Protected RS			99.996%
RF Drive Switch	100,000	60	99.940%
Radiobeacon	40,000	60	99.850%
Sub-System Total			99.783%
Control Sub-System			
<i>PLC</i>	<i>170,000</i>	<i>60</i>	<i>99.965%</i>
Protected PLC			100.000%
<i>CS</i>	<i>90,000</i>	<i>60</i>	<i>99.933%</i>
Protected CS			100.000%
<i>Serial Switch</i>	<i>40,000</i>	<i>60</i>	<i>99.850%</i>
Protected Serial Switch			100.000%
Sub-System Total			100.000%
Non Prime Mission Sub-System			
UPS	160,000	60	99.963%
Sub-System Total			99.963%
Summary			
RF Sub-System			99.783%
Control Sub-System			100.000%
Non-Prime Mission Sub-System			99.963%
DGPS Station Total			99.745%

This ensures that the DGPS stations are continuously transmitting the DGPS corrections, however it does not ensure that the DGPS corrections themselves are free from blunders.

The installations of the DGPS sites were done to maximise the reliability of the

corrections to the users. The GPS antennas were situated to minimise multipath and maximise satellite visibility. To help reduce multipath, the GPS antennas also contain either a ground plane or a chokering. The goal was to have near multipath-free observables for all satellites above the horizon.

The reliability of the DGPS corrections is ensured by checking them in real time as follows (RTCM, 1999 and CCG, 1996). The RS checks the magnitude of the pseudorange corrections (PRC) and range rate corrections (RRC). Similarly the IM checks the magnitude of the pseudorange residuals (PRR), range rate residuals (RRR), and the horizontal position error (HPE). Table 1-4 describes the integrity checks and the corrective actions. With these integrity checks and the quality installation of the GPS antennas, one can be assured that the corrections being transmitted are reliable.

Table 1-4 RS and IM Integrity Checks

Threshold	Checked By	Failure	Corrective Action
PRC / RRC	RS	a correction is too large	RS informs CS
PRR / RRR	IM	a residual is too large	IM informs RS and CS RS stops broadcasting corrections for that satellite
HPE	IM	position error is too high	IM informs RS and CS RS changes the broadcast from healthy to do not use.

1.2 Shortcomings of Marine DGPS

While the DGPS corrections from the marine DGPS stations are available and reliable, this does not guarantee that the marine user's position will also be available and reliable due to the following concerns:

- 1) User multipath
- 2) User receiver blunders (wrong code, incorrect time tags, etc.)
- 3) Troposphere and ionosphere spatial decorrelation and mismodelling
- 4) Masking effects resulting in weak or unusable geometry

The first three items introduce blunders into the observables, which if undetected will bias the navigation solution. Blunders can be detected and isolated by testing the least squares residuals or Kalman filter innovation sequence. However, in order to detect and isolate the blunders, redundancy must exist. Masking effects can reduce the redundancy to the point where reliable navigation is not possible. This does not mean that the position is necessarily “bad”, it merely means that an undetected blunder could bias the position more than the specified threshold. Assuming that the GPS receiver employed a real time reliability algorithm, the mariner would be notified when the geometry / redundancy was insufficient and the mariner could act accordingly. While this would seem to be a standard feature for any navigation receiver, many GPS receivers do not employ any type of reliability algorithm (CHAPTER 6). If a blunder occurred these receivers would pass incorrect and misleading information to the mariner. This could be potentially dangerous.

The navigation solution is available if the dilution of precision (DOP) is less than a predefined threshold. For marine navigation a horizontal dilution of precision (HDOP) of 2.0 is usually used. Since availability is based solely on geometry, only the masking effects of the environment affects the availability. Most availability problems for marine navigation and positioning occur in constricted waterways and during hydrographic surveying. In open areas GPS does not have an availability problem (section 4.2.1). Thus there are two main problems with the current marine DGPS navigation and positioning systems:

- 1) In constricted waterways and during hydrographic surveying DGPS navigation is often unavailable and/or unreliable, due to signal masking.
- 2) Even when redundancy exists, many marine user receivers do not employ an internal reliability algorithm, which allows blunders to bias their navigation solution.

The availability and reliability of the navigation solution was studied by Morley (1997) through augmenting DGPS with pseudolites and a height constraint. While the height constraint is very applicable to marine navigation, augmenting DGPS with pseudolites

can be problematic. A pseudolite can only cover a small area and is very expensive to install and maintain, since an entire remote site must be built and maintained to house the pseudolite. While pseudolite augmentations are ideal for local constricted waterways such as the approaches to Montréal, Québec City, or Vancouver harbour, it is not feasible for general marine navigation augmentation. The USCG has tested augmenting single point GPS with single point Global Navigation Satellite System (GLONASS) (Spalding and van Diggelen, 1997, and Spalding, 1998), and found that it could be used to “replace the use of horizontal sextant angles for positioning USCG aids to navigation around the world.”

The USCG has also tried to address the second problem of the user receivers not employing an internal reliability algorithm, by developing an external algorithm in conjunction with NAVSYS Corporation (van Diggelen et al., 1993, and Spalding et al., 1993). While the initial algorithm performed well during its first series of tests, the navigation availability during subsequent field tests was extremely low. The subsequent addition of tidal information into the model significantly improved the navigation availability (LaMance et al., 1995), however, availability improvements are still required.

1.3 Thesis Components

The next logical step is to augment DGPS with other satellite-based navigation systems and constraints. This thesis concentrates on investigating the improvements in availability and reliability attained by augmenting DGPS with the following additional navigation systems and constraints:

- 1) Russia’s GLONASS System added in single point mode (currently available)
- 2) Russia’s GLONASS System added in differential mode (user must install a base station)
- 3) Europe’s Galileo System added in differential mode (currently in the planning stage)

- 4) Geostationary satellites added in differential mode (being implemented for satellite-based augmentation systems (SBAS) world-wide)
- 5) Height constraint (specifying a height variance or process noise value)
- 6) Clock constraint (specifying a clock variance or process noise value)
- 7) Dynamic constraints (specifying the process noise values for a particular vessel)

The availability improvement attained through augmentations is a function of geometry, and can be determined without an explicit analysis of the DGPS error sources. However, the reliability improvement depends on the types of blunders (i.e. DGPS error sources) that can occur. Thus the DGPS error sources must be analysed, as discussed in section 2.5 and CHAPTER 3. Once the blunder's characteristics have been defined, the next task is to determine the reliability model that will be used to detect and isolate them, which is discussed in section 2.6. The dynamic constraints augmentation is implemented through a tuned Kalman filter, section 2.9 describes how the filter parameters were determined. Once the types of blunders, the reliability theory, and the Kalman filter parameters have been determined, the analysis of the availability and reliability improvements attained through augmentations were performed as follows:

- 1) Software simulations (CHAPTER 4) were conducted to investigate the improvements in reliability and availability attained through augmentation.
- 2) Static tests (CHAPTER 5) were conducted using an integrated GPS and GLONASS receiver, to validate the receiver and processing software.
- 3) Hardware simulations (CHAPTER 6) using a DGPS signal simulator were conducted for several marine user receivers, to assess the receiver's internal reliability algorithms, as well as external least squares and Kalman filter reliability algorithms.
- 4) A field trial (CHAPTER 7) was conducted in Saanich Inlet, British Columbia using an integrated GPS and GLONASS receiver to assess the reliability and availability improvements achieved through augmentations in an actual hydrographic surveying environment.

CHAPTER 2

THEORY

Before the improvements in availability and reliability attained by augmenting DGPS can be discussed, the theory and background behind satellite-based navigation and positioning must be presented. GPS and GLONASS, components of the global navigation satellite system (GNSS)-1, will be introduced, followed by Galileo, Europe's future system. Galileo and the modernised components of GNSS-1 will comprise GNSS-2. Potential SBAS will then be discussed. This is followed by a detailed discussion of the GNSS error sources, with emphasis on the potential blunder magnitudes. The chapter concludes with least squares and Kalman filter reliability theory.

2.1 GPS Overview

The GPS system is a U.S. military owned and operated satellite-based navigation system. It is a world wide all weather navigation system providing real time measures of position, velocity, and time. The U.S. military began work on the GPS system in 1973 building on their experience with the Transit navigation system (Parkinson, 1996). The GPS system reached full operational capability (FOC) on July 17, 1995 (Office of the Assistant Secretary of Defense, 1995). The GPS system, like all satellite-based navigation systems, is composed of three segments: the space, control and user segments. The space segment consists of a nominal constellation of 24 medium earth orbiting (MEO) satellites inclined at 55° with an orbital radius of 26,560 km (12 sidereal hour period). The constellation was designed with six equally spaced orbital planes with four unequal spaced satellites in each plane. The satellites were unequally spaced to minimise the effect of a single satellite outage on the availability of the navigation service (Spilker, 1994b). The orbital

locations of the current constellation of 28 satellites is shown in Figure 2-1, using the YUMA almanac for week 1167 (week of May 19, 2002). Note the six orbital planes and the unequal spacing within each plane. The four satellites above the nominal 24 satellite constellation are almost adjacent to an older satellite.

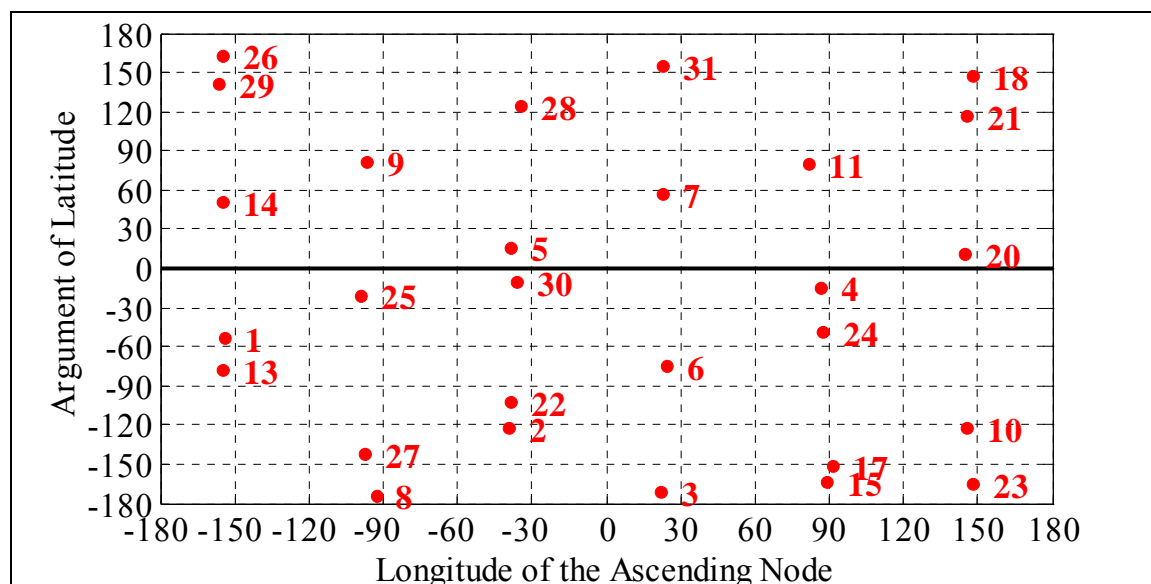


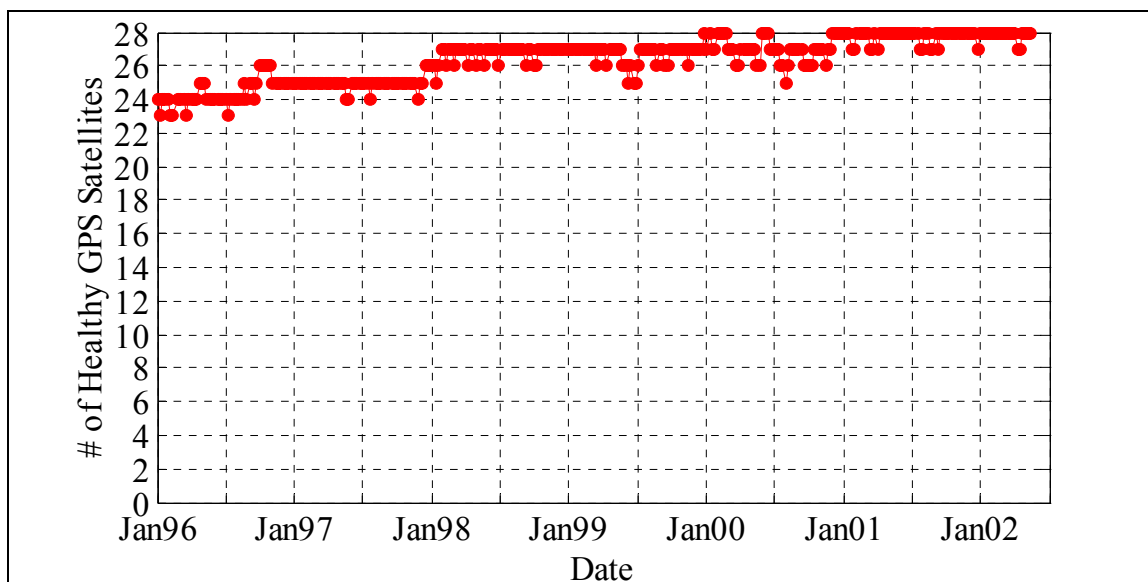
Figure 2-1 Orbital Locations for the GPS Constellation (YUMA Almanac 1167)

The satellites transmit on two frequencies L1 (1575.42 MHz) and L2 (1227.60 MHz), which enable authorised users to correct for the effect of the ionosphere. The GPS system transmits two codes: the clear acquisition or coarse acquisition (C/A) code, and the precise (P) code. Table 2-1 lists the code specifications. On L1 both the C/A and P codes are transmitted in phase quadrature to each other, while on L2 only the P code is transmitted. Code division multiple access (CDMA) is employed, with each satellite transmitting a different C/A code (Gold Code). Although the P Code's period is greater than 38 weeks, each satellite only transmits one week of the total code. The P code is currently encrypted (Y code), which prevents authorised receivers from being spoofed by a potential jamming signal. This is called anti-spoofing (AS). The U.S. has offered the GPS standard positioning service to the worldwide civilian community for free (Office of Science and Technology Policy, 1996).

Table 2-1 GPS Code Specifications

Code	Length Chips	Rate	Period	Chip Length
C/A	1023	1.023 MHz	1 ms	293 m
P	4.1547×10^{14}	10.23 MHz	38.058 weeks	29.3 m

In order to have reliable satellite-based navigation, the health of the GPS constellation is paramount. Figure 2-2 shows the number of healthy GPS satellites reported from the GPS almanac since January 1996. During the past year the minimum number of healthy GPS satellites has been 27 with a high of 28. The one satellite jumps in the figure are caused by the U.S. military performing maintenance on the constellation. From a classical black box reliability standpoint the GPS system has been highly reliable.

**Figure 2-2 Number of Healthy GPS Satellites vs. Time**

Even as GPS was reaching FOC, both public and private organisations were augmenting the constellation to improve its accuracy, integrity, and to a lesser degree its availability. These augmentations are still being deployed for surveying, marine, land, and aviation applications. To respond to the growing user requirements in both the civilian and military communities for additional ranging signals and increased power, the GPS system itself is being modernised (Office of the U.S. Vice President, 1999). The modernisation

program has been broken into two stages: GPS II and GPS III. These are summarised in Table 2-2.

GPS II will see a second civilian frequency added to L2, and a third safety of life civilian signal added at 1176.45 MHz (L5). New military signals will also be added to both L1 and L2. The civilian signal added to L2, called L2C, will be added to the last 12 block IIR satellites (IIR-M). The L2C and L5 civilian signals will be added to the block IIF satellites. There are currently no plans to increase the size of the constellation or to include integrity monitoring within the GPS II constellation. The first block IIR-M satellite is scheduled to be launched in 2003.

Table 2-2 GPS Modernisation Activities (Lachapelle and Ryan, 2001)

Activity	Implementation Date
SA Set to Zero	May 2000
GPS IIR-M Enhancements <ul style="list-style-type: none"> • New Civil code on L2, M-Code on L1 and L2 	2003-2006
GPS IIF Enhancements <ul style="list-style-type: none"> • New Civil code on L2, M-Code on L1 and L2, L5 	2005-2010
GPS III Enhancements <ul style="list-style-type: none"> • New Civil code on L2, M-Code on L1 and L2, L5 • Increased power for the M Code • Future Capabilities 	2010 – To Be Determined
Operational Control Segment Enhancements	2000-2008

Although satellites with L2C will soon be launched (in 2003) it will still be several years until enough L2C equipped satellites are in orbit for users to realise the benefits of the second civilian signal. Similarly the first space vehicle (SV) equipped with L5 will not be launched until approximately 2005. Figure 2-3 shows the estimated time frame for the deployment of the L2C and L5 civilian signals. The figure highlights when the signals will reach initial operating capability (IOC) and FOC.

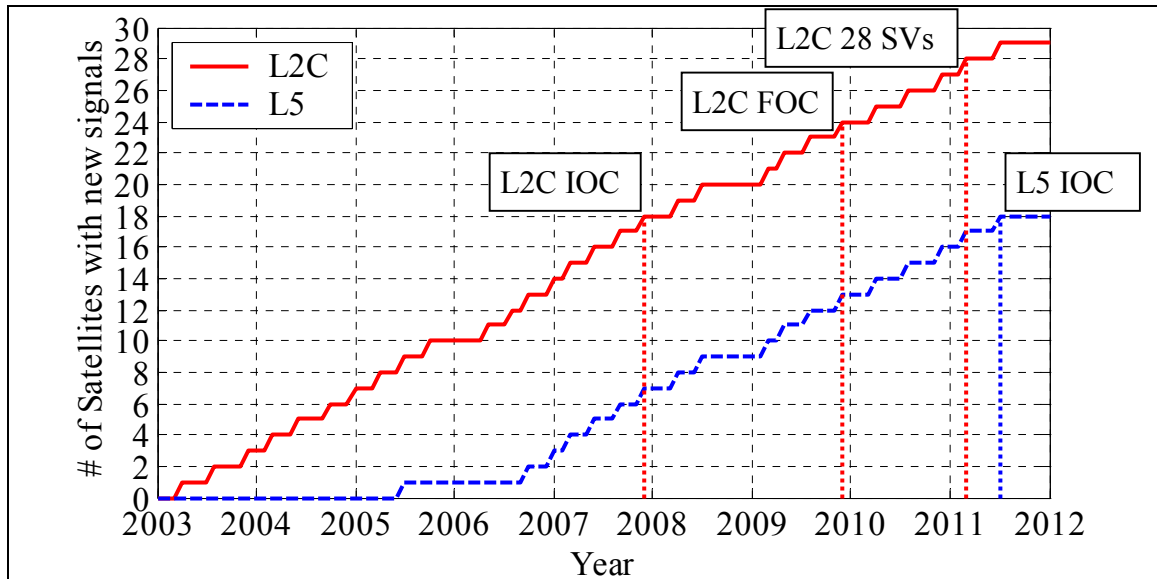


Figure 2-3 Number of Satellites with L2C and L5 signals (Fontana et al., 2001a).

GPS II will have the following effects on marine navigation (Lachapelle and Ryan, 2001):

- 1) Dual frequency civilian receivers will allow marine users to correct for the ionospheric delay, which should reduce the single point positioning accuracy from approximately 20 m to 8 m (95%), which should meet many of their positioning requirements.
- 2) Signal acquisition and tracking will be greatly improved, due to the more robust L2C (Fontana et al., 2001a, and Fontana et al., 2001b), and L5 (Van Dierendonck and Hegarty, 2000) signal formats.
- 3) The reliability and availability of carrier phase positioning will be greatly improved due to the second and third civilian frequency. As the additional signals become operational, public OTF / real time kinematic (RTK) systems will become practical.

However, since the constellation will not contain real time integrity information, a combination of a receiver autonomous integrity monitoring (RAIM) / reliability

algorithm and marine DGPS systems will be required to provide a reliable navigation solution.

The design for the next generation of GPS satellites, GPS III, has already begun. GPS III may contain new ranging signals, a larger constellation, and real time integrity monitoring. These decisions will be influenced by the design and implementation of Europe's Galileo System. Thus the effects that GPS III will have on marine navigation are more difficult to quantify. While this is the case the following general comments can be made (Lachapelle and Ryan, 2001):

- 1) An increase in the number of satellites, will increase the availability and reliability (increased RAIM/reliability algorithm performance) of the navigation solution.
- 2) With GPS III providing real time integrity warnings, additional integrity augmentation systems will no longer be required.
- 3) Improving the accuracy of the GPS measurements will result in improved OTF / RTK performance.

For a more detailed treatment of GPS see Parkinson and Spilker (1996), Kaplan (1996), or Leick (1995).

2.2 *GLONASS Overview*

GLONASS is the Russian equivalent to the GPS system, and is under the control of The Russian Space Command. The first GLONASS satellite was launched in 1982 (Russian Federation Ministry of Defence, 2002) and the constellation reached full operational status with 24 satellites in early 1996 (DLR, 2002). While conceptually identical to GPS, the implementation of GLONASS is significantly different. Table 2-3 compares the technical characteristics of the two systems.

Table 2-3 Comparison of GPS and GLONASS (U.S. Department of Defence, 1999 and Russian Federation Ministry of Defence, 1995)

Parameter	GPS	GLONASS
Standard Precision Signal Rate (L1)	1.023 MHz	0.511 MHz
Precise Precision Signal Rate (L1/L2)	10.23 MHz	5.11 MHz
Selective Availability	Yes set to 0.	No
Anti-Spoofing	Yes	No
Signal Separation	CDMA	FDMA
Carrier Frequency k is frequency number	1575.42 MHz 1227.60 MHz	1602 +k*0.5625 MHz 1246 +k*0.4375 MHz -7<k<24
Number of Satellites (Design vs. Operational)	24 28 Operational	24 7 Operational
Number of Orbital Planes	6	3
Satellites per plane	4, unevenly spaced	8, evenly spaced
Orbital inclination	55°	64.8°
Orbital Period	11h 58m	11h 15m
Time Reference	GPS Time	UTC(SU, Russia)
Geodetic Datum	WGS-84	PZ-90
Control Segment	World wide network of stations	Network of stations in Russia.

These technical differences result in the following problems when integrating GPS and GLONASS observations together:

- 1) Since the two system time bases are not synchronised with each other, an extra parameter must be added to the navigation solution to account for the time difference. If an epoch by epoch least squares navigation solution is being employed, this extra parameter reduces the navigation redundancy by one, since the previous values and variances of the parameter cannot be propagated to the

current epoch. However, if a navigation filter (Kalman filter) is used, the slowly varying nature of the bias can be used within the filter to predict the additional parameter. When operating in differential mode the additional parameter is embedded within the differential corrections, thus the user's navigation algorithm does not have to take it into account. The system time difference parameter is only a factor in single point least squares positioning.

- 2) Since the satellite co-ordinates are referenced to different Datums, the GLONASS satellite's positions must be transformed from PZ-90 into WGS-84. This just adds extra processing to the navigation algorithm since the transformation is well known (Mitrikas et al., 1998 and Misra et al., 1996).
- 3) Since the GLONASS chip rate is half that of GPS the code measurement noise and the code's susceptibility to multipath will be doubled (assuming that all of the other factors such as correlator spacing, carrier to noise ratio, et cetera are identical). These errors are further discussed in Sections 2.5.4 and 2.5.5.
- 4) GLONASS's use of frequency division multiple access (FDMA) leads to the following problems with the GLONASS observations. First, the double difference carrier phase ambiguity is no longer an integer, due to the different satellite transmitting frequencies. Since the ambiguities cannot be fixed to integers, redundancy is lost in floating the values. Second, frequency dependent biases can corrupt the measurements due to the receiver channel's frequency response. The frequency biases are further discussed in Section 2.5.6.

However, the biggest problem with GLONASS has been the reliability of the constellation. Figure 2-4 shows the number of healthy GLONASS satellites reported from the GLONASS almanac since January 1996 (almanacs courtesy of DLR, 2002). The number of healthy GLONASS satellites has decreased from a high of 24 in 1996 to a low of four in 2002. There are currently only seven healthy satellites in the GLONASS constellation.

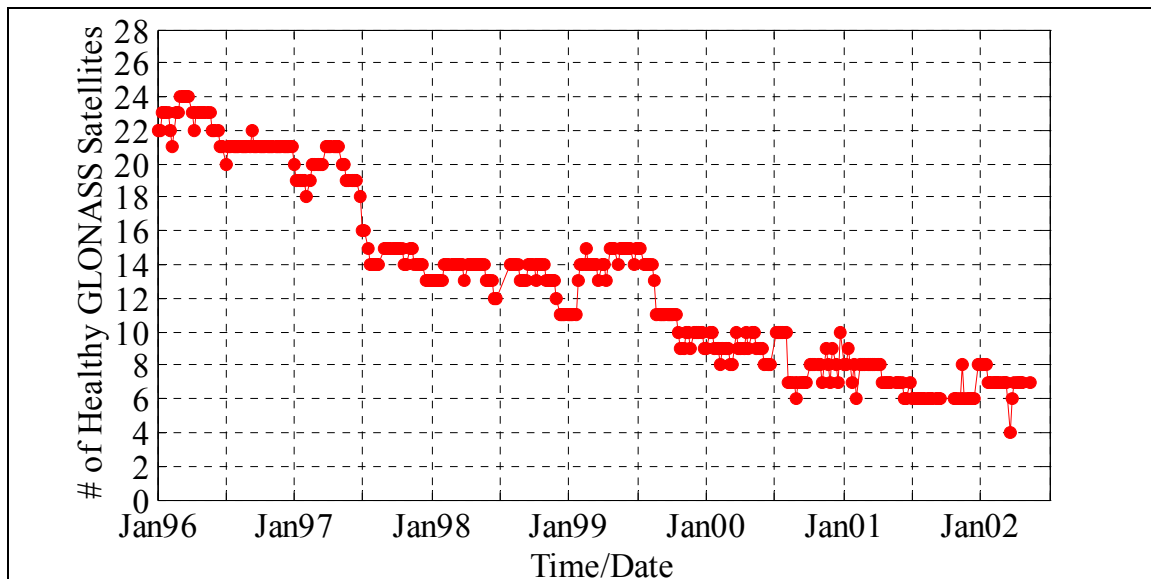


Figure 2-4 Number of Healthy GLONASS Satellites vs. Time

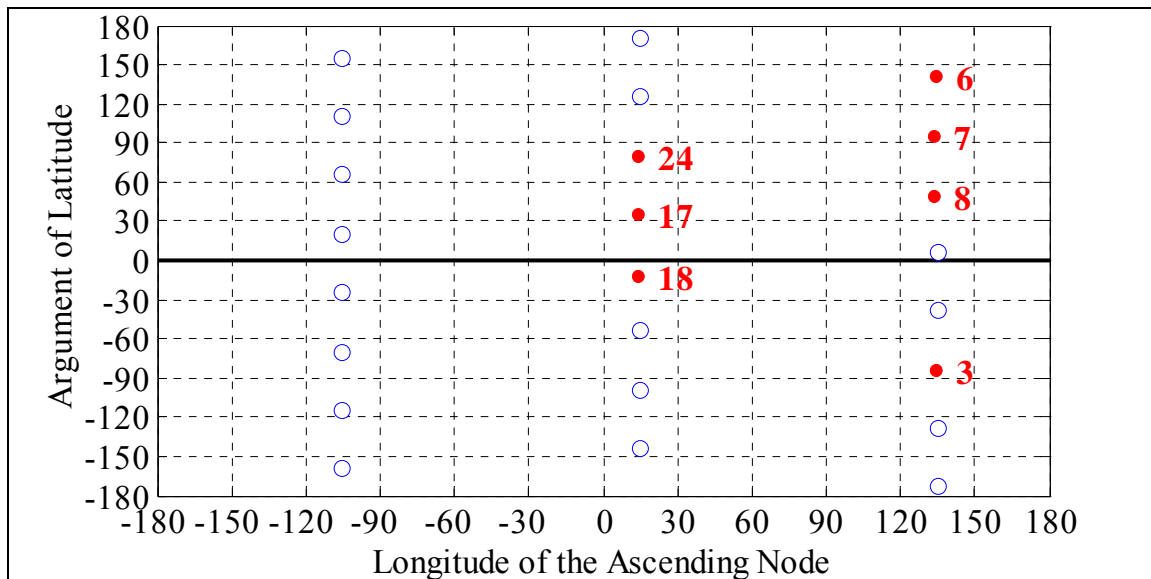


Figure 2-5 Orbital Locations for the GLONASS Constellation (GLONASS Almanac for GPS Week 1167, in YUMA Format)

The orbital locations for the nominal 24 satellite constellation and the locations of the seven healthy satellites, is shown in Figure 2-5. One orbital plane is completely devoid of satellites. With only seven healthy satellites, GLONASS cannot provide a continuous

world wide navigation service on its own. Assuming GLONASS is maintained by the Russian Federation, it is still a viable augmentation scheme for GPS, as shown in CHAPTER 4. However, this a rather large assumption given:

- 1) the political and economic instability within the Russian Federation,
- 2) the slow demise of the GLONASS constellation as depicted in Figure 2-4,
- 3) the rise of Europe's own satellite-based navigation system, reducing the need for a Russian only system.

The reliability of the GLONASS constellation is further compounded by the following two events that were reported by Cook (2001):

- 1) the launch of three new GLONASS satellites in October 2000 was plagued with problems,
- 2) a Y2K error was introduced into the GLONASS constellation on December 25, 1999. The sign of the relativistic correction was reversed and it took the GLONASS control segment 10 months to correct the error.

While GLONASS has both technical and reliability problems, if it is maintained it can have the following general benefits to navigation users:

- 1) increasing the number of observations, increases the redundancy and thus improves the availability and reliability of the navigation solution. This is true any time one increases the number of measurements.
- 2) From a classical reliability standpoint using two independent systems improves the overall reliability of the navigation solution. A latent defect in one system should not be found in the other system.

2.3 *Geostationary Augmentation Overview*

Although geostationary satellites (geosynchronous earth orbiting (GEO)) are not currently part of any operational satellite-based navigation system, the following GPS augmentations plan to use them in the future:

- 1) U.S.'s Wide Area Augmentation System (WAAS)
- 2) Europe's European Geostationary Navigation Overlay Service (EGNOS)
- 3) Japan's Multi-Function Transport Satellite (MTSAT) Satellite Augmentation System (MSAS)

The geostationary satellites that will make up these SBAS will transmit real time integrity information as well as a GPS ranging signal. The SBAS systems plan to use the following International Marine/Maritime Satellite (INMARSAT) satellites:

- 1) Pacific Ocean Region (POR) - 178° E
- 2) Indian Ocean Region (IOR) - 64° E
- 3) Atlantic Ocean Region West (AOR-W) - 54° W
- 4) Atlantic Ocean Region East (AOR-E) - 15.5° W

WAAS may augment the INMARSAT satellites with additional geostationary satellites at 100° W and 140° W (Enge and Van Dierendonck, 1995). Thus in the future a total of six geostationary satellites may be used to augment GPS.

The effectiveness of the geostationary satellite's augmentation depends on the location of the user, since the elevation angle of a geostationary satellite is a function of the user's latitude and the user's longitude in relation to the satellite. Figure 2-6 shows the elevation angles for a geostationary satellite at 0° longitude using colour contours drawn in 5° increments. At mid to high latitudes the geostationary satellite can be blocked by obstructions. For example the elevation angle to a geostationary satellite for a user at 51° N with a relative longitude of 0° is 32°, however, this drops to 10° for relative longitudes of ±60°. Contrast this with a user at the equator where even with a relative longitude of ±60° the elevation angle is 22°.

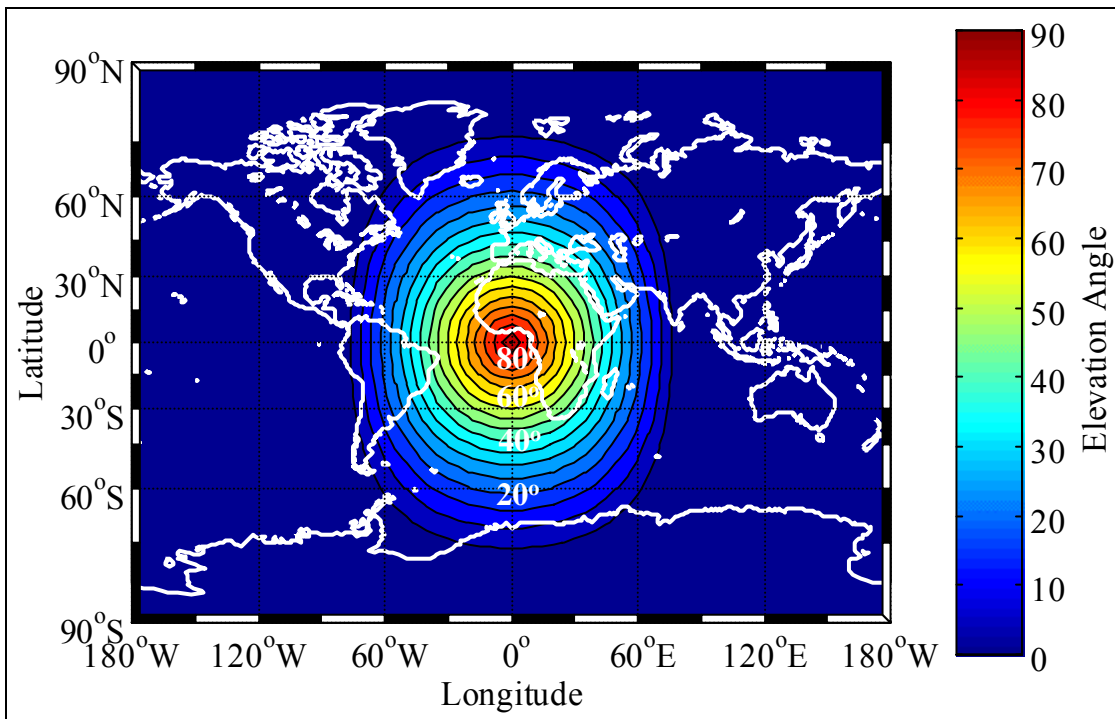


Figure 2-6 Geostationary Satellite Elevation Angle

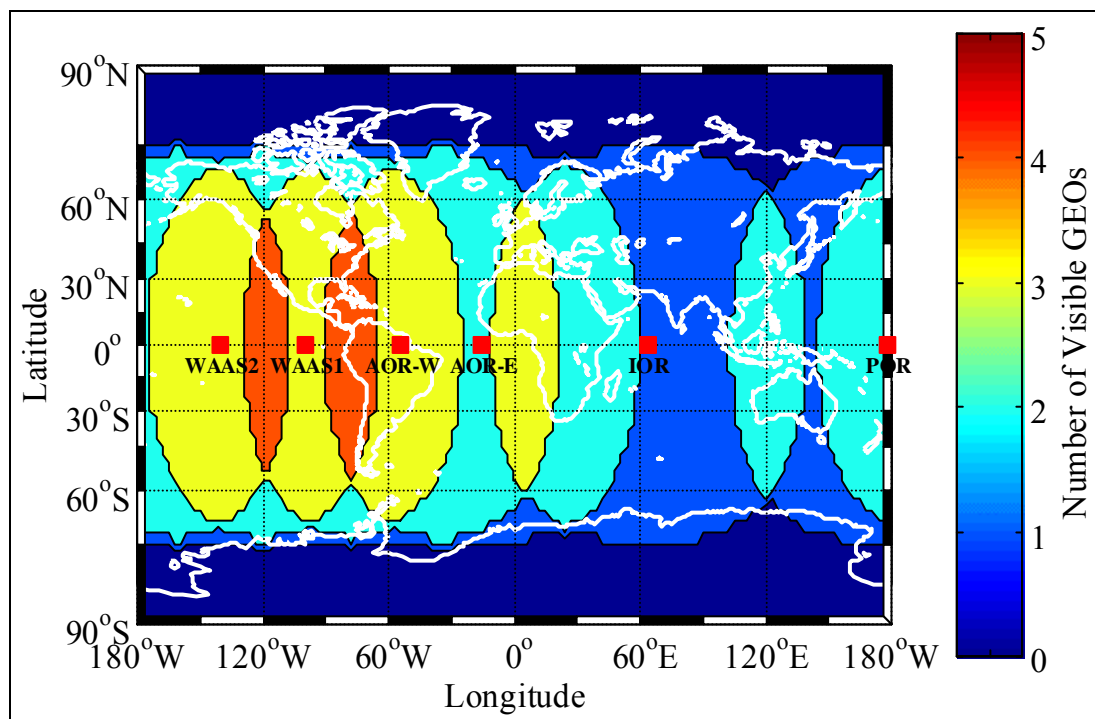


Figure 2-7 Number of Visible Geostationary Satellites (Mask Angle of 5°).

Taking the six potential GEO satellites into account, Figure 2-7 shows the number of visible geostationary satellites using an isotropic mask angle of 5° . Since these augmentations are being planned primarily for civil aviation, 5° is a reasonable isotropic mask angle. For this benign mask condition, parts of North America can see four satellites, with the majority seeing three. However, once one gets to the higher Canadian latitudes, this drops to two, one and then zero in the high north. Overall this is very good coverage for the populated areas of North America.

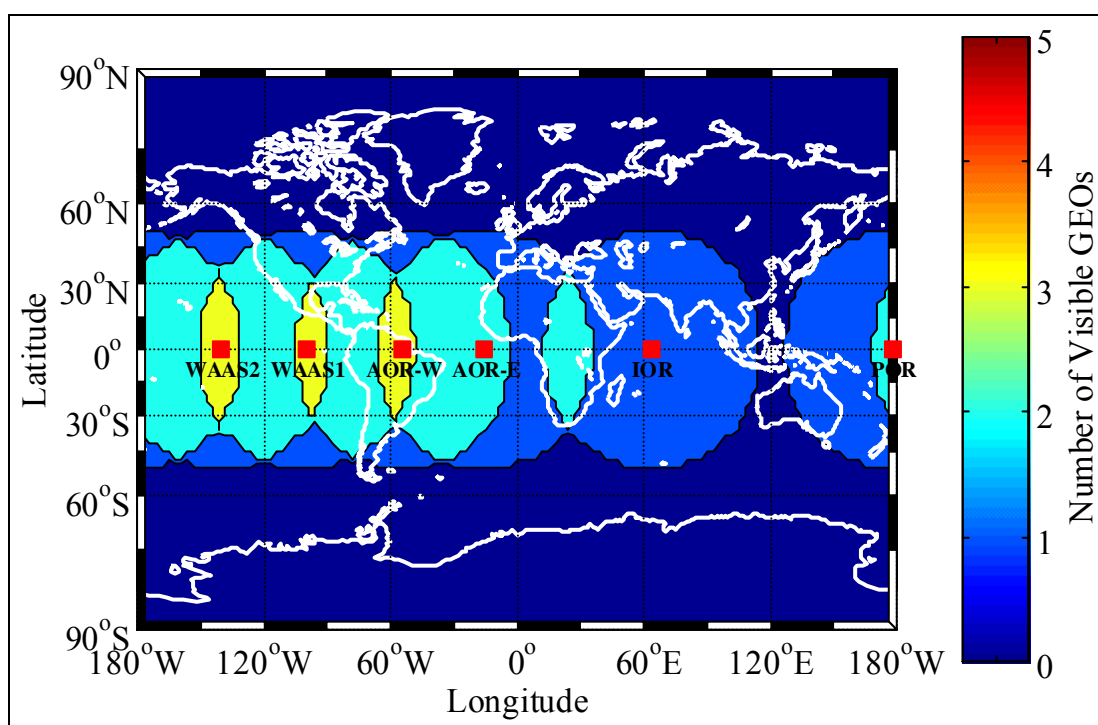


Figure 2-8 Number of Visible Geostationary Satellites (Mask Angle of 30°).

However, in order to make geostationary satellites applicable for marine navigation, the isotropic mask angle must be increased. Some of the most severe masking conditions for marine navigation occur within constricted waterways and during hydrographic surveying near cliff walls, where the need for an available and reliable position is paramount. Figure 2-8 shows the number of visible geostationary satellites using an isotropic mask angle of 30° . These results are in stark contrast to those for the 5° mask case of Figure 2-7. The continental U.S. (except Alaska) can see one or two GEOs,

however, Canada and Europe have poor visibility, with most areas unable to even see one GEO.

Figure 2-8 illustrates the weakness of the geostationary augmentations for the high latitudes under high masking conditions. The improvements that geostationary satellites can have on the availability and reliability of marine navigation will be shown in detail in CHAPTER 4.

2.4 *Galileo Overview*

Galileo is Europe's future satellite-based navigation system. The definition phase of the project was completed in 2001. To start the next phase of the project, the development phase, the European Space Agency (ESA) and the European Council had to each release € 550 million. While the ESA released its € 550 million on November 15, 2001 (ESA 2001), in December 2001 the European Council postponed its approval until the next European Council meeting in March 2002 (Genesis Office, 2001a). The reason stated for the delay was to give member nations time to review the Galileo economic impact study prepared by PricewaterhouseCoopers (Genesis Office, 2001a). The United States diplomatic efforts against Galileo (Genesis Office, 2001b) were probably also a factor in the postponement. However, even with the U.S. political pressure, the Council of European Transport Ministers approved the start of Galileo's developmental phase on March 26, 2002, with the release of the remaining € 450 million and the creation of a Joint Undertaking to manage the development phase (Genesis Office, 2002a). Figure 2-9 shows the Galileo development schedule. The Galileo system is being developed to reach FOC by 2008, a very aggressive schedule given that no satellites have yet been built.

Galileo's designers plan the system to be interoperable with other GNSS systems such as GPS, but at the same time completely independent and under European civilian control. Galileo will be a global navigation satellite system with global, local and regional components. The constellation will contain MEO satellites transmitting L-band RF ranging signals.

ID	Task Name	2000	2001	2002	2003	2004	2005	2006	2007	2008
1	Definition	█								
2	Design and Development		█							
3	System Validation				█					
4	Deployment							█		
5	Mission Validation							█		
6	Galileo IOC							█		
7	Galileo FOC									█
8	EGNOS Operation					█				

**Figure 2-9 Galileo Development Schedule
(EUROPA, 2002a and Tytgat and Campagne 2001)**

Galileo plans to offer the following five services (Genesis Office, 2002b, EUROPA, 2002b, Hein et al., 2001, Tytgat and Campagne, 2001, and Weber et al., 2001):

- 1) Open Services: The ranging codes and the navigation data will be transmitted in the clear on multiple frequencies. While users will not have access to integrity information they will be able to remove ionospheric errors. This service is very similar to GPS II.
- 2) Commercial Services: This service will use the same ranging codes and navigation data as the open service with commercially encrypted value added data. A third commercially-encrypted ranging code with commercially-encrypted data will also be provided, enabling three frequency carrier phase ambiguity resolution (TCAR). The value-added data could include integrity warnings, ionosphere information, differential corrections, et cetera. Users will directly pay for these services.
- 3) Safety of Life Services (SOL): This service will use the same ranging codes and navigation data as the open service with added integrity data. The integrity data may be encrypted. This service is aimed primarily at civil aviation users who need high accuracy, integrity and certified navigation systems. Revenue will be generated though regulatory bodies.

- 4) Public Regulated Services (PRS): This service will have government encryption on both the ranging codes and on the navigation data. Two frequencies will be used, resulting in similar accuracy performance to the open service. This service is being tailored to law enforcement agencies, critical infrastructure, and strategic interests.
- 5) Search and Rescue Services: The Galileo satellites will contain a COSPAS-SARSAT transponder. However, in addition to receiving the signal from the emergency beacon the Galileo system will transmit an acknowledgement back to the person in distress. This service is being co-ordinated with COSPAS-SARSAT.

The satellite constellation and the ground control segment dedicated to controlling the constellation, constitutes the global components of Galileo. A separate and independent ground control segment will be employed to determine the integrity of the Galileo satellite signals. This integrity segment may be global or regional in nature, this will be determined during the next phase of the Galileo design (Weber et al., 2001). If the integrity segment is global in nature, a global network of integrity monitors will be used to verify the ranging signals of each satellite. Integrity warnings would then be uploaded to the Galileo satellites for dissemination to the users. If regional integrity segments are employed, Galileo will provide the regional integrity infrastructure for Europe, and non-European Galileo partners will provide the infrastructure required for their area. In either case it is envisioned that the Galileo satellites will transmit the regional integrity warnings. The local components of Galileo will provide differential corrections, additional ranging signals (pseudolites), the interface to other communication networks, and other value added services.

Figure 2-10 shows the current GNSS frequency plan for GPS, GLONASS, and Galileo. Galileo plans to use three frequency bands E5a+E5b, E6, and E2+L1+E1, each capable of supporting wide bandwidth signals. Galileo plans to overlap some of the GPS frequency bands.

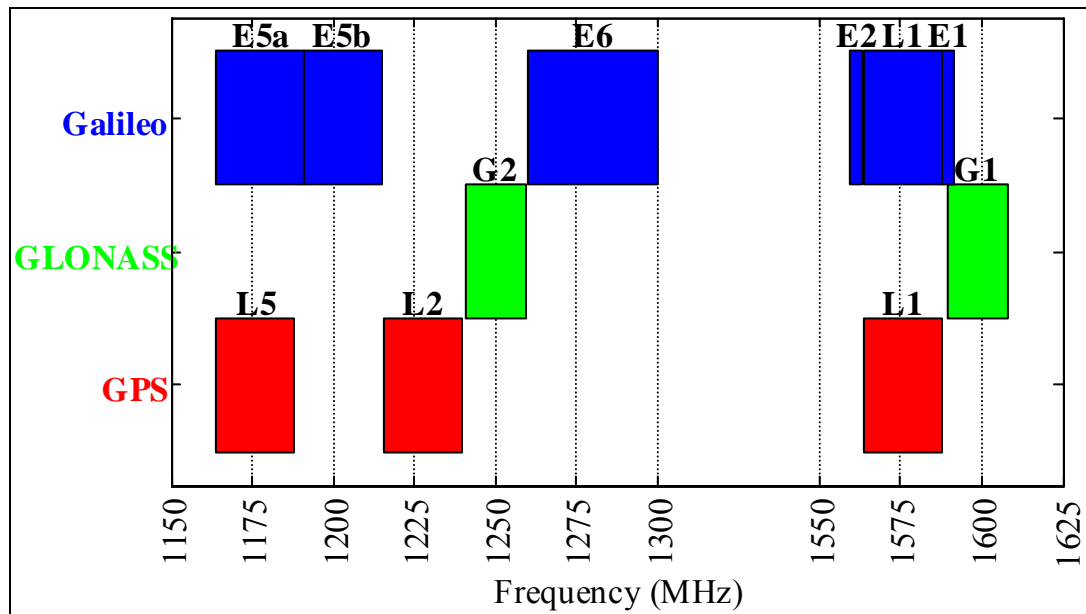


Figure 2-10 GNSS Frequency Plan

Within these three frequency bands Galileo plans to transmit a total of 10 different ranging codes in order to provide the navigation services described above. Figure 2-11 shows one potential multiplexing arrangement (Genesis Office, 2002b and Hein et al., 2001) for these codes.

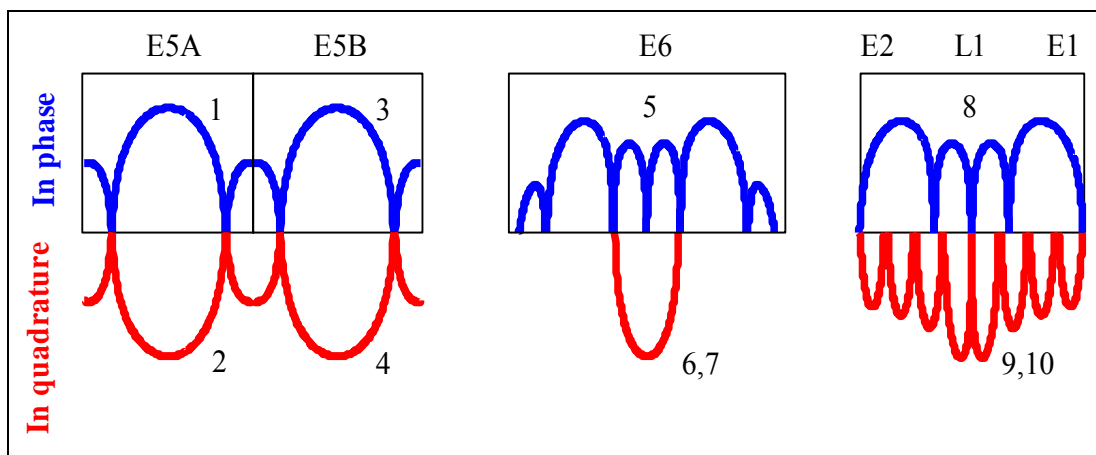


Figure 2-11 Galileo Signals (Genesis Office, 2002b)

To transmit this many codes within the allotted frequency bands some signals will be transmitted in phase quadrature while others will be time multiplexed together. Two

modulation schemes are being used, binary phase shift keying (BPSK) and binary offset carrier (BOC), with rectangular pulse shaping. Various chipping rates and bandwidths will be used for the 10 ranging codes. The final multiplexing scheme will be determined during the next phase of the Galileo project.

As stated above, some of the ranging codes will be transmitted in the clear while others will have either commercial or government encryption. Similarly the data modulated on the codes can be transmitted in the clear or encrypted with either commercial or government encryption. Table 2-4 maps the Galileo navigation services to the codes and data.

Table 2-4 Galileo Navigation Services Mapping to Signals (Genesis Office, 2002b)

Signal	Navigation Services				Signal Characteristics	
	Open	Commercial	SOL	PRS	Code	Data
1,2,3,4,9,10	X	X	X		Open	Navigation Integrity Commercial
6,7		X			Commercial	Commercial
5,8				X	Government	Government

Although the design is not finalised, Galileo will offer multiple wide bandwidth signals for each service. Thus the measurement noise and multipath mitigation of Galileo will be comparable to GPS.

During Galileo's definition phase there were two constellation baseline configurations, one consisted of only MEO satellites and the second contained both MEO and GEO satellites (Lucas and Ludwig, 1999, and Wolfrum et al., 1999). Within each baseline configuration there were various altitude, orbital plane, and satellite spacing possibilities. The following four potential Galileo constellations were discussed in Lucas and Ludwig (1999) and Wolfrum et al. (1999):

- 1) 24 MEOs in three orbital planes, with an altitude of 24,000 km, inclination (i) of 55° , augmented with three GEOs

- 2) Same as (1), but at an altitude of 19,500 km
- 3) Same as (1), but at an altitude of 24,126 km, with nine GEOs for world wide coverage using a Walker 24/3/2 constellation.
- 4) 30 MEOs in three planes, with an altitude of 24,000 km

The Galileo optimisation process selected a modified version of constellation #4, with 30 MEO satellites arranged in a 27/3/1 Walker configuration with three active spares, at an inclination of 56°, and an altitude of 23,616 km (Weber et al., 2001). A detailed analysis of several different Galileo constellations and a description of the Walker configuration is included in Appendix A. Both of the original baseline constellations will be included in CHAPTER 4's simulation results. Table 2-5 shows the constellation configurations that were chosen for the simulations performed herein.

Table 2-5 Galileo Satellite Constellations

#	MEOs	Altitude	Orbital Radius	i	Walker	GEOs
GAL24	24	23,616 km	29,994 km	56°	24/3/2	9
GAL30	30	23,616 km	29,994 km	56°	30/3/2	0

Instead of simulating the Walker 27/3/1 constellation, an integrated 30 MEO constellation has been assumed. Only time will tell if Galileo employs a true 27/3/1 constellation or integrates the three active spares into the constellation. GAL24 contains nine GEO satellites equally spaced (40° spacing) around the globe from 160° W to 160° E. As previously shown in Figure 2-6, GEO satellites provide excellent visibility at low latitudes, however, as the user's latitude increases, the elevation angle steadily decreases. Figure 2-12 plots the number of visible GEO satellites using GAL24, assuming an isotropic mask angle of 30°. The locations for the nine GEO satellites are displayed as red squares on the equator. At least two GEO satellites are visible within ±45° latitude. However, at higher latitudes the number of visible satellites quickly drops to one and then zero. GAL30 which does not contain any GEO satellites should outperform GAL24 at high latitudes under moderate to extreme masking conditions.

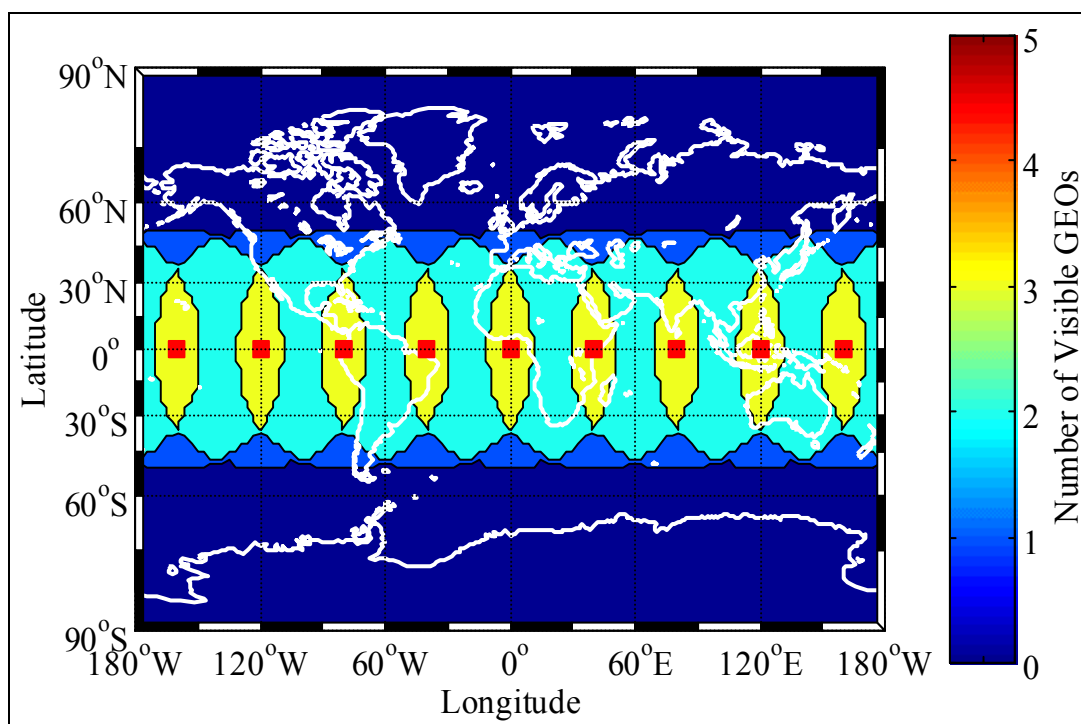


Figure 2-12 Number of Visible Geostationary Satellites, Galileo #1, 30° Mask Angle

Figure 2-13 shows the locations of the MEO satellites within their orbital planes for both Galileo constellations. With the orbital radius of 29,994 km (period of 51,697 seconds or $1\frac{2}{3}$ revolutions / day), the Galileo ground trace will repeat every three sidereal days (5 orbits). Figure 2-14 shows the ground trace for one Galileo satellite, which starts at 0° N 0° E (large red circle) and the ground trace for every sidereal day is a different colour. While it takes three sidereal days for a satellite to repeat its ground trace the user's geometry may repeat at a higher frequency. For example for GAL24, after 28721 seconds the constellation looks identical to Figure 2-13 (a) except that different satellites are in the orbital locations. PRN 2 would be in PRN 21's location. Thus the user's geometry repeats every 8 sidereal hours for GAL24. Due to the different satellite phasing for GAL30, the constellation does not actually repeat until the individual satellite ground traces repeat, which is every three sidereal days.

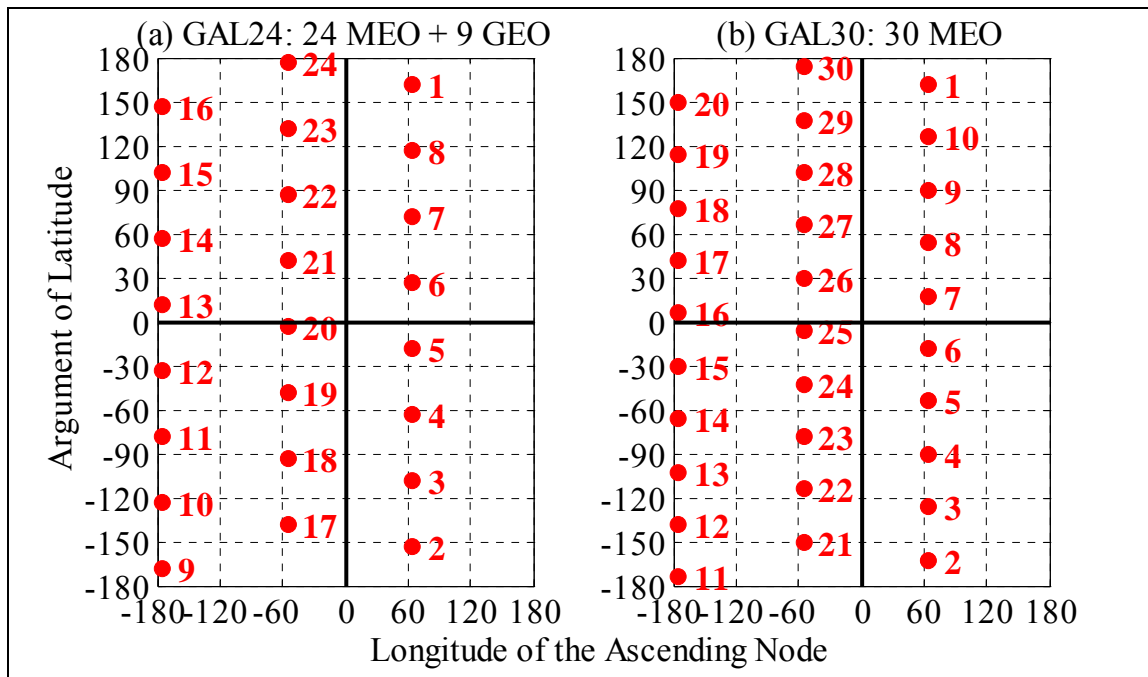


Figure 2-13 Galileo Constellations

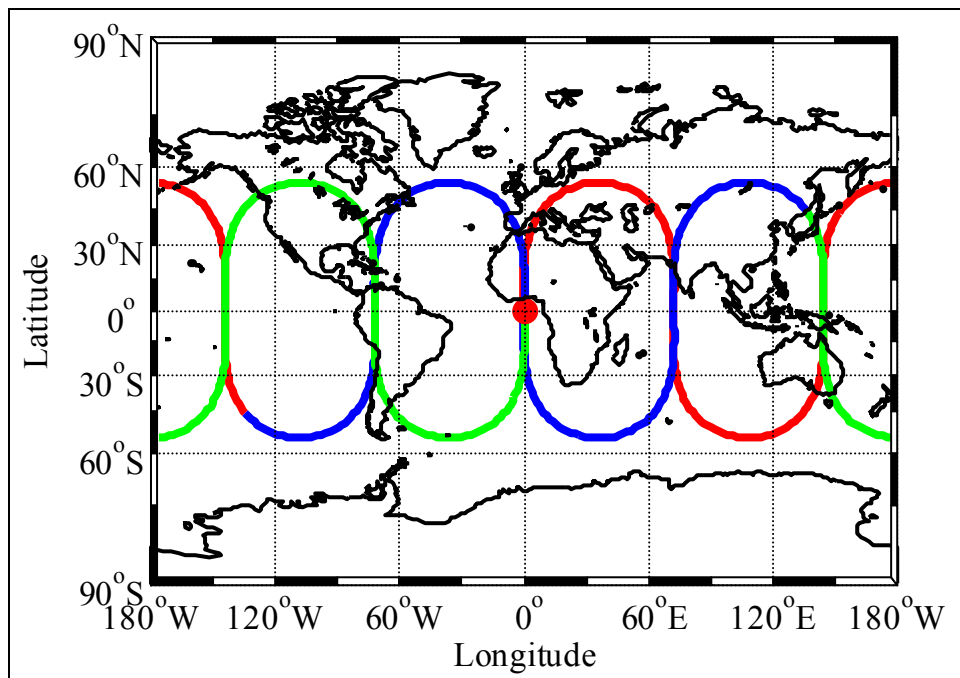


Figure 2-14 Galileo Satellite Ground Trace

2.5 GNSS Error Sources

The fundamental pseudorange and carrier phase GNSS measurement equations are:

$$\begin{aligned} p &= \rho + dp + c(dt_{RX} - dT_{SV}) + d_{ion} + d_{trop} + \epsilon(p) + m(p) + df_{RX} \\ \Phi &= \rho + dp + c(dt_{RX} - dT_{SV}) + \lambda N - d_{ion} + d_{trop} + \epsilon(\Phi) + m(\Phi) + df_{RX} \end{aligned} \quad (2-1)$$

where p	pseudorange
Φ	carrier phase
ρ	true geometric range
dp	orbital error
c	speed of light
dt_{RX}	receiver clock bias
dT_{SV}	satellite clock bias
d_{ion}	ionospheric error
d_{trop}	tropospheric error
$\epsilon(p)$	pseudorange measurement noise
$\epsilon(\Phi)$	carrier phase measurement noise
$m(p)$	pseudorange multipath error
$m(\Phi)$	carrier phase multipath error
df_{RX}	receiver frequency bias
λ	carrier phase wavelength
N	carrier phase integer ambiguity

The thrust of this thesis is to examine the improvements in marine navigation availability and reliability that can be attained through augmenting DGPS. In order to quantify the reliability improvements the characteristics of the GNSS error sources must be examined in detail. The remainder of this section attempts to address each of the potential GNSS error sources and relates them to marine navigation, specifically the reliability of the position. This information will be used in CHAPTER 4's simulations.

2.5.1 Orbital Error

The first error source contained in equation (2-1) is δp , the satellite orbital error. When SA was first activated it contained both orbit and clock components, thus there could be a significant error in the GPS broadcast orbit due to the effect of SA. In recent years SA was only contained on the clock and not the orbit. When SA was removed from the orbits the accuracy of the broadcast orbits became better than 20 m (Lachapelle, 1997). DGPS cannot completely remove this error since it will map differently into the two ranges. The rule of thumb is every 20 m of orbital error induces 1 ppm error into the baseline. Can the orbital errors introduce any blunders into the differentially computed positions that could be caught by reliability theory? The following data was analysed to determine the current accuracy of the GPS broadcast orbits.

Broadcast and precise GPS ephemeris data were downloaded from the International GPS Service (IGS) web site for GPS week 1068. The IGS precise ephemerides were treated as truth since their one sigma value is 5 cm (IGS, 2002). 26 of the 28 GPS satellites had complete ephemerides for the entire week, thus only 26 satellites were analysed. The difference between the broadcast orbits and the precise orbits were computed for each satellite every 15 minutes for the entire week. Since the broadcast orbits are referenced to the antenna phase centre and the precise orbits are referenced to the mass centre the broadcast orbits were shifted by the antenna phase centre offset. The position error was then rotated into the radial, along track, and out of plane directions. Figure 2-15 shows the three position error components as well as the 3D position error for the 26 satellites overlaid on one another for GPS week 1068. The maximum errors in the three directions were 9.5 m, 23.9 m, and 3.6 m for the out of plane, along track, and radial directions respectively. The maximum 3D position error was 24.2 m.

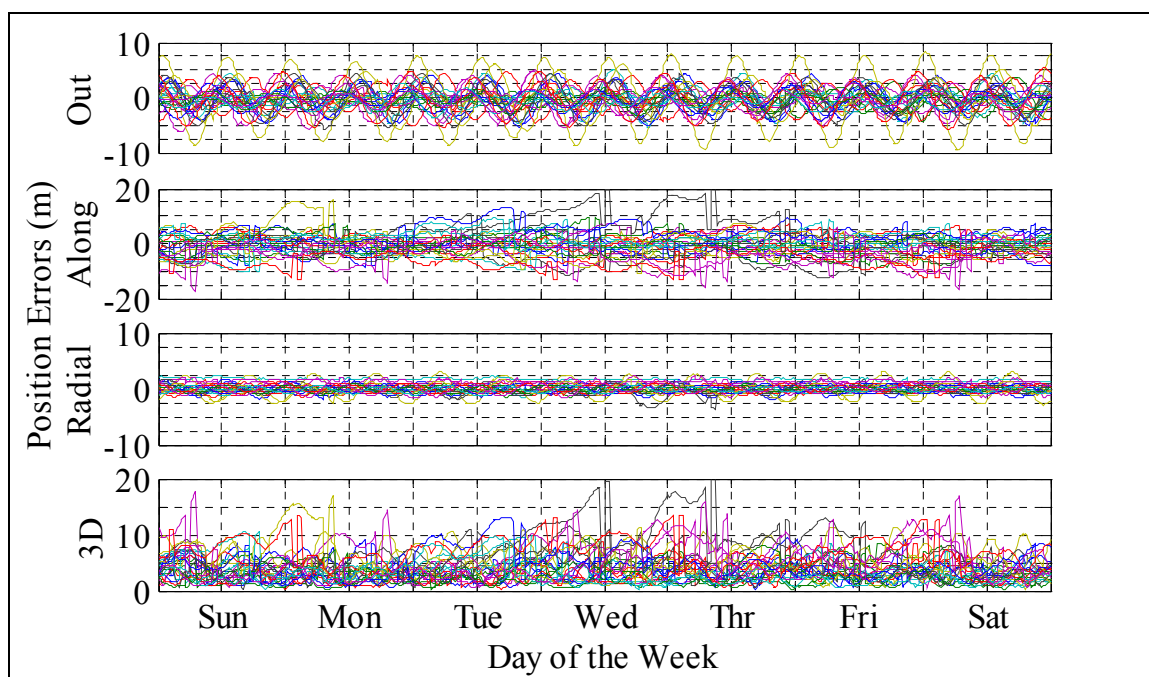


Figure 2-15 GPS Broadcast Orbit Position Errors

Each satellite's position error was analysed separately, with the results for the 50%, 95%, and maximum values plotted in Figure 2-16. The results for the radial direction are very consistent across all of the GPS satellites. In the out of plane direction PRN 6 shows the highest errors while in the along track direction several satellites have maximum errors exceeding 15 m, with PRN 16 having the largest error of 23.9 m. The results for the 3D position error show consistent results for the 50% and 95% with all satellites around the 5 m and 10 m level respectively. Three satellites have maximum errors greater than 15 m. The 3D position error results for the 26 satellites batched together are given in Table 2-6. The 3D error was converted to a rough ppm by dividing the error by the GPS altitude.

Table 2-6 Results for all of the Satellites

	50%	68%	95%	99%	Max
3D Error (m)	3.5	4.7	9.2	12.7	24.2
ppm	0.18	0.23	0.46	0.63	1.21

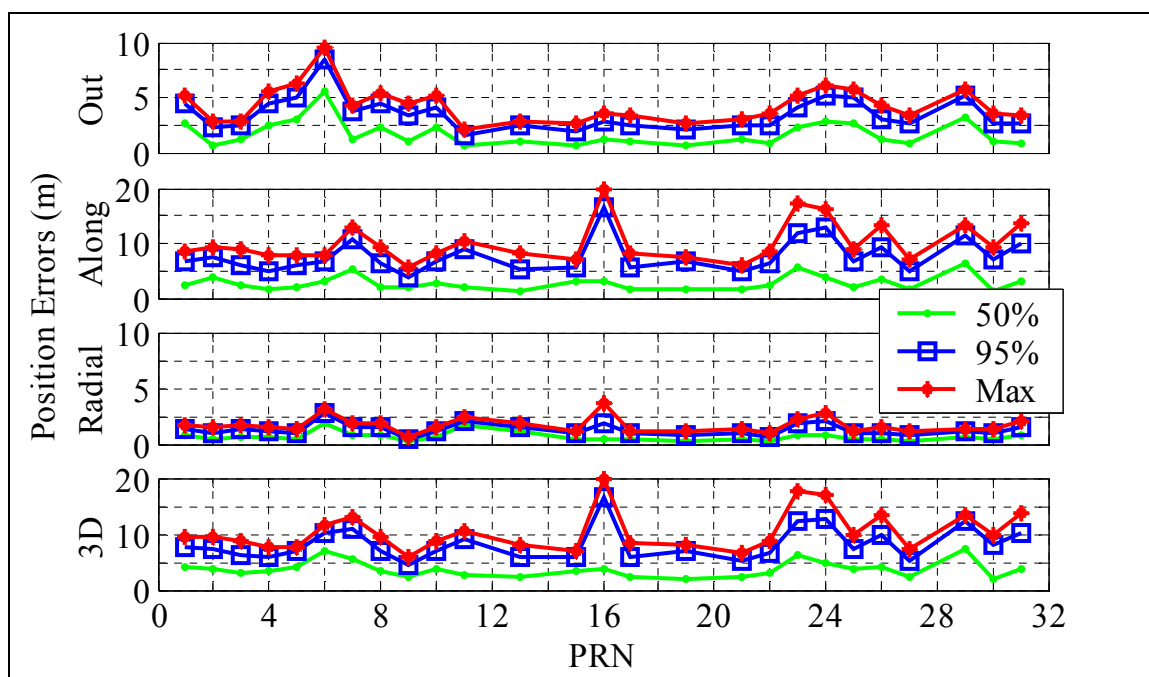


Figure 2-16 GPS Broadcast Orbit Statistical Analysis for each Satellite

These results do not show the magnitude of the observation or position biases that will occur when DGPS is used. To demonstrate this, the ephemeris errors were used to generate observation misclosures and position errors for the 556 km baseline from Cardinal, Ontario, to Rivière-du-Loup, Quebec, on the St. Lawrence Seaway. Figure 2-17 shows the baseline and the five CCG DGPS stations currently on the river.

The single difference misclosures for the 26 satellites over the seven day period is plotted in Figure 2-18. The misclosure results for the 26 satellites batched together are given in Table 2-7. Note that the maximum misclosure was only 43 cm, with the 95% value being approximately $\frac{1}{3}$ of this or 14 cm.

Table 2-7 Single Difference Misclosures for all 26 Satellites

	50%	68%	95%	99%	Max
Misclosures (m)	0.03	0.05	0.14	0.20	0.43
ppm	0.06	0.10	0.25	0.36	0.77

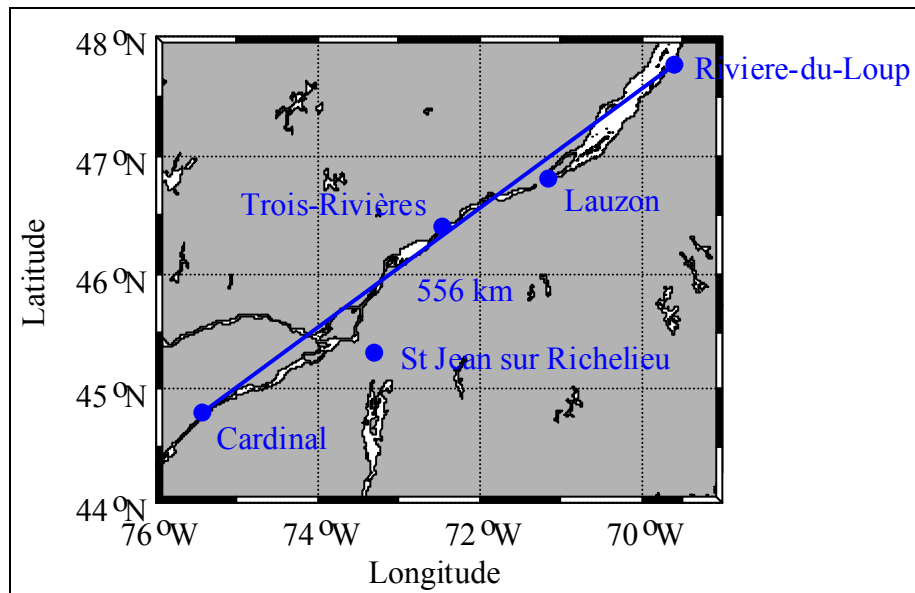


Figure 2-17 St. Lawrence Seaway CCG DGPS Stations and the Selected Baseline

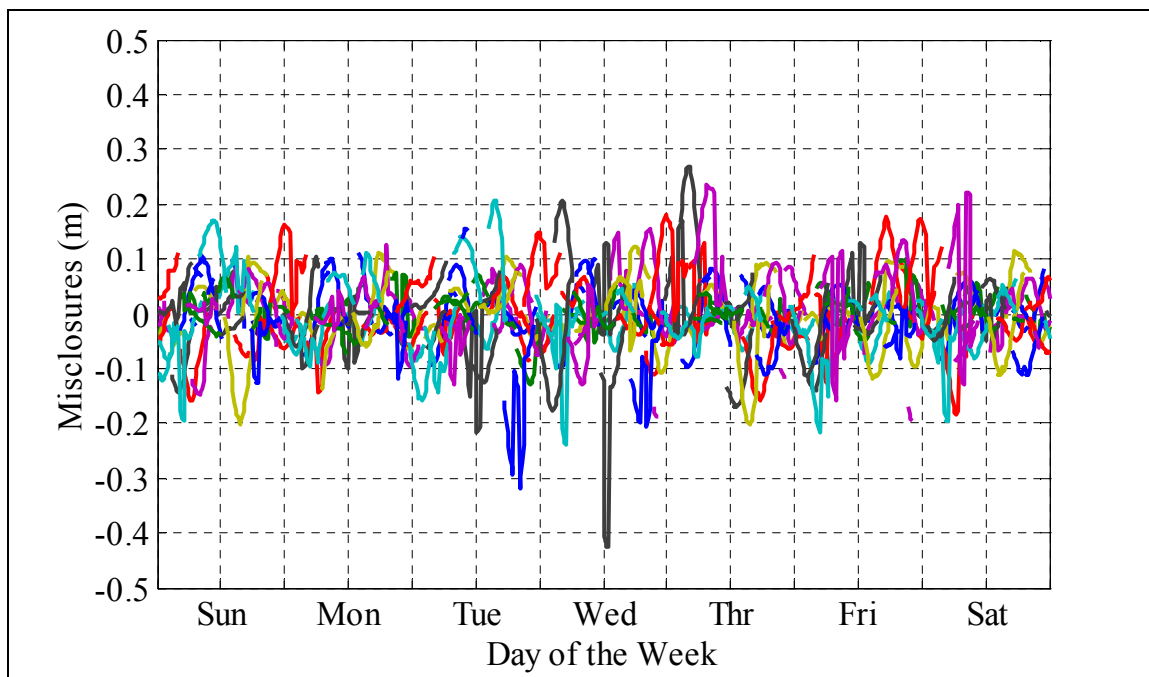


Figure 2-18 Single Difference Satellite Misclosures

Mapping these misclosures to the position domain results in the HPE and the vertical position error (VPE) plotted in Figure 2-19, with the error statistics given in Table 2-8. The 99% horizontal and vertical errors are less than 26 cm and 39 cm respectively, with

corresponding 99% HDOP and vertical dilution of precision (VDOP) values of 2.5 and 4.3 respectively. These error limits are quite acceptable for a code based positioning system where metre level accuracy is desired.

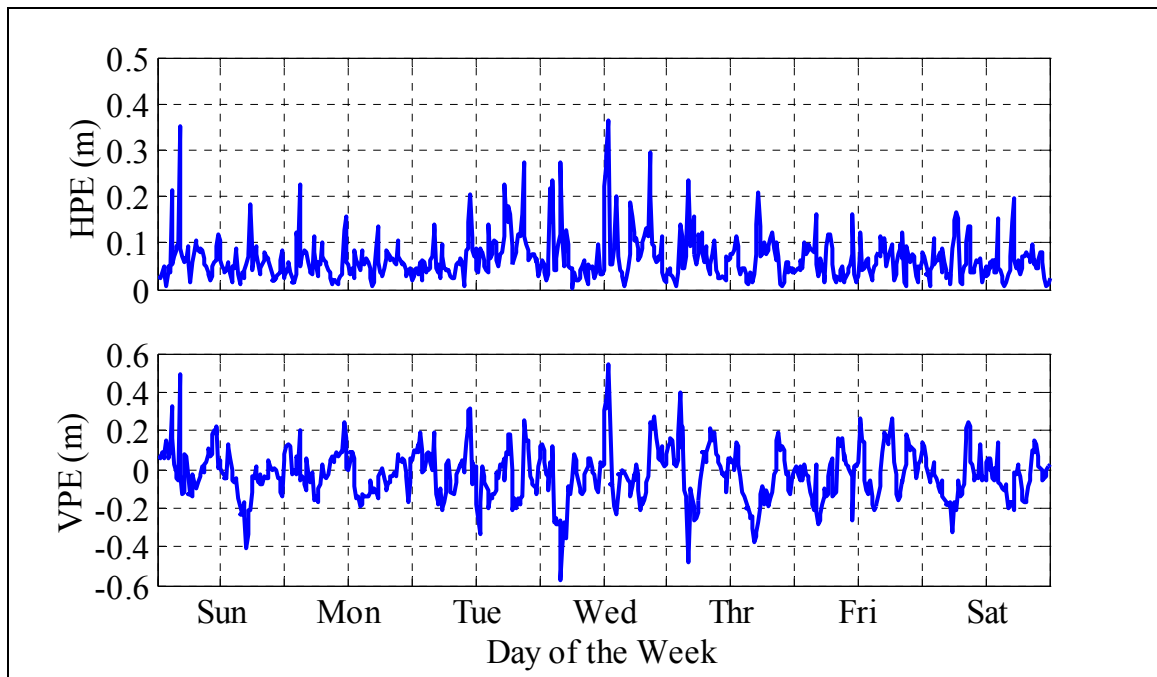


Figure 2-19 HPE and VPE due to Ephemeris Errors for a 556 km Baseline

Table 2-8 HPE and VPE Statistics due to Ephemeris Errors for a 556 km Baseline

	50%	68%	95%	99%	Max
HPE (m)	0.06	0.07	0.15	0.26	0.36
VPE (m)	0.08	0.13	0.26	0.39	0.58

Thus the errors in the current GPS broadcast orbits cause only a small biases in the range observations as shown in Figure 2-18 and Table 2-7. The majority of the misclosures (99%) were ≤ 20 cm. This is an extremely small error when the code noise and code multipath are considered which are described in sections 2.5.4 and 2.5.5. Thus the ephemeris errors will not be considered in the remainder of this thesis.

2.5.2 Tropospheric Error

The regions within the atmosphere can be categorised using a number of different parameters that vary with altitude, such as temperature, the magnetic field, ionisation and RF propagation as shown in Figure 2-20 (Seeber, 1993 and Hargreaves, 1992). The lower 40-50 km of the atmosphere is composed of non-ionising particles, and is non-dispersive for GNSS frequencies. As shown in the temperature categorisation of Figure 2-20 this area is composed of the troposphere and the stratosphere. The GNSS convention is to follow the propagation category and to call the entire area the troposphere. The troposphere has the following three effects on GNSS satellite signals: attenuation, scintillation, and delay.

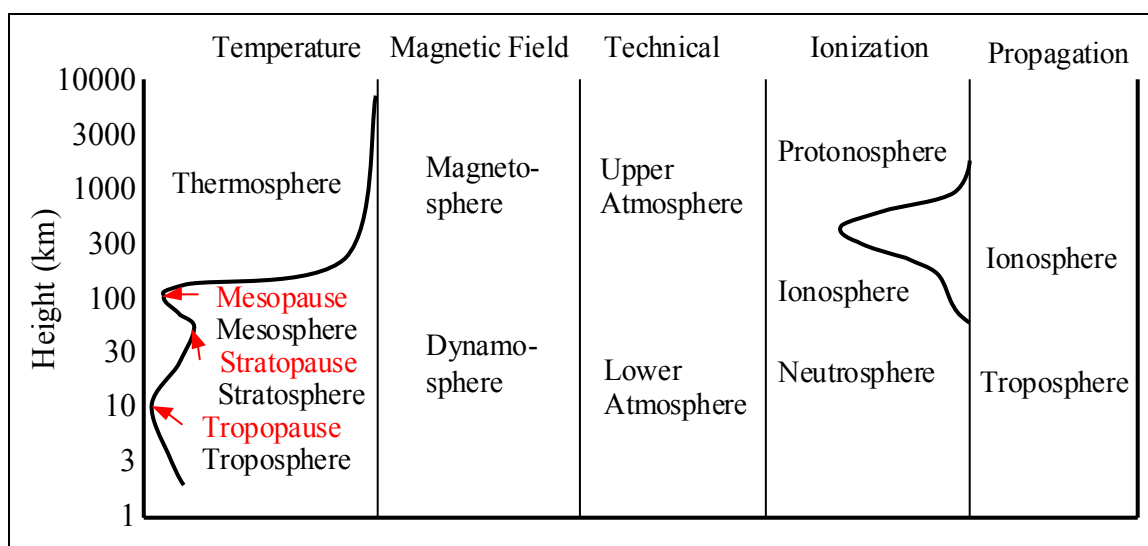


Figure 2-20 Atmosphere Regions (Seeber, 1993)

At GNSS frequencies the tropospheric attenuation is primarily caused by oxygen, and is approximately 0.035 dB at zenith (Spilker, 1994c). As the satellite's elevation angle decreases, the path length through the troposphere and hence the attenuation increases. Assuming that the troposphere is a uniform spherical shell the resulting tropospheric attenuation is given by equation (2-2) and is plotted in Figure 2-21 (Spilker, 1994c). At a

5° elevation angle the tropospheric attenuation is only 0.38 dB, which increases the code measurement noise by approximately 4% and is insignificant for GNSS, see section 2.5.4.

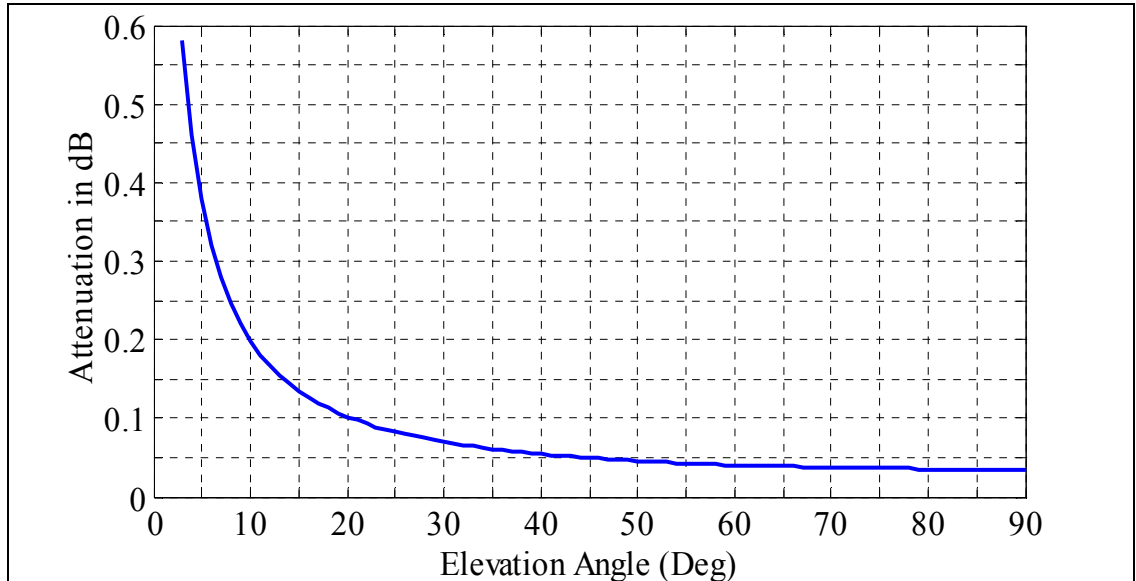


Figure 2-21 Tropospheric Attenuation vs. Elevation Angle

$$\text{Attenuation} \cong \frac{2 * A_{\text{Zenith}} * (1 + a/2)}{\sin(E) + \sqrt{\sin(E)^2 + 2 * a + a^2}} \quad (\text{dB}) \quad (2-2)$$

where A_{zenith} tropospheric attenuation for a satellite at zenith, i.e. 0.035 dB

$$a = \frac{h_m}{R_e}$$

h_m equivalent height for oxygen

R_e earth's radius

E satellite's elevation angle

Scintillation is the rapid change of the amplitude and / or the phase of the GNSS signal. Tropospheric scintillation is caused by small scale irregularities in the water vapour and temperature of the atmosphere (e.g. clouds), and has minimal effect on the GNSS signals (Spilker, 1994c).

The primary effect that the troposphere has on the GNSS signal is the delay, which is caused by the index of refraction (n) being greater than one. This causes two separate effects, the first is the slowing down of the signal as the index of refraction increases, and the second is the bending of the signal as it propagates through regions with changing indices of refraction (Snell's Law). Equation (2-3) gives the total tropospheric delay which is the sum of these two effects.

$$d_{\text{trop}} = \underbrace{\int_{\text{Actual}} (n-1) ds}_{\text{Slowing Down}} + \underbrace{\left(\int_{\text{Actual}} ds - \int_{\text{Geometric}} ds \right)}_{\text{Bending}} \quad (2-3)$$

The delay caused by bending is normally ignored. This simplification introduces a small error which is inversely proportional to elevation angle. For elevation angles greater than 20° it results in millimetres of range error, this increases to centimetres at 10° , and to decimetres at 5° (Spilker, 1994c).

Since the index of refraction is so close to 1, the tropospheric refractivity $N = (n-1) * 10^6$ is normally used in calculations. The tropospheric refractivity is calculated using the ideal gas law with compressibility factors, and is a function of temperature, partial pressure of dry air, and partial pressure of water vapour, as shown in equation (2-4) (Thayer, 1974). The third term in the equation is due to dipole orientation effects of the permanent dipole moment of the water molecules (Davis et al., 1985).

$$N = \underbrace{\frac{K_1 * P_d}{T * Z_d}}_{\text{Dry Component}} + \underbrace{\frac{K_2 * e}{T * Z_w} + \frac{K_3 * e}{T^2 * Z_w}}_{\text{Wet Component}} \quad (2-4)$$

where K_1 , K_2 , and K_3 constants

P_d partial pressure of dry air

e partial pressure of water vapour

T temperature

Z_d dry compressibility factor

Z_w wet compressibility factor

Equation (2-4) separates the partial pressures of the dry and wet air. However, a more convenient form is to discuss the hydrostatic component (total pressure) and the non-hydrostatic component (remaining water vapour). Replacing P_d in equation (2-4) with total and wet densities, using the ideal gas law with compressibility factors, and simplifying, results in the following alternate expression for the refractivity:

$$N = \underbrace{\frac{K_1 * R * \rho}{M_d}}_{\text{Hydrostatic Component}} + \underbrace{\left(K_2 - \frac{K_1 * M_w}{M_d} \right) * \frac{e}{T * Z_w} + \frac{K_3 * e}{T^2 * Z_w}}_{\text{Wet Component}} \quad (2-5)$$

where ρ total density

M_d molecular weight of dry air

M_w molecular weight of wet air

R universal gas constant

To determine the tropospheric delay, substitute equation (2-5) in equation (2-3) and integrate along the actual signal path. An alternate formulation for the tropospheric delay is to calculate the zenith delays and then map them to the slant range.

$$d_{\text{trop}} = \Delta_{\text{HZ}} * m_{\text{H}}(E) + \Delta_{\text{WZ}} * m_{\text{W}}(E) \quad (2-6)$$

where Δ_{HZ} hydrostatic delay at zenith

$m_{\text{H}}(E)$ hydrostatic mapping function

Δ_{WZ} wet component delay at zenith

$m_{\text{W}}(E)$ wet component mapping function

Many researchers, such as Hopfield (1969), Saastamoinen (1973), and Davis et al. (1985), have developed models for calculating the zenith hydrostatic delay using surface atmospheric measurements. Other models such as the one developed by RTCA (1998)

utilises user location and time of year to estimate the zenith delay. Figure 2-22 plots the zenith delay using the RTCA (1998) algorithm, the user's latitude, height, and time of year were all varied. The multiple lines within each height cluster show the variation throughout the year. The user's height has the largest effect on the zenith delay. On the ellipsoid the zenith delay is normally assumed to be 2.3 m. The wet component is extremely variable (0-80 cm at zenith) and cannot be accurately modelled even with surface atmospheric measurements (Schüler 2001). For a more detailed treatment of the troposphere see Spilker (1994c), Skone (1999), Schüler (2001), and Mendes (1999).

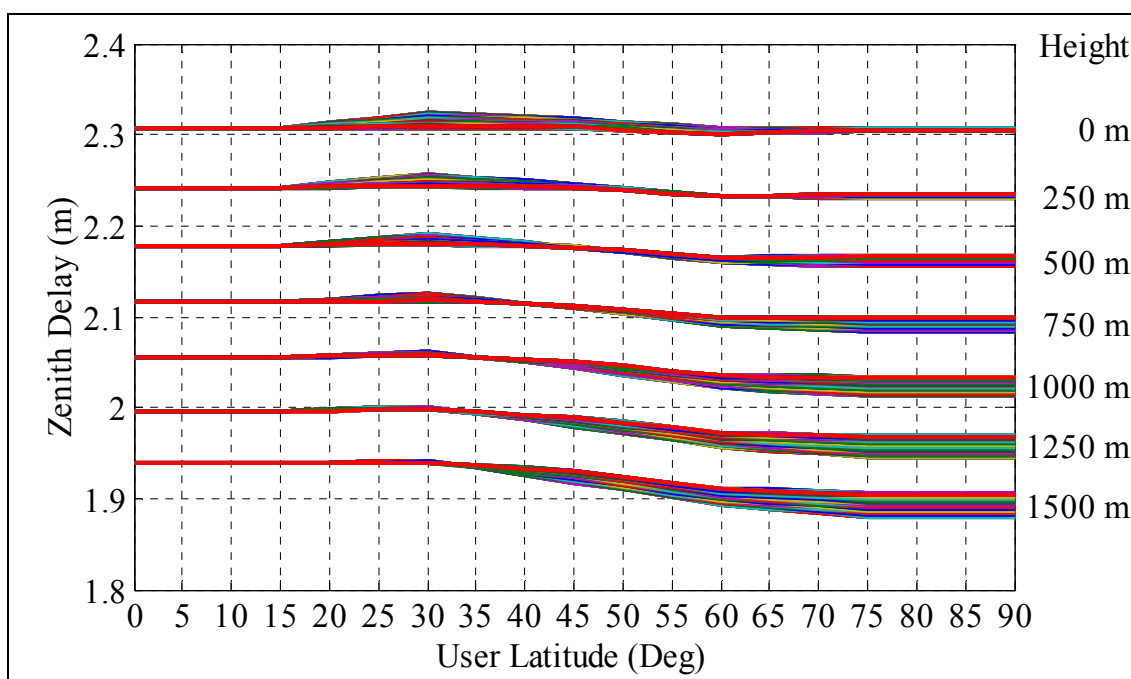


Figure 2-22 Zenith Hydrostatic Delay

Similar to the zenith delays, the mapping functions of equation (2-6) use either surface atmospheric measurements and user location, or only user location and time of year (Niell, 2000). Most mapping functions fall within either the quartic profile, the truncated form of a continued fraction, or the cosecant law (Mendes, 1999). In Bisnath et al. (1997) the Niell mapping function was one of the mapping functions recommended for use. Figure 2-23 plots the hydrostatic delay using the Niell mapping function (Niell, 1996)

assuming a zenith delay of 2.3 m. At 5° elevation angle the mapping function reached a value of 10, resulting in a hydrostatic delay of 23 m. However, this does not mean that 23 m of error is truly added to the range. Users can apply the tropospheric models mentioned above as well as differential corrections. Some marine user receivers only use the differential corrections, they do not apply the tropospheric models (Leica, 2002). In this case the derivative of the tropospheric delay vs. elevation angle becomes important and is plotted in Figure 2-24. Note that at a 5° elevation angle the derivative approaches -4 m° . The question remains, what is the resulting impact on the differential user?

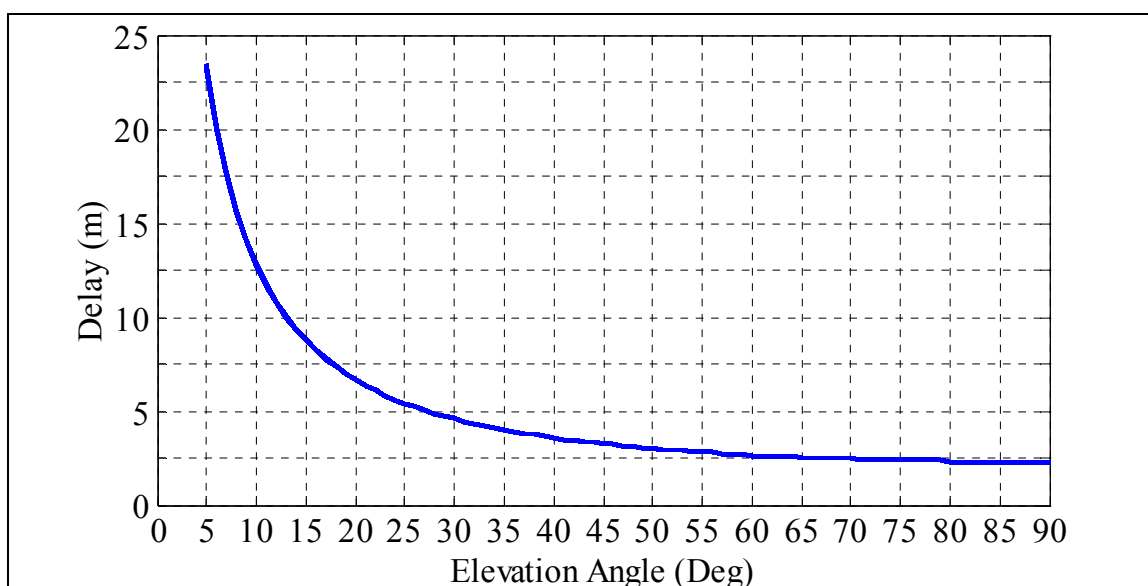


Figure 2-23 Tropospheric Delay vs. Elevation Angle using Niell's Mapping Function

This question will be answered by running a tropospheric simulation on the 556 km baseline between Cardinal, Ontario, and Rivière-du-Loup, Quebec (Figure 2-17). Since 80-90% of the tropospheric delay is attributed to the hydrostatic component, and the wet component is so variable (Lachapelle, 1997), the wet component will not be included in the simulation. The tropospheric delay will be calculated using the Niell mapping function (Figure 2-23). Figure 2-25 plots the single difference misclosures over a 24 hour period for the Cardinal to Rivière-du-Loup baseline. Only observations above 7.5° were

used since this is the marine DGPS cut-off angle (CCG, 1996). The largest misclosure was 9.8 m, with 95% of them below 6.0 m.

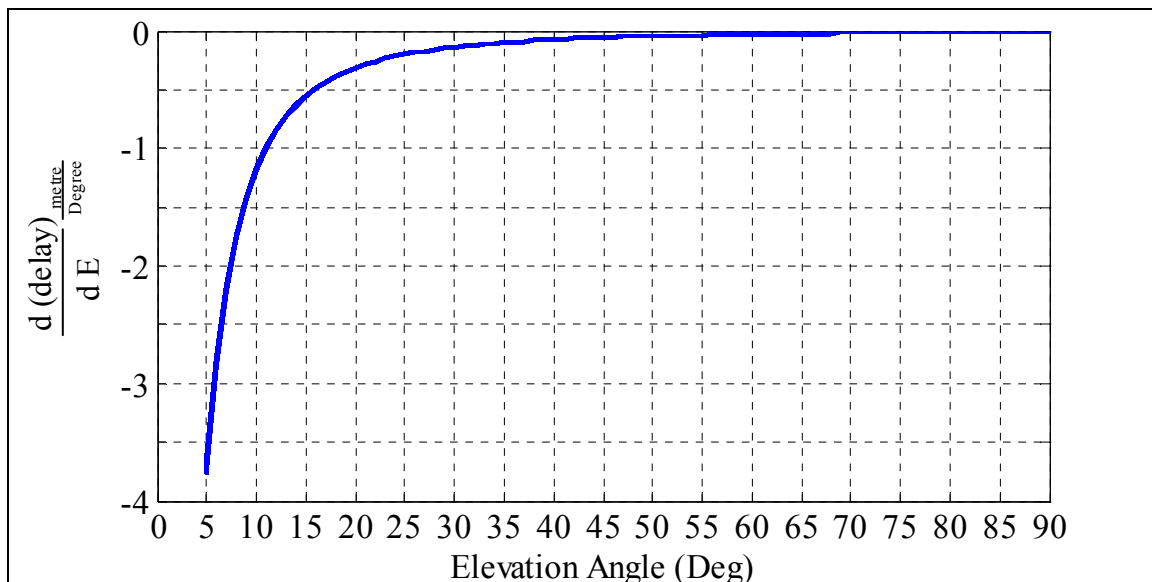


Figure 2-24 Derivative of the Tropospheric Delay vs. Satellite Elevation Angle

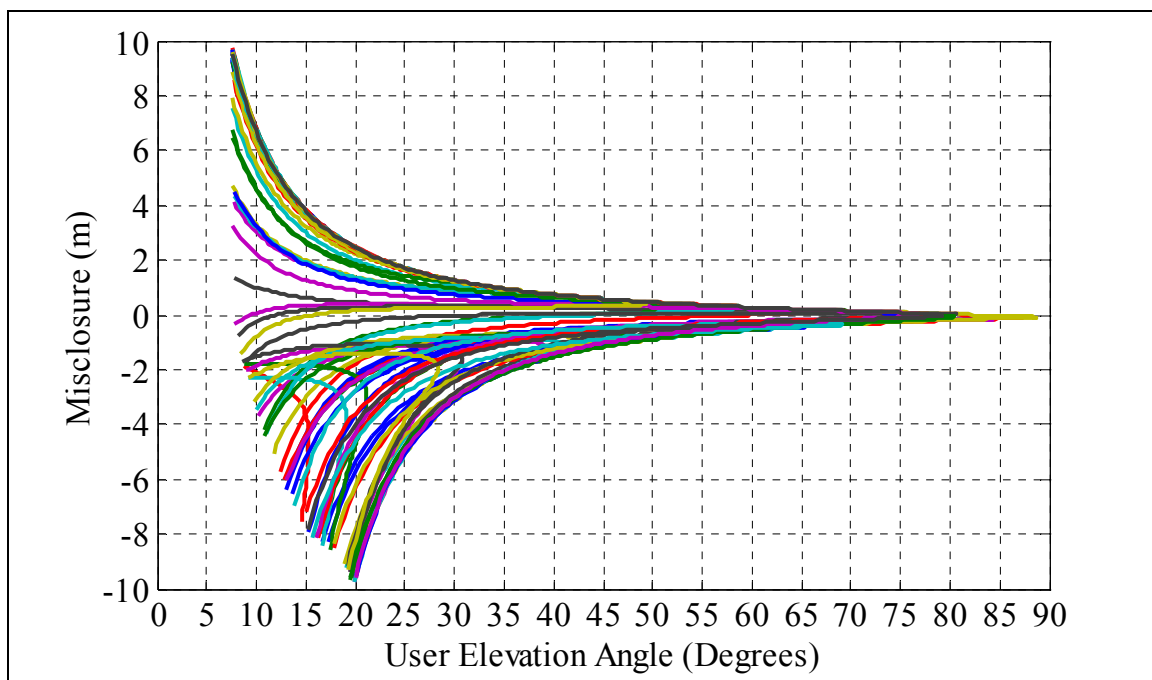


Figure 2-25 Tropospheric Simulation Single Difference Misclosures

These misclosures were propagated into the position domain first assuming an identity (I) observation covariance matrix (C_1) and second weighting (W) the C_1 matrix using the Niell mapping function. Figure 2-26 and Table 2-9 shows the results for the horizontal and vertical errors. As expected, applying the Niell mapping function removed the largest position errors. However, even after applying the weighting, the 95% HPE was still 3.8 m. This is an extremely large position error, however, no models have been applied. The next simulation will apply the Niell mapping function to both locations and will make assumptions on the accuracy of the models.

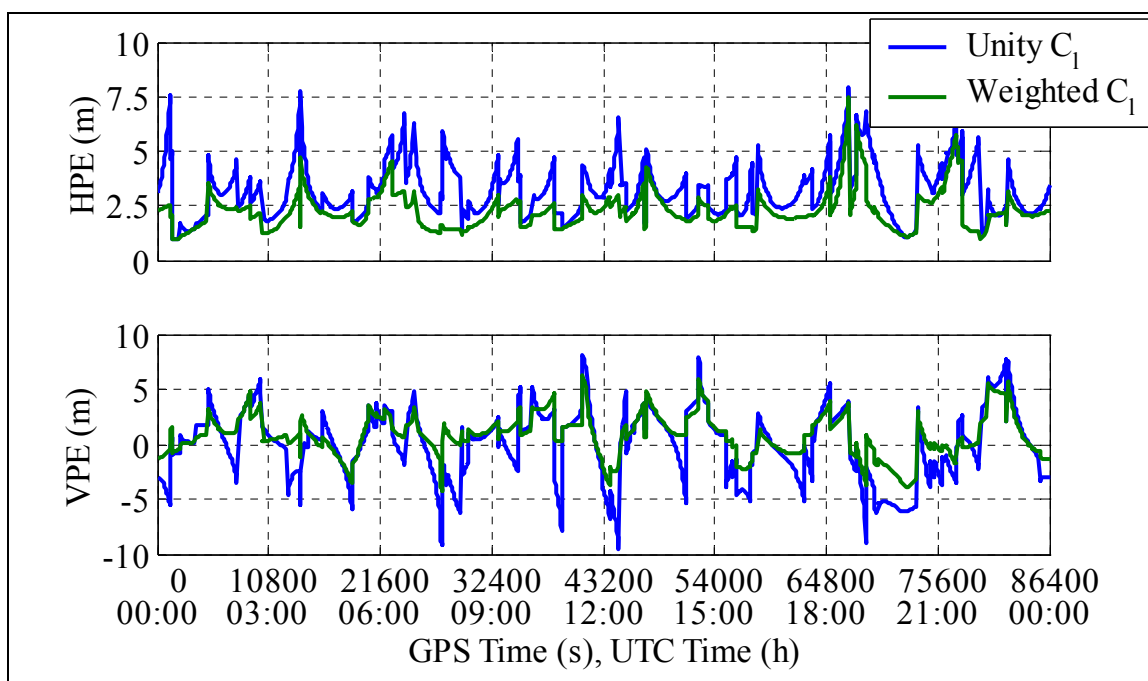


Figure 2-26 HPE and VPE due to the Tropospheric Misclosures

Table 2-9 HPE and VPE due to the Tropospheric Misclosures

	50%	68%	95%	99%	Max
$C_1 = I$, HPE (m)	3.0	3.6	5.5	6.6	7.9
$C_1 = I$, VPE (m)	2.2	3.1	6.0	7.5	9.6
$C_1 = W$, HPE (m)	2.1	2.4	3.8	5.4	7.5
$C_1 = W$, VPE (m)	1.2	2.0	4.0	5.2	6.3

If the marine user was to apply a tropospheric model, it should remove most of the hydrostatic component (Lachapelle, 1997). The wet term would be left, which is normally 10-20% of the total delay. The simulation will be run assuming that 80% of the misclosures are removed through modelling. Thus the single difference misclosures in Figure 2-24 are multiplied by 0.20, before the least squares adjustment is performed. Figure 2-27 and Table 2-10 show the results under these assumptions. The 95% position errors are now sub-metre assuming the correct weighting is applied. These errors are more in line with what should be expected from the troposphere in an extreme case.

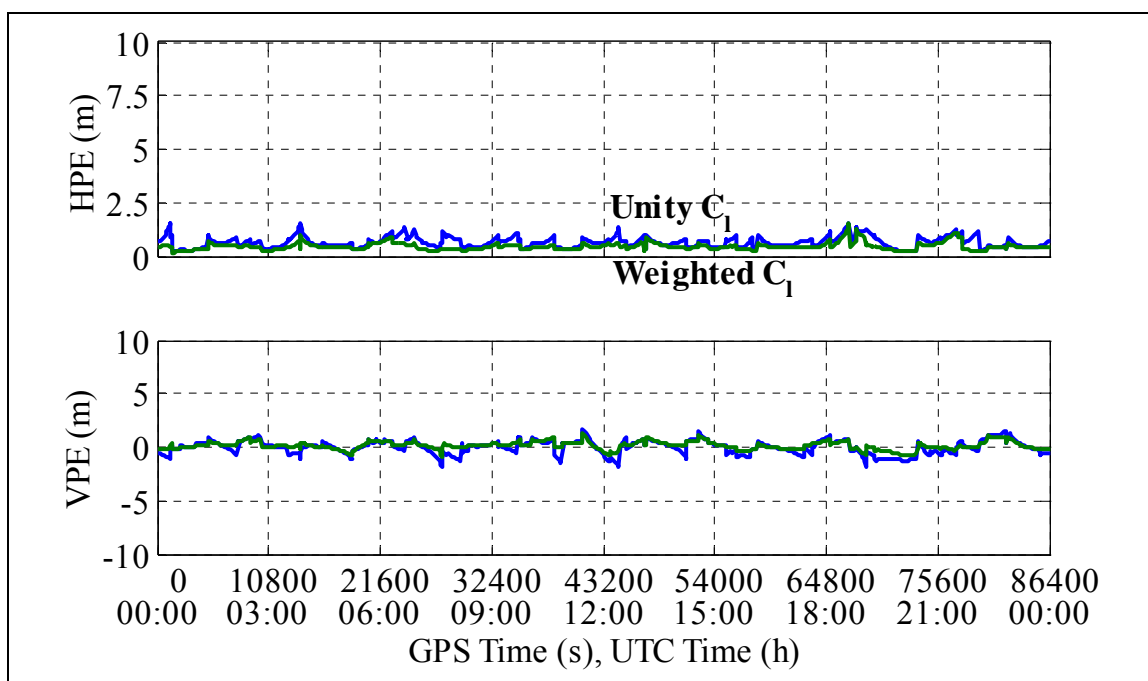


Figure 2-27 HPE and VPE with the Misclosures Scaled by a Factor of 0.20

Table 2-10 HPE and VPE with the Misclosures Scaled by a Factor of 0.20

	50%	68%	95%	99%	Max
$C_1 = I$, HPE (m)	0.6	0.7	1.1	1.3	1.6
$C_1 = I$, VPE (m)	0.4	0.6	1.2	1.5	1.9
$C_1 = W$, HPE (m)	0.4	0.5	0.8	1.1	1.5
$C_1 = W$, VPE (m)	0.3	0.4	0.8	1.1	1.3

The differential delays and the position error magnitudes in Table 2-10 are slightly smaller than those due to receiver code noise (section 2.5.4). Rather than explicitly including the tropospheric error in the reliability and availability simulations of CHAPTER 4, it will be combined with the code measurement noise to estimate the overall measurement variance.

2.5.3 Ionospheric Error

As shown in Figure 2-20 the ionosphere reaches from approximately 50 km to 1000 km, where the protonosphere begins. Within the ionosphere neutral atoms are broken into free electrons and ions by solar emissions (solar radiation and solar wind). The ionosphere can be subdivided into layers (D, E, F1, and F2) as shown in Figure 2-28. Since the ionosphere's refractive index is not equal to 1, it has the following effects on the GNSS signal: attenuation, Faraday rotation, Doppler shift, scintillation, and delay.

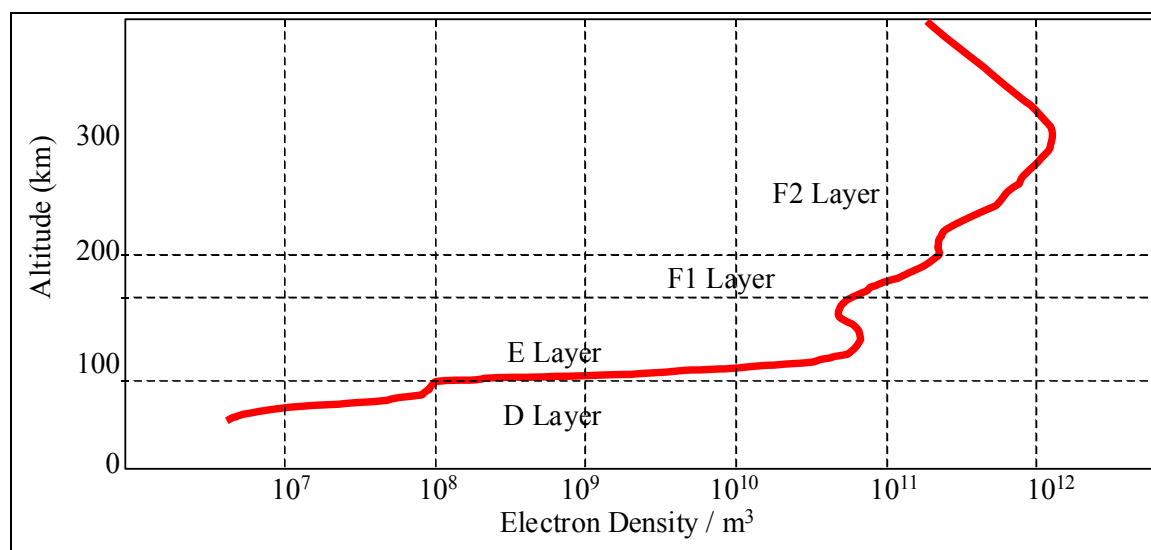


Figure 2-28 Ionospheric Layers and Electron Densities

The ionosphere's major effects on the GNSS signal is scintillation and delay, the other effects will be briefly described.

Attenuation: The D region of the ionosphere attenuates the GNSS signal by approximately 0.2 dB (Skone, 1999). Similar to the troposphere this amount of attenuation is not significant for GNSS.

Faraday Rotation: The polarisation of all RF signals rotate as they pass through the ionosphere, called Faraday rotation. This is caused by the nonisotropy of the medium generating two indices of refraction (Collin, 1985). Since GNSS signals are circularly polarised this additional rotation does not cause a problem.

Doppler Shift: A Doppler shift, of a fraction of a Hertz, is induced by the rate of change of the index of refraction. This is well within the receiver's tracking bandwidths and does not cause a tracking problem (Klobuchar, 1996).

Scintillation is caused by small scale irregularities in the ionosphere changing the amplitude and / or phase of the GNSS signal. It is present in three main areas of the world: the polar cap, auroral oval, and equatorial region. In the auroral region amplitude fades of 20 dB and phase variations of 10-20 cm are possible (Skone, 1999). Similar amplitude fades are possible in the equatorial regions. However, equatorial scintillations have diurnal and seasonal dependencies (Wanninger, 1993). Scintillations can cause several problems for GNSS users. First if the signal amplitude drops below the receiver's tracking threshold for a long enough time interval, the receiver will lose lock on that satellite. Even if lock is maintained the measurement noise will increase, due to the reduced signal to noise ratio. For the L1 C/A code this should not be a problem except for extreme cases. However, for user's tracking the L2 signal using codeless or semi-codeless techniques, the amplitude fades may completely wipe out the L2 signal as shown by Wanninger (1993) and Fortes (2002).

The phase scintillation will have similar effects on the GPS receivers. Typical L1 C/A code phase lock loops (PLL) can tolerate 45° of phase error (Ward, 1996), or 2 cm at L1. If the phase changes more than this, the receiver will lose lock on the carrier. Depending on the receiver, the code measurement may be rejected as well. Again this is the extreme case for the L1 C/A code. However, if L2 is being tracked using codeless or semi-

codeless techniques the tracking loop bandwidths are much narrower than for L1 (Van Dierendonck, 1994) making it susceptible to phase scintillation. Thus ionospheric scintillation will impact the L2 user much more than the L1 C/A code user.

The ionosphere varies diurnally, seasonally, with the 11 year solar cycle, and based on the users geographic location. There are also several types of disturbances that affect the ionosphere. In Skone (1999) the following major ionospheric characteristics are described:

Diurnal: The maximum total electron content (TEC) occurs at 2:00 p.m. local time, with a second local maximum at 10:00 p.m. local time and a minimum before sunrise. Thus there are east-west gradients in TEC.

Seasons: The TEC is lowest in summer and peaks at the equinoxes. This is due to the balancing between the production and the recombination mechanisms.

Solar Cycle: Increased solar activity increases the emissions which break the neutral atoms into free electrons and ions. The entire ionospheric activity increases.

Equatorial Anomaly: There are two local maximums that are symmetric around the geomagnetic equator (approximately $\pm 10^\circ$). These maximums are generated by the neutral wind and can produce strong gradients in the 50 ppm range as well as scintillations (Wanninger, 1993).

Geomagnetic Sub-Storms: The aurora borealis, around the magnetic poles, is caused by the geomagnetic sub-storms. It is caused by a build up of energy in the magnetotail, and sudden current wedges. The equatorward side of the aurora contains a depleted (trough) region of electrons. Within the trough gradients of 15 ppm are possible (Foster, 2000) in addition to scintillations.

Magnetic Storms: Magnetic storms are more global events with their signature being a large scale ring current rotating around the earth in a East-West direction.

Ionospheric Storms: Similar to magnetic storms except the TEC varies as opposed to the magnetic fields. Often occurs in conjunction with the magnetic storms.

Storm Enhanced Density: During geomagnetic sub-storms and equatorward of the aurora's trough, an area of storm enhanced density (SED) can be formed with electrons from later local times and lower latitudes. Gradients of 75 ppm have been seen during a SED (Foster, 2000).

As stated above all of the ionosphere's effects on the GNSS signals stem from the fact that the refractive index is not equal to 1. The phase index of refraction (n_p) is given by the Appleton-Hartree formula:

$$n_p^2 = 1 - \frac{X}{1 - jZ - \frac{Y_T^2}{2(1 - X - jZ)} \pm \sqrt{\frac{Y_T^4}{4(1 - X - jZ)^2} + Y_L^2}} \quad (2-7)$$

where $X = \frac{Ne^2}{\epsilon_0 m \omega^2} = \frac{\omega_p^2}{\omega^2}$, $Y_L = \frac{eB \cos(\theta)}{m\omega} = \frac{\omega_g \cos(\theta)}{\omega}$, $Y_T = \frac{eB \sin(\theta)}{m\omega} = \frac{\omega_g \sin(\theta)}{\omega}$,

$$Z = \frac{\nu}{\omega}$$

N electron density

e electron charge

ϵ_0 permittivity of free space

m electron mass

ω angular frequency

ω_p plasma frequency

ω_g gyro frequency

B earth's magnetic field

θ angle between the RF signal and the earth's magnetic field

ν electron collision frequency

Taking equation (2-7) and assuming that the contribution due to the gyro frequency and the collision frequency are 0 (i.e. $Z=0$, $Y_T=0$, and $Y_L=0$), and taking the binomial expansion to the first term result in:

$$n_p^2 = 1 - X = 1 - \frac{\omega_p^2}{\omega^2} \quad (2-8)$$

$$n_p \approx 1 - \frac{1}{2} \frac{\omega_p^2}{\omega^2} \quad (2-9)$$

This first order approximation is accurate to 1% using an extremely high plasma frequency and to 0.1% using a typical plasma frequency (Klobuchar, 1996). The group index of refraction is given by (Seeber, 1993):

$$n_g = \omega \frac{dn_p}{d\omega} + n_p \quad (2-10)$$

Taking the first order approximation of n_p in equation (2-9) and substituting in equation (2-10) results in the following group index of refraction

$$n_g = \omega \frac{d}{d\omega} \left(1 - \frac{1}{2} \frac{\omega_p^2}{\omega^2} \right) + \left(1 - \frac{1}{2} \frac{\omega_p^2}{\omega^2} \right) = 1 + \frac{1}{2} \frac{\omega_p^2}{\omega^2} \quad (2-11)$$

The phase and group indices of refraction have opposite effects. The phase is advanced while the group is delayed. However, information is still travelling slower than the speed of light, since only the group velocity carries information.

To generate the ionospheric delay equation (2-9) or (2-11) must be substituted in equation (2-3) and integrated along the path. Similar to the troposphere, the second term of equation (2-3) due to bending is normally ignored. This results in a 10 mm and 100 mm error at a 7.5° elevation angle for low and high ionospheric levels respectively (Brunner and Gu, 1991). The resulting ionospheric delay is a function of the transmitting frequency (f) and the TEC.

$$d_{\text{ion}} = \int_{\text{Actual}} (n - 1) ds = \int_{\text{Actual}} \left(1 \pm \frac{1}{2} \frac{\omega_p^2}{\omega^2} - 1 \right) ds = \int_{\text{Actual}} \left(\pm \frac{1}{2} \frac{Ne^2}{\epsilon_0 m \omega^2} \right) ds \quad (2-12)$$

$$d_{\text{ion}} = \pm \frac{1}{2} \frac{e^2}{\epsilon_0 m \omega^2} \underbrace{\int_{\text{Actual}} (N) ds}_{\text{TEC}} = \pm \frac{40.3 * \text{TEC}}{f^2} \quad (2-13)$$

Since the ionospheric delay depends on frequency, dual frequency GNSS receivers will be able to compensate for the delay, as long as any frequency dependent biases in the satellite and receiver are taken into account. However, the current GPS constellation only has one civilian frequency. Civilian receivers can track the L2 signal using codeless and semi-codeless techniques, however, these receivers are expensive and experience a significant squaring loss (10-40 dB) depending on the tracking method employed (Van Dierendonck, 1994 and Woo, 1999). These receivers are normally used for high accuracy applications, for general navigation only L1 C/A code receivers are employed. While standard user receivers only have access to one frequency they can apply the GPS broadcast ionospheric algorithm. This algorithm was designed to model the monthly median behaviour and should remove 50% of the ionospheric range error (Klobuchar, 1996). Since the algorithm is not real time and must represent the world's ionosphere using only 13 bytes spread over 8 coefficients (U.S. Department of Defence, 1999), it cannot compensate for any short duration changes in the ionosphere. Differential corrections can be used to reduce the ionospheric error.

Like tropospheric models, ionospheric models estimate the zenith delay and then use a mapping function to convert the zenith delay to the slant range.

$$d_{\text{ion}} = d_{\text{ion}}(\text{zenith}) * m(E) \quad (2-14)$$

One common ionospheric model assumes that all of the electrons are in a shell 350 - 400 km above the earth. This results in the mapping function in equation (2-15), and is

plotted in Figure 2-29 (Skone and Cannon, 1997). Note that the mapping function is only 3 at a 5° elevation angle.

$$m(E) = \frac{1}{\sqrt{1 - \left(\frac{\cos(E)}{1 + \frac{h}{R_e}} \right)^2}} \quad (2-15)$$

where h user's height
 R_e mean radius of the earth

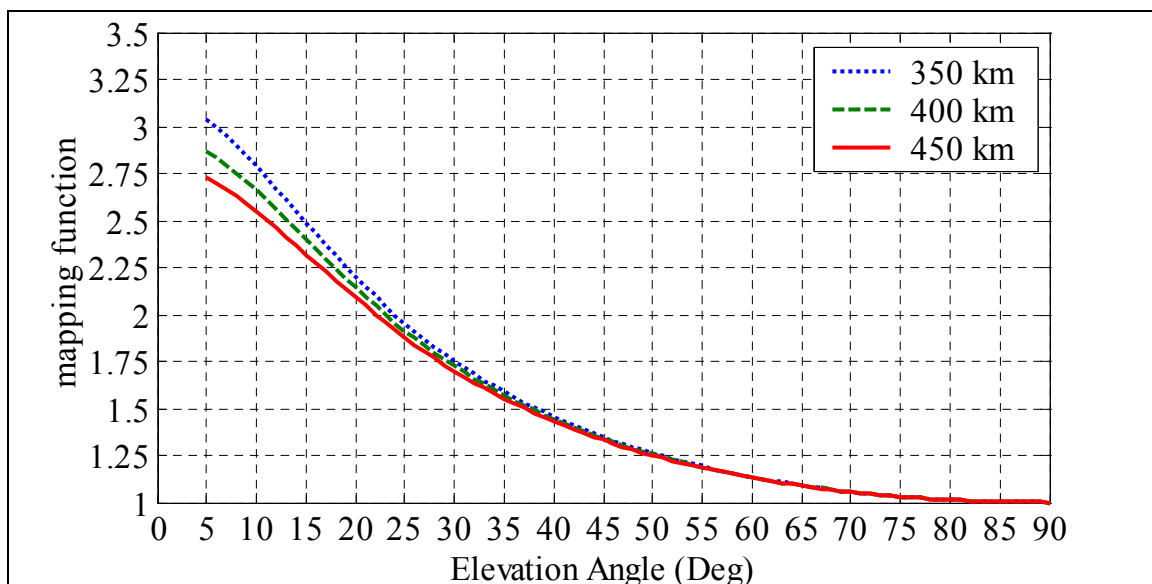


Figure 2-29 Typical Ionospheric Mapping Function for Different Shell Heights

The question that must be answered is what effect will the ionosphere have on navigation users? In Klobuchar, et al. (1995), ionospheric spatial de-correlation errors of 3 m, 95%, were reported using data from a 500 km baseline during a low in the solar cycle. The authors expected this to double during solar maximum, which would lead to 6 m of error. As mentioned above, gradients of 15 ppm (Foster, 2000), 30 ppm (Wanninger, 1993), and 75 ppm (Foster, 2000) have been reported under various ionospheric phenomena. A 10 ppm gradient was reported in Lachapelle, et al. (1999) on the St. Lawrence Seaway using the CCG DGPS stations during a 1998 test.

To determine the potential impact of these various ionosphere gradients, a similar simulation to that conducted for the ephemeris and troposphere will be conducted for the ionosphere. Three of the ionospheric profiles discussed in Foster (2000) will be simulated as shown in Figure 2-30.

- 1) Steep TEC Gradient observed over Millstone Hill (mid – latitudes)
- 2) Ionospheric Trough observed during disturbed conditions
- 3) SED observed during a major geomagnetic disturbance

Figure 2-30 plots the latitude vs. the vertical total electron content units ($\text{TECU} = 1 \times 10^{16}$ Electrons). At the GPS L1 frequency 1 TECU equals a range error of 0.16 m, using equation (2-12). The simulation will be conducted over 24 hours in 60 second increments to simulate all possible GPS geometries. The reference station will be simulated from 20° N to 70° N in 1° increments, with the user 5° north of the reference station. This equates to a baseline of 555 km which is similar to the baseline length used in the other simulations. A longitude of 60° W and an height of 0 m were used for both the user and reference station. For each simulation only the ionospheric error generated from Figure 2-30 will be used. In order to run the simulation from 20° N to 70° N the ionosphere

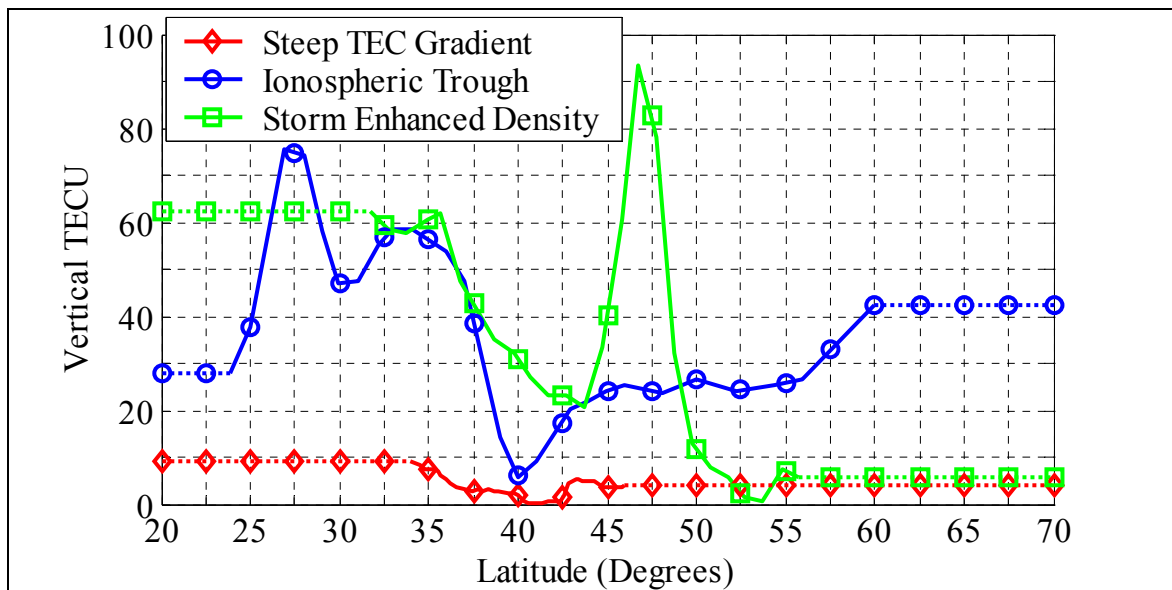


Figure 2-30 Ionospheric Profile (Foster, 2000)

must be defined for all of the possible pierce points. Therefore a constant TEC was assumed at the beginning and end of each profile, which is plotted as a dashed line in the figure. The simulation further assumes that the ionosphere only varies with latitude and not with longitude.

Figure 2-31 contains the 95% single difference misclosures for each simulation location and ionospheric profile. As expected from Figure 2-30, the SED misclosures are the largest. The 95% peak is 28.6 m and it exceeds 10 m for almost 25° of latitude (29° N - 44° N). The maximum misclosure of 40.0 m occurred with the reference station at 41° N. The ionospheric trough also generates 95% misclosures exceeding 10 m for 22° of latitude (20° N - 42° N). However, its 95% peak was 18.2 m and its overall maximum was 23.1 m, both of these values are approximately half of the SED's corresponding values. The steep TEC gradient causes minimal misclosures. Its 95% maximum misclosure was only 2.3 m, and its overall maximum value was 3.0 m. Thus the Steep TEC gradient should not dramatically bias the resulting DGPS position.

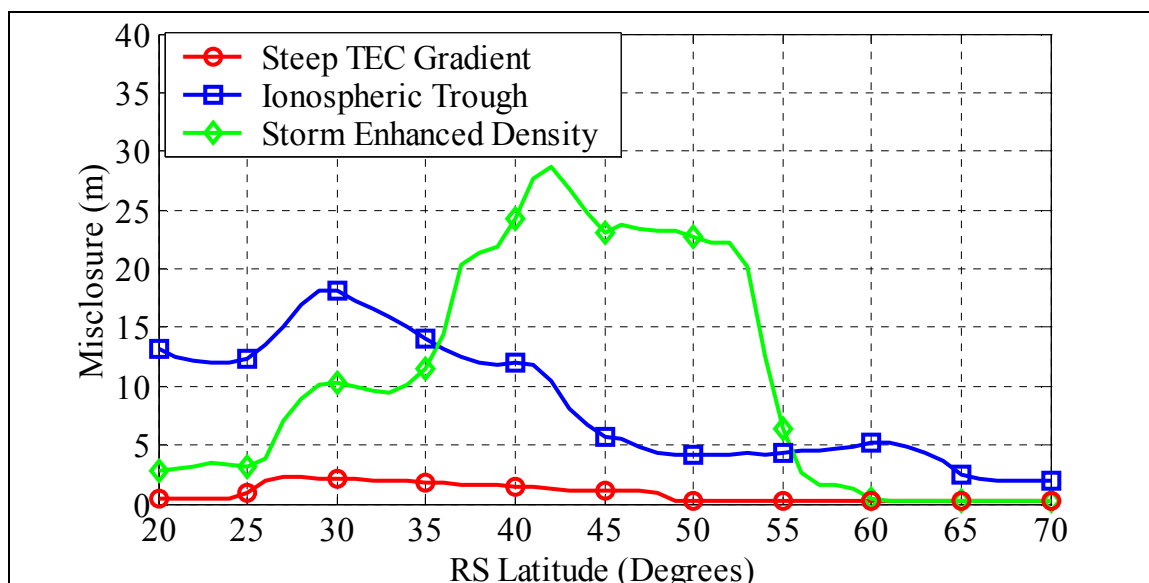


Figure 2-31 Differential Satellite Misclosures (95%)

Another way to analyse the misclosures is to investigate the size of the simultaneous misclosures. Figure 2-32 takes each ionospheric profile and plots the 95% largest, second largest, and third largest simultaneous misclosure. As mentioned above the maximum misclosure for the steep TEC gradient was 3.0 m, therefore when plotted on the same scale as the other two profiles the misclosures are almost flat lined. The ionospheric trough on the other hand shows three distinct lines, from 20° to 47° the average difference between the relative maximums are 6.3 m and 3.5 m respectively. Above 47° both differences are below 2 m. The spread of the SED is even more pronounced, between 34° and 57° the average differences were 9 m and 6 m respectively. Outside this range both differences were less than 2 m.

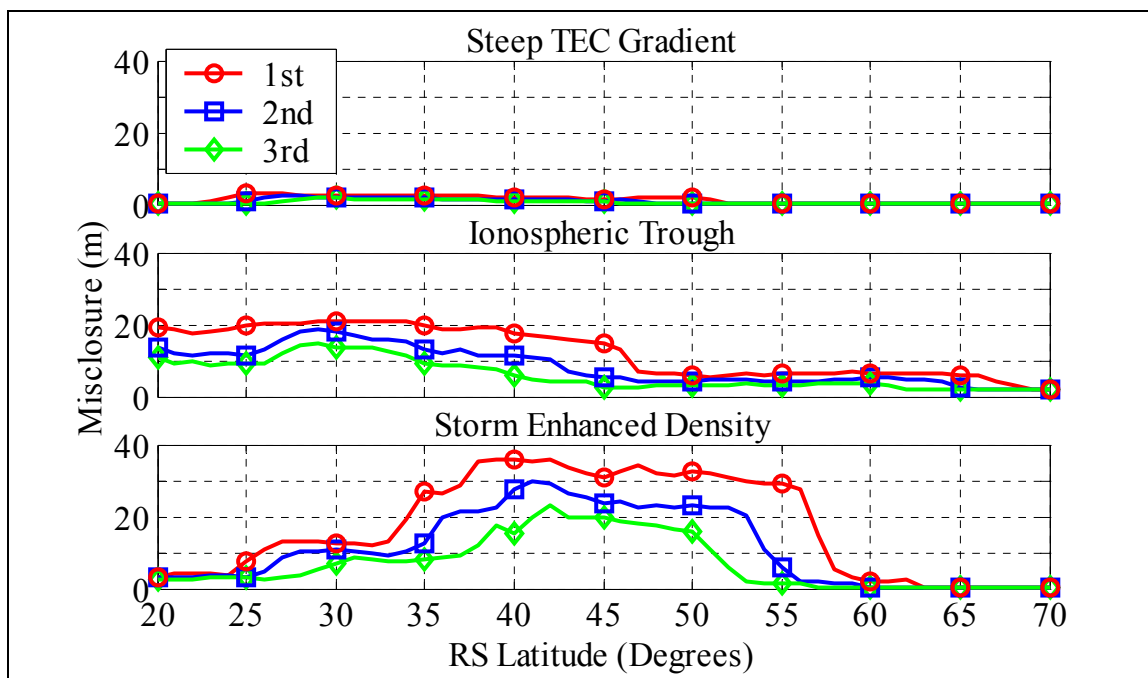


Figure 2-32 1st, 2nd, and 3rd Simultaneous Differential Satellite Misclosures (95%)

The misclosures were then propagated into the position domain. Figure 2-33 plots the 95% results for the HPE and VPE. Table 2-11 shows the RS latitude with the maximum 95% HPE and then the RS latitude with the overall maximum HPE. In addition to the position errors for the ionospheric trough and SED being very large they were both above

10 m for approximately 20° of latitude. Thus the errors are spread out over a wide expanse of latitudes.

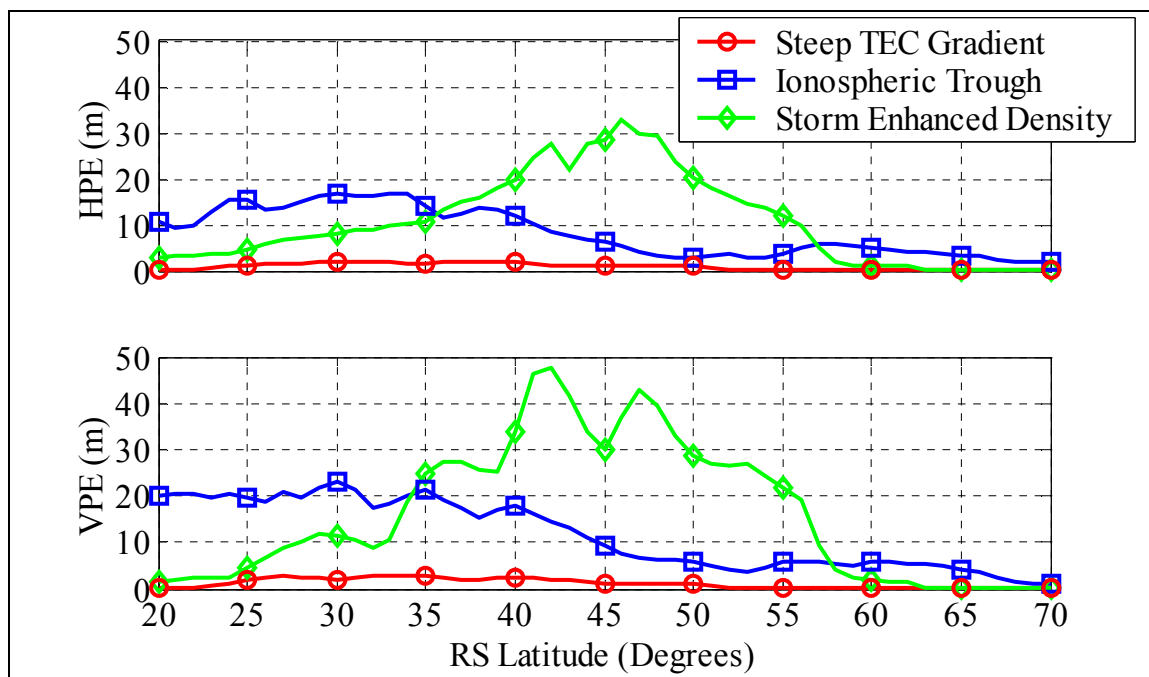


Figure 2-33 95% Position Errors

Table 2-11 Maximum Value for each Parameter (Latitude Simulation)

Parameter	Latitude with Max 95% HPE	Latitude with Overall Max HPE
Steep TEC Gradient	2.1 m (31°)	4.2 m (34°)
Ionospheric Trough	16.8 m (34°)	28.7 m (34°)
SED	32.6 m (46°)	68.3 m (42°)

The misclosures and the resulting position errors are two orders of magnitude greater than the ephemeris errors and one order of magnitude greater than the troposphere. As shown in the results, significant misclosures and position errors can be generated by the extreme ionospheric phenomenon. The more benign steep TEC gradient did not produce significant errors. The results for a second simulation with the user 3° north of the reference station is given in Appendix D. Significant misclosures and position errors

occurred for the 3° baseline. These results will be used in the simulation sections to justify the magnitude of the selected blunders.

2.5.4 Measurement Noise

The pseudorange and carrier phase measurements of equation (2-1) are usually made with a delay lock loop (DLL) and phase lock loop (PLL) respectively. This section discusses the resulting pseudorange ($\epsilon(p)$) and carrier phase ($\epsilon(\Phi)$) measurement noises.

The DLL measurement errors are composed of thermal noise and dynamic stress error (Ward, 1996). If the vehicle dynamics are benign or if the PLL is used to aid the DLL (thereby removing most of the signal dynamics), the thermal noise dominates the measurement errors. In Ward (1996) the following equation was given for the DLL's thermal noise:

$$\sigma_{\text{DLL}} = \lambda_{\text{Code}} * \sqrt{\frac{4 * F_1 * d^2 * B_n}{c/n_o} \left[2(1-d) + \frac{4 * F_2 * d}{T * c/n_o} \right]} \quad (\text{m}) \quad (2-16)$$

where λ_{Code} GLONASS (C/A) = 586 m, GPS (C/A) = 293 m, GPS (P) = 29 m

F_1 DLL correlator factor (1 for time shared and 0.5 for dedicated correlators)

F_2 DLL type factor (1 for early/late and 0.5 for dot product)

d correlator spacing (wide = 0.5 and narrow = 0.05)

B_n Code Loop Noise Bandwidth (Hz)

T Predetection Integration Time

C/N_o carrier to noise power in decibels (dB-Hz)

c/n_o carrier to noise power as a ratio ($10^{C/N_o/10}$)

In most modern receivers the DLL factors are both set to 0.5. As shown in equation (2-16) the thermal noise is directly proportional to the code loop's bandwidth and the correlator spacing and inversely proportional to the predetection integration time and the carrier to noise ratio (c/n_o). The square root term of equation (2-16) is independent of the

code's wavelength (λ_{Code}). Thus the performance of different codes (GPS C/A, GPS P, and GLONASS C/A) would be identical once the results were divided by the corresponding wavelength. Using equation (2-16) the noise performance for five different code and correlator combinations were generated and are plotted in Figure 2-34, with a predetection integration time of 20 ms and $B_n = 0.8$ Hz (Ward, 1996). The wide and narrow correlators used 0.5 and 0.05 chip spacing respectively.

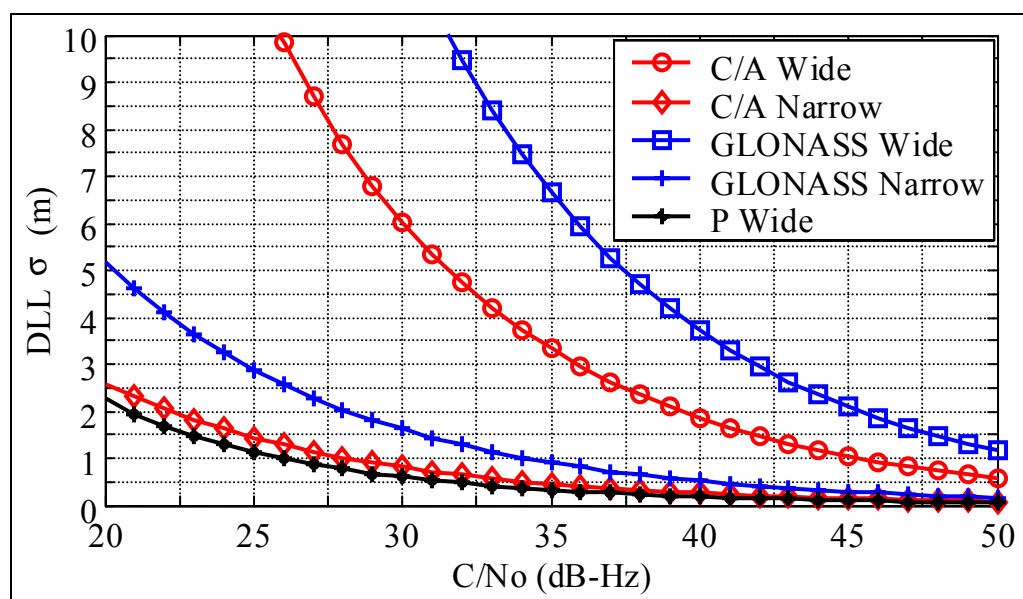


Figure 2-34 DLL Thermal Noise Performance

The C/N_0 is a function of the satellite's transmitted power, transmitting antenna gain pattern, free spacing loss, atmospheric absorption, and the receiving antenna gain pattern. The minimum RF signal strength for the GPS and GLONASS systems and the resulting C/N_0 assuming a noise value of -205 dBW/Hz are given in Table 2-12 (U.S. Department of Defence, 1999 and Russian Federation Ministry of Defence, 1995). The GPS signals however often exceed the specifications given in Table 2-12 by as much as 7.3 dB (Spilker, 1994a). For the 45 dB-Hz case, the GPS C/A wide and narrow correlator one sigma noise values are 1.0 and 0.14 m respectively, with GLONASS double these values. For weaker signals (35 dB-Hz) the GPS C/A narrow correlator still performs very well

with a one sigma value of 0.45 m, however the GPS C/A wide correlator has a one sigma value of 3.3 m, GLONASS is again double these due to its longer chip length.

Table 2-12 Minimum Received RF Signal Strength

Channel and Code	Minimum RF Signal Strength	C/N ₀
GPS L1 C/A Code	-160.0 dBW	45 dB-Hz
GPS L1 P Code	-163.0 dBW	42 dB-Hz
GPS L2 P Code	-166.0 dBW	39 dB-Hz
GLONASS C/A	-161.0 dBW	44 dB-Hz

What effect does the troposphere and ionosphere attenuation described in sections 2.5.2 and 2.5.3 have on the code measurement accuracy? From equation (2-16) and Figure 2-34, 1 dB of additional attenuation will increase the code noise by approximately 12%. Thus as was stated in sections 2.5.2 and 2.5.3, the added attenuation has little effect.

From this theoretical analysis pseudorange measurement standard deviations of < 0.5 m and < 3 m are expected for the GPS C/A narrow and wide correlators respectively.

The carrier PLL measurement errors are more complicated than the code's. The PLL's measurement is a function of thermal noise, vibration induced oscillator jitter, Allan variance induced oscillator jitter, and dynamic stress (Ward, 1996). If the steady state error due to vehicle dynamics is zero (function of dynamics and PLL loop filter) and a good quality oscillator and receiver frequency plan are employed, the thermal noise once again dominates and can be determined from the following (Ward, 1996):

$$\sigma_{\text{PLL}} = \frac{\lambda_{\text{Carrier}}}{2 * \pi} \sqrt{\frac{B_n}{c/n_0} \left[1 + \frac{1}{2 * T * c/n_0} \right]} \quad (\text{m}) \quad (2-17)$$

where λ_{Carrier} GLONASS (L1) = 0.186 m, GPS (L1) = 0.190 m, GPS (L2) = 0.244 m

B_n Carrier Loop Noise Bandwidth (Hz)

The carrier loop bandwidth must be chosen to ensure carrier lock during the expected dynamic periods. A third order PLL, which is often used in high dynamic applications, remains stable for bandwidths ≤ 18 Hz (Ward, 1996). Figure 2-35 shows the carrier phase measurement performance for three different loop filters of 2, 10, and 18 Hz. Using the 18 Hz bandwidth, the PLL standard deviation varies from 2.3 to 0.4 mm for C/N_0 from 35 to 50 dB-Hz. This is orders of magnitude smaller than the code measurement noises.

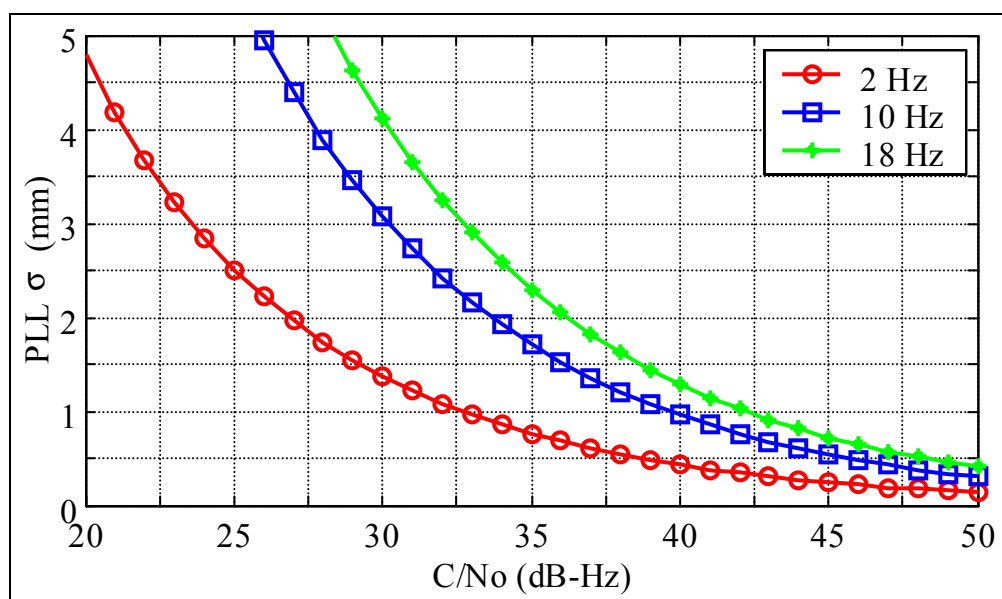


Figure 2-35 PLL Thermal Noise Errors for Various Bandwidths

This is the theoretical performance for the code and carrier phase measurement errors. What is experienced in practice? A four hour zero baseline test was conducted with two Ashtech GG24™ integrated GPS and GLONASS receivers. Double difference code and carrier phase measurements were generated to determine the pseudorange and carrier phase measurement errors. A zero baseline double difference removes the orbit, troposphere, ionosphere, and multipath errors, leaving only noise and the carrier phase ambiguity. The individual pseudorange and carrier phase measurement error were calculated assuming that if the satellite's elevation is greater than 45° then the measurement noise is approximately constant. Thus the base satellite for the double differences was kept above 45° . For the four hour period three different base satellites

were used, all of them were GPS satellites. The results were generated for 5° elevation angle bins from 5° to 90° for GPS and GLONASS separately. Figure 2-36 summarises the results for the pseudorange and carrier phase.

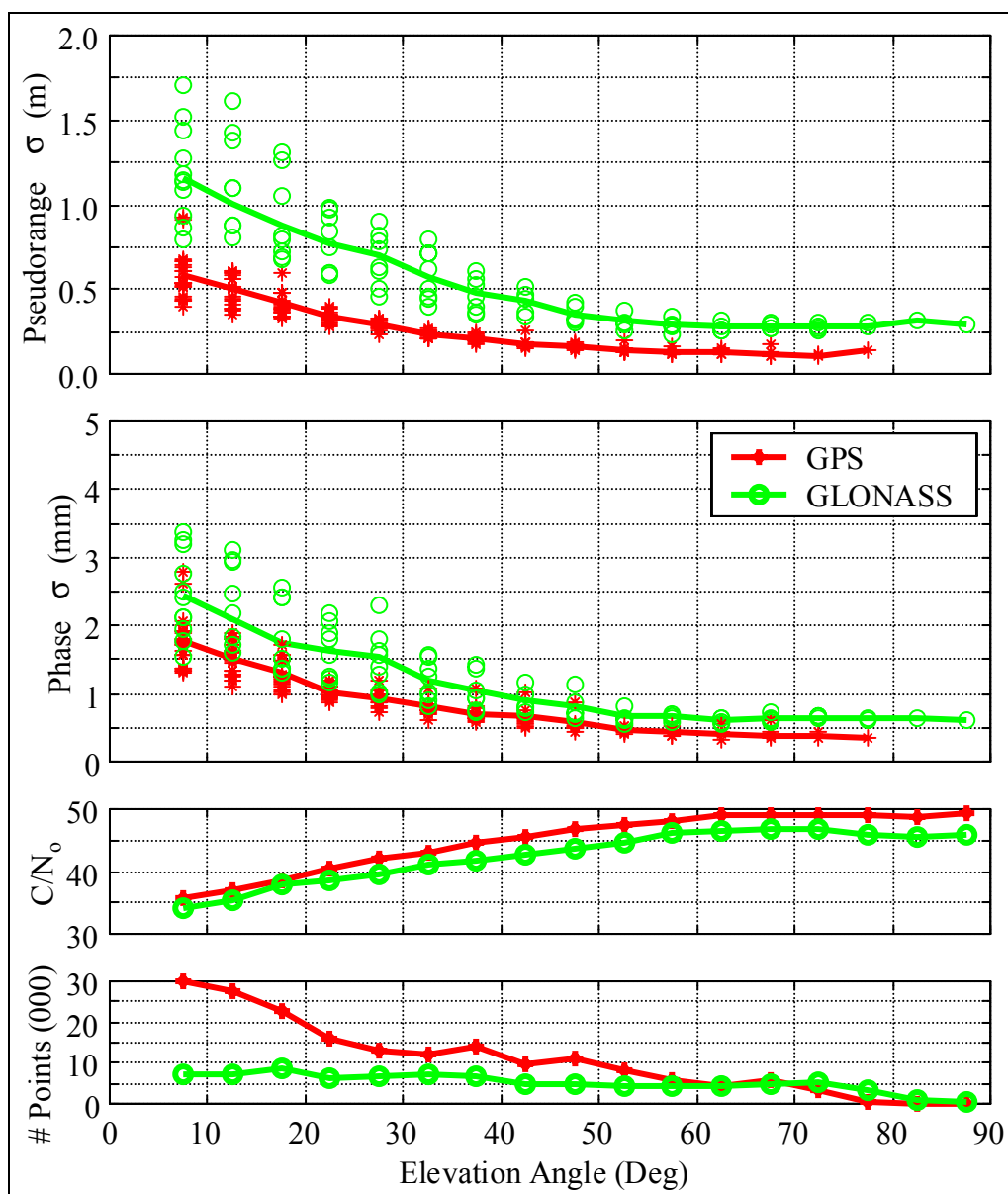


Figure 2-36 Pseudorange and Carrier Phase Measurement Accuracy for the Ashtech GG24™ Integrated GPS / GLONASS Receiver

The pseudorange and carrier phase results from Figure 2-36 show the individual results for the 22 GPS and 12 GLONASS satellites that were tracked during this four hour period. The individual satellite results are plotted as the green circle and red asterisk for GLONASS and GPS respectively. The overall results are plotted as the solid lines in green and red, again for GLONASS and GPS respectively. The bottom two graphs show the C/N_0 and the number of points there were used to generate these results. The Ashtech GG24™ receiver employs an Edge™ Correlator which shows similar noise performance to the narrow correlator (Van Dierendonck and Braasch, 1997). When the C/N_0 is taken into account the pseudorange measurement standard deviation is very similar to the theoretical results of Figure 2-34.

The theoretical and practical noise errors are consistent. Since the carrier phase measurement noise is at the millimetre level, it will be ignored, only the code measurement noise will be included in CHAPTER 4's simulations.

2.5.5 Multipath Error

The one error source from equation (2-1) that depends on the local user's environment is multipath. Multipath occurs whenever the direct GNSS signal reflects off of a near by

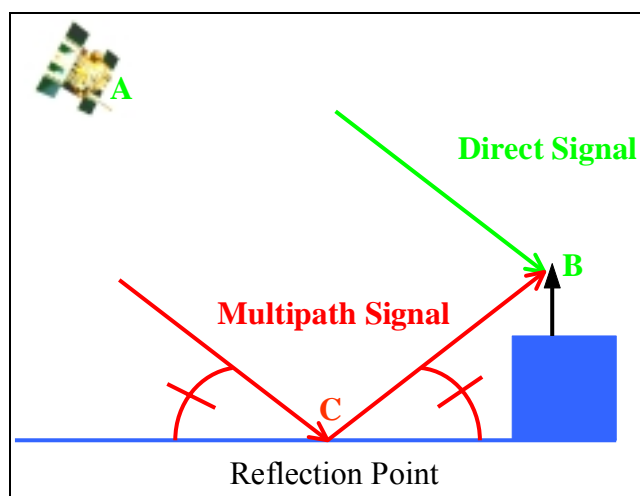


Figure 2-37 Multipath and Direct GNSS Signals

object resulting in multiple copies of the GNSS signal reaching the receive antenna, as shown in Figure 2-37. In order to calculate the multipath's effect the composite received signal must be generated. The code delay, phase delay, and amplitude must be determined for each multipath signal in order to generate the composite signal.

The multipath time delay (τ) is the path length difference (δr) divided by the speed of light (c),

$$\tau = \frac{\delta r}{c} \quad (2-18)$$

while the multipath phase delay (θ) is the path length difference divided by the GPS wavelength (λ) converted to radians, plus any phase delay caused by the reflecting surface (θ_s).

$$\theta = \frac{2 \cdot \pi \cdot \delta r}{\lambda} + \theta_s \quad (2-19)$$

The multipath's signal amplitude is a function of the reflection coefficient and the receiving antenna's gain pattern. The resulting composite signal is as follows:

$$s(t) = A * c(t - \tau_0) * \cos(2\pi f_0 + \theta_0) + A * \sum_{i=1}^{i=n} \alpha_i \cdot c(t - \tau_0 - \tau_i) \cdot \cos(2\pi f_0 + \theta_0 + \theta_i) \quad (2-20)$$

where

A	amplitude of the direct signal
α_i	relative amplitude for the i th multipath signal
c	PRN code
τ_0	direct signal's code phase
τ_i	multipath signals' code delay
f_0	GPS carrier frequency
θ_0	direct signal's carrier phase

θ_i multipath signals' carrier phase delay
 t time

The remaining sections discuss the multipath code and carrier phase error. Before the errors are calculated the amplitude of the resulting multipath signal must be determined.

2.5.5.1 Multipath Amplitude

What happens when a plane wave is reflected from a surface? Figure 2-38 shows a pictorial representation of an incident plane wave in medium 1 reflecting off medium 2. Since the transmitted wave (refracted wave) will not cause any multipath effects it will not be considered. The electric field of the incident wave is composed of two components. The perpendicular (\perp) also called the horizontal component is perpendicular to the plane of incidence xy . The parallel (\parallel) also called the vertical component is parallel to the plane of incidence xy . The continuity of the tangential fields (electric and magnetic) at the boundary between the two mediums is used to generate the values for the reflected and transmitted values of the plane wave. The reflected wave resulting from the interaction of the incident wave and the boundary between the two media is normally written as the product of the incident wave and a reflection coefficient for each of the electric field components:

$$\begin{aligned} E_{r\parallel} &= \rho_{\parallel} \cdot E_{i\parallel} \\ E_{r\perp} &= \rho_{\perp} \cdot E_{i\perp} \end{aligned} \tag{2-21}$$

where ρ_{\parallel} reflection coefficient in the parallel direction

ρ_{\perp} reflection coefficient in the perpendicular direction

$E_{i\parallel}$ incident electric field in the parallel direction

$E_{i\perp}$ incident electric field in the perpendicular direction

$E_{r\parallel}$ reflected electric field in the parallel direction

$E_{r\perp}$ reflected electric field in the perpendicular direction

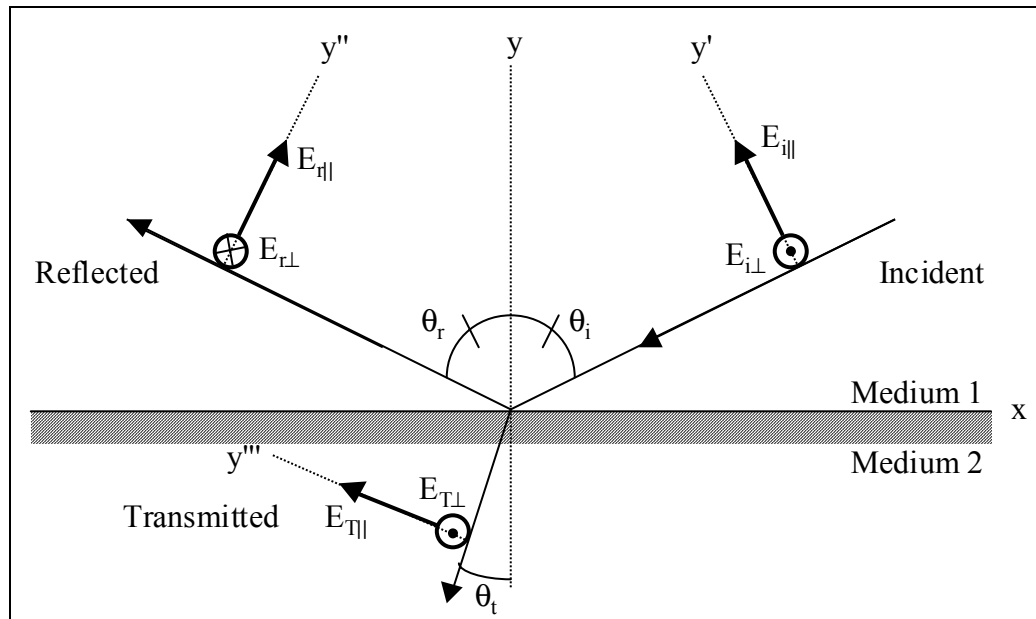


Figure 2-38 Reflected and Incident Plane Waves (Hecht, 1990)

The reflection coefficients for the two electric field components are found using Fresnel equations (Collin, 1985):

$$\rho_{\parallel} = \frac{(\kappa - j\chi) \sin(\phi) - \sqrt{\kappa - j\chi - \cos(\phi)^2}}{(\kappa - j\chi) \sin(\phi) + \sqrt{\kappa - j\chi - \cos(\phi)^2}}$$

$$\rho_{\perp} = \frac{\sin(\phi) - \sqrt{\kappa - j\chi - \cos(\phi)^2}}{\sin(\phi) + \sqrt{\kappa - j\chi - \cos(\phi)^2}} \quad (2-22)$$

where κ relative permittivity

ϕ grazing angle

$$\chi = \frac{\sigma}{\epsilon_0 * 2\pi f}$$

σ conductivity

The incident GPS signal is right hand circularly polarised (RHCP), with an axial ratio (AR) on L1 of ≤ 1.2 dB and ≤ 1.8 dB for the block II/IIA and IIR satellites respectively (U.S. Department of Defence, 1999). Figure 2-39 shows the RHCP GPS signal propagating out of the page with two different axial ratios. The dashed line is for a perfect circularly polarised signal and the solid line has the maximum AR found on L1.

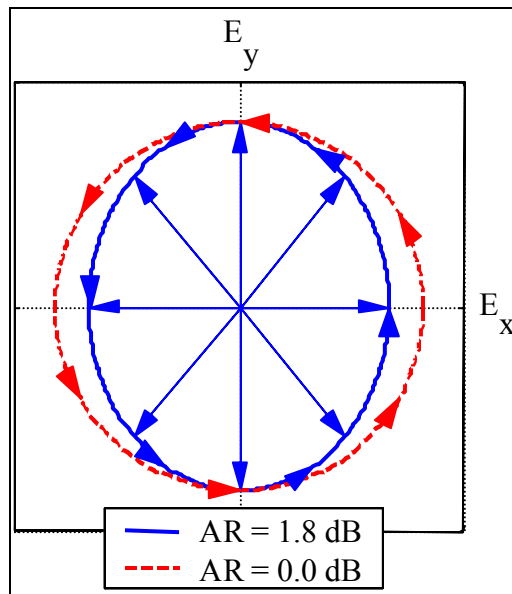


Figure 2-39 GPS Signal Maximum Axial Ratio

The equation for the GPS signal's electric field as shown in Figure 2-39 and the AR is:

$$\vec{E} = A_x \cos(2\pi ft - \beta z) \cdot \hat{x} + A_y \cos(2\pi ft - \beta z + \delta) \cdot \hat{y} \quad (2-23)$$

$$AR = 20 \cdot \log \frac{E_{\max}}{E_{\min}}$$

where δ phase difference between the two components.

f frequency, for GPS L1 $f = 1575.42$ MHz

E_{\min} minimum value of the electric field

E_{\max} maximum value of the electric field

A_x x component amplitude

A_y y component amplitude

β phase constant

If $A_x = A_y$ and $\delta = -90^\circ$, the resulting signal is RHCP. If $\delta = +90^\circ$ then the signal would be left hand circular polarised (LHCP). For other values of δ and when the magnitudes of the two components are not equal, various elliptical polarisations result (i.e. the GPS signal). The signal becomes linearly polarised if $\delta = 0^\circ$, $\delta = 180^\circ$, or if one of the components amplitude is zero.

Applying equation (2-21) for seawater results in the reflection coefficients shown in Figure 2-40. The parallel component of the incident wave goes through a minimum at the low grazing angles, this minimum is called the Brewster angle. Below this angle the reflected wave's polarisation is right hand elliptically polarised (RHEP), near the Brewster angle the reflected wave will be almost linearly polarised, while above the Brewster angle the resulting wave will be left hand elliptically polarised (LHEP). The reflected signal is elliptically polarised for all grazing angles greater than 0° and less than 90° , since the reflection coefficients magnitudes are not equal to each other.

If instead of seawater, dry land was used as the reflecting surface ($\kappa = 4$ and $\sigma = 0.001$ S) the reflection coefficients given in Figure 2-41 would occur. At the Brewster angle of 26.5° the magnitude of the parallel component goes to zero and the resulting signal is linearly polarised. The phase transition for the parallel component is a step function at the Brewster angle. Thus reflections from the dry ground will still be RHEP up to the Brewster angle of 26.5° .

For high conductivity surfaces (i.e. steel and metals) the Brewster angle is $< 0.25^\circ$ grazing angle. Above the Brewster angle the magnitude of both reflection coefficients is one, while the phase response is 180° and 0° for the perpendicular and parallel components respectively. Thus reflections from a smooth metallic surface have 0 dB loss and are LHCP.

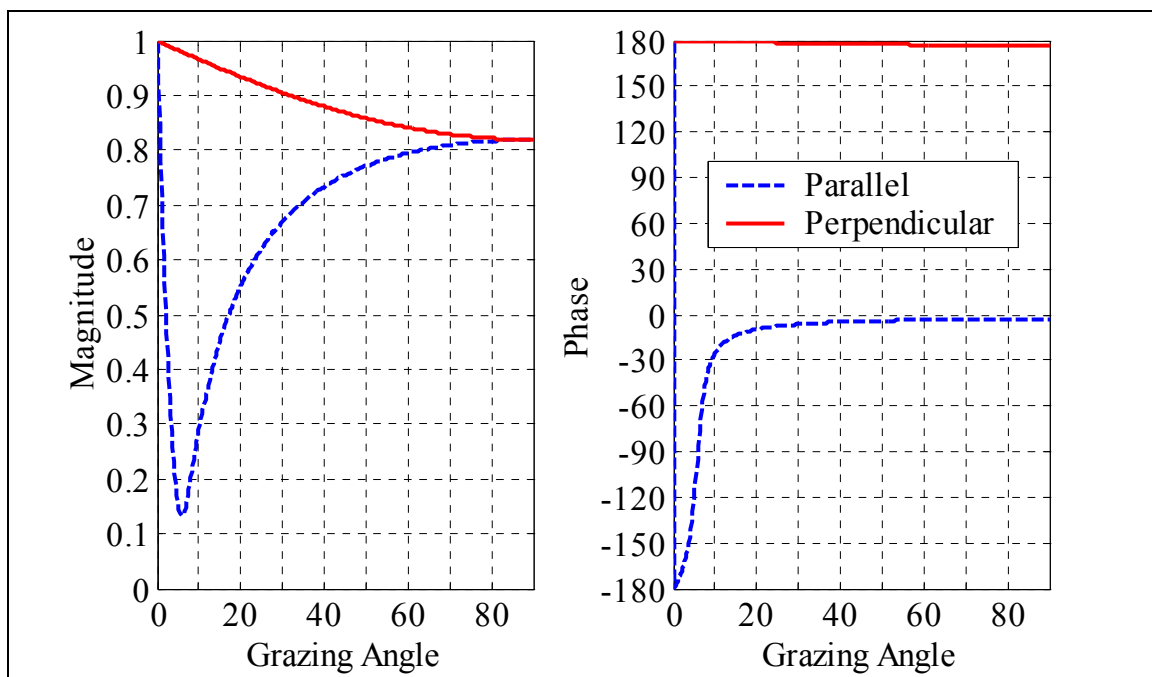


Figure 2-40 Reflection Coefficients for Seawater ($\kappa = 81$ and $\sigma = 4$ S)

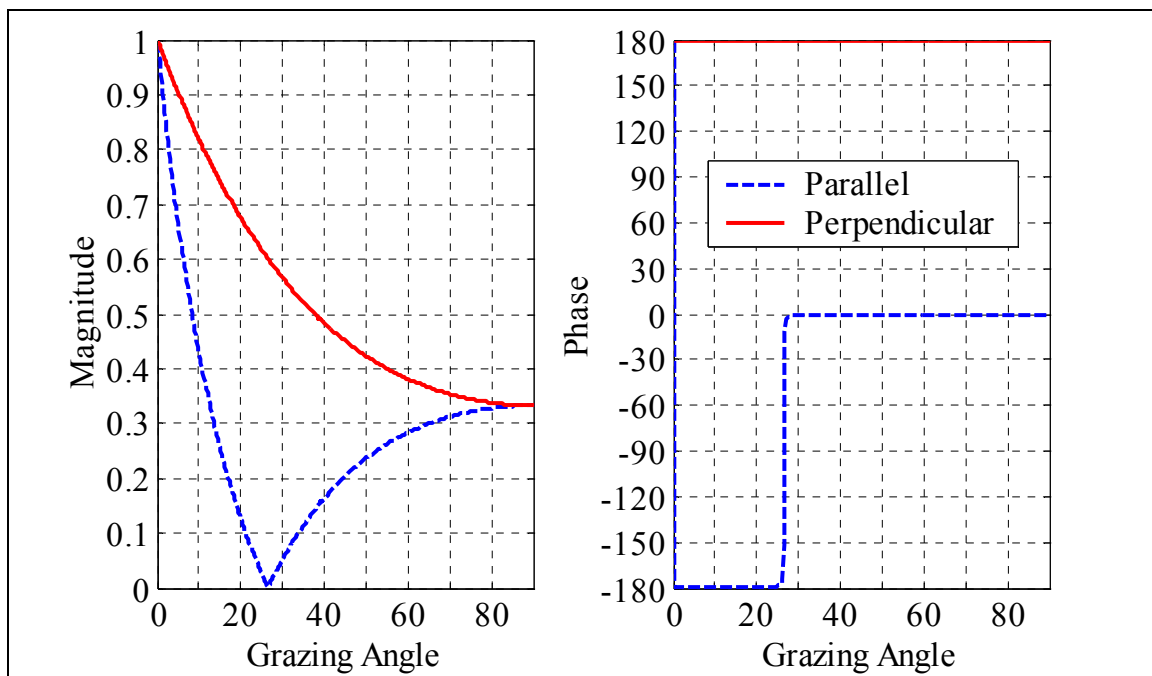


Figure 2-41 Reflection Coefficients for Dry Land ($\kappa = 4$ and $\sigma = 0.001$ S)

The reflected signal's magnitude and polarisation must then be combined with the receiving antenna's gain and polarisation response to calculate the multipath's received signal power. Figure 2-42 shows the gain pattern for a typical GPS patch antenna, a Sensor System's GPS patch antenna model S67-1575-Series (Sensor Systems, 2002).

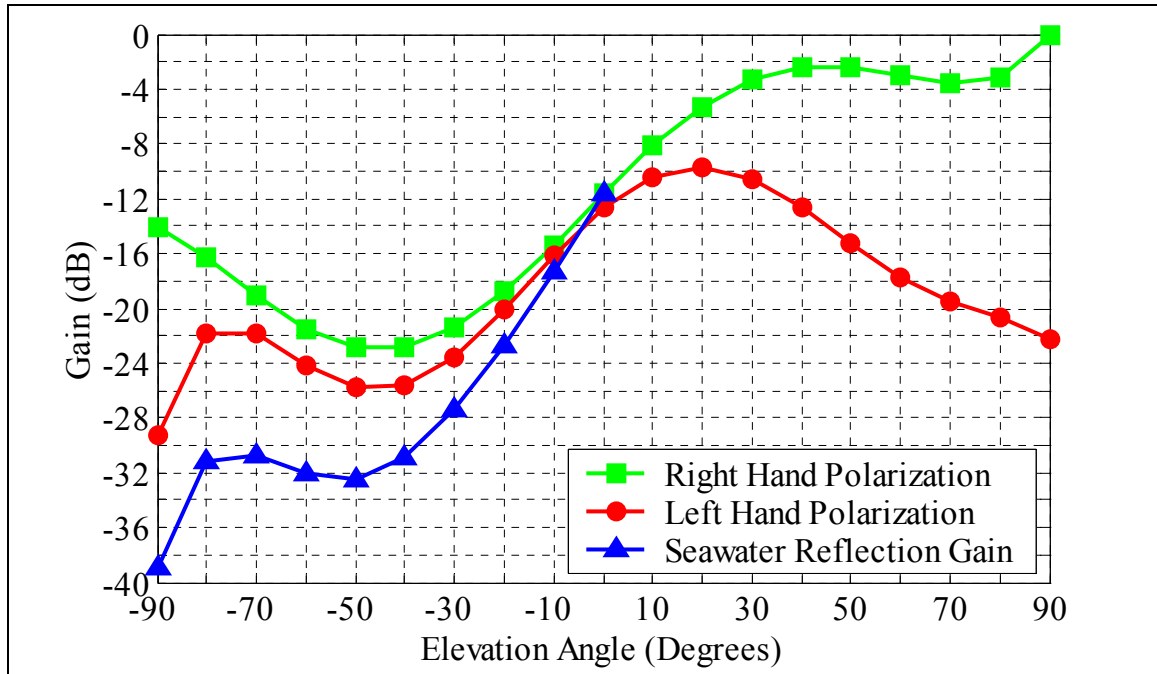


Figure 2-42 Sensor Systems Antenna Gain Response

If the receiving GPS antenna was RHCP, it would completely attenuate reflections from metals, which are LHCP. However, as shown in Figure 2-42 there is little discrimination between left and right handed signals from +20° to -60° elevation angle. Reflections from metals will follow the red line in Figure 2-42, since the signals are LHCP. Reflections from seawater are more complex, since the reflected signal is elliptically polarised and undergoes a reflection loss. The multipath received signal power will be the dot product of the reflected signal's electric field and the antenna pattern (Collin, 1985):

$$\begin{aligned}
V_{oc} &= \vec{E}_{Mul} \bullet \vec{h}_{Antenna} \\
\vec{E}_{Mul} &= A_{\perp} * |\rho_{\perp}| * e^{\angle \rho_{\perp}} * \hat{\perp} + A_{\parallel} * e^{-\frac{\pi}{2}} * |\rho_{\parallel}| * e^{\angle \rho_{\parallel}} * \hat{\parallel} \\
\vec{h}_{Antenna} &= \frac{E_r + E_l}{\sqrt{2}} * \hat{\perp} + \frac{E_r - E_l}{\sqrt{2}} * e^{+\frac{\pi}{2}} * \hat{\parallel}
\end{aligned} \tag{2-24}$$

where V_{oc} open circuit voltage
 \vec{E}_{Mul} incident multipath electric field to the antenna
 A_{\parallel} direct signal parallel amplitude
 A_{\perp} direct signal perpendicular amplitude
 E_r RHCP gain
 E_l LHCP gain
 $\hat{\parallel}$ unit vectors in the parallel direction
 $\hat{\perp}$ unit vectors in the perpendicular direction

Equation (2-24) assumes that the receiving antenna's maximum electric field occurs in the perpendicular direction with no tilt to the polarisation ellipse, and the satellite's direct signal is RHCP. Under these assumptions the received signal power for seawater reflections is shown in Figure 2-42 as the blue line, assuming no scattering due to sea state. For example, if a satellite was at a 20° elevation angle, the gain of the direct signal would be -4 dB, a reflection from a horizontal metallic surface would enter the antenna at a -20° elevation angle with a gain of -19.5 dB (LHCP). Thus the multipath signal will be 15.5 dB below the direct signal. If the reflection was from seawater the resultant loss would be approximately 1 dB worse or 16.5 dB.

For a detailed treatment of electromagnetic waves polarisations and reflections see Collin (1985), Kraus and Carver (1973), Jordan and Balmain (1968), Griffiths (1989), and Hecht (1990).

2.5.5.2 Code Error

The code ranging error is determined by the type of DLL and the bandwidth of the input signal. There are many special types of DLL, for example NovAtel's MET™ and MEDLL™, Ashtech's Edge™, Strobe™, and Enhanced Strobe™. These DLLs attempt to mitigate code multipath over that of the standard early minus late DLLs. Table 2-13 lists four common implementations of the standard non-coherent early minus late DLL discriminators (Ward, 1996). The one that requires the least computation burden is the dot product power which is often employed within GNSS receivers.

Table 2-13 Common DLL Discriminators (Ward, 1996)

Name	Discriminator
Dot Product Power	$\sum IP * (IE - IL) + \sum QP * (QE - QL)$
Early Minus Late Power	$\sum (IE^2 + QE^2) - \sum (IL^2 + QL^2)$
Early minus late envelope	$\sum \sqrt{IE^2 + QE^2} - \sum \sqrt{IL^2 + QL^2}$
Early minus late envelope normalised	$\frac{\sum \sqrt{IE^2 + QE^2} - \sum \sqrt{IL^2 + QL^2}}{\sum \sqrt{IE^2 + QE^2} + \sum \sqrt{IL^2 + QL^2}}$

where I in-phase component
 Q quadra-phase component
 P prompt correlator
 E early correlator
 L late correlator

With the discriminator selected (Dot Product Power), the spacing between the three correlators (Early, Prompt, and Late) must be specified. Two standard designations for correlator spacing are wide and narrow, with 1.0 and 0.1 chip spacing between the early and late correlators respectively. With the selection of the correlator spacing the bandwidth of the input signal must be selected. A wide correlator does not require a wide band signal and thus to reduce the input noise value, normally only the main lobe of the

GNSS signal is passed (2.046 MHz for GPS C/A code). When the narrow correlator is being used, a larger bandwidth is required, thus a 10 MHz bandwidth will be considered.

As shown in Table 2-13 the dot product discriminator employs six correlators. Taking equation (2-20) and correlating the input signal with the receiver's internal replicate of the GNSS signal results in the following equation for the six correlators:

$$\begin{aligned}
 IP &= A \cdot R(\hat{\tau} - \tau_0) \cdot \cos(\theta_0 - \hat{\theta}) + A \cdot \sum_1^n \alpha_i \cdot R(\hat{\tau} - \tau_0 - \tau_i) \cdot \cos(\theta_0 + \theta_i - \hat{\theta}) \\
 IE &= A \cdot R(\hat{\tau} - \tau_0 - td) \cdot \cos(\theta_0 - \hat{\theta}) + A \cdot \sum_1^n \alpha_i \cdot R(\hat{\tau} - \tau_0 - \tau_i - td) \cdot \cos(\theta_0 + \theta_i - \hat{\theta}) \\
 IL &= A \cdot R(\hat{\tau} - \tau_0 + td) \cdot \cos(\theta_0 - \hat{\theta}) + A \cdot \sum_1^n \alpha_i \cdot R(\hat{\tau} - \tau_0 - \tau_i + td) \cdot \cos(\theta_0 + \theta_i - \hat{\theta}) \\
 QP &= A \cdot R(\hat{\tau} - \tau_0) \cdot \sin(\theta_0 - \hat{\theta}) + A \cdot \sum_1^n \alpha_i \cdot R(\hat{\tau} - \tau_0 - \tau_i) \cdot \sin(\theta_0 + \theta_i - \hat{\theta}) \\
 QE &= A \cdot R(\hat{\tau} - \tau_0 - td) \cdot \sin(\theta_0 - \hat{\theta}) + A \cdot \sum_1^n \alpha_i \cdot R(\hat{\tau} - \tau_0 - \tau_i - td) \cdot \sin(\theta_0 + \theta_i - \hat{\theta}) \\
 QL &= A \cdot R(\hat{\tau} - \tau_0 + td) \cdot \sin(\theta_0 - \hat{\theta}) + A \cdot \sum_1^n \alpha_i \cdot R(\hat{\tau} - \tau_0 - \tau_i + td) \cdot \sin(\theta_0 + \theta_i - \hat{\theta})
 \end{aligned} \tag{2-25}$$

where R autocorrelation function of the filtered input GNSS signal with the internal replica of the GNSS Signal
 $\hat{\tau}$ receiver code tracking point
 $\hat{\theta}$ receiver phase tracking point
td correlator spacing

The code tracking point $\hat{\tau}$ is the value of τ that makes the discriminator output zero.

$$DLL(\hat{\tau}) = IP * (IE - IL) + QP * (QE - QL) = 0 \tag{2-26}$$

If the direct signal's delay (τ_0) is assumed to be zero, the code ranging error is simply $\hat{\tau}$.

In Ray (2000) it was shown that the phase tracking point ($\hat{\theta}$) does not affect the dot product discriminator assuming that frequency lock is maintained. Thus when equations

(2-25) are inserted into the dot product discriminator function equation (2-26) and simplified, $\hat{\theta}$ can be eliminated. The simplified expression with $\hat{\theta}$ eliminated for the one and two multipath cases can be found in Ray (2000).

The autocorrelation function depends on the input GNSS signal's bandwidth. Figure 2-43 shows the resulting autocorrelation functions for five filter bandwidths of PRN 10's C/A code (Matlab was used to generate the correlation functions using a 100 order finite impulse response digital filter). The red box in the top panel of Figure 2-43 is expanded in the figure's second panel. As expected the lower bandwidth signals are rounded at the peak with the wider bandwidths approaching the autocorrelation triangle.

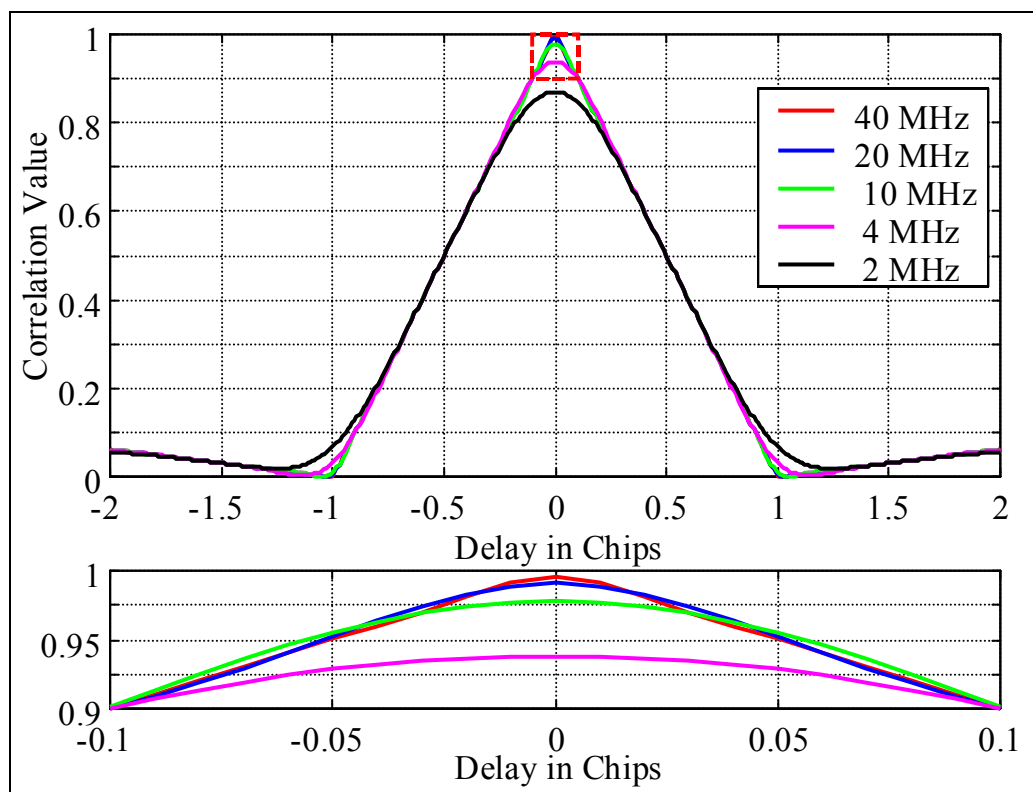


Figure 2-43 Autocorrelation Functions for various input GNSS Signal Bandwidths

Taking the autocorrelation functions in Figure 2-43 for the 2 MHz, 10 MHz, and infinite bandwidth cases, the resulting multipath error envelopes for the wide and narrow correlators are shown in Figure 2-44. This assumes one multipath signal with a relative

amplitude of 0.5 (signal to multipath ratio (SMR) = $20 \log(\alpha) = 6 \text{ dB}$), and a multipath delay of 0 m to 600 m. The dot product DLL discriminator was assumed for both cases. The resulting maximum errors were 73 m, 71 m, 60 m (wide correlator) and 7 m, 10 m, 33 m (narrow correlator) for the infinite, 10 MHz, and 2 MHz bandwidths respectively. The wide correlator's maximum multipath error decreases for narrow bandwidths, while the narrow correlator's error requires the wider bandwidth to mitigate the multipath errors. Note that the multipath error goes to zero at 1.5 Chips and 1.05 Chips for the wide and narrow correlators respectively. For the infinite bandwidth cases the multipath signal delayed by these amounts does not affect the correlator measurements. Figure 2-45 shows the correlation triangles for the infinite bandwidth case with the multipath signal delayed by 1.5 chips. Note that no multipath is present at the correlator locations.

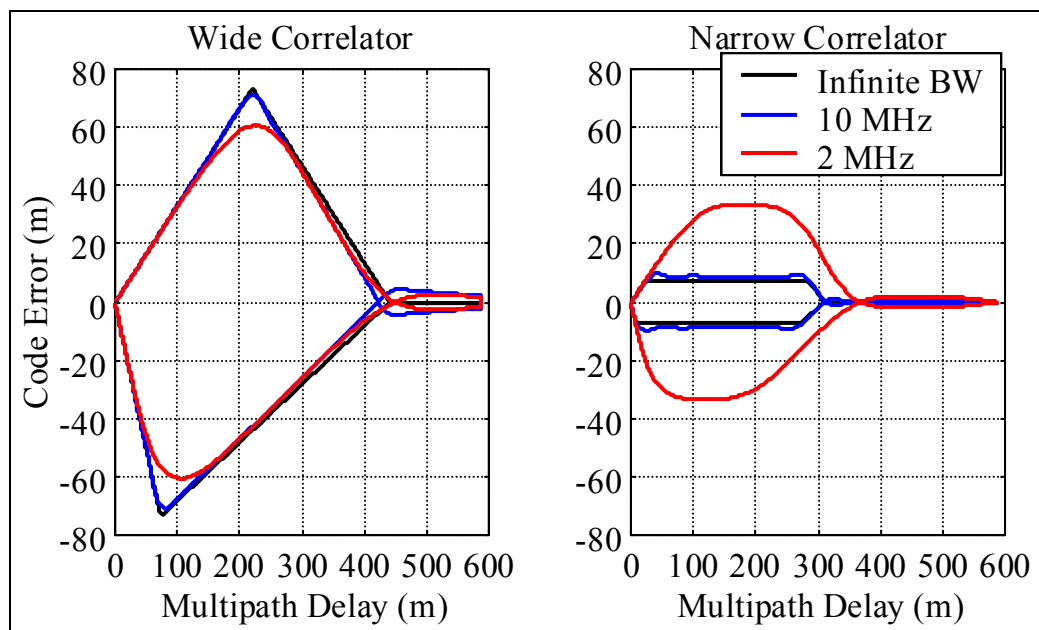


Figure 2-44 Multipath Error Envelope, SMR = 6 dB

This shows how the multipath error changes for different bandwidths. How it changes for different multipath strengths is a different question. Figure 2-46 plots the wide and narrow correlator error envelopes for SMR from 0 to -20 dB. The wide correlator was

assumed to use a 2 MHz two sided bandwidth, while the narrow correlator was assumed to use a 10 MHz two sided bandwidth.

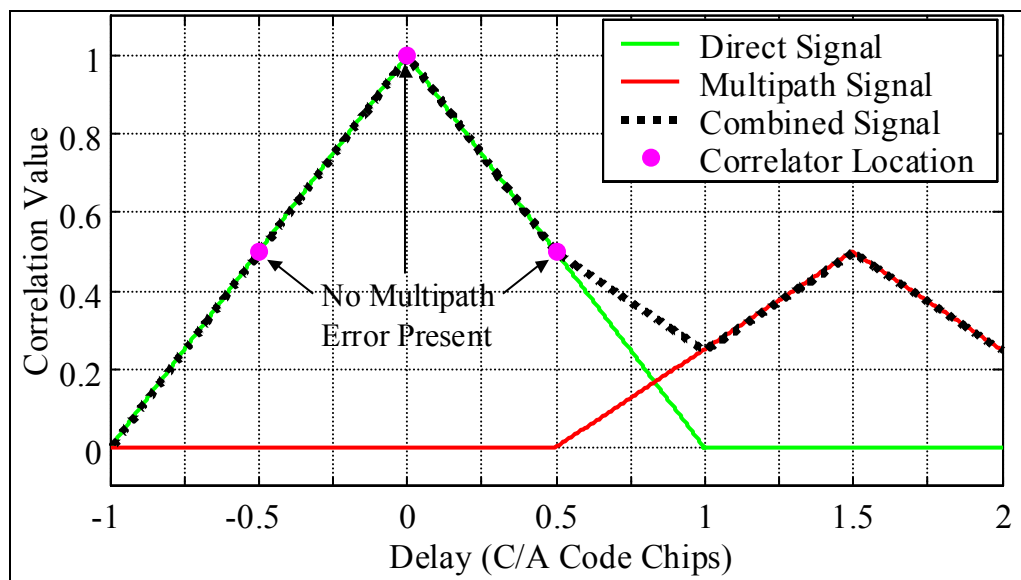


Figure 2-45 Multipath Signal Delayed by 1.5 Chips (Infinite Bandwidth)

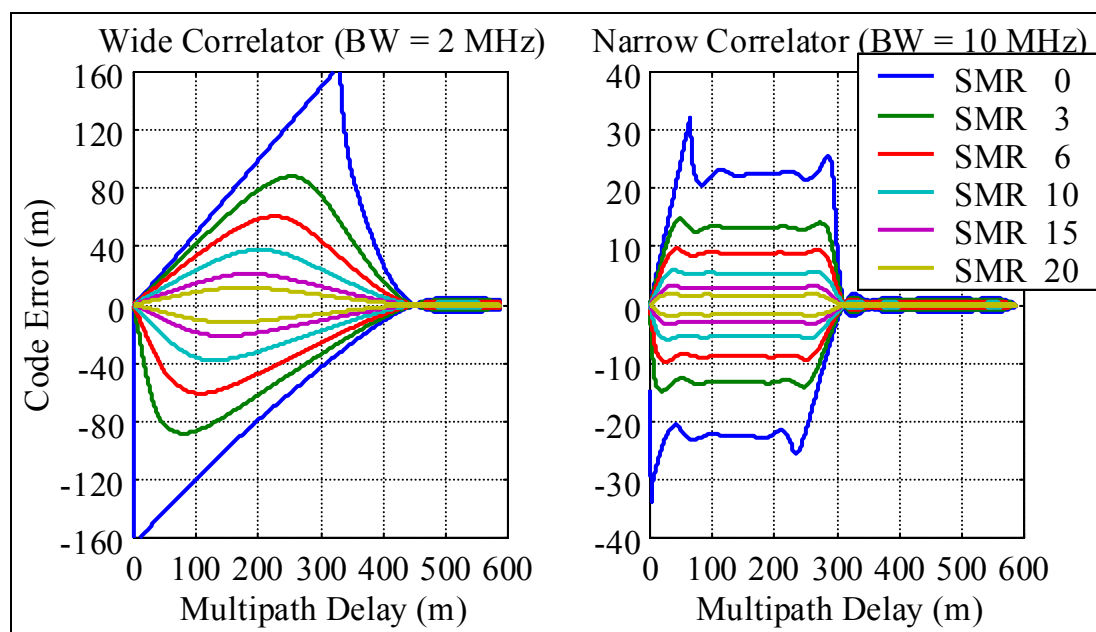


Figure 2-46 Multipath Error Envelopes for the Wide and Narrow Correlators for Different SMRs

The performance improvements of the narrow correlator as compared with the wide correlator for long delay multipath are excellent as shown in Figure 2-44, however, what is not evident from the figure is that both correlators perform almost identically for short delay multipath. Figure 2-47 plots the short delay multipath errors for the wide correlator (BW = 2 MHz) and narrow correlator (BW = 10 MHz). The results are essentially identical for both receivers. Thus while the narrow correlator will greatly reduce the maximum multipath error (long multipath) it will not reduce the effect of short delays.

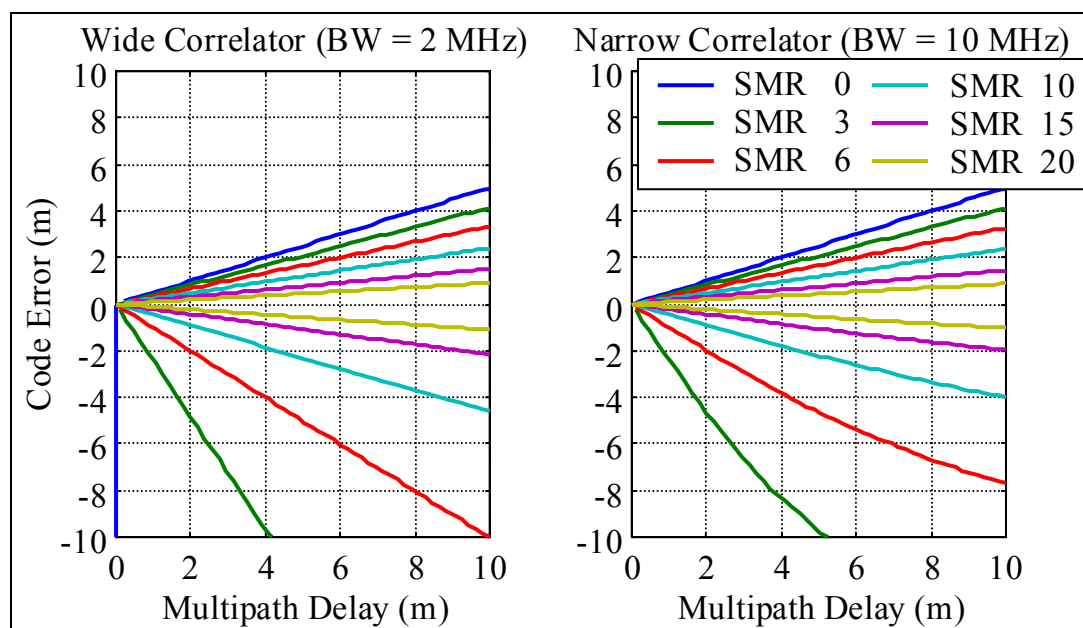


Figure 2-47 Short Delay Multipath Errors for the Wide and Narrow Correlators

For a better understanding of the multipath performance, a modified version of Figure 2-45 will be used. Infinite bandwidths are assumed and one multipath signal with a delay of 190.3 m ($200 * \text{wavelength of L1}$) and a relative amplitude of 0.5 is being simulated. The direct, multipath, and combined signals correlation functions are shown in Figure 2-48 as the green, red, and black lines respectively. The resulting correlator locations for the wide and narrow correlators are shown as the magenta circles and blue squares respectively. The multipath induced error is the location of the prompt correlator, since it should be at 0 m delay. The wide correlator has a 64 m error while the narrow correlator

has a 7 m error. The errors are shown by the dashed blue and magenta lines from the prompt correlators. The multipath distortion of the correlation function is evident as well as the behaviour of the wide and narrow correlators.

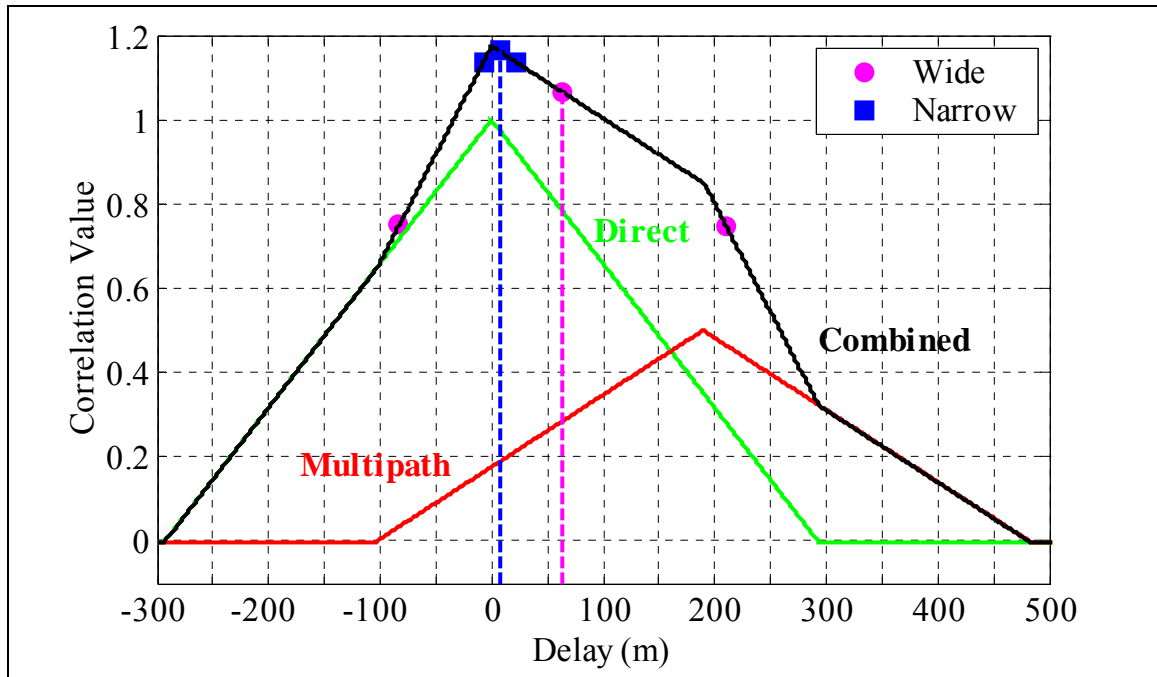


Figure 2-48 Correlation Triangles and Resulting Multipath Error for one Multipath Signal with Delay of 200*wavelength of L1 and Amplitude of 0.5

2.5.5.3 Carrier Phase Tracking Error

The carrier phase tracking error due to multipath is determined by the tracking error within the PLL. Similar to the code DLL discriminator there are many difference PLL discriminator functions that a receiver may employ. The most common discriminator is the two quadrant arctangent function $\tan^{-1}\left(\frac{QP}{IP}\right)$. This discriminator produces a linear function of the phase error between $\pm 90^\circ$ error (Ward, 1996). The equations for the QP and IP correlators have been extracted from equation (2-25) and repeated below:

$$\begin{aligned}
 IP &= A \cdot R(\hat{\tau} - \tau_0) \cdot \cos(\theta_0 - \hat{\theta}) + A \cdot \sum_1^n \alpha_i \cdot R(\hat{\tau} - \tau_0 - \tau_i) \cdot \cos(\theta_0 + \theta_i - \hat{\theta}) \\
 QP &= A \cdot R(\hat{\tau} - \tau_0) \cdot \sin(\theta_0 - \hat{\theta}) + A \cdot \sum_1^n \alpha_i \cdot R(\hat{\tau} - \tau_0 - \tau_i) \cdot \sin(\theta_0 + \theta_i - \hat{\theta})
 \end{aligned}
 \tag{2-27}$$

Assuming that only one multipath signal is present, what phase error will occur for difference phase offsets between the direct and multipath signals? Figure 2-49 shows the phasor addition of six difference combinations for the direct and multipath signals. The maximum quadra-phase component occurs when the direct and multipath signals are 90° offset from each other, panel (b) and (f). However, this does not produce the maximum multipath error, which occurs in panels (c) and (e) when the direct and multipath signals are almost exactly out of phase with each other. There is zero error when the two signals are exactly in phase or out of phase with one another.

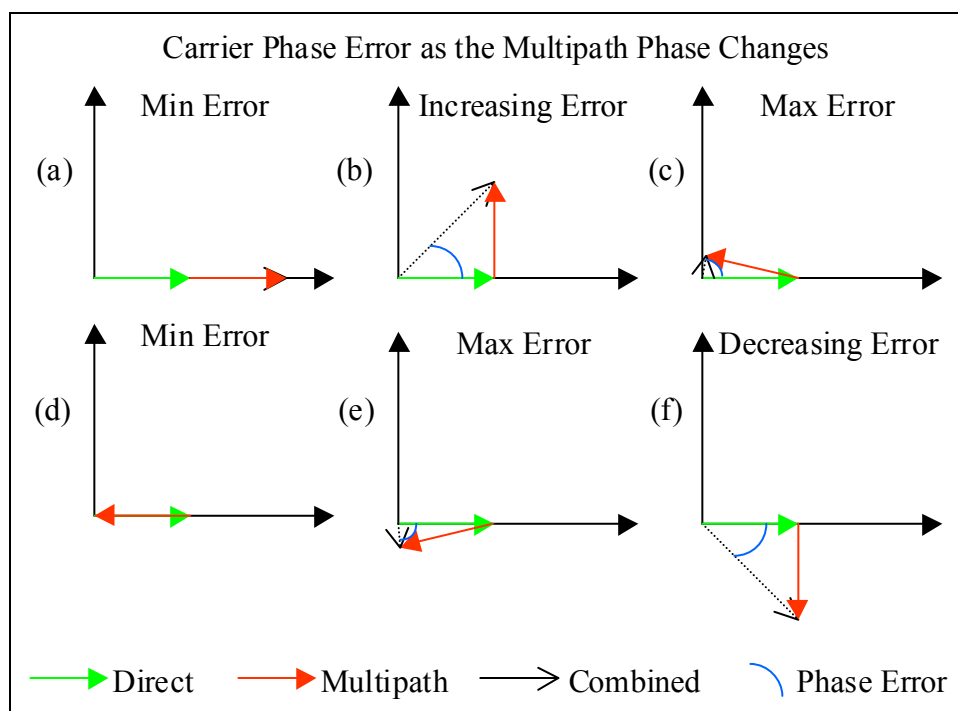


**Figure 2-49 Multipath Induced Carrier Phase Tracking Error
for Various Multipath Phase Offsets**

Caution must be exercised when interpreting panels (c), (d), and (e), since the combined input signal is almost zero. Thus although error curves can be produced for these cases, it is possible that the GNSS receiver will lose lock on any satellites due to the low signal strength.

Assuming that the direct signals code and carrier phase are zero ($\tau_0 = \theta_0 = 0$), the phase tracking error is (Ray, 2000):

$$\Delta\phi = \tan^{-1} \left(\frac{\sum_1^n \alpha_i \cdot R(\hat{\tau} - \tau_i) \cdot \sin(\theta_i)}{R(\hat{\tau}) + \sum_1^n \alpha_i \cdot R(\hat{\tau} - \tau_i) \cdot \cos(\theta_i)} \right) \quad (2-28)$$

which depends on the signal strength of the multipath signal (α_i) and its delay (τ_i). The carrier phase error envelopes for several SMR are given in Figure 2-50.

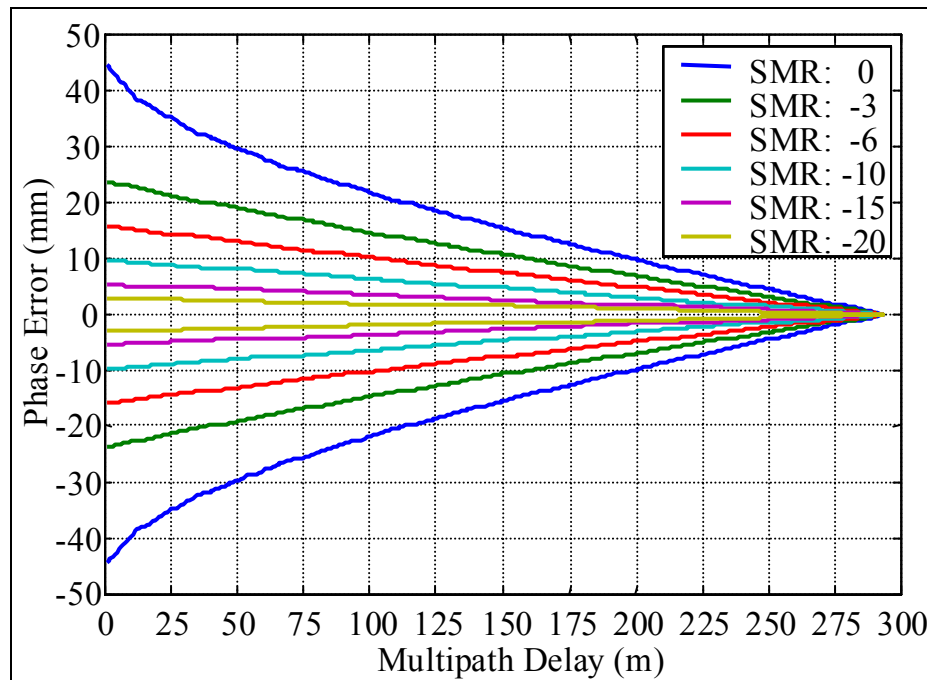


Figure 2-50 Carrier Phase Multipath Error Envelopes for Various SMRs

The maximum phase error of $\frac{1}{4}$ cycle or 47 mm occurs when the multipath signal is delayed by 0^+ m and has the same magnitude as the direct signal. This corresponds to Figure 2-49 panels (c) and (e), however, as was stated previously this would probably reduce the received signal level below the tracking threshold. The maximum practical error is below the $\frac{1}{4}$ cycle theoretical value. Even if the maximum error was 47 mm, it is still three orders of magnitude less than the DLL code errors of Figure 2-46. Therefore the multipath induced phase errors will be ignored for the remainder of this research.

For a more detailed treatment of GPS code and carrier phase multipath see van Nee (1995), Ray (2000), Breeuwer (1991), and Braasch (1995).

2.5.5.4 Marine Multipath Found through Data Analysis

Several researchers have estimated marine multipath effects. In Tranquilla and Carr (1990) the multipath signatures from land and water sites were analysed. They found that reflections from water produced code range errors on the order of 10 metres, and stated that for hydrographic applications code range errors in the 2-10 metre range were expected. In Van Dierendonck and Braasch (1997) marine multipath effects were qualitatively described. They stated that reflections from seawater were “diffuse and easy for smoothing reduction”, while reflections from the ship’s superstructure produced “short-delay multipath which cannot be mitigated using current correlation techniques”. In Lachapelle et al. (1996) data collected from a 1,600 ton Canadian Department of Defence ship showed a root mean square (RMS) code ranging errors of 1.1 m using a wide correlator C/A code receiver.

In 2000 the CCG started a research and development project (CCG, 2000) to determine the multipath errors on CCG ships. The first stage of this project involved collecting data from several locations on the CCGS Martha L. Black (see Appendix F for a picture of the ship) in an attempt to detect multipath. Multipath errors in the tens of metre were detected using a wide correlator receiver (Lachapelle et al., 2002a).

As shown from previous research the multipath error is truly a function of the user's local environment and receiver. To obtain a better appreciation for the types of errors that are possible in a marine environment, CHAPTER 3 contains a detailed marine multipath simulation. The results from this multipath simulation will be used as input to the reliability and availability simulations in CHAPTER 4.

2.5.6 Frequency Dependent Error

The receiver's frequency bias (df_{RX}) is caused by each satellite's signal experiencing a different hardware delay depending on the frequency of the incoming signal as it is processed by the receiver. The receiver's filters produce the majority of these biases. If all of the satellites transmit on the same frequency (i.e. employed CDMA) $df_{RX} = 0$. This is the case for GPS, and will be the case for Galileo. GLONASS on the other hand employs FDMA, thus the receiver will introduce biases into each measurement based on its frequency. The bias is not eliminated when between receiver single differences are formed, since the frequency response of the two receiver's will be slightly different. In order to determine the magnitude of the receiver frequency dependent biases, four zero baseline tests were conducted using two Ashtech GG24™ GPS /GLONASS receivers. Two 4 hour and two 12 hour zero baseline data sets were collected over four days.

The results of the tests are shown in Figure 2-51. The two 12 hour tests were broken into three four hour segments, thus there were a total of eight four hour tests reported. For each test the pseudorange double difference was computed between a GPS satellite and a GLONASS satellite and the mean value was plotted for that GLONASS satellite. The mean double difference value for all of the data for each GLONASS satellite is plotted as the green line. In addition to plotting the mean double difference values the GLONASS frequency numbers (see Table 2-3) were also plotted as the red line on the bottom of the figure. The GLONASS code double difference values have an approximate mean value of 0.5 m, with small variations ± 0.1 m between GLONASS satellites. The 0.5 m bias is caused by the frequency differences between GPS and GLONASS which is approximately

30 MHz, with the smaller variations between the GLONASS satellites being caused by the smaller frequency differences between them (maximum difference of 13.5 MHz). When the average bias (green line) is compared with the frequency number (red line) they are very similar. While they are not identical, the trend is quite clear. The biases in the double difference code measurements are being caused by the receiver's different frequency response to the GLONASS frequencies.

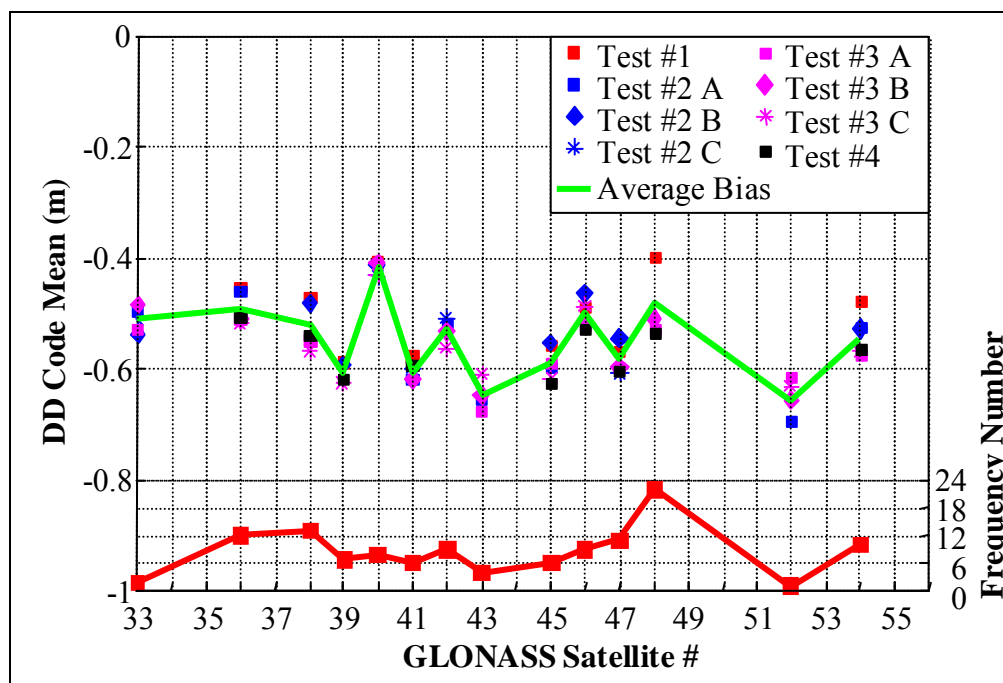


Figure 2-51 GLONASS Code DD Bias for all Four Tests

The 0.5 m bias will effect all GLONASS measurements, therefore an additional parameter must be estimated. If an epoch by epoch least squares approach is being used, then one degree of freedom is lost to estimate this bias. If a Kalman filter is being employed then a random constant model may be used. The biases between the GLONASS satellites is more difficult to handle, since they are on the 10 cm level. Solving for these biases using code measurements would not be practical. The optimum solution would be for the receiver manufacturer to remove the bias through calibration. However, this may be problematic since the biases are often temperature dependent. The

other option is to ignore the between GLONASS satellite bias, however this would increase the GLONASS code measurement noise by several centimetres, depending on which satellites were being tracked. This is well within the GLONASS code measurement accuracy (Figure 2-36). The between GLONASS satellite errors will be ignored in the simulation sections. The 0.5 m bias between the GPS and GLONASS satellites will be addressed in the simulation sections.

2.5.7 Changes with the Removal of SA

How has the removal of SA changed marine navigation and positioning? Since SA was only applied to the broadcast clock, marine DGPS systems were able to completely remove its effects. SA's only real effect on marine DGPS was on the correction latency. Therefore discontinuing SA will not improve the accuracy of marine DGPS, however, it should increase the maximum allowable correction latency. However, discontinuing SA has dramatically improved the accuracy of standalone GPS from a horizontal accuracy of 100 m (95%) (U.S. Department of Defense, 1995) to a horizontal signal in space accuracy of 13 m (95%) (U.S. Department of Defense, 2001). Standalone GPS accuracy has improved by an order of magnitude. From an accuracy perspective, marine DGPS is only required if the user routinely requires a horizontal accuracy of better than 10 m (95%).

DGPS however does more than just improve the accuracy of the GPS system, it also provides an independent integrity check for the GPS system. Why is an independent check required, isn't GPS a reliable system? The answer is yes, GPS is a reliable system, however, even reliable systems make mistakes. There have been two separate incidents over the past two years where the integrity of the GPS system has been compromised and DGPS systems have automatically addressed the problem.

- 1) On July 28, 2001 PRN 22's satellite clock failed, producing enormous range and range rate errors. The clock failed at approximately 22:07 UTC, however, the Master Control Segment only flagged it as unhealthy at 23:58 UTC (Skalski, 2001

and Langley, 2001). This unhealthy condition lasted for almost two hours. If a receiver included this satellite in its navigation solution it would be biased from metres to kilometres. This would seem to be an easy blunder to be caught by a receiver's reliability algorithm (see section 2.6). However, most marine receivers do not employ built-in reliability algorithms (see CHAPTER 6), therefore they might accept the error. The marine DGPS reference stations immediately caught the blunder and began transmitting the do not use codes for that satellite, which removed it from the DGPS users position solution. Thus DGPS did its function and addressed the GPS system error.

- 2) From May 28 through June 2, 2002 the GPS constellation transmitted an incorrect ionospheric model (Gallagher, 2002). Single frequency users who applied the incorrect model would have experienced range errors in the ± 16 m range. During this time period the model predicted a flattened ionospheric correction as opposed to the standard half cosine correction. DGPS users, on the other hand, rely on the differential corrections to mitigate the ionospheric error, and were unaffected by this blunder.

These examples reaffirm the need for an independent integrity check for GPS. Since most marine user receivers do not contain an internal reliability algorithm, DGPS is a requirement.

What does the removal of SA mean for DGPS correction latency? Before SA was removed, mariners were cautioned not to use corrections older than 30 seconds. Figure 2-52 shows the 95% HPE for a four hour data set collected just before SA was turned off. The high and nominal values of SA (RTCM, 1998), and the single point position accuracy are also shown. After only 50 seconds the 95% HPE reached 8.9 m.

However, once SA was removed the latency effect was greatly reduced. Figure 2-53 and Figure 2-54 show the differential positional accuracy for latencies from 0 to 900 seconds. After 120 second latency the 95% HPE is only 1.1 m. After 600 s the 95% HPE is 3.6 m. It takes 15 minutes for the DGPS 95% HPE to reach the single point limit. While this is a

very small sample, it does highlight that with the removal of SA higher latency values may be used. Therefore, in the simulation section the assumption will always be made that the user has access to DGPS corrections. This was not necessarily the case with the 30 second latency limit.

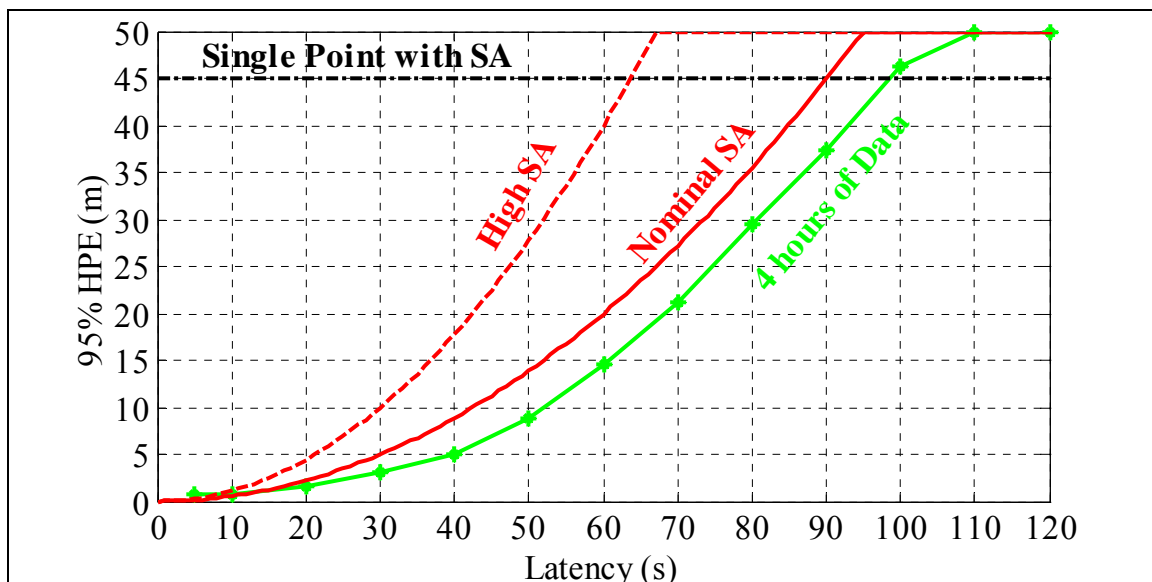


Figure 2-52 HPE 95% Using Four Hours of Data Prior to SA's Removal

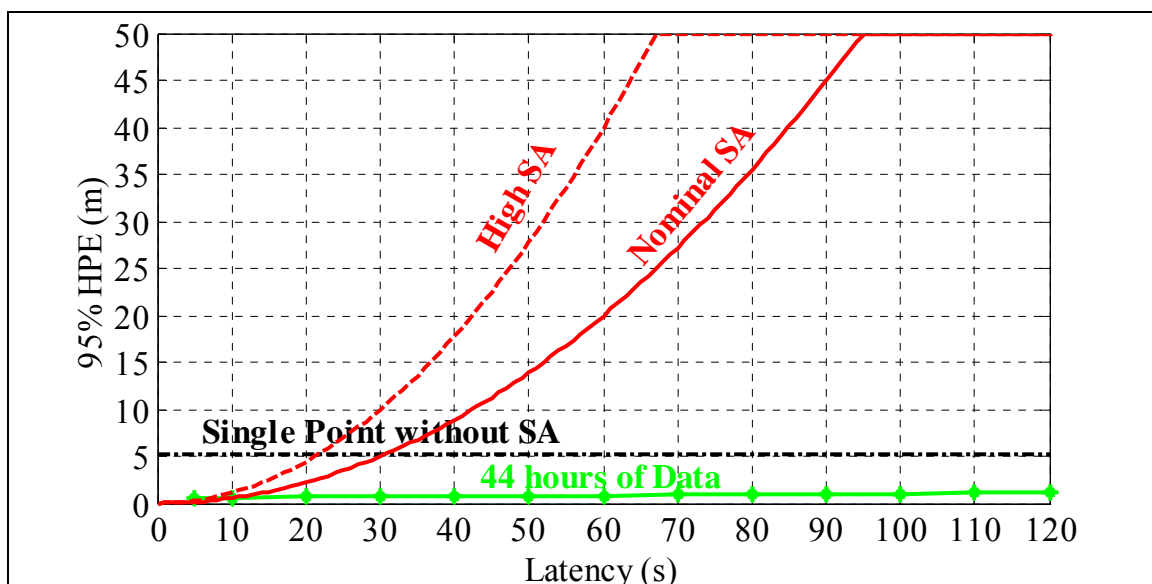


Figure 2-53 HPE 95% Using 44 Hours of Data After SA's Removal

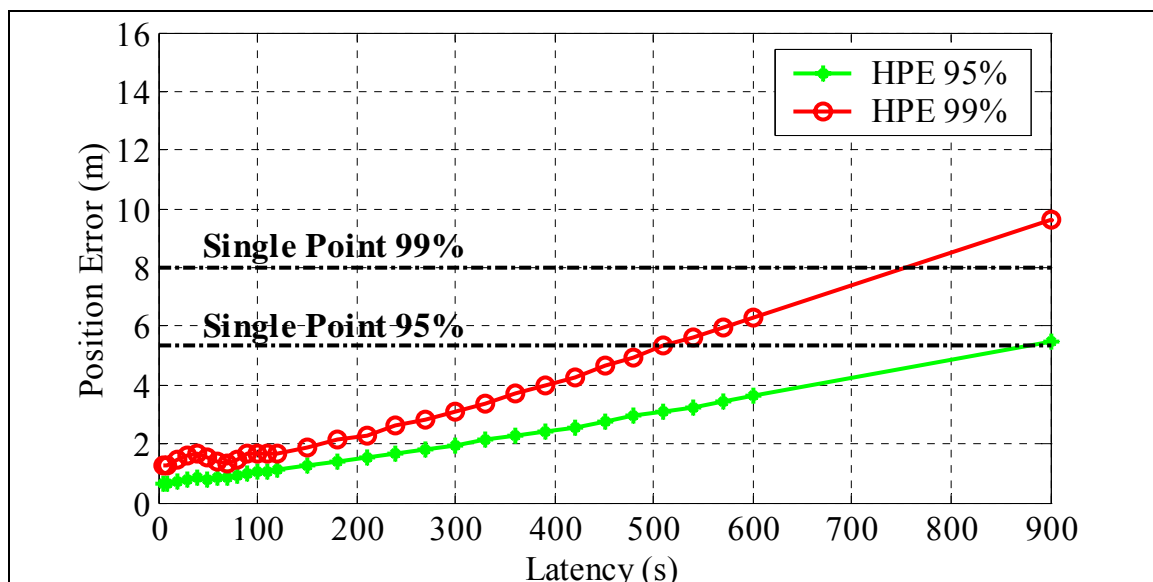


Figure 2-54 HPE 95% and 99% Using 44 Hours of Data After SA's Removal

2.6 Reliability Theory

Reliability refers to the ability to detect blunders in the measurements and to estimate the effects of undetected blunders on the parameters. Reliability can be sub-divided into internal and external reliability. Internal reliability quantifies the smallest blunder that can be detected on each observation through statistical testing of the least squares residuals / Kalman filtering innovation sequence. Once the internal reliability has been determined, external reliability quantifies the impact that an undetected blunder can have on the estimated parameters. The reliability theory described here-in was invented by Baarda (1967 and 1968), and was extended to dynamic models by Teunissen (1990).

2.6.1 Least Squares Single Blunder Detection

In order to detect a blunder using an epoch by epoch least squares approach, a statistical test must be performed on the residuals. Hence, redundancy must exist in order to detect the blunder. An unknown blunder vector will bias the least squares residuals according to:

$$\hat{\mathbf{f}} = -\mathbf{C}_{\hat{\mathbf{f}}} * \mathbf{C}_1^{-1} * \nabla = -\mathbf{R} * \nabla \quad (2-29)$$

$$\mathbf{C}_{\hat{\mathbf{f}}} = \mathbf{C}_1 - \mathbf{A}(\mathbf{A}^T \mathbf{C}_1^{-1} \mathbf{A})^{-1} \mathbf{A}^T \quad (2-30)$$

where $\hat{\mathbf{f}}$ least squares residuals
 ∇ unknown blunder vector
 $\mathbf{C}_{\hat{\mathbf{f}}}$ residuals covariance matrix
 \mathbf{C}_1 observation covariance matrix
 \mathbf{A} design matrix
 $\mathbf{R} = \mathbf{C}_{\hat{\mathbf{f}}} \mathbf{C}_1^{-1}$ redundancy matrix

The trace of \mathbf{R} equals the observation redundancy (ν), since \mathbf{R} is idempotent and the trace of an idempotent matrix equals its rank (Leick, 1995). Each diagonal element of \mathbf{R} corresponds to that observation's contribution to the overall redundancy. Assuming that the observation covariance matrix is diagonal (i.e. uncorrelated observations), the diagonal elements (ν_i) are:

$$\nu_i = \frac{C_{\hat{f}_{ii}}}{C_{l_{ii}}} \quad (2-31)$$

Equation (2-30) shows that $C_{\hat{f}_{ii}} \leq C_{l_{ii}}$, applying this to equation (2-31) results in the following limits on the diagonal elements:

$$0 \leq \nu_i \leq 1 \quad (2-32)$$

When ν_i is close to zero that observation has very little redundancy, however, when ν_i is close to one redundancy exists. A balanced solution would have all of the diagonal elements approximately equal, thus there would be no weaknesses in the solution.

Assuming that one blunder can occur at a time, the blunder vector (∇) contains only one non-zero element. Using local residual checking, assuming uncorrelated observations, each standardised residual is tested according to:

$$\left| \frac{\hat{r}_i}{\sqrt{C_{\hat{r}_{ii}}}} \right| \geq n_{1-\frac{\alpha}{2}} \quad (2-33)$$

The underlying assumption is that the residuals are normally distributed, and that a blunder, while biasing the residual, does not change its variance. Two types of errors can be made whenever a statistical test is performed.

- 1) A Type I error occurs whenever a good observation is rejected. The probability associated with a Type I error is denoted α .
- 2) A Type II error occurs whenever a bad observation is accepted. The probability associated with a Type II error is denoted β .

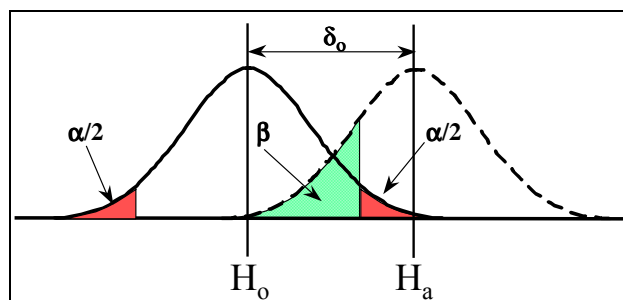


Figure 2-55 Type I/II Errors & Non Centrality Parameter

Figure 2-55 shows a graphical representation of the relationship between the Type I/II errors and the bias in the standardised residual called the non centrality parameter (δ_0). By selecting values for two of the three parameters the third can be generated as shown in Table 2-14. The last four rows of Table 2-14 have δ_0 constant at 4.57 and vary α and β . Increasing α causes β to decrease, and vice versa. The selection of α and β depend on the specific navigation application. For aviation applications the following values are used $\alpha = 3.3 \cdot 10^{-7}$, $\beta = 10^{-3}$, and $\delta_0 = 8.19$, for one degree of freedom (Kelly, 1998). Marine

users do not require the same level of reliability, therefore the simulations in CHAPTER 4 use a $\delta_o = 4.57$.

Table 2-14 Non Centrality Parameter (Leick, 1995)

α	β	δ_o
5.0%	20%	2.80
2.5%	20%	3.10
5.0%	10%	3.24
2.5%	10%	3.52
0.1%	20%	4.12
0.1%	10%	4.57
0.3%	5%	4.57
0.9%	2.5%	4.57
2.5%	1%	4.57

Once α , β , and δ_o have been determined, the smallest blunder that can be detected through statistical testing of residual “i” is computed by substituting equation (2-29) into (2-33) and letting $n_{1-\frac{\alpha}{2}} = \delta_o$:

$$|\nabla_i| = \frac{\delta_o * \sqrt{C_{\hat{r}_{ii}}}}{R_{ii}} = \frac{\delta_o * C_{l_{ii}}}{\sqrt{C_{\hat{r}_{ii}}}} = \frac{\delta_o * \sqrt{C_{l_{ii}}}}{\sqrt{v_i}} \quad (2-34)$$

This is called the Marginally Detectable Blunder (MDB). Each observation has a different MDB since each observation’s redundancy number (v_i) is different. The lower the individual observation’s redundancy number the higher the MDB. Once all of the MDBs have been calculated, the impact of each MDB on the parameters is assessed separately using:

$$\hat{\delta} = -N^{-1} * A^T * C_l^{-1} * \nabla_o \quad (2-35)$$

where A design matrix

$$N = A^T * C_1^{-1} * A \quad \text{normal matrix}$$

∇_o column vector containing all zero's except for the MDB in the i th position.

Since horizontal positioning is of interest in marine navigation the HPE corresponding to each MDB is calculated using equation (2-35) as follows:

$$HPE_i = \sqrt{\Delta\phi_i^2 + \Delta\lambda_i^2} \quad (2-36)$$

where $\Delta\phi_i$ is the error in latitude due to the i th blunder

$\Delta\lambda_i$ is the error in longitude due to the i th blunder

The largest horizontal error is termed the Maximum Horizontal Error (MHE) and represents the external reliability for that epoch. For more information on least squares see Krakiwsky (1992) and Vaníček and Krakiwsky (1986).

2.6.2 Least Squares Multiple Blunder Detection

If multiple blunders are to be detected, the blunder vector (∇) contains two non-zero elements. The impact of the blunders on the residuals and the parameters still follow equations (2-29) and (2-35) respectively. For the two blunder case the internal reliability is defined by MDB pairs, and the MDB pair that produces the MHE represents the external reliability.

The standardised residuals will again be tested in order to detect the blunders. However, the redundancy matrix's off diagonal terms must now be taken into account. Assume that there are blunders on satellites "i" and "j", and the residual for satellite "k" is being tested. The bias in the standardised residual is given by:

$$\frac{\hat{r}_k}{\sqrt{C_{\hat{r}_k}}} = \frac{R_{ki} * \nabla_i + R_{kj} * \nabla_j}{\sqrt{C_{\hat{r}_k}}} \quad (2-37)$$

In order for the blunders to be detected, the bias in the standardised residual must be greater than δ_o . Thus by testing residual “k”, the blunders ∇_i and ∇_j are being constrained by:

$$\left| R_{ki} * \nabla_i + R_{kj} * \nabla_j \right| \geq \delta_o * \sqrt{C_{i_{kk}}} \quad (2-38)$$

With “n” observations, there will be “2*n” constraint equations. The areas defined by these constraint equations will generate a MDB polygon in “i” and “j” blunder space assuming that the redundancy number is ≥ 2 .

Instead of the local residual tests described above, the global Chi-Squared (χ^2) test can be used to detect the blunders. The Chi-Squared degrees of freedom equals the redundancy (ν), and the global Chi-Squared significant level (α_g) is calculated to be consistent with the local significant level (α_l) (Krakiwsky et al., 1999, Leick, 1995, and Kok 1984). In this case the blunders would be detected when the bias in the weighted sum squared residuals is greater than δ_o^2 as follows:

$$\begin{aligned} \hat{\mathbf{r}}^T * \mathbf{C}_1^{-1} * \hat{\mathbf{r}} &\geq \chi_{\alpha_g}^2(\nu) \\ (\mathbf{R} * \nabla)^T * \mathbf{C}_1^{-1} * (\mathbf{R} * \nabla) &\geq \delta_o^2 \end{aligned} \quad (2-39)$$

Substituting equation (2-37) for the residuals into equation (2-39) results in the equation of an ellipse in “i” and “j” blunder space:

$$\begin{aligned} \sum_{k=1}^{k=n} (R_{ki} * \nabla_i + R_{kj} * \nabla_j) * C_{l_{kk}}^{-1} * (R_{ki} * \nabla_i + R_{kj} * \nabla_j) &\geq \delta_o^2 \\ \sum_{k=1}^{k=n} (R_{ki}^2 * \nabla_i^2 + 2 * R_{ki} * R_{kj} * \nabla_i * \nabla_j + R_{kj}^2 * \nabla_j^2) * C_{l_{kk}}^{-1} &\geq \delta_o^2 \end{aligned} \quad (2-40)$$

The MHE will occur along one of the principle axes of the ellipse.

A simulation was conducted using the blunder detection scenario described above. Seven GPS satellites were visible for the selected epoch. The MHE occurred when satellites 9

and 15 contained blunders. Figure 2-56 shows the 14 constraint lines and the resulting MDB polygon from the local tests, as well as the ellipse from the global test. As should be expected the global ellipse is bounded by the MDB polygon. This will be the case as long as the same δ_0 is used for the local and global tests (Krakiwsky et al., 1999, Leick, 1995, and Kok 1984).

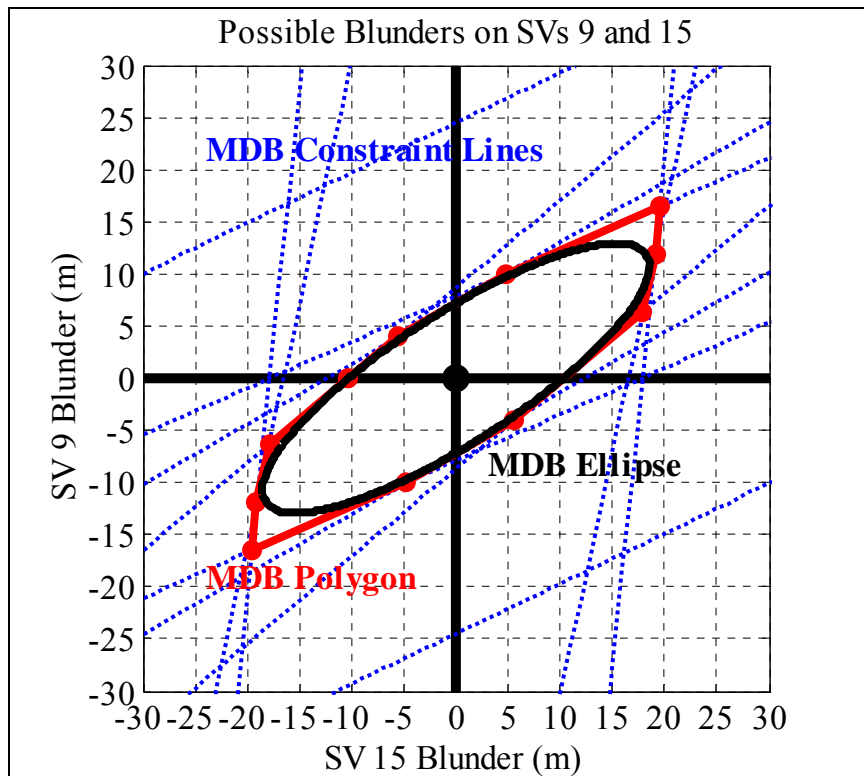


Figure 2-56 Local MDB Polygon and Global Ellipse

Similar to equation (2-35), the external reliability for the multiple blunder case is calculated as:

$$\hat{\delta} = -N^{-1} * A^T * C_1^{-1} * \nabla_{i\&j} \quad (2-41)$$

where $\nabla_{i\&j}$ column vector containing all zeros except for the blunders in the i^{th} and j^{th} positions.

The corresponding HPE is calculated using equation (2-36).

The local and global test described above will detect multiple blunders. To isolate them the more general form of equation (2-33) must be used, see Koch (1999) for the derivation of this equation:

$$\hat{\mathbf{r}}^T * \mathbf{C}_1^{-1} * \mathbf{I}_c * \left(\mathbf{I}_c^T * \mathbf{C}_1^{-1} * \mathbf{C}_\hat{\mathbf{r}} * \mathbf{C}_1^{-1} * \mathbf{I}_c \right)^{-1} * \mathbf{I}_c^T * \mathbf{C}_1^{-1} * \hat{\mathbf{r}} \geq \chi_c^2 \quad (2-42)$$

where c number of simultaneous blunders being tested
 \mathbf{I}_c $n \times c$ matrix containing all zero's except for ones in the locations of the residuals being tested

For more information on multiple blunder detection and isolation see Koch (1999), Teunissen (1998), and Kok (1984).

2.6.3 Internal Reliability using Kalman Filtering

Similar to least squares, a statistical test must now be performed on the Kalman innovation sequence to detect a blunder in the observations (Lu and Lachapelle, 1992). The normalised sum squared innovations (SSI) is biased by the unknown blunder vector (∇) as

$$\text{SSI} = \nabla^T * \mathbf{C}_i^{-1} * \nabla \quad (2-43)$$

where $\mathbf{C}_i = \mathbf{A}_k \mathbf{C}_{\hat{\mathbf{x}}_k}^- \mathbf{A}_k^T + \mathbf{C}_{1k}$

\mathbf{A}_k Kalman design matrix for epoch k

$\mathbf{C}_{\hat{\mathbf{x}}_k}^-$ parameter covariance matrix before measurement update, epoch k

\mathbf{C}_{1k} observation covariance matrix, epoch k

SSI χ^2 distribution with mean $(\delta_o)^2$

The MDB is calculated assuming (a) only one blunder is present in the observations at a given epoch, (b) this is the first epoch with a blunder, and (c) the α and β significance levels are the same as the least squares case, as

$$\text{MDB}_i \Rightarrow |\nabla_i| = \frac{\delta_o}{\sqrt{(C_i^{-1})_{ii}}} \quad (2-44)$$

While the Kalman filtering MDB has a different form than the least squares MDB, they are mathematically identical if a priori information on the parameters is added to the least squares model.

2.6.4 Kalman Filtering External Reliability

Once the MDB for each observation has been calculated the impact of this blunder on the unknown parameters must be determined. Each MDB is applied separately to assess its impact on the parameters as:

$$\Delta \hat{\delta}_i = -C_{\hat{x}_k}^+ A_k^T C_{l_k}^{-1} \nabla_o \quad (2-45)$$

where $C_{\hat{x}_k}^+$ parameter covariance matrix after measurement update, epoch k

∇_o column vector containing all zeros except for the MDB in the i^{th} position.

The resulting HPE for each blunder is calculated as:

$$\text{HPE}_i = \sqrt{\Delta \phi_i^2 + \Delta \lambda_i^2} \quad (2-46)$$

The MDB that produces the MHE represents the external reliability for the software simulations in CHAPTER 4.

2.7 Receiver Autonomous Fault Detection and Exclusion Integrity Monitoring

Receiver autonomous fault detection and exclusion integrity monitoring is a reliability method usually employed for aviation applications. One algorithm which falls under this method is the maximum residual algorithm (MRA) derived by Kelly (1998). The MRA uses the standardised residuals as the test statistic. This is identical to the least squares reliability theory described in section 2.6.1.

In Kelly (1998) the following four reliability algorithms were shown to be equivalent:

- 1) MRA
- 2) Standard Parity Space Algorithm,
- 3) Parkinson Single Deletion Algorithm, and
- 4) Brenner Parity Space Algorithm.

Thus least squares reliability theory is also equivalence to these other reliability algorithms.

The least squares external reliability is given by the MHE, which is the maximum horizontal error from equation (2-36). The MHE represents the potential bias in the estimated parameters. To calculate the overall position error, the MHE must be combined with the parameters covariance matrix ($C_{\hat{x}}$). Combining the MHE and $C_{\hat{x}}$ is equivalent to the horizontal protection limit (HPL) described in Kelly (1998). Thus least squares and the theory described in Kelly (1998) are equivalent.

2.8 Kalman Filtering Theory

Kalman filtering allows one to generate an a priori estimate of the current parameters using previous measurements (Brown and Hwang, 1997). The dynamics and measurement model for the Kalman filter are given by:

$$x_k = \Phi_k * x_{k-1} + w_{k-1} \quad (2-47)$$

$$z_k = A_k * \delta_k + e_k \quad (2-48)$$

where x filter parameters
 Φ_k transition matrix
 w input process noise with covariance q
 z_k linearized measurement vector, epoch k
 $\delta_k = x_k - x_{\text{linearization point}}$ parameter corrections
 A design matrix
 e measurement noise with covariance C_1

The Kalman filter propagates the parameters and the parameters' covariance matrix ($C_{\hat{x}}$) from the previous epoch to the current epoch via:

$$\hat{x}_k^- = \Phi_k * \hat{x}_{k-1}^+ \quad (2-49)$$

$$C_{\hat{x}_k}^- = \Phi_k * C_{\hat{x}_{k-1}}^+ * \Phi_k^T + Q_{k-1} \quad (2-50)$$

where Q_{k-1} discrete time process noise
 $(^+)$ indicates after measurement update
 $(^-)$ indicates before measurement update
 k and $k-1$ indicate the epoch number

The linearized measurements are used to update the parameter corrections and the parameter covariance matrix ($C_{\hat{x}}$) via:

$$\hat{\delta}_k^+ = \hat{\delta}_k^- + K_k (z_k - A_k * \hat{\delta}_k^-) \quad (2-51)$$

$$C_{\hat{x}_k}^+ = C_{\hat{x}_k}^- - K_k * A_k * C_{\hat{x}_k}^- \quad (2-52)$$

where $K_k = C_{\hat{x}_k}^- A_k^T (A_k C_{\hat{x}_k}^- A_k^T + C_{l_k})^{-1}$ Kalman gain

$$i = (z_k - A_k * \hat{\delta}_k^-) \quad \text{Innovation Sequence}$$

Kalman filtering's power is in its ability to take past measurements and aid the current epoch. It does this by propagating past measurements to the present, as shown in equation (2-47). The dynamic model with its associated process noise value, are key to this. If the model is wrong, the solution will be suboptimal even with good measurements. The following sections describe some of the dynamic models that are used with navigation systems.

2.8.1 GPS Receiver Clock Model

As shown in equation (2-1) the receiver clock bias is one of the parameters in the navigation solution. Different types of clocks / oscillators have different stability characteristics. This a priori knowledge should be used to improve the navigation solution. Brown and Hwang (1997) stated that the receiver clock's frequency and phase will random walk over time. The resulting state diagram is given in Figure 2-57 and the state equation in (2-53).

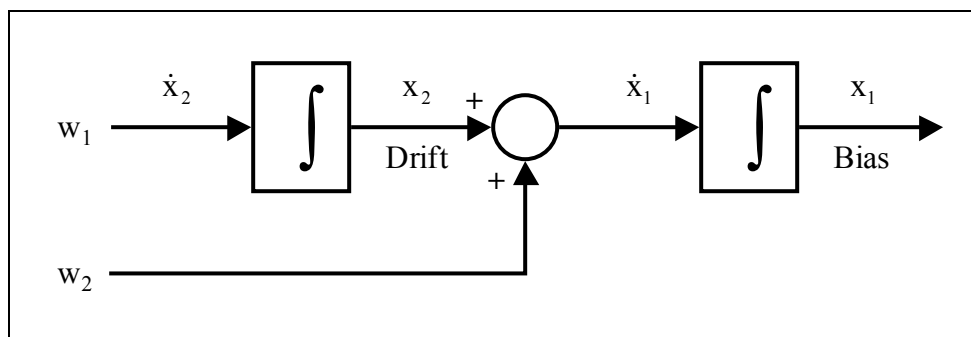


Figure 2-57 GPS Receiver Clock Model State Diagram

$$\begin{bmatrix} \dot{x}_1 \\ \dot{x}_2 \end{bmatrix} = \begin{bmatrix} 0 & 1 \\ 0 & 0 \end{bmatrix} \cdot \begin{bmatrix} x_1 \\ x_2 \end{bmatrix} + \begin{bmatrix} S_b & 0 \\ 0 & S_d \end{bmatrix} \cdot w$$

$$\dot{\mathbf{x}} = \mathbf{F} \cdot \mathbf{x} + \mathbf{G} \cdot \mathbf{w}$$
(2-53)

where $\dot{\mathbf{x}}$ time derivative of the parameters
 x_1 clock bias
 x_2 clock drift
 w white noise driving function
 F state space parameter matrix
 G state space noise matrix
 S_b spectral amplitude for the clock bias
 S_d spectral amplitude for the clock drift

The state transition matrix (ϕ) is the inverse Laplace transform of the resolution matrix $(s \cdot I - F)^{-1}$:

$$\phi = L^{-1} \left((s \cdot I - F)^{-1} \right)_{t=\delta t}$$
(2-54)

Substituting the value of F from equation (2-53) into equation (2-54) and performing the inverse Laplace transform results in the following state transition matrix:

$$\phi = \begin{bmatrix} 1 & \delta t \\ 0 & 1 \end{bmatrix}$$
(2-55)

Thus when the state transition matrix is used to propagate the states via $x_{n+1} = \phi \cdot x_n$ this expands to:

$$\begin{aligned} x_{n+1} &= x_n + \delta t \cdot \dot{x}_n \\ \dot{x}_{n+1} &= \dot{x}_n \end{aligned}$$
(2-56)

The process noise covariance matrix (Q_k) must be determined using:

$$Q_k = \int_{t_0}^t \phi(t-\tau) \cdot G(\tau) \cdot Q(\tau) \cdot G^T(\tau) \cdot \phi^T(t-\tau) \cdot d\tau \quad (2-57)$$

Substituting the expressions for G from equation (2-53) and for ϕ from equation (2-55) and I for Q into equation (2-57) and simplifying, results in the following expression for Q_k :

$$Q_k = \begin{bmatrix} S_b^2 \cdot \delta t + \frac{S_d^2 \cdot \delta t^3}{3} & \frac{S_d^2 \cdot \delta t^2}{2} \\ \frac{S_d^2 \cdot \delta t^2}{2} & S_d^2 \cdot \delta t \end{bmatrix} \quad (2-58)$$

The spectral densities in equation (2-58) are based on the type of GPS receiver clocks employed. Table 2-15 contains the Allan variance parameters for several typical GPS receiver clock models, where $S_b^2 = h_0/2$ and $S_d^2 = 2\pi^2 h_{-2}$. To convert these parameters from units of seconds to metres, multiply by the speed of light squared.

**Table 2-15 Allan Variance GPS Receiver Clock Parameters
(Brown and Hwang, 1997)**

Clock Type	h_0	h_{-1}	h_{-2}
Crystal	$2*10^{-19}$	$7*10^{-21}$	$2*10^{-20}$
Ovenized Crystal	$8*10^{-20}$	$2*10^{-21}$	$4*10^{-23}$
Rubidium	$2*10^{-20}$	$7*10^{-24}$	$4*10^{-29}$

2.8.2 First Order Gauss Markov Acceleration Model

The constant position, velocity, and acceleration dynamic models are derived in Appendix E. None of them are really applicable to marine navigation. Constant velocity, which assumes that the acceleration is white, and constant acceleration which assumes that the jerk is white, do not take the time correlation of the acceleration into account.

The state model which takes the time correlation into account is the first order Gauss Markov model. The model order indicates the number of integrators that must be used to

represent the model in state space, as well as the number of previous measurements that must be used to predict the future value of the process. The autocorrelation function for the first order Gauss Markov processes is shown in Figure 2-58.

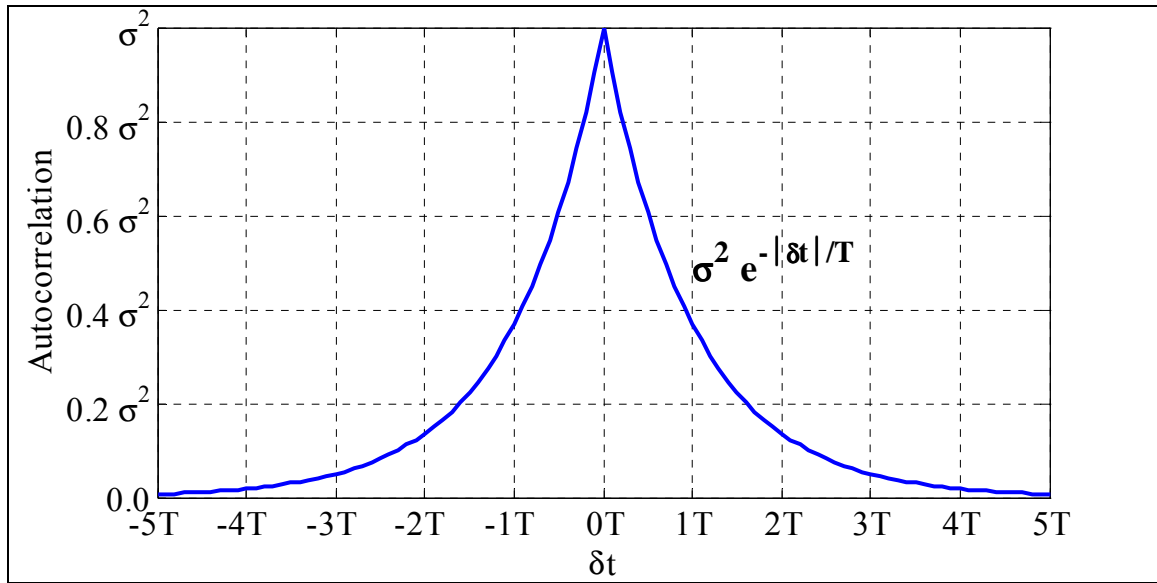


Figure 2-58 Autocorrelation Function for a First Order Gauss Markov Process

The state space representation for the first order Gauss Markov process is shown in Figure 2-59 with the state equation in (2.56).

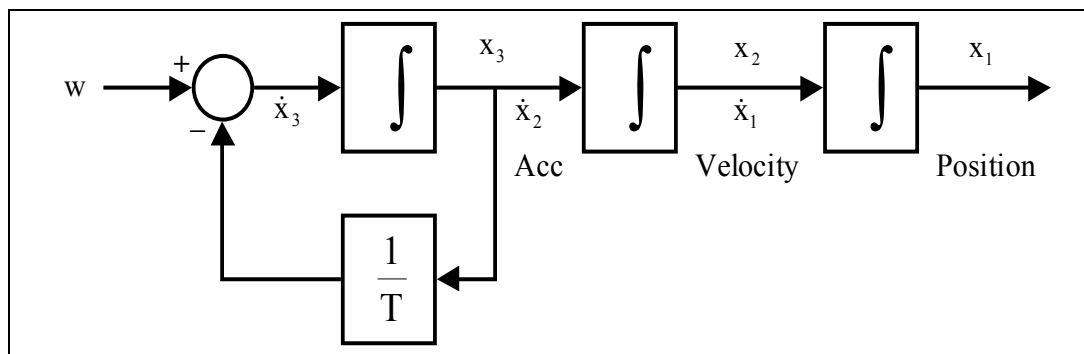


Figure 2-59 First Order Gauss Markov Acceleration State Diagram

$$\begin{aligned} \begin{bmatrix} \dot{x}_1 \\ \dot{x}_2 \\ \dot{x}_3 \end{bmatrix} &= \begin{bmatrix} 0 & 1 & 0 \\ 0 & 0 & 1 \\ 0 & 0 & -\frac{1}{T} \end{bmatrix} \cdot \begin{bmatrix} x_1 \\ x_2 \\ x_3 \end{bmatrix} + \begin{bmatrix} 0 \\ 0 \\ S \end{bmatrix} \cdot w \\ \dot{x} &= F \cdot x + G \cdot w \end{aligned} \quad (2-59)$$

where x_1 position
 x_2 velocity
 x_3 acceleration
 T time constant
 S spectral amplitude for the white noise driving function

The state representation is driven by white Gaussian noise with covariance of $Q = I$. The state transition matrix (ϕ) is the inverse Laplace transform of the resolution matrix:

$$\phi = L^{-1} \left((s \cdot I - F)^{-1} \right) \Big|_{t=\delta t} \quad (2-60)$$

Substituting the value of F from equation (2-59) into equation (2-60) and performing the inverse Laplace transform results in the following state transition matrix:

$$\phi = \begin{bmatrix} 1 & \delta t & T \cdot (\delta t - T \cdot (1 - e^{-\delta t/T})) \\ 0 & 1 & T \cdot (1 - e^{-\delta t/T}) \\ 0 & 0 & e^{-\delta t/T} \end{bmatrix} \quad (2-61)$$

When the state transition matrix is used to propagate the states via $x_{n+1} = \phi \cdot x_n$ this expands to:

$$\begin{aligned} x_{n+1} &= x_n + \delta t \cdot \dot{x}_n + T \cdot (\delta t - T \cdot (1 - e^{-\delta t/T})) \cdot \ddot{x}_n \\ \dot{x}_{n+1} &= \dot{x}_n + T \cdot (1 - e^{-\delta t/T}) \cdot \ddot{x}_n \\ \ddot{x}_{n+1} &= e^{-\delta t/T} \cdot \ddot{x}_n \end{aligned} \quad (2-62)$$

The propagated accelerations decrease exponentially to zero.

To complete the first order Gauss Markov process model the process noise covariance matrix (Q_k) must be determined using:

$$Q_k = \int_{t_0}^t \phi(t-\tau) \cdot G(\tau) \cdot Q(\tau) \cdot G^T(\tau) \cdot \phi^T(t-\tau) \cdot d\tau \quad (2-63)$$

Substituting the expressions for G from equation (2-59) and for ϕ from equation (2-61) and I for Q into equation (2-63) and simplifying, results in the following expression for Q_k :

$$Q_k = \begin{bmatrix} Q_{k11} & Q_{k12} & Q_{k13} \\ Q_{k21} & Q_{k22} & Q_{k23} \\ Q_{k31} & Q_{k32} & Q_{k33} \end{bmatrix} \quad (2-64)$$

$$\begin{aligned} \text{where } Q_{k11} &= \frac{S^2 \cdot T^5}{2} \cdot \left(1 + \frac{2 \cdot \delta t}{T} - \frac{2 \cdot \delta t^2}{T^2} + \frac{2 \cdot \delta t^3}{3 \cdot T^3} - \frac{4 \cdot \delta t}{T} \cdot e^{-\frac{\delta t}{T}} - e^{-\frac{2 \cdot \delta t}{T}} \right) \\ Q_{k12} = Q_{k21} &= \frac{S^2 \cdot T^4}{2} \cdot \left(1 - \frac{2 \cdot \delta t}{T} + \frac{\delta t^2}{T^2} - 2 \cdot e^{-\frac{\delta t}{T}} + \frac{2 \cdot \delta t}{T} \cdot e^{-\frac{\delta t}{T}} + e^{-\frac{2 \cdot \delta t}{T}} \right) \\ Q_{k13} = Q_{k31} &= \frac{S^2 \cdot T^3}{2} \cdot \left(1 - \frac{2 \cdot \delta t}{T} \cdot e^{-\frac{\delta t}{T}} - e^{-\frac{2 \cdot \delta t}{T}} \right) \\ Q_{k22} &= \frac{S^2 \cdot T^3}{2} \cdot \left(-3 + \frac{2 \cdot \delta t}{T} + 4 \cdot e^{-\frac{\delta t}{T}} - e^{-\frac{2 \cdot \delta t}{T}} \right) \\ Q_{k33} &= \frac{S^2 \cdot T}{2} \cdot \left(1 - e^{-\frac{2 \cdot \delta t}{T}} \right) \\ Q_{k23} = Q_{k32} &= \frac{S^2 \cdot T^2}{2} \cdot \left(1 - 2 \cdot e^{-\frac{\delta t}{T}} + e^{-\frac{2 \cdot \delta t}{T}} \right) \end{aligned}$$

2.9 *Stochastic Dynamic Behaviour of Ships*

A Kalman filter is only as good as the accuracy of the dynamics model and process noise. If the dynamics model and process noise are pessimistic, the Kalman filter will not improve the availability and reliability over least squares. However, if the dynamics model and the process noise are too optimistic the filter will be unable to track the actual vehicle dynamics, resulting in systematic errors. Thus it is imperative that the dynamics model and process noises match reality, or are slightly pessimistic. In order to ensure that the simulation results are correct, actual ship data was used to generate the dynamics model and the input process noise for the Kalman filter. The dynamic behaviour of the following two hydrographic survey vessels (see Appendix F for ship pictures) were analysed to generate the dynamics model and process noises using the procedure outlined in Brown and Hwang (1997):

- 1) catamaran survey vessel - CCGS F.C.G. Smith - 8 hours of data
- 2) small fast survey launch - CCG Survey Launch Raven - 1 hour of data

Eight hours of data was collected at one Hertz while the CCGS F.C.G. Smith was performing a hydrographic survey on the St. Laurence River, in October 1998 (Fortes et al., 1999). The ship's accelerations were generated using the DGPS determined velocities. The DGPS velocities were calculated using a first order central difference of the carrier phase. Previous analysis (Hebert et al., 1997) has shown that this method of determining velocity is very accurate during periods of constant velocity ($3D_{\text{rms}} = 2\text{-}3 \text{ mm/s}$), and shows a systematic error correlated with jerk during dynamics ($\text{bias} = 0.18 * J(t)$). Accurate accelerations will be generated under moderate to low dynamics, which is the case for the CCGS F.C.G. Smith.

The acceleration estimates during the eight hours were used to generate the acceleration auto-correlation function in the north, east, and up directions as:

$$R_a(\tau) = \frac{1}{T - \tau} \int_0^{T-\tau} A(t) * A(t + \tau) dt \quad (2-65)$$

where R autocorrelation function
 T length of the time eight hours
 A acceleration.

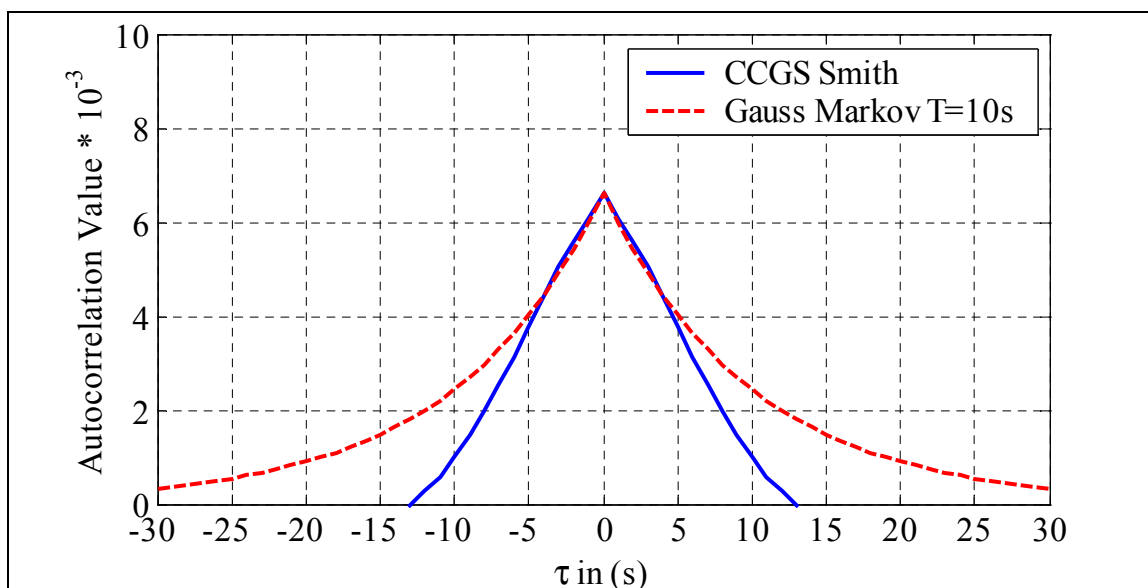


Figure 2-60 North Acceleration Autocorrelation Function for CCGS F.C.G. Smith

Figure 2-60 shows the north auto-correlation function that was generated using the CCGS F.C.G. Smith's acceleration data, and the corresponding first order Gauss-Markov process with a 10 second time constant. The east and up directions were also matched with the closest first order Gauss-Markov process.

The same procedure was performed using one hour of data from the CCG Survey Launch Raven (CHAPTER 7). The acceleration autocorrelation functions were again generated and compared with the first order Gauss-Markov process with different time constants. Table 2-16 summarises the results from the two ship data sets. The software simulations in CHAPTER 4 will use these two filters as well as two additional filters, one with ½ the

process noise variance of the CCGS F.C.G. Smith, and the other with twice the process noise variance of the CCG survey launch. See Brown and Hwang (1997), and Schwarz et al., (1989) for a discussion of dynamic models.

Table 2-16 Kalman Filter Process Noise Parameters

Kalman Filter #1		
Direction	$\sigma^2 (10^{-3})$	Time Constant
North & East	5	10 s
Up	0.5	1 s
Kalman Filter #2 - CCGS F.C.G. Smith		
Direction	$\sigma^2 (10^{-3})$	Time Constant
North & East	10	10 s
Up	1	1 s
Kalman Filter #3 – CCG Survey Launch		
Direction	$\sigma^2 (10^{-3})$	Time Constant
North & East	100	10 s
Up	5	1 s
Kalman Filter #4		
Direction	$\sigma^2 (10^{-3})$	Time Constant
North & East	300	10 s
Up	10	1 s

CHAPTER 3

MULTIPATH SIMULATIONS

3.1 *Description*

From section 2.5 on the GNSS error sources, one of the errors that is most likely to cause blunders is multipath. The multipath errors are dependent on the local environment and on the user's equipment (Tranquilla and Carr, 1990, Van Dierendonck and Braasch, 1997, and Lachapelle et al., 1996). In order to determine the improvements in reliability attained through augmenting DGPS, the magnitudes and behaviour of multipath blunders must be determined. To obtain an estimate of marine multipath's behaviour, a detailed marine multipath simulation program was developed. The simulations should answer the following questions:

- 1) What is the maximum multipath blunder that can occur for different ships?
- 2) Will multiple multipath blunders occur simultaneously?
- 3) If multiple blunders occur simultaneously, what is the maximum error for the second blunder?
- 4) What multipath periods are possible?

The simulation program uses a YUMA almanac to calculate the signal path lengths and directions. Planer polygons are used to define the multipath environment, with the magnitude and phase of the reflection coefficient specified per polygon. The receiving antennas left and right hand polarisation gain patterns are used to determine the received signals amplitude and phase. The receiver's correlator spacing and discriminator function are used to generate the code and carrier phase tracking errors. Figure 3-1 shows the program flowchart, see Appendix B for a more detailed description of the program.

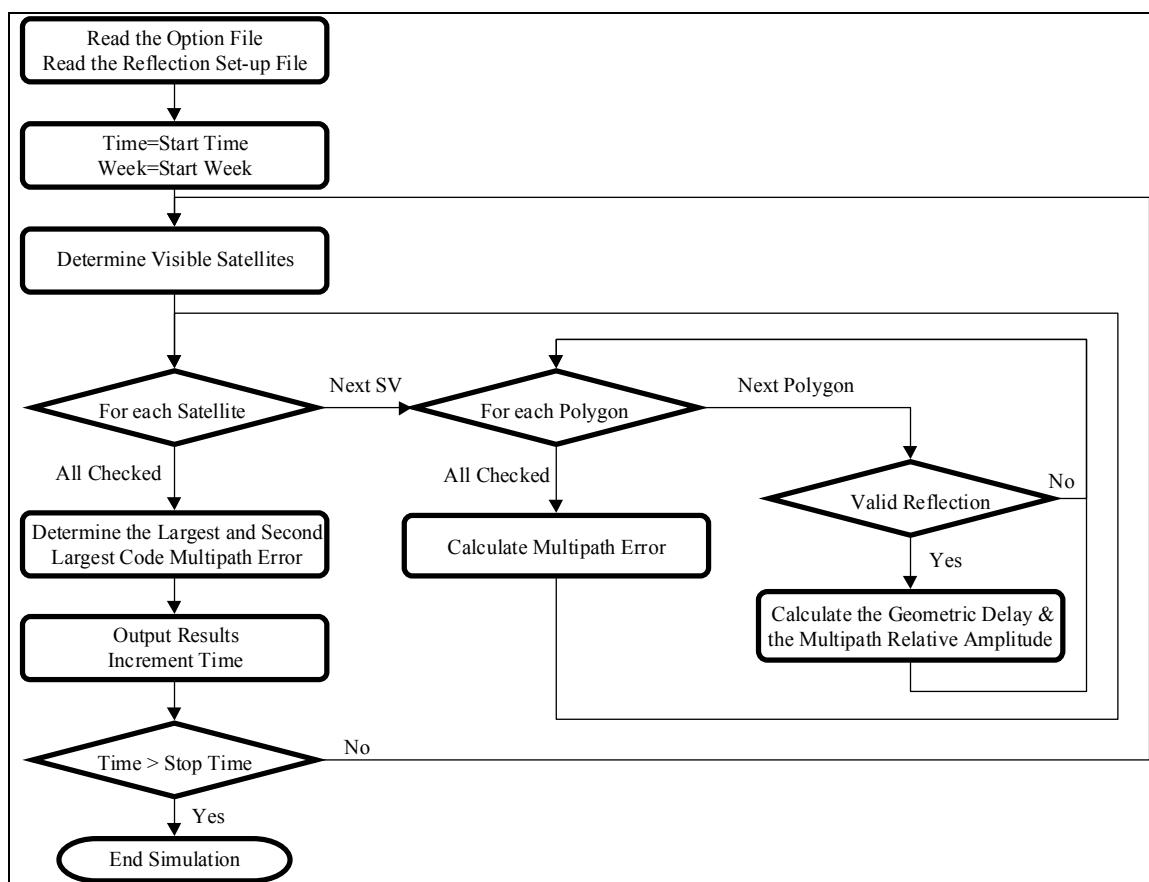


Figure 3-1 Multipath Simulation Program Flowchart

As stated above the multipath behaviour is significantly affected by the local environment, in the marine case the vessel's design. The simulation program was used to generate the multipath errors for the two ships shown in Figure 3-2 and Figure 3-3. The large ship approximates the performance of an icebreaker or buoy tender, such as the CCGS Martha L. Black. While the second ship will cover survey launches, barges, lifeboats, et cetera. The dimensions for the survey launch in Figure 3-3 were based on the CCGC Tofino (CCG, 2002), see Appendix F for pictures of the CCG ships. Both ships have the same types of reflecting surfaces as follows; sea surface (white), main structure and deck (red), wheel house (blue), mast, radar scanner (green), and small structures near the antenna (purple). The black triangle is the GPS antenna. Simple rectangular plates, were used to define all of the ships structures.

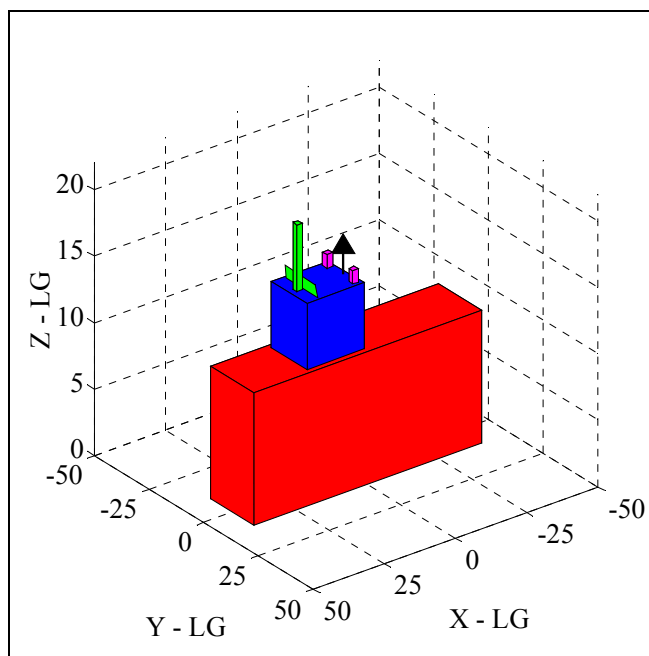


Figure 3-2 Large Simulated Ship

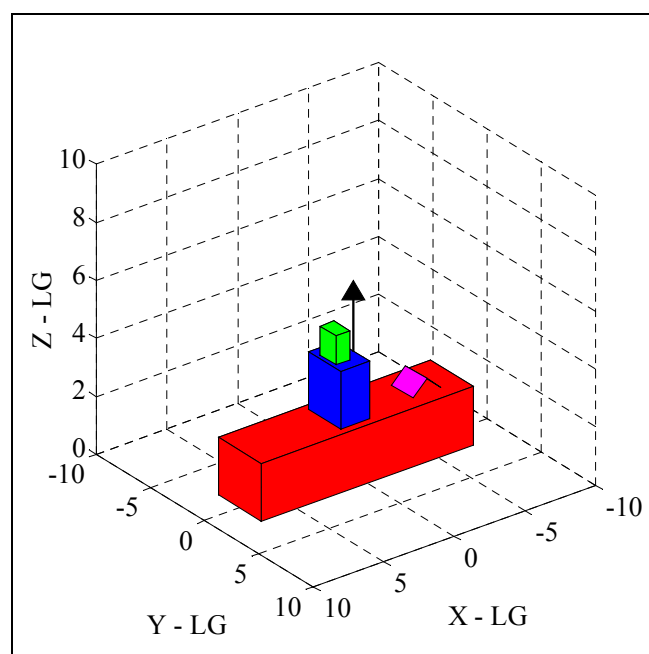


Figure 3-3 Simulated Survey Launch

All horizontal surfaces including the sea (white) below the height of the antenna can produce valid reflection points. All vertical surfaces above the antenna can produce valid

reflection points. Angled surfaces may produce valid reflection points depending on the geometry.

At each epoch the program checks every polygon, that defines the ship and surrounding environment, for valid reflection points for all visible satellites. The satellite's azimuth and elevation are assumed constant over the simulation area, which simplifies identifying the reflection point. If a valid reflection point is found within the polygon, all of the other polygons are checked to ensure they do not block the incident or the reflected signal. The receiving antenna was assumed to be the Sensor Systems' Antenna shown in Figure 2-42. For marine use a chokering or a ground plane is not practical due to the pitching and rolling of the ship. As described in section 2.5.5.1 the multipath amplitude is a function of the reflecting surfaces' electrical characteristics as well as the surface roughness. Reflections from the ship's superstructure are assumed to reflect from metallic surfaces, therefore the reflection coefficient should be one with a change in the polarisation from RHCP to LHCP. However, to take surface roughness into account all of the ship's superstructure was assigned a reflection coefficient of $\alpha = 0.707$ (i.e. a 3 dB attenuation). The reflection from seawater is elliptically polarised and the resulting combination of the reflection coefficient and the receiving antenna's gain pattern is illustrated in Figure 2-42. The received signal power for seawater reflections is shown in Figure 2-42 as the blue line, assuming no scattering. In order to take the sea state into account, all seawater reflections are also attenuated by an additional 3 dB. If all of the reflections are not attenuated by an additional 3 dB, it results in the extremely large unrealistic multipath errors as shown in Appendix C. Once all of the polygons have been searched for a given satellite the resulting code range error is calculated using equation (2-26) and the carrier phase error is calculated using equation (2-28). Once all of the satellites have been checked the largest and second largest code multipath error are determined for that epoch.

The following simplifications have been made in these simulations:

- 1) The Fresnel zone has not been considered, the Fresnel zone is the area that reflects the plane wave and contains the locus of points that are $\lambda/2$ phase away.

- 2) Diffraction multipath has not been considered, only reflected multipath.
- 3) All of the surfaces are assumed to be smooth. The 3 dB attenuation was added to take this into account.

The multipath simulation example was conducted over 24 hours in five second increments using the March 12, 2000 GPS almanac. This ensures that all possible satellite geometries are tested. The University of Calgary was used as the simulation location ($51^{\circ} 00' \text{ N}$, $114^{\circ} 07' \text{ W}$). Since the simulated ships shown in Figure 3-2 and Figure 3-3 are not symmetric, the simulations were conducted 12 times with the ships heading rotated 30° each time. This ensures that a representative subset of ship orientations were tested. Narrow and wide correlator receivers previously mentioned were both simulated. The results for the two ships are analysed in the next section.

3.2 *Multipath Simulation Results*

If all of the simulation data were to be presented, a four dimensional figure would be required (ship orientation, time, largest and / second largest error, and correlator type). Instead of presenting the time series for the 48 different day long simulations, only the results for one orientation of each ship is presented (ship heading north) followed by a summary of all of the results.

Figure 3-4 shows the largest code ranging error for each epoch for the large ship and survey launch. Panels (a) and (b) show the performance of the wide and narrow correlators for the large ship. The wide correlator has several spikes that exceed 50 m (#1), however, the narrow correlator usually limits these spikes to 10 m. Even when the large spikes are ignored, the wide correlator has numerous 5 m multipath spikes (#2) which the narrow correlator successfully mitigates. The short delay multipath (#3) produces small errors for both the wide and narrow correlators. The performance of the two correlators under the short delay multipath, should be as expected after looking at the multipath error envelopes in Figure 2-47. Thus the narrow correlator's great advantage

for the large ship is that it greatly reduces the extreme (50 m range) and moderate multipath (5 m range) errors.

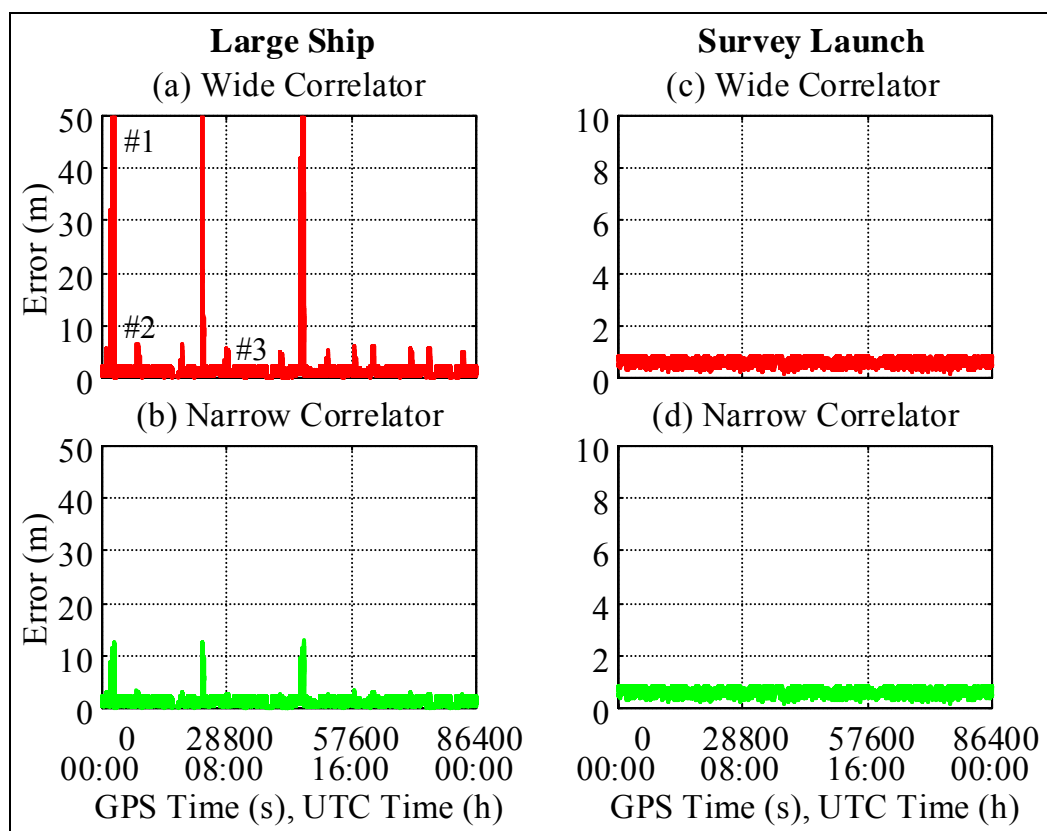
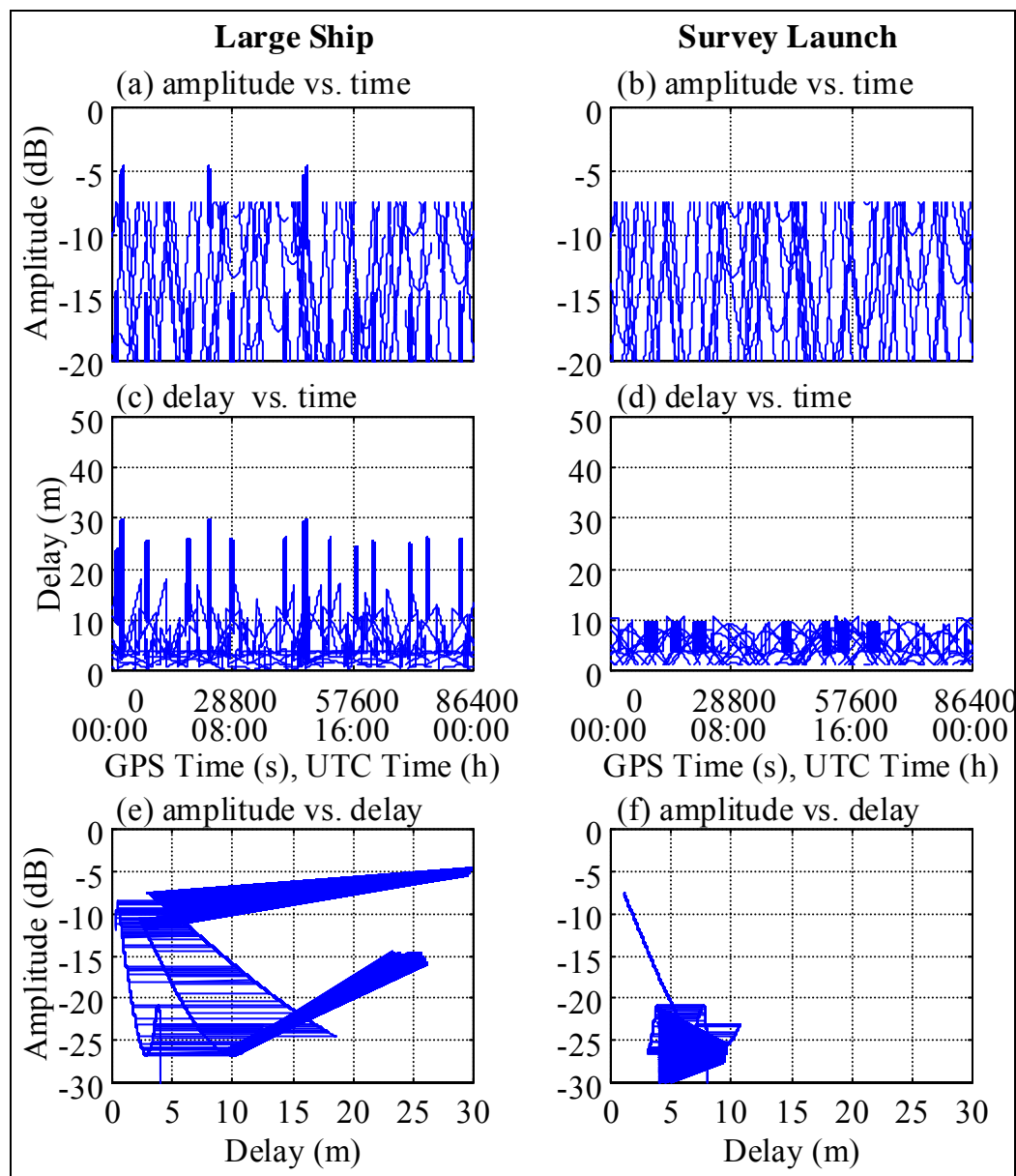


Figure 3-4 Largest Error for the Large Ship and Survey Launch for both the Wide and Narrow Correlators

The results for the survey launch panels (c) and (d) show a completely different multipath behaviour. The performance of both correlators is identical, with neither showing any large multipath errors. This is only possible, if the multipath reflections are either greatly attenuated or very short delay. In order to determine if this is the case, the amplitude and delay of all of the multipath reflections were examined. The multipath's amplitude and delay for every satellite for both the large ship and the survey launch are plotted in Figure 3-5. The multipath amplitude and delay are first plotted against time (panels (a)-(d)) and then against each other (panels (e) and (f)).



**Figure 3-5 Multipath Amplitude and Delay for all Satellites
for both the Large Ship and the Survey Launch**

The amplitude patterns for both ships in panels (a) and (b) look almost identical except for the three spikes for the large ship. This behaviour can be explained by examining the assumed antenna's gain pattern and the reflecting surfaces. For this simulation a simple representation of the ship was entered with almost all of the reflecting surfaces being

either horizontal or vertical surfaces. When this is the case there are only two types of reflections possible:

- 1) Reflections from horizontal surfaces below the antenna. The reflected signal will enter the antenna at the negative of the direct signal's elevation angle.
- 2) Reflections from vertical surfaces above the antenna. In this case the reflected signal will enter the antenna at the same elevation angle as the direct signal.

The resulting multipath losses for reflections from metallic objects for these two cases is:

$$\begin{aligned}
 \text{Horizontal Surfaces below the antenna} &= \text{LHCP}(-\theta) - \text{RHCP}(+\theta) - 3 \text{ dB} \\
 \text{Vertical Surfaces above the antenna} &= \text{LHCP}(+\theta) - \text{RHCP}(+\theta) - 3 \text{ dB}
 \end{aligned}
 \tag{3-1}$$

where θ = satellite's elevation angle

Applying equation (3-1) to the Sensor System's antenna gain pattern (Figure 2-42) results in the multipath discrimination curves of Figure 3-6 for the two reflecting surfaces.

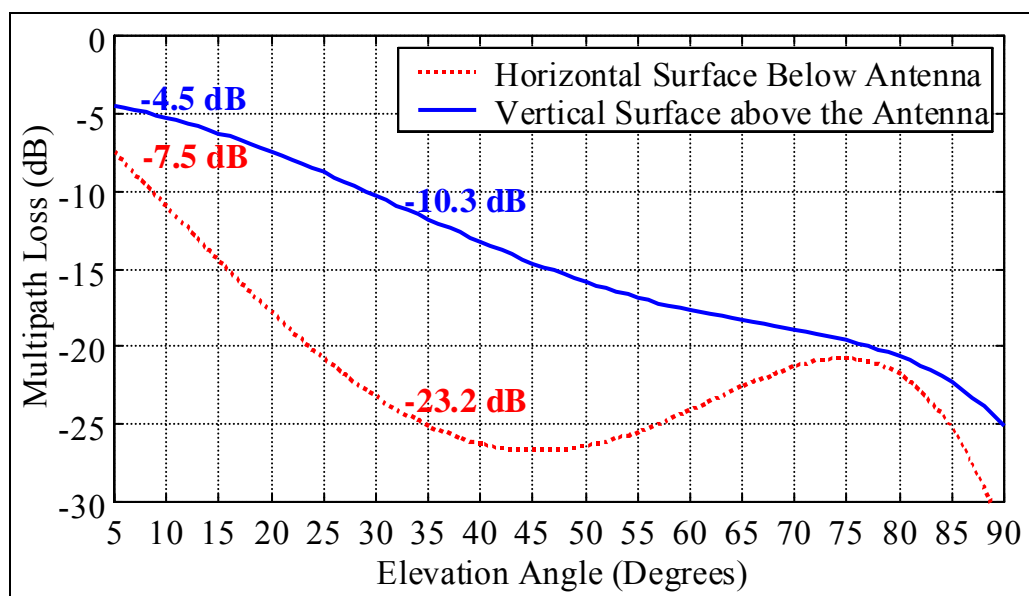


Figure 3-6 The Simulation's Multipath Discrimination

Thus for the survey launch since all of the reflections must come from below the antenna, the maximum multipath signal is -7.5 dB below the direct signal, which occurs at the 5° elevation cut off angle. As the satellite rises the multipath amplitude decreases almost linearly to -23.2 dB at a 30° elevation angle. This also occurs for the large ship, however, reflections from the ship's mast follow the vertical surfaces above the antenna and therefore have a maximum magnitude of -4.5 dB.

The major difference in the reflection's performance is seen in the multipath delays. The survey launch's multipath delays are all less than 11 m (Figure 3-5 panel (d)). Examining Figure 2-47 for the short delay multipath performance, shows that the narrow and wide correlators perform almost identically at this multipath delay. When the multipath amplitude is plotted against delay (Figure 3-5 panel (f)) the maximum signal for a delay of 5 m is only -20 dB, which will result in < 1 m range error (Figure 2-47). Thus the multipath results for the survey launch in Figure 3-4 panels (c) and (d) make sense.

The second largest simultaneous multipath blunder is shown in Figure 3-7 for both the large ship and the survey launch, again for both correlators. There is a noticeable difference between the largest errors of Figure 3-4 and the second largest errors of Figure 3-7. There are no large spikes in the second largest errors. The second largest error for this orientation was 4 m and 1 m for the large ship and survey launch respectively. These simulation results suggest that while multiple blunders will occur, the second and subsequent blunders will be much smaller. The second largest multipath blunder is essentially identical for both the wide and narrow correlators. This suggests that short delay multipath is the cause.

Figure 3-4 and Figure 3-7 showed how the largest and second largest multipath errors varied over time for both ships heading north. Figure 3-8 summarises the multipath simulation results for all of the ship orientations. The simulation results were grouped according to the ship (large ship / survey launch), correlator used (wide / narrow), and error type (largest / second largest). For each group the following five percentiles were

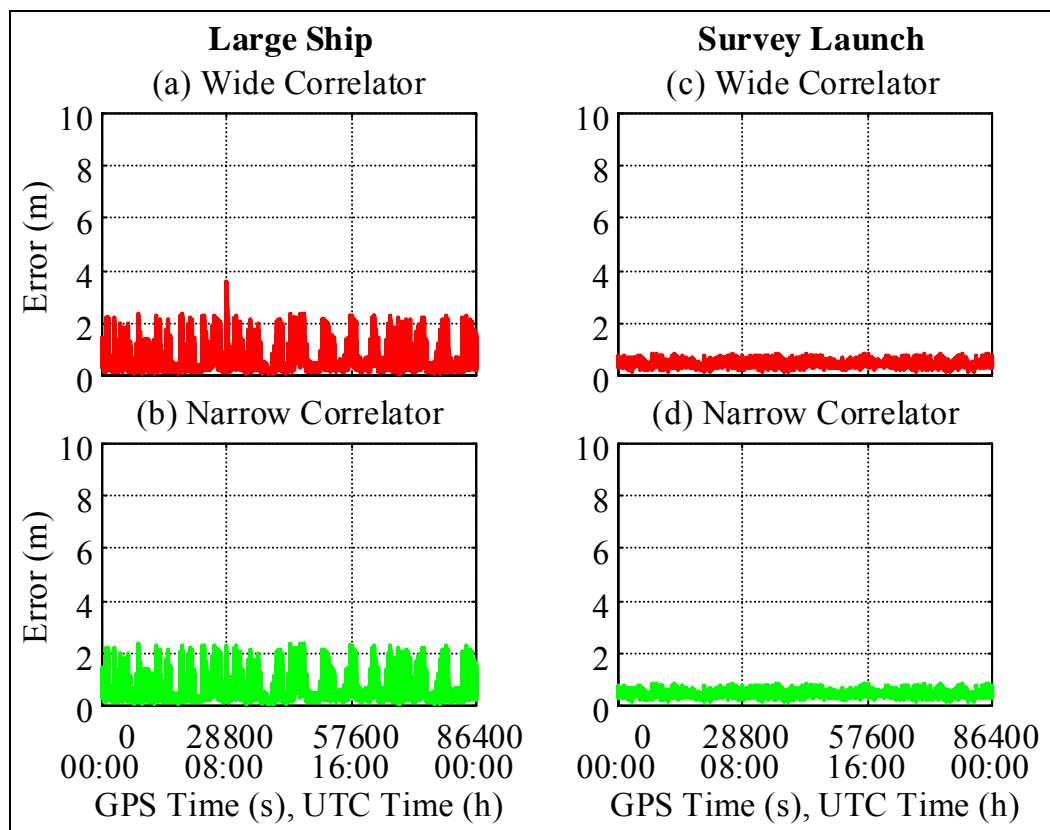


Figure 3-7 Second Largest Error for the Large Ship and Survey Launch for both the Wide and Narrow Correlators

plotted 68%, 95%, 99%, 99.9%, and 100%. The results for the two ships are consistently different, at the 68% percentile the large ship and survey launch have maximum errors of 1.4 m and 0.6 m respectively. For higher percentiles the large ship's error continues to increase while the survey launch remains at the 1 m level. The two correlators provide almost identical results up to and including the 95% level, where the maximum errors for the large ship were 3.6 m and 2.3 m for the wide and narrow correlators respectively. However, for the higher percentiles the large ship wide correlator's errors are evident. At the 99% level there is only a 4 m difference between the two, however, at the 99.9% level this has grown to a 32.3 m difference. The most compelling difference is the overall maximum error for the two correlators of 131.8 m and 14.0 m for the wide and narrow correlators. These summary results agree with the previous time series plots, where the

only differences between the two correlators were the infrequent large spikes, and the moderate level (5 m) errors.

Examining the second largest error shows that the 100% value was 6.1 m and 3.2 m for the wide and narrow correlators. At the 99% percentile all four combinations of vessel and correlator are < 2.1 m. Thus from these simulations, there is little probability of a second large simultaneous blunder.

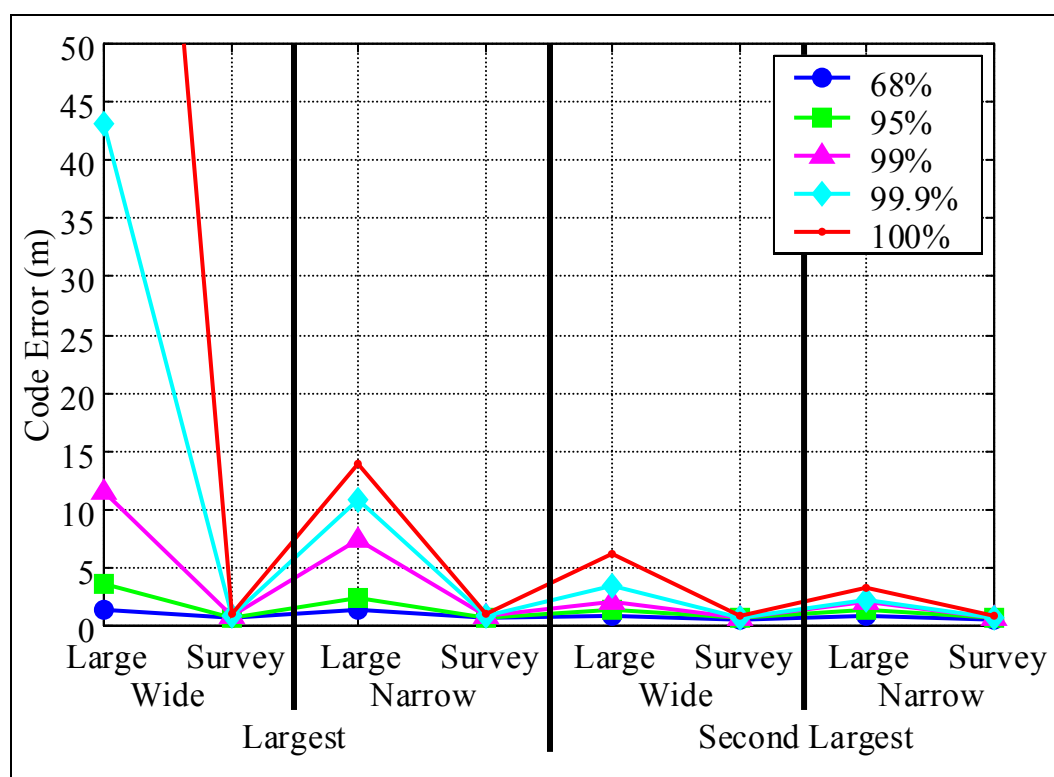


Figure 3-8 Multipath Simulation Results Summary

While these multipath simulations made a number of assumptions and simplifications, they have provided a good first order approximation of the types of blunders that can occur in a marine environment. The summary results from Figure 3-8 will be used in CHAPTER 4 to limit the magnitude of the blunders, based in the correlator type. Table 3-1 lists the blunder limits that will be used in CHAPTER 4.

Table 3-1 MDB Limits from the Multipath Simulations

Blunder Type	Wide Correlator	Narrow Correlator
Single Blunder	43 m	11 m
Double Blunder	43 m / 4 m	11 m / 4 m

The 99.9% values for the large ship were used to generate the limiting values for the largest blunders. While there are differences between the second largest blunder for the wide and narrow correlator, for the purposes of the reliability simulations the same value of 4 m will be used. Although this did not occur in these multipath simulations, it will be considered as the overall limiting event.

3.3 Multipath Period

The multipath period will be examined from a geometrical perspective using reflections from a horizontal surface. Figure 3-9 shows an incident wave (constant phase \overline{AB}) approaching the GPS receiving antenna at point “C” (height “h” above the ground). The incident wave is reflected from point “A”. The resulting multipath delay is:

$$\tau = |\overline{AC}| - |\overline{BC}| = \frac{h}{\sin \theta} \cdot [1 - \sin(90 - 2\theta)] \quad (3-2)$$

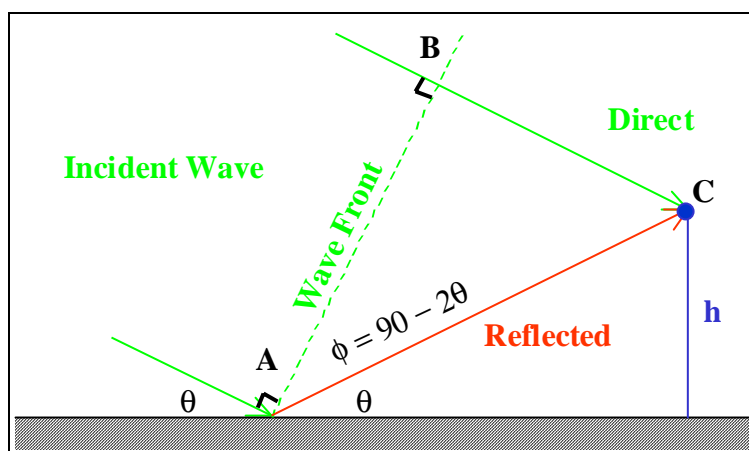


Figure 3-9 Multipath Reflection from a Smooth Horizontal Surface

By definition the multipath period is the time taken for the multipath delay to change by one wavelength, (19 cm for GPS L1). Taking the derivative of equation (3-2) results in:

$$\frac{d\tau}{dt} = \left[\frac{-h \cdot \cos \theta}{(\sin \theta)^2} \cdot [1 - \sin(90 - 2\theta)] + \frac{h}{\sin \theta} \cdot [2 \cdot \cos(90 - 2\theta)] \right] \cdot \frac{d\theta}{dt} \quad (3-3)$$

where θ = satellite elevation angle

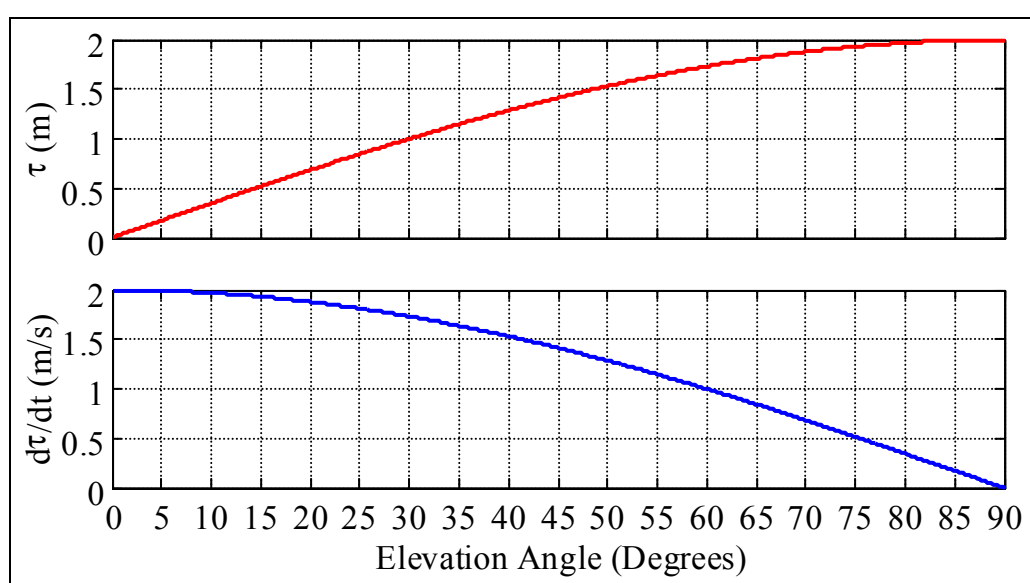


Figure 3-10 Multipath Delay (τ) and Delay Rate ($d\tau/dt$) with $h = 1$ and $d\theta/dt = 1$

Equation (3-3) is a function of the antenna height, satellite's elevation angle, and the rate of change of the satellite's elevation angle. Figure 3-10 plots equations (3-2) and (3-3) with $h = 1$ and $d\theta/dt = 1$ vs. elevation angle. The antenna height and rate of change of the satellite's elevation angle are both scale factors. The maximum multipath delay occurs when the satellite is at its zenith ($2 \cdot h$) and it goes to zero at the horizon since there is no longer a reflection point. The rate of change of the satellite's elevation angle must now be combined with the delay rate to determine the multipath's period. A typical rate of change of the satellite's elevation angle is shown in Figure 3-11 for PRN 1's satellite pass

during the multipath simulations. While numerous satellite pass patterns are possible, this simple function will be used to estimate the multipath period.

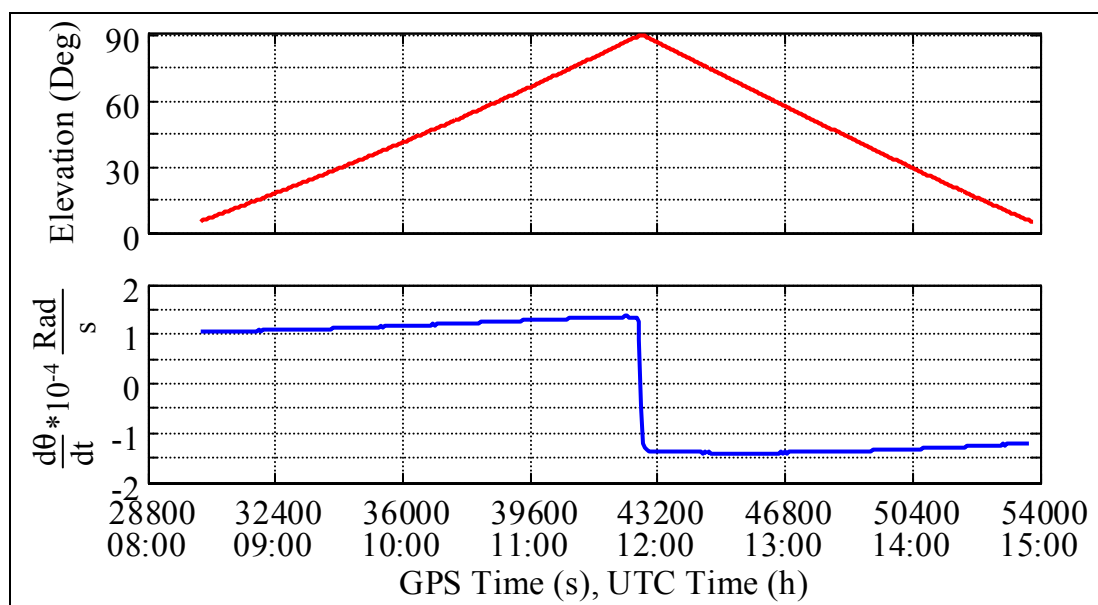


Figure 3-11 PRN 1's Elevation Angle and Elevation Angle Rate vs. Time

Combining Figure 3-10 with Figure 3-11 results in the multipath periods vs. elevation angle, shown in Figure 3-12. Figure 3-12 must be scaled by the antenna height, thus for a 10 m antenna height the multipath period for a satellite at 5° would be 91 s. Even for a 70° elevation satellite the period would only increase to 214 s for the same antenna height.

Taking the satellite pass given in Figure 3-11 and using equation (3-1) the corresponding multipath delay is plotted in Figure 3-13 assuming $h = 1$ m. The red circles on the multipath delay graph mark each time the delay goes through a L1 cycle. The corresponding periods are also included. These multipath periods represent reflections from horizontal surfaces for one typical satellite pass. Reflections from other surfaces and for different satellite patterns will produce different results. The multipath period is defined by the rate of change of the multipath delay, which is a function of the receiver to reflector dynamics, and is affected by the sea state, ship's orientation (pitch and roll), and

the satellite motion. These results give an indication of the potential periods that could occur in practice.

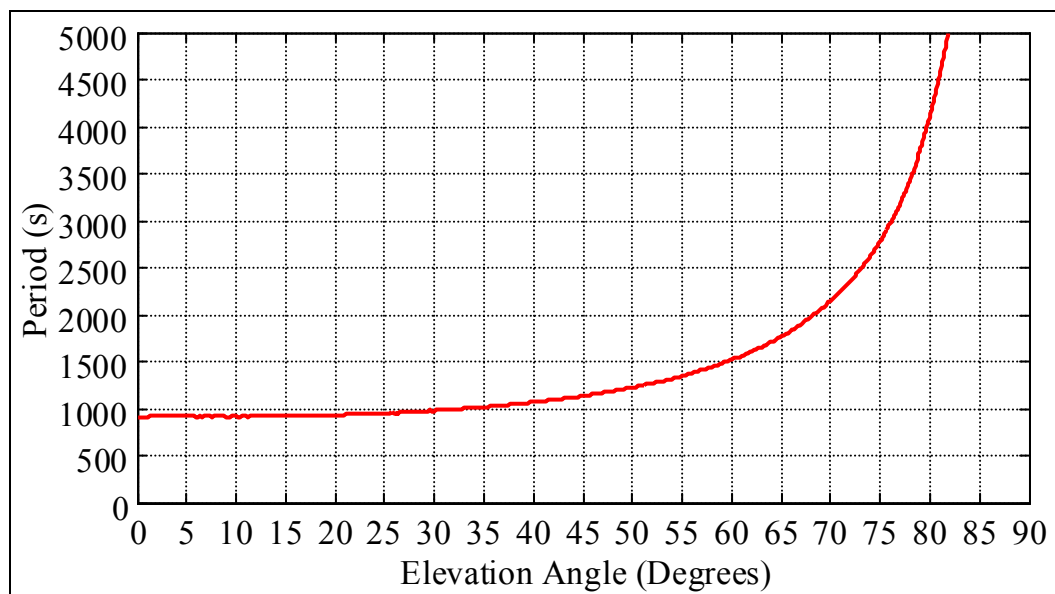


Figure 3-12 Multipath Period vs. Elevation Angle with $h = 1$ m

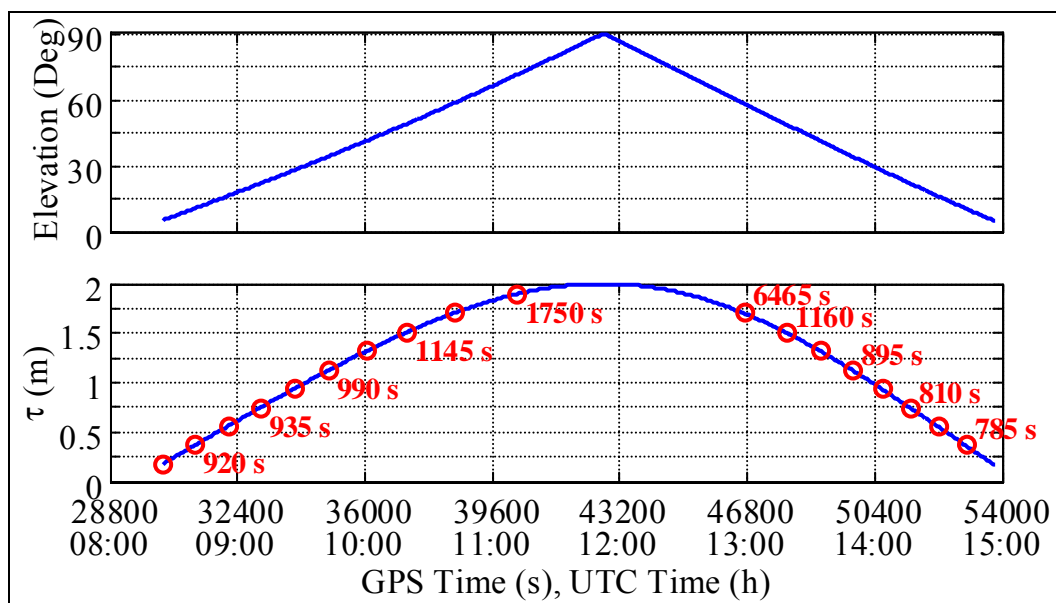


Figure 3-13 PRN 1's Elevation Angle, Multipath Delay and Multipath Period.

CHAPTER 4

SIMULATION ANALYSIS

4.1 *Introduction*

The previous chapters introduced several satellite based augmentations for DGPS and analysed the GNSS error sources. That information will be used in this chapter to analyse the availability and reliability improvements attained by augmenting DGPS under different masking environments. The following masking environments will be simulated:

- 1) Constant mask angle 0° - 40° in 10° increments
- 2) Constricted waterway / urban canyon with a maximum mask angle of 56.3°
- 3) Hydrographic surveying example

All of the potential augmentations and augmentation combinations will be tested under the first two masking environments. The hydrographic surveying example will simulate the GPS and GLONASS constellations available in July 1997 when the field campaign discussed in CHAPTER 7 was conducted.

In the future users may have three different satellite constellations that can be used to augment DGPS: GLONASS, Galileo, and GEO satellites. While GLONASS is currently available, the number of healthy satellites has been consistently dropping since 1996 as shown in Figure 2-4. Therefore two GLONASS constellations will be included in the simulations. A complete 24 satellite constellation will be included using the orbital parameters from the GLONASS almanac for GPS Week 845 (GLO24), and a 10 satellite constellation using the GLONASS almanac for GPS Week 1065 (GLO10). Differential GLONASS is not publicly available in North America and it may never be available

given the health of the GLONASS constellation. Thus a single point GLONASS (GLOSP) augmentation using the GLO10 constellation will be used, following the initial analysis. The two Galileo constellations defined in Table 2-5 will be simulated with the 24 MEO and 9 GEO constellation designated GAL24 and the 30 MEO constellation called GAL30. Finally, the six GEO satellites that may be implemented for aviation applications discussed in section 2.3 will be included as GEO6.

These are the individual augmentation constellations, however, which potential constellation combinations will be used. While it has not been stated by either the European Union nor the Russian Federation, it is extremely unlikely that both GLONASS and Galileo will be operational at the same time. Therefore GLONASS and Galileo will not be combined. The GEO6 augmentations will be implemented in the near future and will therefore overlap with the GLONASS constellation. However, which GLONASS constellation should be added to GEO6? Since it has been approximately six years since the GLONASS constellation had 24 healthy satellites, only GLO10 will be combined with GEO6. Galileo is a different story, since the GAL24 constellation already contains nine GEO satellites the GEO6 will not be added to it. Since the GAL30 constellation does not contain any GEOs, GEO6 will be combined with it. Therefore the following nine satellite system combinations will be simulated:

- 1) DGPS
- 2) DGPS+GLO24
- 3) DGPS+GLO10
- 4) DGPS+GEO6
- 5) DGPS+GAL24
- 6) DGPS+GAL30
- 7) DGPS+GLO10+GEO6
- 8) DGPS+GAL30+GEO6
- 9) DGPS+GLOSP (presented after)

For each satellite system combination the following four constraints will be employed:

- 1) No Constraints – “N”
- 2) Height Constraint – “H”
- 3) Clock Constraint – “C”
- 4) Both Height and Clock Constraints – “B”

Thus 36 different positioning methods were simulated

In order to simulate both high and low quality user receivers two satellite measurement variances are used, 1 m^2 and 9 m^2 for the narrow and wide correlators respectively. These variance values encompass the orbital errors (2.5.1), tropospheric errors (2.5.2), and measurement noise(2.5.4).

Taking tidal variation and other effects such as swell and waves into account the height constraint variance was set to 4 m^2 . Assuming a good quality ovenized quartz clock is used, the clock constraint variance was set to 1 m^2 .

A least squares reliability algorithm was used for the simulations. It assumed that the residual testing was done epoch by epoch using no a priori knowledge of the trajectory. Four different blunder combinations were simulated, using the limiting values specified in Table 3-1.:

- 1) single unlimited blunder
- 2) single limited blunder, based on the type of correlator
- 3) double unlimited blunder
- 4) double limited blunder, based on the type of correlator

The simulation was run over 24 hours in 60 second increments for each of the computation points shown in Figure 4-1. A total of 118 computation points were used to represent the world. The simulation was run using the University of Calgary’s GPS GLONASS Pseudolite Analysis Program (GGPLAN). At each epoch the HDOP and the MHE are calculated using the specified constellation combination and constraints. In the

first two subsections least squares reliability checking is used to generate the MHE. A Kalman filter is used in the Hydrographic surveying example to demonstrate the benefits of dynamic constraints. The following reliability parameters were used for all of the simulations $\alpha = 0.1\%$, $\beta = 10\%$, and $\delta_o = 4.57$, see section 2.6 for more detailed information.

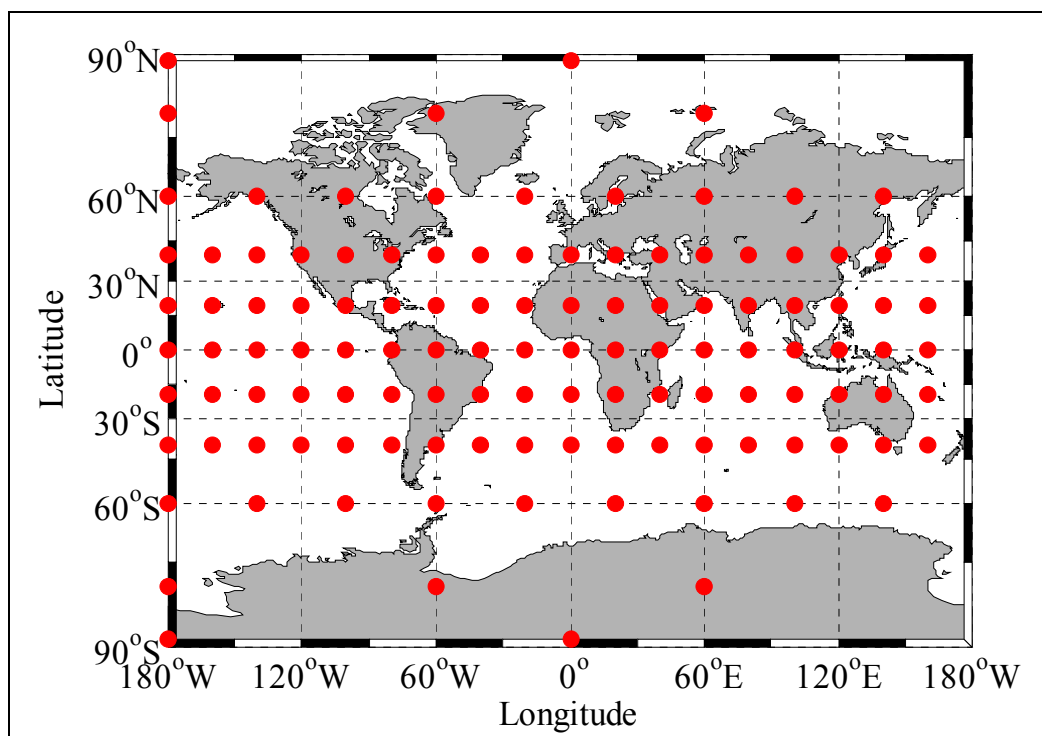


Figure 4-1 Simulation Computation Points

The improvements attained by augmenting DGPS with the satellite constellations and constraints were evaluated by looking at the improvement in precision (HDOP) and reliability (MHE). Since DGPS is the base system, the DOP matrix is generated by dividing the parameters' covariance matrix ($C_{\hat{x}}$) by the DGPS variance (σ_{DGPS}^2).

$$\text{DOP} = \frac{1}{\sigma_{\text{DGPS}}^2} * C_{\hat{x}} = \frac{1}{\sigma_{\text{DGPS}}^2} * (A^T * C_1^{-1} * A)^{-1} = (A^T * P * A)^{-1} \quad (4-1)$$

where P weight matrix

The HDOP is calculated using the first two diagonal elements of the DOP matrix.

$$\text{HDOP} = \sqrt{\text{DOP}_{1,1} + \text{DOP}_{2,2}} \quad (4-2)$$

When the variances of all the observations are equal (i.e. P equals the identity matrix), the HDOP is based solely on geometry. Otherwise the HDOP is a function of the geometry and weight matrix. In GGPLAN the height and clock constraints are added as quasi-observables to the design matrix and thus they are also included in the weight matrix.

$$P = \begin{bmatrix} \frac{\sigma_{\text{DGPS}}^2}{\sigma_{\text{DGPS}}^2} = 1 & \dots & 0 & 0 \\ \sigma_{\text{DGPS}}^2 & \ddots & 0 & 0 \\ \vdots & & \frac{\sigma_{\text{DGPS}}^2}{\sigma_{\text{Height}}^2} = \frac{1}{4} & 0 \\ 0 & 0 & 0 & \frac{\sigma_{\text{DGPS}}^2}{\sigma_{\text{Clock}}^2} = 1 \end{bmatrix} \quad (4-3)$$

Changing the satellite observation variance from 1 to 9 m² will only marginally change the weight matrix (as shown in equation (4-3)) and hence the HDOP.

4.2 *Isotropic Mask Angles*

If all of the isotropic mask angle simulation data were to be presented, a five dimensional figure would be required; computation point, positioning method, isotropic mask angle, time and HDOP / MHE. Instead of presenting any time series, the 95% HDOP / MHE were calculated for:

- 1) each computation point
- 2) all 118 computation points batched together to generate world values

In addition to calculating the 95% values, the percentage of time that the HDOP ≤ 2 and the MHE ≤ 10 m were also calculated for the cases listed above. These limits were chosen since for many marine navigation applications the position is only considered

available if the HDOP ≤ 2 , and the required positional accuracy is 10 m. The percentage of available / reliable positions quoted in the following sections are in the context of these values.

4.2.1 Availability Results

A summary of the isotropic mask angle availability results for the world are given in Figure 4-2 and Figure 4-3. The results are presented in graphical form with the 32 positioning methods on the x-axis grouped according to the satellite constellations employed. Within each group are the four constraints. Figure 4-2 plots the overall world 95% HDOP, while Figure 4-3 plots the overall world percentage of HDOPs ≤ 2 .

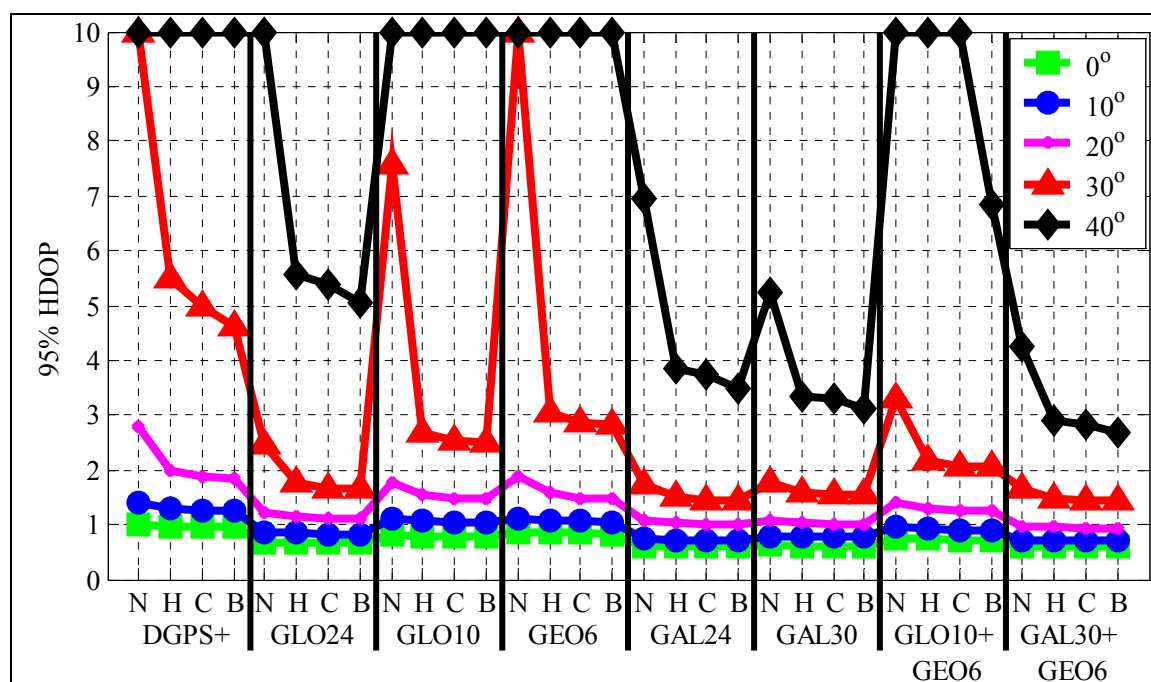


Figure 4-2 95% HDOP, for the World, Isotropic Mask Angles

The availability improvements attained by augmenting DGPS are graphically seen as the slope of the lines. As the mask angle increases the slope also increases, indicating increased improvements. The HDOP is improved through augmentation but the improvement is not impressive. These results show that unaugmented DGPS provides

available navigation for the benign masking conditions of 0° and 10° with 95% HDOPs of 1.0 and 1.4 respectively. Even for the 20° mask case, the 95% HDOP is 2.8 and the availability is 88%. Augmenting DGPS with either a height or clock constraint improves the 95% HDOP to 2.0 and 1.9 respectively using a 20° mask angle. Thus for the 20° mask case no additional satellite navigation system is required to meet the availability requirements. This is not the case for the two higher mask angles.

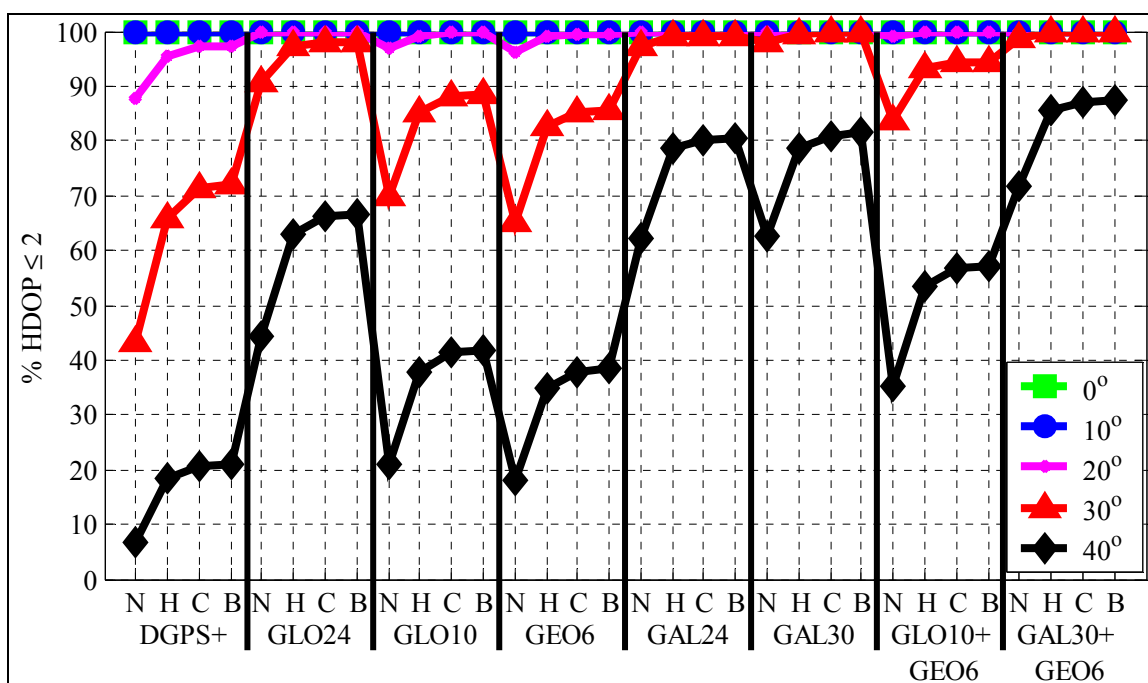


Figure 4-3 Percent HDOP \leq 2.0, for the World, Isotropic Mask Angles

For the 30° mask case, DGPS + both constraints has a 95% HDOP of 4.6 and an availability of 72%. When DGPS and constraints do not provide available navigation, a second satellite based system is required. The GLO10 constellation requires at least one constraint to bring the 95% HDOP below 3.0, however, the constellation is too depleted to bring the value below 2.0. The full GLO24 constellation with at least one constraint is required to drop the 95% HDOP below 2.0. The GEO6 augmentation results are similar to the GLO10's. The GEO6 augmentation can reduce the HDOP below 3.0 when constraints are added, but it cannot meet the 2.0 threshold. This is due to the lack of GEO

visibility at higher latitudes, as shown in Figure 2-8. The Galileo augmentations perform the best. Once DGPS is augmented with either Galileo constellation without constraint the 95% HDOP decreases to less than 1.8 with an availability of greater than 97%. Adding both constraints to the DGPS + Galileo constellations increases the availability to greater than 99%. There is very little visible difference between the two Galileo constellation results.

At the highest isotropic mask case of 40°, only full constellation augmentations have any real effect. The fully constrained GLO10 with GEO6 has a 95% HDOP of 6.8 with an availability of 57%. This is far from an available navigation. The fully constrained full constellation augmentations of GLO24, GAL24 and GAL30 have 95% HDOP values and availability's of 5.1 / 66%, 3.5 / 80%, and 3.1 / 81% respectively. The two Galileo constellations have slightly different results. While this is an extreme masking condition, these results show that the combination of GPS and Galileo with constraints can provide available navigation. The GLO24 and GAL24 results are different not only because of the different constellation of 24 MEO satellites, but also because the GAL24 constellation contains 9 additional GEO satellites.

The summary results provide a world view of the availability performance, but mask any regional differences. The regional differences first become apparent for the 30° mask case using DGPS + height. Figure 4-4 is a contour graph of the 95% HDOP using the individual computation point values. The overall 95% HDOP is 5.5 with a 66% availability. However, there are large variations in the 95% HDOP with locations ranging from a low of 1.6 to a high of > 10. Unavailability bands are found in the 30°-75° latitudes. Although on the world scale DGPS + height for the 30° mask case does not provide available navigation, some locations still show acceptable availability values.

Unfortunately the converse is also true, methods with good world availability values will have availability holes. For example the overall world performance for DGPS + GAL24, for the 30° mask case, is extremely good with a 95% HDOP of 1.7 and 97% availability.

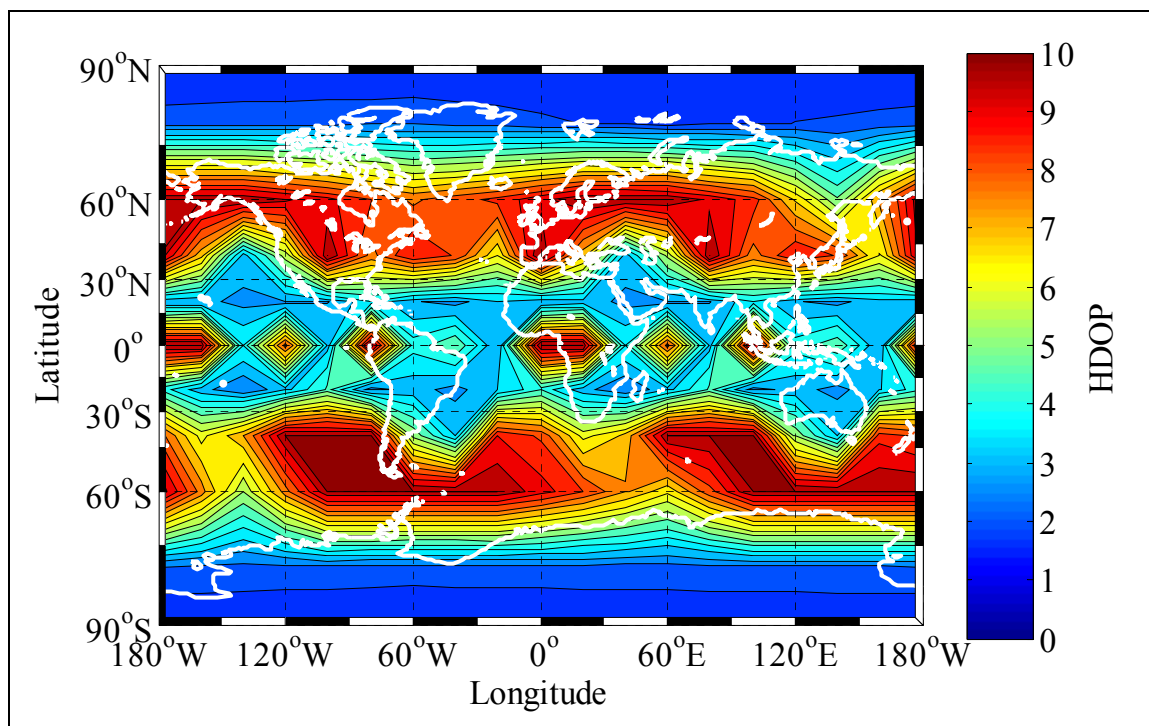


Figure 4-4 95% HDOP, DGPS + Height, 30° Mask Angle

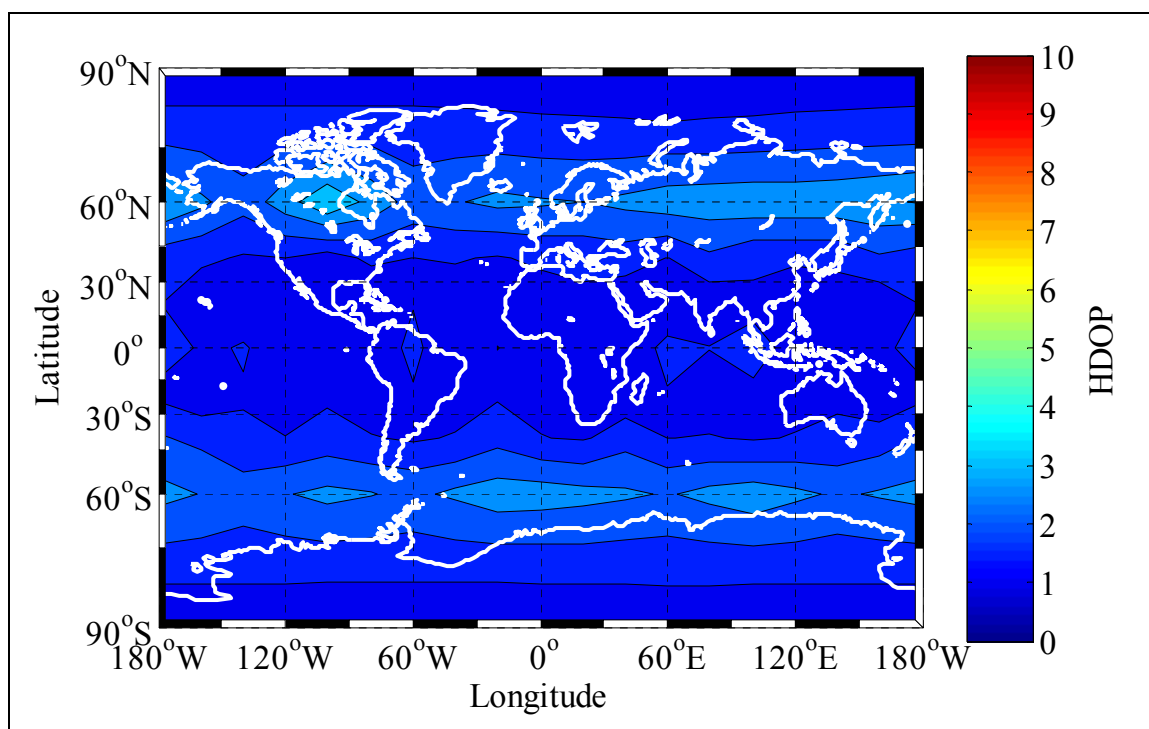


Figure 4-5 95% HDOP, DGPS + GAL24, 30° Mask Angle

However, as shown in Figure 4-5 the 95% HDOP varies from 1.1 to 3.4. Availability holes are again found around $\pm 60^\circ$ latitude. These variations are not as problematic as in Figure 4-4, however there are variations based on the user's locations.

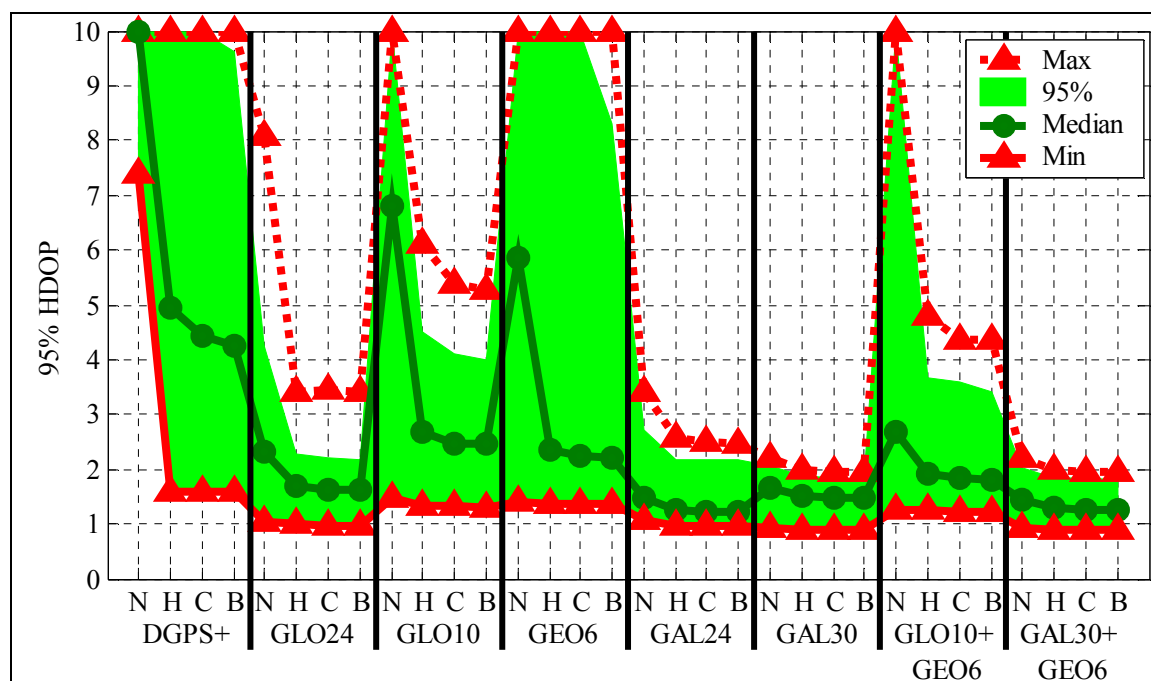


Figure 4-6 Computation Points Statistics, 95% HDOP, 30° Mask Angle

The following statistics were generated for the 95% HDOP values for the 118 computation points (30° mask case) for each positioning method:

- 1) maximum value
- 2) 95% value
- 3) median value
- 4) minimum value

Figure 4-6 shows the results of this analysis, the maximum and minimum values are the red lines with red triangle markers. The median value is the dark green line with dark green “o” markers. The 95% value is the light green shaded area. When DGPS is only augmented with constraints, there are large variations between the minimum and maximum values. The same is true when DGPS is augmented with GEO6. This is due to

the fact that at high latitudes there are no GEO satellites available under these masking conditions. The GLO10 constellation shows slightly better results. The subtle differences between the two Galileo constellations are shown in this figure. The maximum HDOP for the GAL24 and GAL30 constellations are 3.4 and 2.2 respectively. While GAL24 has a median value that is 0.1 less than GAL30. Thus the GAL30 constellation tends to moderate the results, with slightly higher median values, and lower maximum values.

4.2.2 Reliability Results: 1 m² Measurement Variance

The reliability results will be presented in a similar manner as the availability results. The results will first be presented using a measurement variance of 1 m² assuming the single worst case blunder occurred. A summary of the isotropic mask angle reliability results for the world are given in Figure 4-7 and Figure 4-8 for the 95% MHE and the percentage of MHE ≤ 10 m respectively.

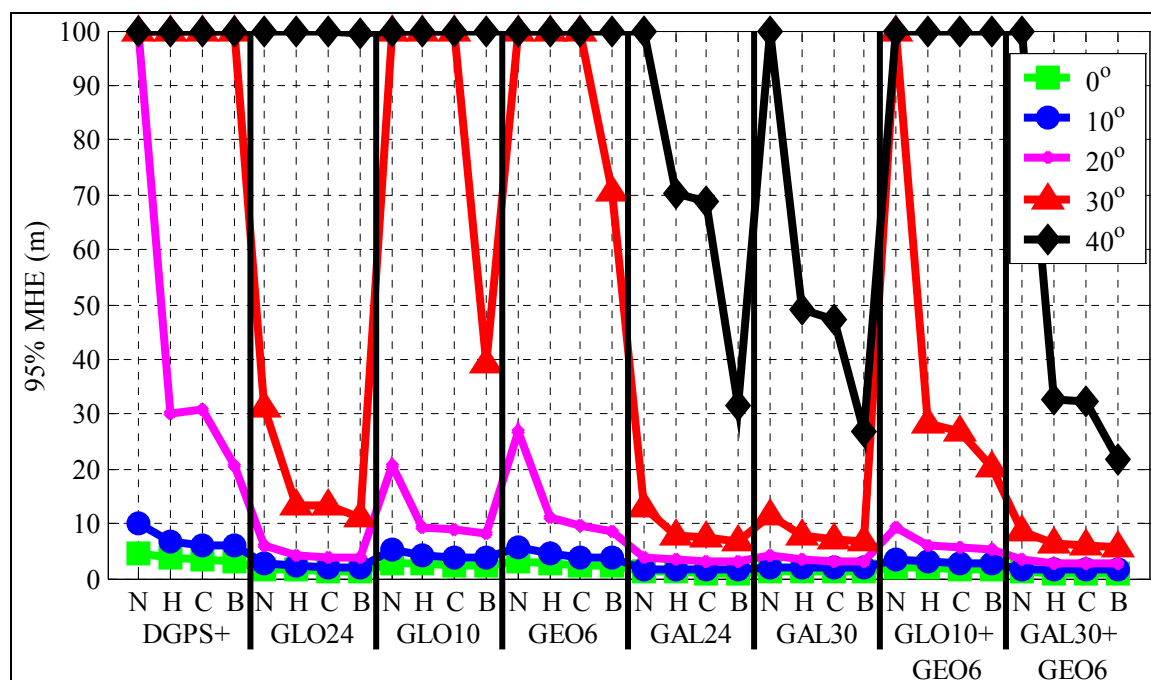


Figure 4-7 95% MHE, for the World, Single Unlimited Blunder, $\sigma = 1$ m

DGPS with constraints showed available positioning for the 0°, 10°, and 20° masking cases. However, reliable navigation is only possible for the 0° and 10° masking cases. For the 20° mask case, unaugmented DGPS has a 95% MHE of > 100 m with a corresponding reliability of 56% (% of MHE ≤ 10 m). Augmenting DGPS with both constraints improves the 95% MHE to 20.6 m and increases the reliability to 85%. This however does not meet the reliability target of 95%. The reliability target is met once DGPS is augmented with one of the full constellations (GLO24, GAL24, or GAL30). The partial constellations (GLO10 and GEO6) require a constraint in order to meet the 10 m target. The most augmented method of GAL30 + GEO6 + B has a 95% MHE of 2.6 m.

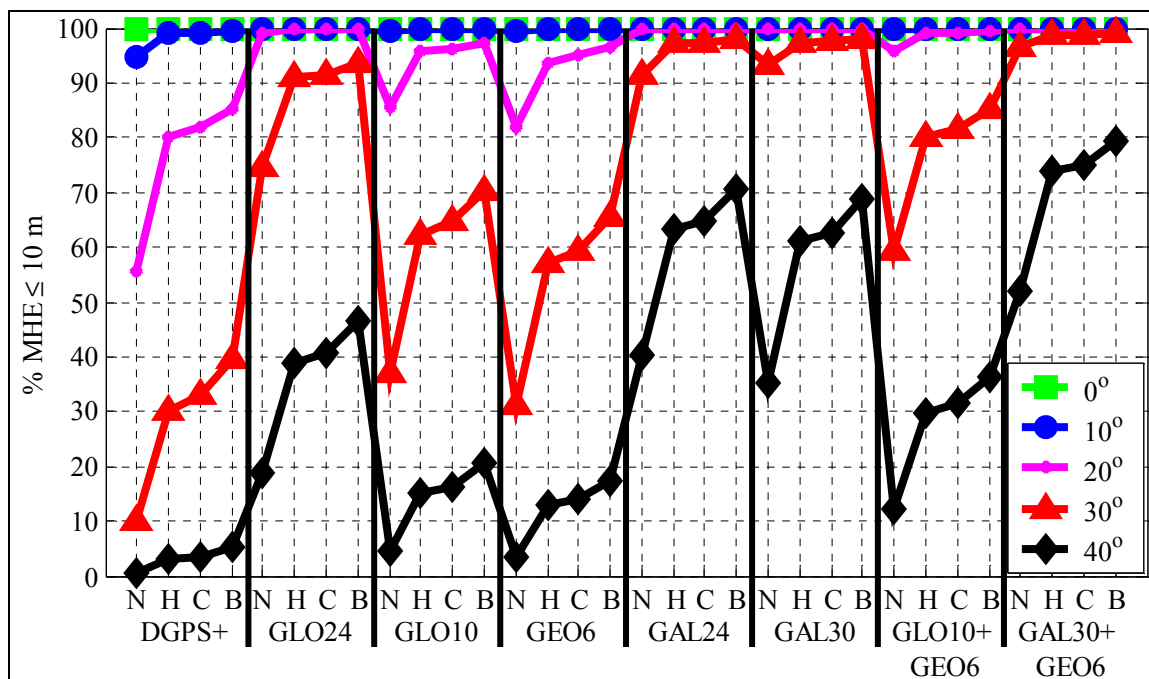


Figure 4-8 Percent MHE ≤ 10 m, for the World, Single Unlimited Blunder, $\sigma = 1$ m

At the 30° mask angle, DGPS with both constraints has a 95% MHE of > 100 m, with a corresponding reliability of 40%. This is well below the desired target. The partial constellations are ineffective at improving the reliabilities. The GLO10 and GEO6 with both constraints have 95% MHE of 40 m and 71 m respectively. They have insufficient satellites to provide reliable navigation. The fully augmented GLO24 constellation on the

other hand, has a 95% MHE of 11 m. Augmenting with either Galileo constellation and a constraint results in a 95% MHE of 7.7 m. Which means that reliable navigation is possible even under this extreme masking condition. As the mask angle increases the ability of the partial constellations to improve the reliability quickly drops.

This is especially the case for the 40° mask case. Only the Galileo constellations have 95% values less than 100 m. Even then the most augmented Galileo constellation has a 95% MHE of 27 m with a 71% reliability. While this does not meet the reliability target, it does mean that reliable navigation is possible for specific times and locations.

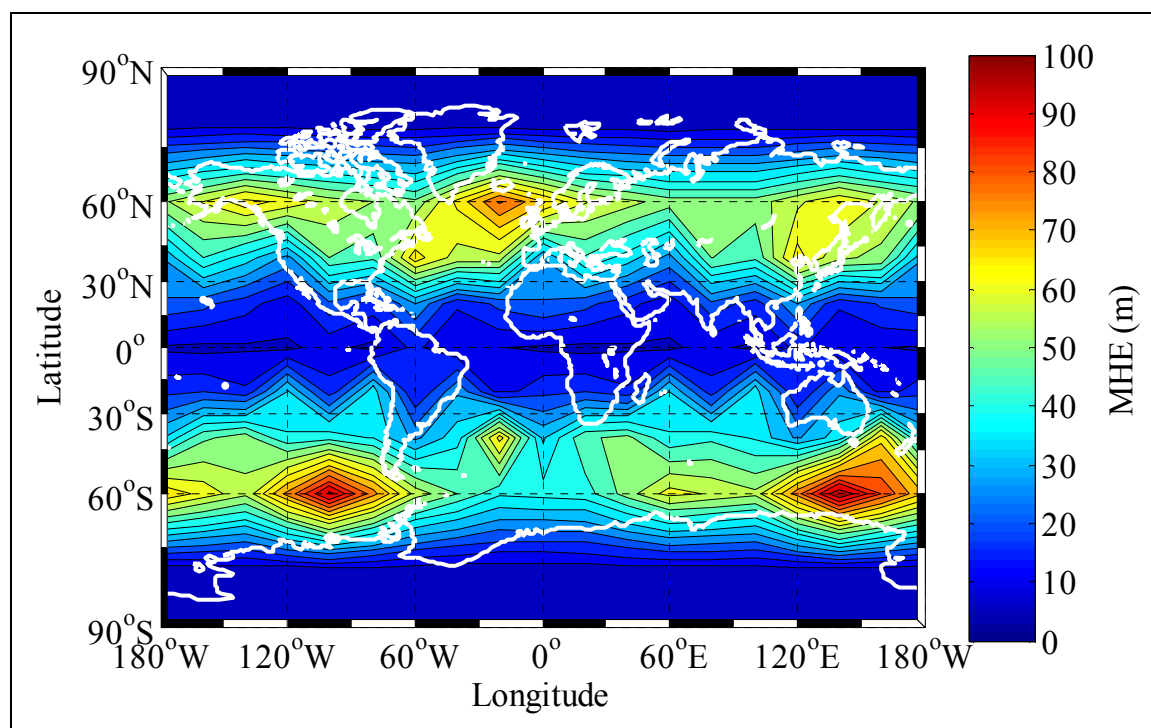


Figure 4-9 95% MHE, DGPS + Height, 20° Mask Angle

The regional reliability differences first become apparent for the 20° mask case using DGPS + height. Figure 4-9 is a contour graph of the 95% MHE. In this case the overall 95% MHE is 30.0 m. However, there are large variations in the 95% MHE with locations ranging from a low of 6.0 m to a high of > 100 m. Regions of poor reliability are found at

$\pm 60^\circ$ latitudes. Although on the world scale DGPS + height for the 20° mask case does not provide reliable navigation, once again some locations still have acceptable values.

The results from analysing the 95% MHE values for the 118 computation points (20° mask case) for each positioning method is shown in Figure 4-10. When DGPS is augmented with constraints there are large reliability variations between computation points. The minimum and maximum 95% MHEs are 5.6 m and 57.0 m respectively for DGPS and both constraints. Similarly the GLO10 augmentation varies from a low of 4.8 m to a high of 73.3 m. The maximum 95% MHE for the full constellations, GLO24, GAL24, and GAL30, are all less than 10 m. Under this masking condition the full constellations provide reliable navigation regardless of the user's location.

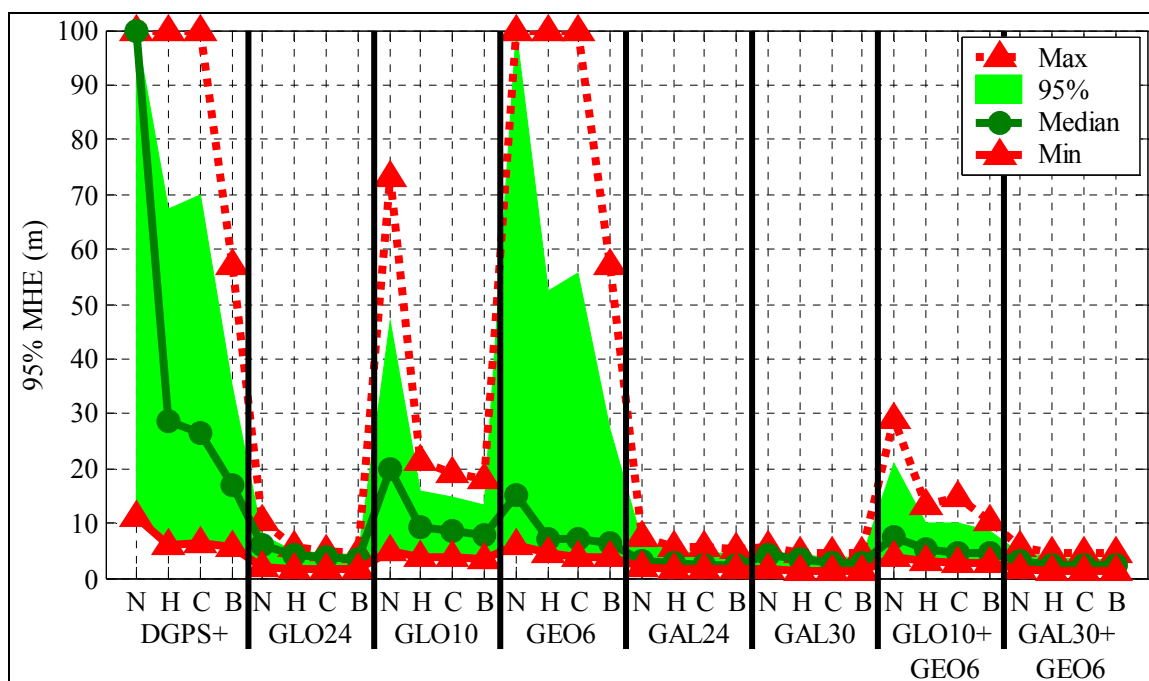


Figure 4-10 Computation Points Statistics, 95% MHE, 20° Mask Angle

The regional reliability differences between the two Galileo constellations become apparent for the 30° mask case as shown in Figure 4-11. With at least one constraint GAL24 and GAL30 have maximum values in the 20 m and 14 m range respectively. This

follows the availability results when GAL30 tended to moderate the results. The same trend is evident for reliability.

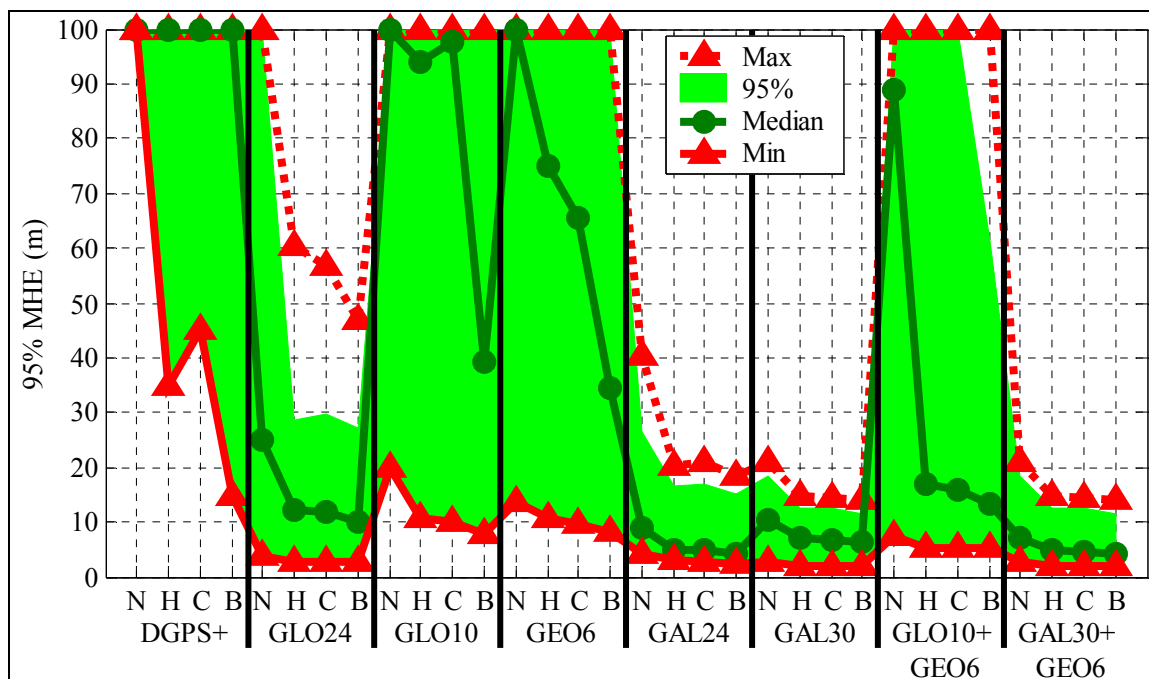


Figure 4-11 Computation Points Statistics, 95% MHE, 30° Mask Angle

4.2.3 Reliability Results: 9 m² Measurement Variance

The reliability results so far have covered high quality receivers (e.g. narrow correlator) under differential operation, with a resulting measurement variance of 1 m². Less expensive receivers normally employ wide correlators with resulting measurement variances under differential operation of approximately 9 m². Receivers in standalone mode, both high and low quality, will have an even higher measurement variance due to the increased user equivalent range error (UERE). How will the reliability results change when the measurement variance is increased to 9 m²? Figure 4-12 shows the results for a receiver with a measurement variance of 9 m². Unaugmented DGPS never meets the reliability target, even for the low mask angles. Comparing the results for the 1 m² and the 9 m², Figure 4-7 and Figure 4-12 respectively, shows an interesting trend. The lower

variance receiver can operate reliably with at least 10° additional masking over the higher variance receiver. This trend is consistent across all of the augmentations. When only the satellite augmentations are taken into account the results for the higher variance receiver is 3 times worse than the lower variance receiver. This should be expected since the MDB defined in equation (2-34) is directly proportional to the measurement standard deviation. Since propagating the MDB to the MHE is a linear operation, scaling the MDBs will result in scaling the MHEs. Since the height and clock constraint's variance do not change the scale factor is less than 3.0 for those positioning cases. For all of the positioning methods the minimum scale factor is 2.6.

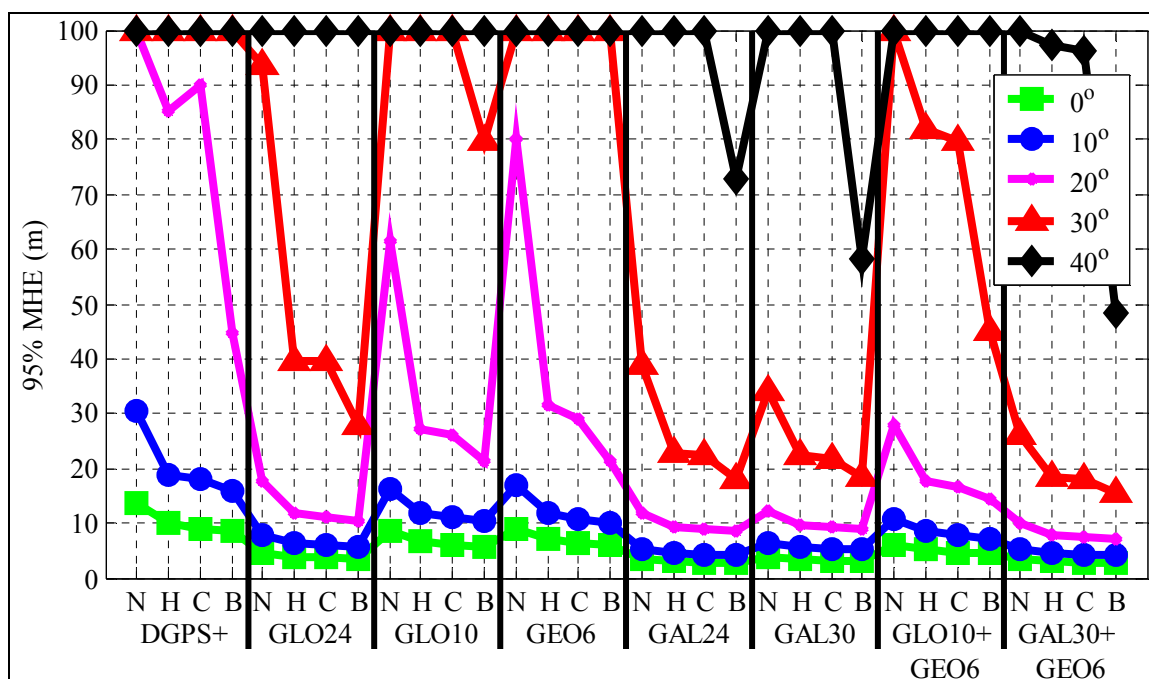


Figure 4-12 95% MHE, for the World, Single Unlimited Blunder, $\sigma^2 = 9 \text{ m}^2$

If changing the satellite measurement variances scales the weight matrix (equation (4-3)) the DOPs will not be affected. Otherwise the DOPs will be marginally affected as discussed in section 4.1. However, the resulting precision ($\sigma_{\text{DGPS}}^2 * \text{HDOP}$) will be scaled. Thus a higher performance receiver (lower measurement variance) can be viewed as an augmentation unto itself. Although differential corrections are usually assumed, they also

can be viewed as an augmentation unto themselves. Without differential corrections there would be little difference between high and low quality receivers.

4.2.4 Reliability Results: Limited and Multiple Blunders

The results from the multipath and ionospheric simulations in CHAPTER 2 and CHAPTER 3 illustrated that infinite blunders do not occur. What effect does limiting the blunder (i.e. MDB) have on the resulting MHE values? Figure 4-13 shows the single worst case and limited blunder results for the 30° mask case, for the narrow correlator (1 m²) and wide correlator (9 m²) receivers. The blunders were limited to 11 m and 43 m for the narrow correlator and wide correlator receivers respectively.

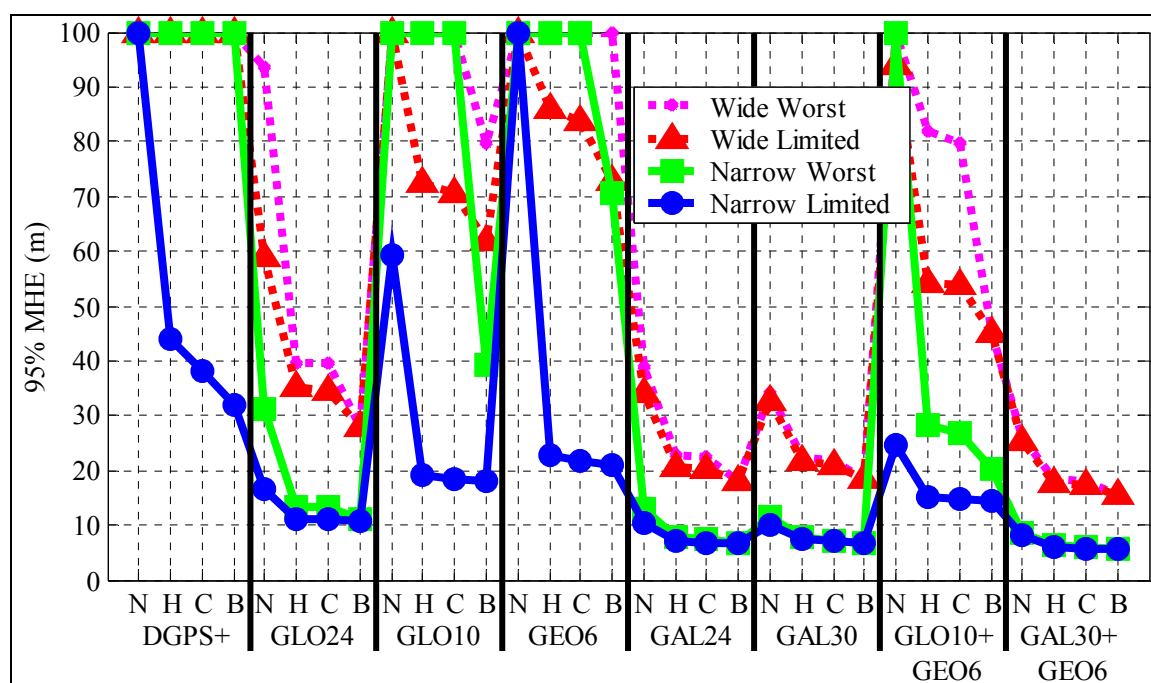


Figure 4-13 95% MHE, for the World, Single Blunder, Mask Angle 30°

In the first panel of Figure 4-13 augmenting DGPS with constraints and limiting the narrow correlator receiver's blunder resulted in a 95% MHE of 32.0 m. While this is an improvement, it still does not provide reliable navigation. Limiting the blunders for the partial constellations of GLO10 and GEO6 show dramatic improvements. Limiting the

MDB (narrow correlator) for the GLO10 + height augmentation caused the 95% MHE to drop from 100 m to 19.3 m. For the full constellation augmentations, GLO24, GAL24, and GAL30, there is very little difference between the worst case and limited blunders. Excluding the GLO24 with no constraints, limiting the MDB in the other 11 positioning cases improved the MHE by less than 3 m.

Why do the reliability results for the worst and limited cases converge as DGPS is augmented? The answer lies in the redundancy number (see section 2.6.1). When DGPS is heavily augmented, the redundancy number increases and the MDBs decrease. Since the MDBs have already been decreased by the added redundancy, limiting them has little to no affect. However, when the redundancy number is very low or zero (i.e. a unique solution) as is often the case for unaugmented DGPS, the MDBs calculated using reliability theory will be large. Limiting these MDBs to 43 m and 11 m for the wide and narrow correlator respectively will greatly improve the resulting MHE.

Similar results are obtained for the wide correlator (9 m^2) cases. The ratio between the wide and narrow correlator for the limited cases has increased from a maximum of 3.0 to 3.8. This is because when the MDBs are limited the ratio is $43/11=3.9$.

How do the positioning methods perform when double blunders are simulated? Figure 4-14 shows the double blunder results for the 30° mask case, for both receivers. In the single blunder case, limiting the blunders only improved the reliability results under unaugmented conditions. This is not true for the double blunder cases. For GLO24 and for both Galileo constellations with no constraints, limiting the blunders dramatically improves the results. Once the double blunders are limited, they are only slightly worse than the single blunder limited case. This should be expected, since the second blunder is limited to 4 m. The full GLO24 constellation in the unlimited case is significantly worse than the GAL24 or GAL30 constellations. The additional redundancy provided by the bigger Galileo constellations is required to detect the second unlimited blunder. A narrow correlator DGPS receiver augmented with either Galileo constellation and a height

constraint has a 95% MHE of less than 19 m under unlimited double blunder conditions. While this is less than the goal of 10 m it does indicate that reliable navigation is possible even under these extreme masking and blunder conditions.

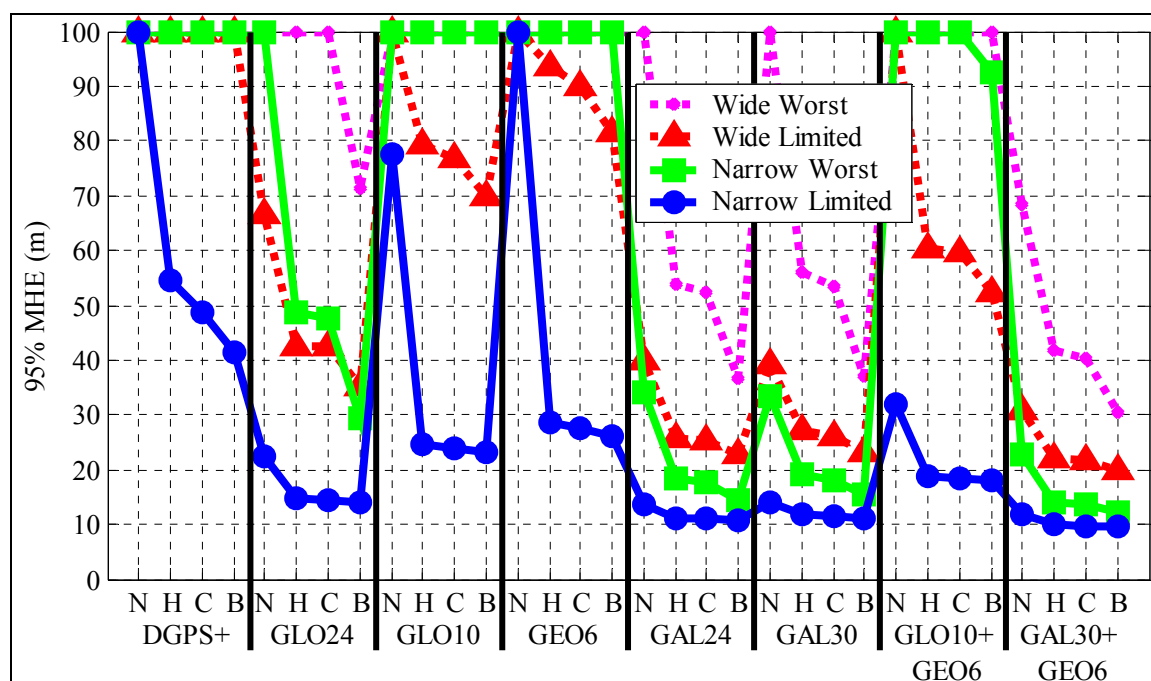


Figure 4-14 95% MHE, for the World, Double Blunder, Mask Angle 30°

4.2.5 Single Point GLONASS

The only augmentations that are currently available are the constraints and single point GLONASS. For comparison purposes DGPS, differential GLONASS (GLO10) and single point GLONASS (GLOSP) will be presented in this section. GLOSP was added by using the same constellation as GLO10, but with a measurement variance of 64 m. The purpose of this section is to quantify the improvements attained by augmenting the constellation in single point mode over DGPS alone and relative to differential GLONASS.

Figure 4-15 plots the 95% HDOP for the 12 positioning methods being used in this section. As expected GLOSP falls between DGPS and GLO10 due to the differences in

measurement variance. At the lower mask angles DGPS already has an extremely good HDOP, thus even the GLO10 augmentation cannot substantially improve it. The augmentation differences are visible at the 30° mask angle. GLO10 shows a noticeable improvement while GLOSP only marginally improves the results. GLO10 improves the HDOP by approximately 50% over DGPS, while GLOSP improves the HDOP by only 8%. For the 20° mask case, GLO10 improves the HDOP by approximately 20% while GLOSP improves the results by only 2%. From an availability standpoint the single point GLONASS augmentation does not dramatically improve the results.

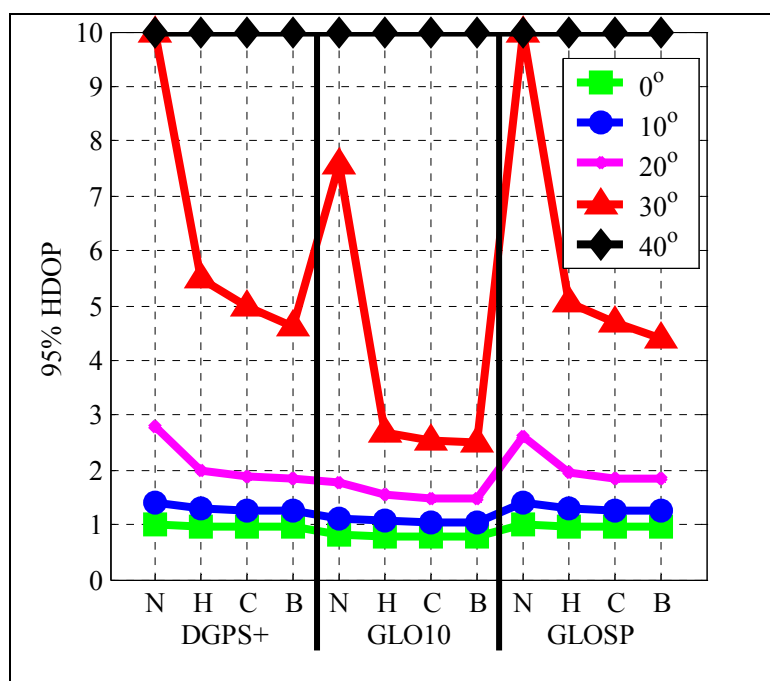


Figure 4-15 95% HDOP, for the World, Isotropic Mask Angles, with GLOSP

Figure 4-16 plots the 95% MHE for the 12 positioning methods. The same trends observed for the availability results are evident here. At the lower mask angles DGPS alone already has an extremely good reliability, thus even the GLO10 augmentation cannot substantially improve it. The differences become visible at the 20° mask angle. GLO10 improves the reliability by approximately 70% and once one constraint is added the 95% MHE drops below 10 m. GLOSP on the other hand only improves the results by

14% to 28%. When constraints are added the 95% MHE drops below 20 m, but it does not reach the 10 m goal. The high variance of the single point augmentation and the small GLONASS constellation prevents a dramatic improvement.

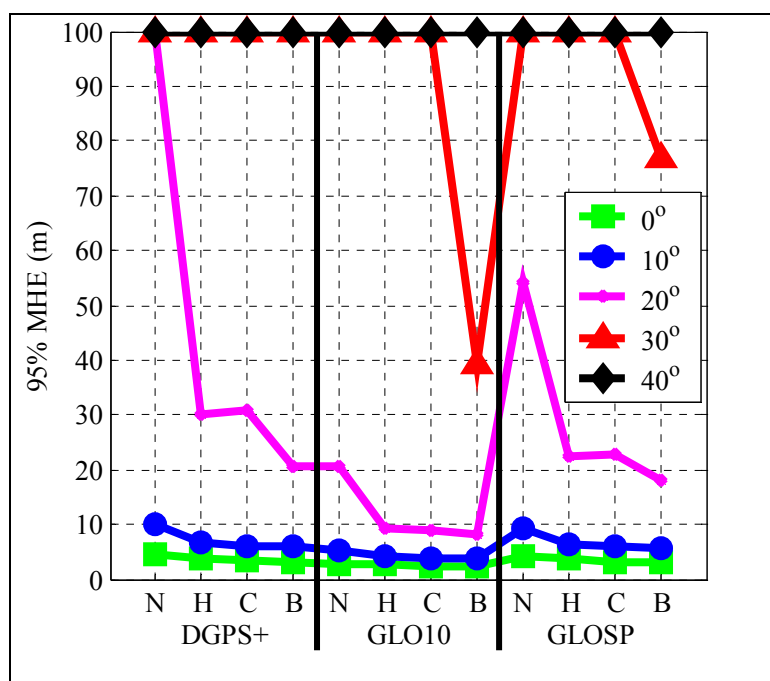


Figure 4-16 95% MHE, for the World, Isotropic Mask Angles, with GLOSP

Since the availability and reliability improvements attained with single point GLONASS are not dramatic, this augmentation will not be used in the remaining simulation sections.

4.3 Constricted Waterway Simulation

4.3.1 Software Simulation Description

The previous section simulated an isotropic masking environment from 0° to 40°. Another common masking scenario is the constricted waterway / urban canyon environment. The constricted waterway simulations were performed using the channel shown in Figure 4-17 oriented in a North / South direction. This channel was rotated 180° in 30° increments to simulate various orientations. Thus a total of six constricted

waterways were simulated and analysed. The shape of the constricted waterway defines the shape of the resulting masking profile, however, the scale of the masking profile must still be specified. Figure 4-18 shows the masking profile with the channel in the North / South orientation.

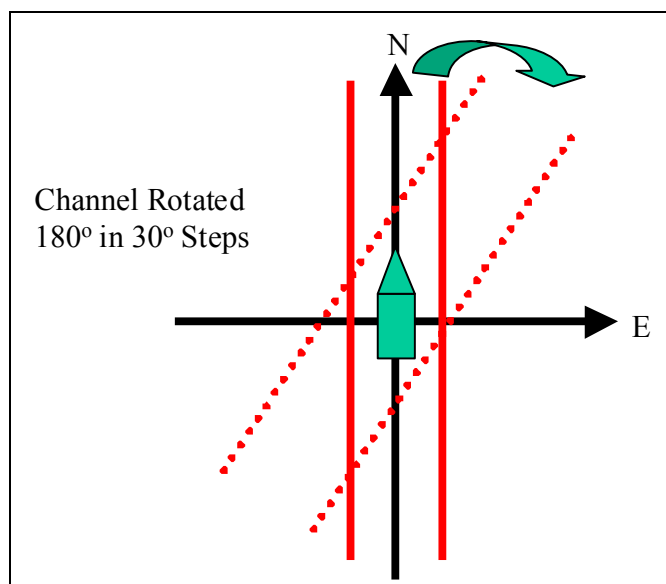


Figure 4-17 Simulated Constricted Waterway

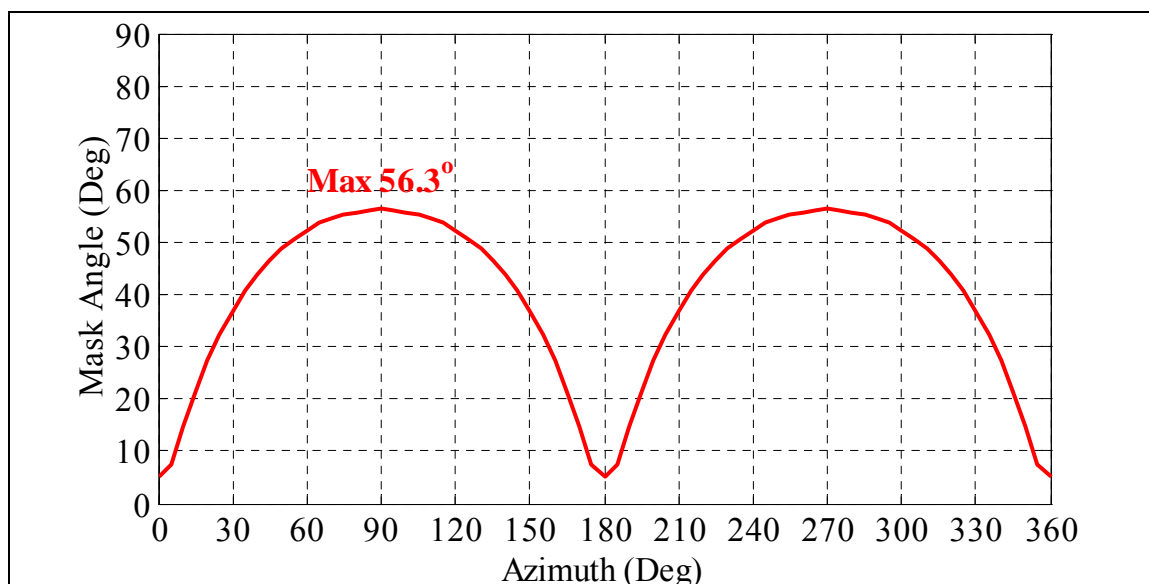


Figure 4-18 Constricted Waterway Mask Angle Profile

The maximum mask angle was set to 56.3° . While this is a very realistic simulation for down town urban canyons, general marine navigation in most constricted waterways will experience much lower masking angles. However, hydrographic surveys conducted near cliff walls will sometimes encounter these extreme masking conditions. Thus these simulations are applicable to both land and marine applications.

The results for the constricted waterway simulations are presented using the same format as the isotropic mask angle results. For each orientation of the constricted waterway (six orientations) and for all of the orientations batched together the 95% HDOP / MHE were calculated:

- 1) for each computation point
- 2) all 118 computation points batched together to generate world values

In addition the percentage of time that the $\text{HDOP} \leq 2$ and the $\text{MHE} \leq 10$ m were also calculated for the cases listed above.

4.3.2 Availability Results

A summary of the constricted waterway availability results for the world are given in Figure 4-19 and Figure 4-20. For each positioning method the 95% HDOP is plotted for each orientation of the constricted waterway (North / South = 0° , 30° , 60° , 90° , 120° , and 150°), with the results for all of the orientations batched together plotted as the solid line. When six data points are not identifiable for a specific case, it is because several points overlap. Figure 4-19 plots the overall world 95% HDOP, while Figure 4-20 plots the overall world percentage of HDOPs ≤ 2 .

The overall results are similar to the 40° isotropic mask angle case. DGPS and both constraints have a 95% HDOP > 10 with a corresponding availability of less than 12%. The partial constellations of GLO10 and GEO6 even with constraints cannot bring the 95% HDOP below 10. Combining GLO10, GEO6, and both constraints results in a 95% HDOP of 7.7 and an availability of 41%. The results for the full GLONASS constellation

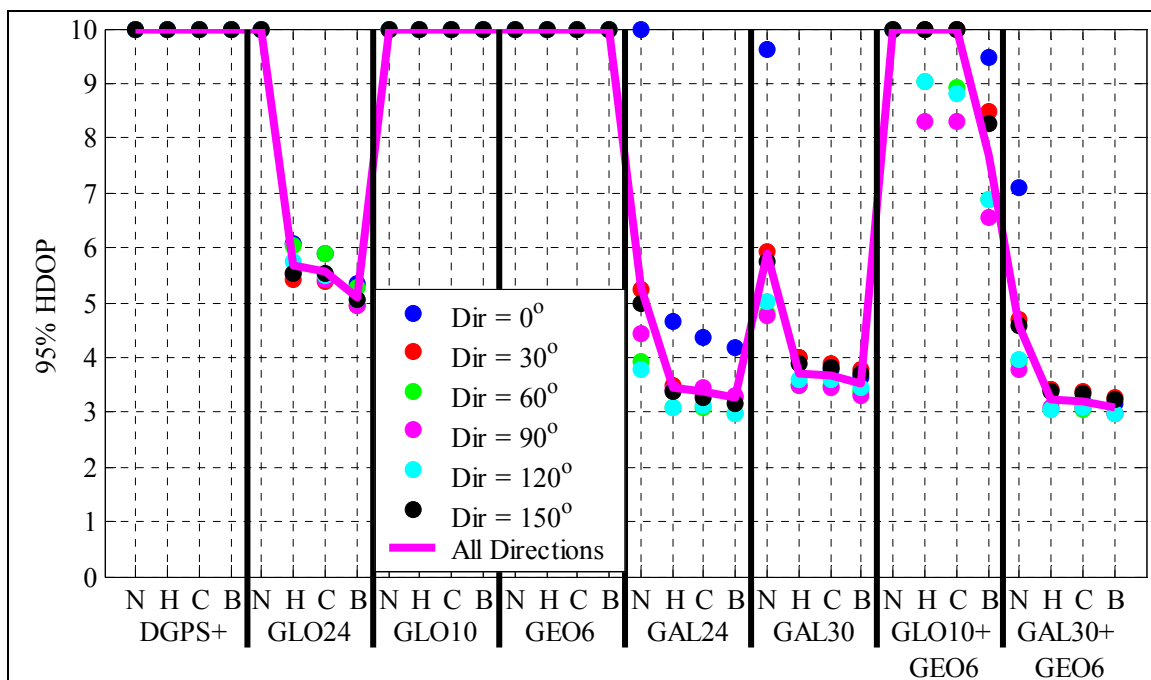


Figure 4-19 95% HDOP, for the World, Constricted Waterway

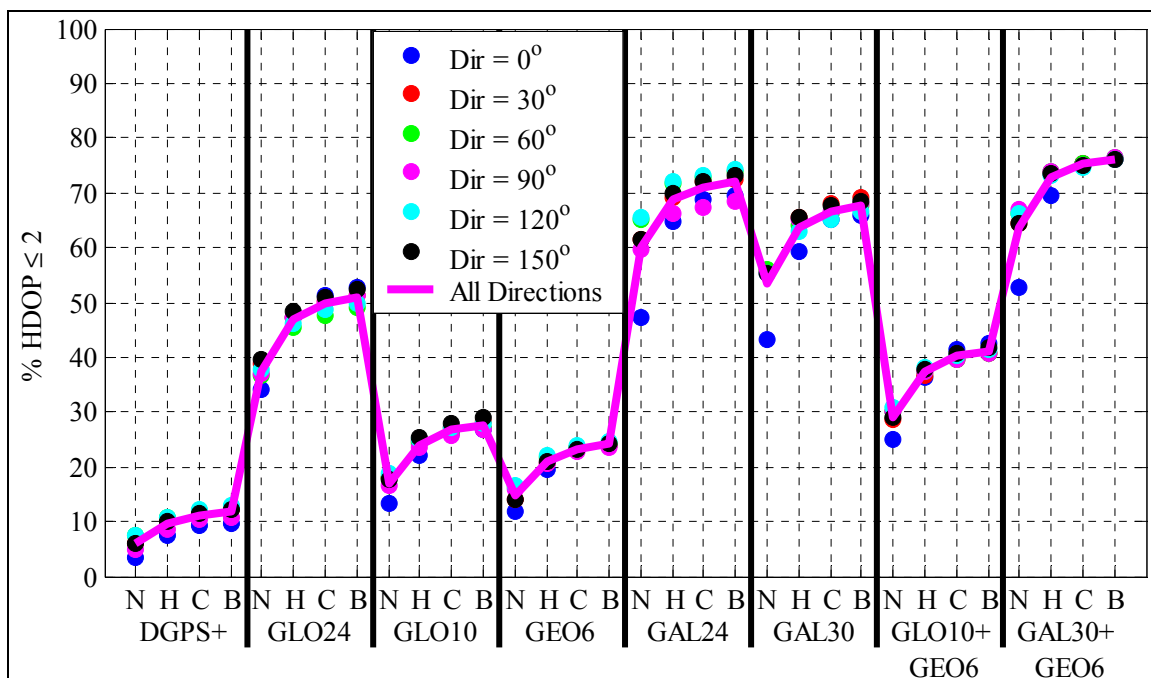


Figure 4-20 Percent HDOP ≤ 2, for the World, Constricted Waterway

GLO24 are not as good as the Galileo constellations. GLO24 with both constraints has an availability of 51% and a 95% HDOP of 5.1. Once either Galileo constellation is added, the results improve to a 95% HDOP of less than 5.9 with an availability of greater than 53%. If one constraint is also added to the DGPS + Galileo methods the HDOP drops below 4.0 and all of the orientations have similar results. While the availability target is not met under any of the augmentations, GAL30 with GEO6 comes the closest with a 95% HDOP of 3.1.

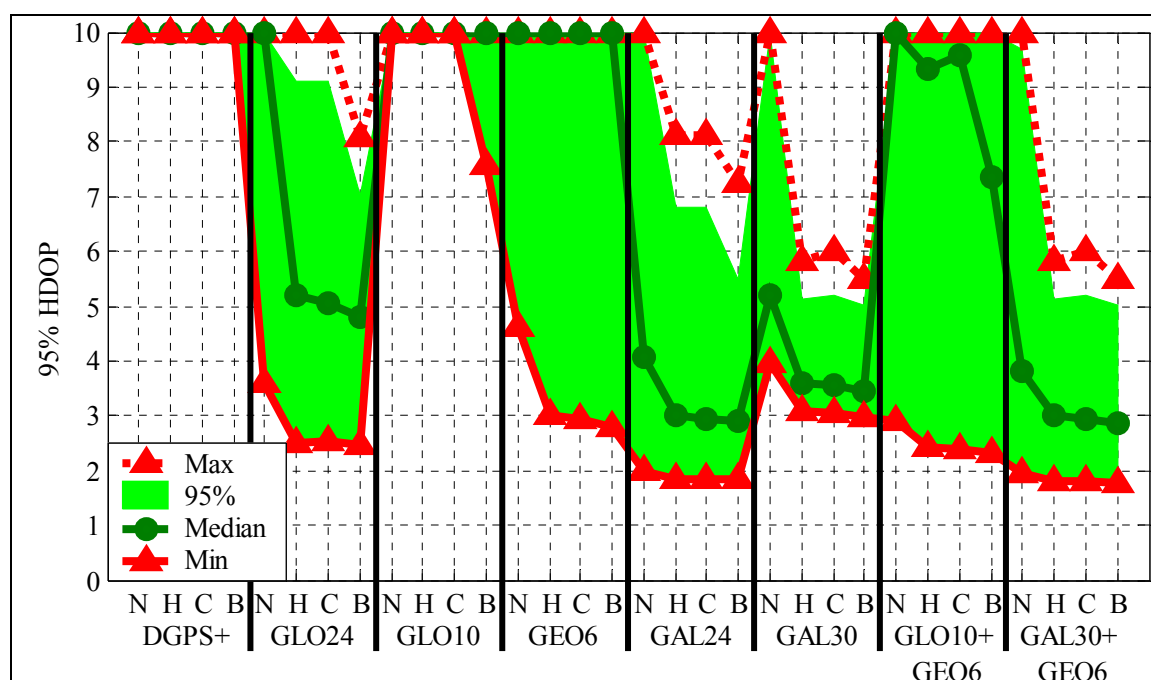


Figure 4-21 Computation Points Statistics, 95% HDOP, Constricted Waterway

In order to examine how the availability results varied with user location, the 95% HDOP statistics for the 118 computation points with all of the orientations batched together were analysed as shown in Figure 4-21. With unaugmented DGPS the 95% HDOP never drops below 10. Augmenting with GLO10 does little to improve the results. The surprising results occur from GEO6. Figure 4-19 shows that the results for GEO6 over the entire world is poor, however, Figure 4-21 shows that some locations have a 95% HDOP less than 3. This occurs for locations close to the equator, where the GEO elevation angle is

maximum. The full GLONASS constellation with constraints has a reasonable minimum value of approximately 2.5, however the maximum value is still > 10 . When DGPS is augmented with GAL24 and constraints the 95% HDOPs ranged from a low of 1.8 to a high of 7.2 with 95% of the locations being less than 5.5. When DGPS is augmented with GAL30 and constraints the 95% HDOPs ranged from a low of 2.9, to a high of 5.5 with 95% of the locations being less than 5.0. Thus GAL30 produces more balanced results when compared with GAL24.

4.3.3 Reliability Results

A summary of the constricted waterway reliability results for the world are given in Figure 4-22 and Figure 4-23. Figure 4-22 plots the overall world 95% MHE, while Figure 4-23 plots the overall world percentage of $MHE \leq 10$ m. Like the availability results the reliability results are very similar to the 40° isotropic mask case. Even augmenting DGPS with both partial constellations GLO10 and GEO6 cannot bring the 95% MHE below

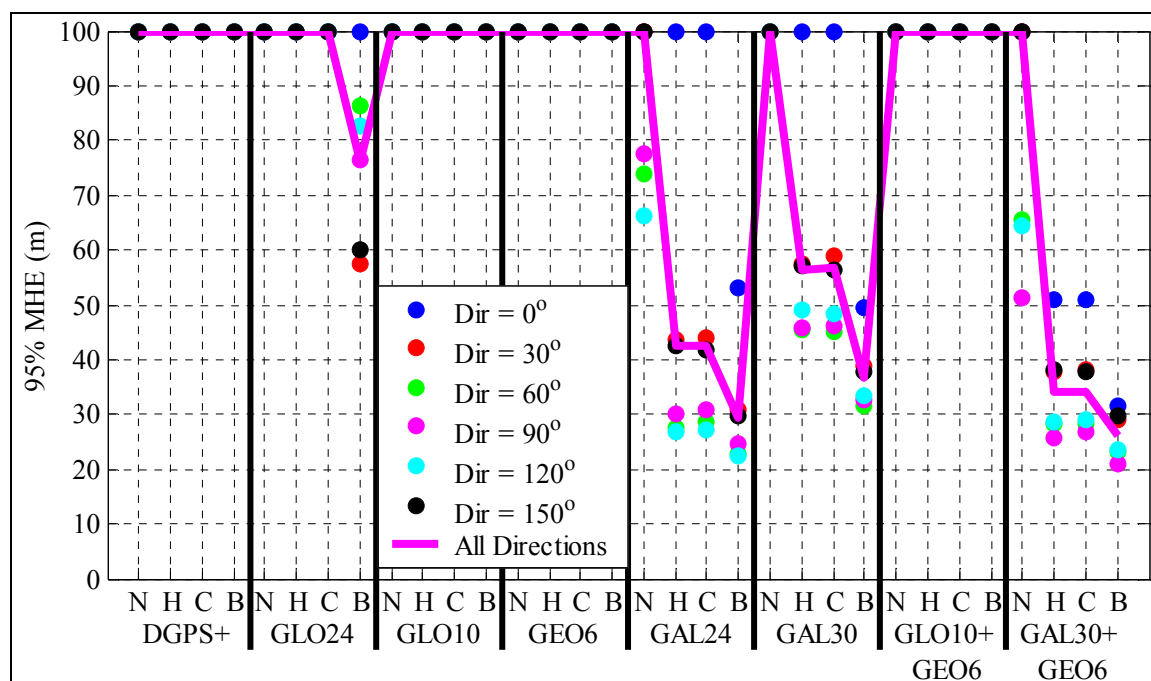


Figure 4-22 95% MHE, for the World, Constricted Waterway, $\sigma^2 = 1 \text{ m}^2$

100 m. The maximum reliability of this augmentation combination is 28%. The full GLONASS constellation requires both constraints in order to bring the 95% MHE below 100 m, and even then it only reaches 76.2 m. The Galileo augmentations increase the reliability to 68% and 60% for GAL24 and GAL30 respectively. While GAL24 with both constraints has a higher reliability than GAL30, there is a 11% variations between channel orientations, while with GAL30 there is only a 3% difference between channel orientations. The most augmented case of GAL30 and GEO6 has a 95% MHE of 26.3 m and a reliability of 72%. Although this does not meet the reliability goal of 10 m 95%, it does mean that reliable navigation is possible during certain times of the day.

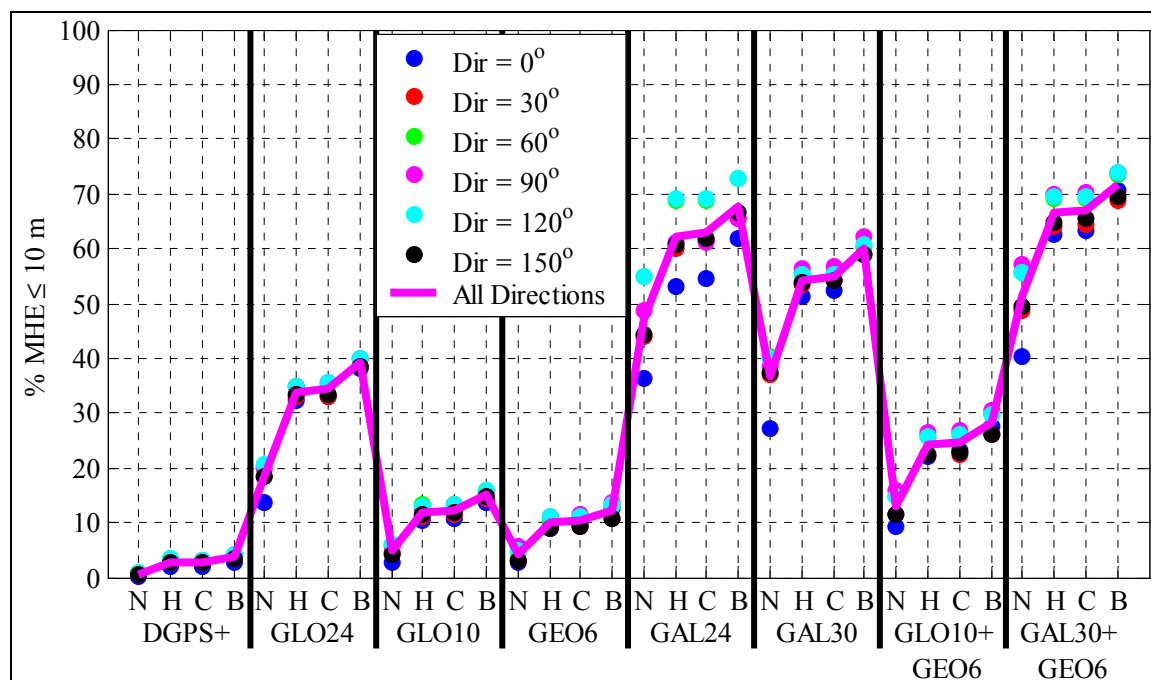


Figure 4-23 Percent MHE ≤ 10 m, for the World, Constricted Waterway, $\sigma^2 = 1 \text{ m}^2$

In order to examine how the reliability results varied with user location, the 95% MHE statistics for the 118 computation points with all of the orientations batched together were analysed as shown in Figure 4-24. When DGPS is augmented with GAL24 and constraints the 95% MHE ranged from a low of 10.9 m to a high of > 100 m with 95% of the locations being < 97.4 m. When DGPS is augmented with GAL30 and constraints the

95% MHE ranged from a low of 25.1 m, to a high of 68.6 m with 95% of the locations being < 56.5 m. Again GAL30 the MEO only constellation tends to moderate the results, with higher minimum values and lower maximum values.

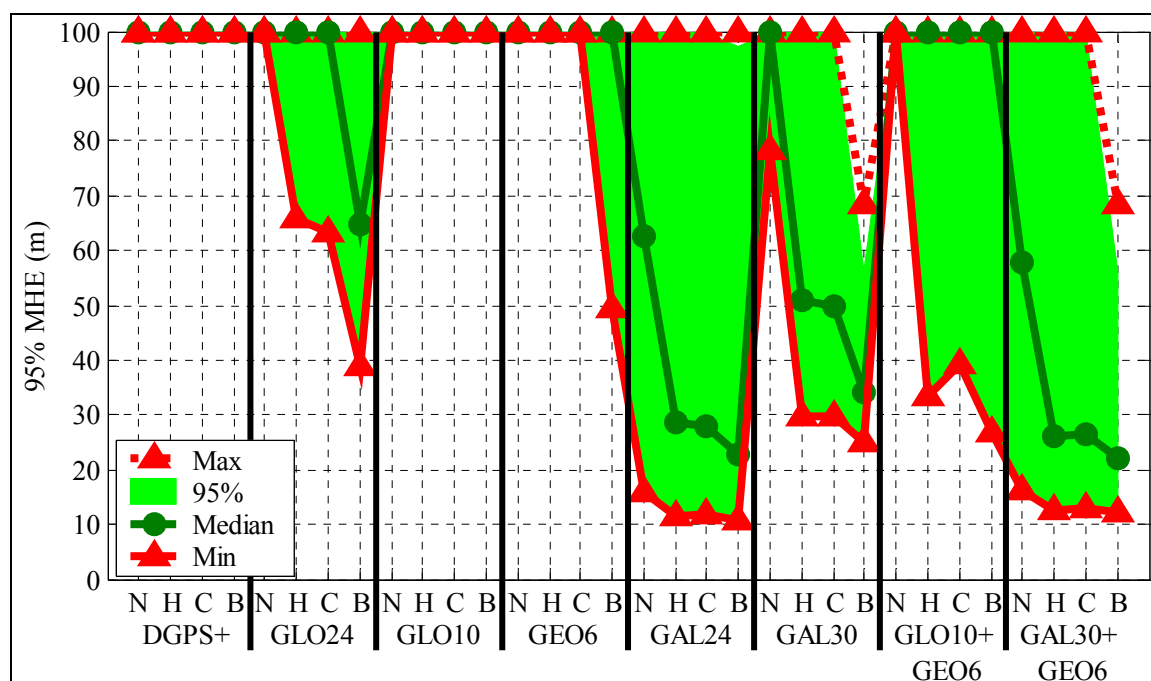


Figure 4-24 Computation Points Statistics, 95% MHE, Constricted Waterway

4.4 Hydrographic Surveying using a Kalman Filter

4.4.1 Simulation Description

The previous simulations used least squares to generate the HDOP and MHE values. This simulation takes a different environment, a hydrographic survey, and uses least squares as well as a Kalman filter to generate the HDOP and MHE. This simulation is loosely based on the field campaign discussed in CHAPTER 7. The four Kalman filters described in Table 2-16 of section 2.9 will be used for this simulation.

The simulation was conducted over 24 hours in 60 second increments, using the July 25, 1997 GPS and GLONASS almanacs. Vancouver Island, British Columbia was used as

the simulation location (48° N, 123° W). The time and location were chosen to match the field campaign. DGPS (25 satellites) was augmented with two additional satellite systems, namely GLONASS (15 satellites) and GEO (6 satellites). Height, clock, and dynamic constraints were also used. The additional satellite systems were added in differential mode as DGLO (differential GLONASS) and DGEO (differential GEO satellites). For this simulation the following four satellite constellation combinations were simulated:

- 1) DGPS
- 2) DGPS + DGLO
- 3) DGPS + DGEO
- 4) DGPS + DGEO + DGLO

For each satellite constellation combination, the following four types of constraints were employed:

- 1) No Constraints – “N”
- 2) Height Constraint – “H”
- 3) Clock Constraint – “C”
- 4) Both Height and Clock Constraints – “B”

For each of these 16 cases, the four Kalman filters and standard least squares were applied. Thus a total of 80 positioning cases were simulated.

A measurement variance of 1 m^2 was used for all observations, hence a narrow correlator receiver was assumed. The least squares height and clock constraints used variances of 4 m^2 and 1 m^2 respectively (the same as the previous simulations). The Kalman filter's clock constraint was implemented by changing the clock's process noise values. When the clock constraint was applied, the process noise for a Rubidium oscillator was used, otherwise the process noise for a crystal oscillator was used. Table 2-15 lists the process noise values for both oscillators.

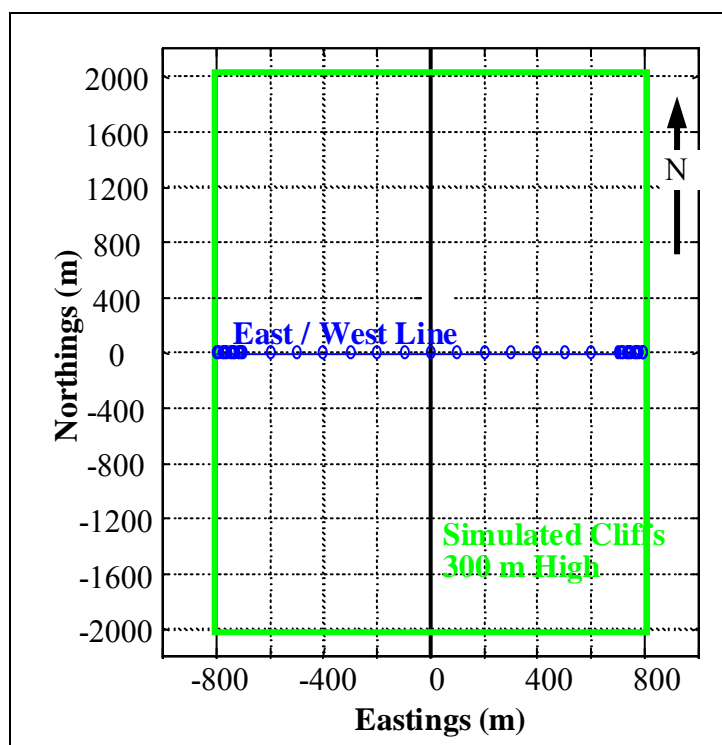


Figure 4-25 Simulated Survey Line

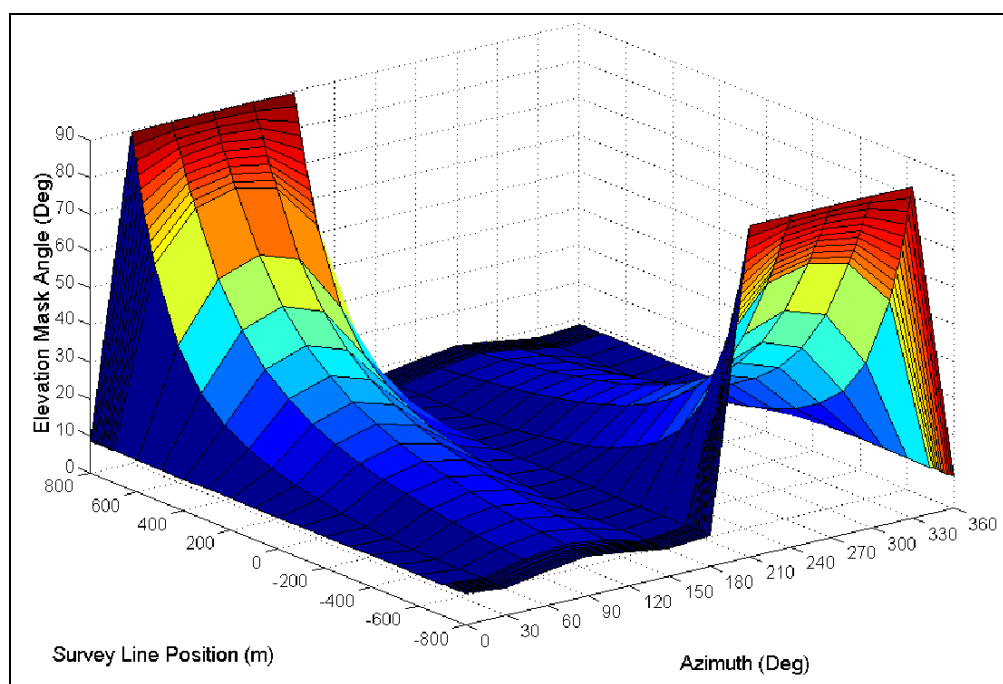


Figure 4-26 East / West Survey Line Mask Profile

An east - west survey line was analysed for a simulated inlet 1600 m by 4000 m with 300 m high cliffs, as shown in Figure 4-25. Satellite visibility ranged from excellent (elevation mask angle $< 10^\circ$) in the centre of the inlet to poor (180° signal masking) near the cliffs. Figure 4-26 shows the masking profile for the east west survey line. The circles indicate the computation points for the survey line. As the survey launch approaches the cliffs, the computation point spacing is shortened in order to increase the resolution of the results. For each epoch, the Kalman filter was first initialised ($(C_{\hat{x}}^-)^{-1} = 0$), and then iterated to steady state. The MHE was generated from the MDB of each observation, using the steady state filter parameters. The underlying assumption is that the MDB did not bias the filter prior to detection. Therefore a “step” blunder is being simulated.

4.4.2 Results

If all of the simulation results were to be presented, a four dimensional figure would be required (positioning method, survey line location, time, and HDOP / MHE). Instead of presenting the entire time series of HDOP and MHE values, the 95% results are presented. Thus for each survey line position and positioning method the 95% HDOP and MHE are plotted using contour graphs. The survey line position is plotted along the y-axis. Thus 800 m corresponds to the east cliff wall, and -800 m corresponds to the west cliff wall. The positioning methods are shown on the x-axis. The positioning cases are grouped according to the satellite constellations and Kalman filter employed.

It was impractical to show all 80 positioning cases on the same figure. Thus several contour graphs are presented illustrating the various positioning cases. For comparison purposes the least squares results for DGPS + constraints and DGPS + DGLO + DGEO + constraints are presented with the Kalman filtering results.

Figure 4-27 shows the availability results for least squares, and each Kalman filter augmenting DGPS. The four filters give almost identical results. A slight availability improvement is noticeable between the first and fourth filters, however, they are

essentially identical. When the filter's constraints are compared there is only a slight improvement between no constraints and the clock constraint. This is due to the fact that a clock constraint is always being applied, under no constraint a crystal oscillator is used while for the clock constraint a Rubidium oscillator is used. The Rubidium oscillator improves the availability in the middle of the channel, but only shows minor improvement at the cliff walls. The minor improvements along the cliff wall are due to the simulation assumption that the filter is initialised for each epoch. Thus if only three observations are available for a given epoch the filter cannot determine the initial clock bias and therefore can never generate a position, regardless of the clock's accuracy. This is also the reason why the least squares clock constraint performs better than the Kalman filter's clock constraint. In the least squares simulations the clock constraint is added as a quasi-observable, hence it assumes that the initial clock bias is known. However, the filter starts with no a priori knowledge of the clock bias. The different assumptions cause

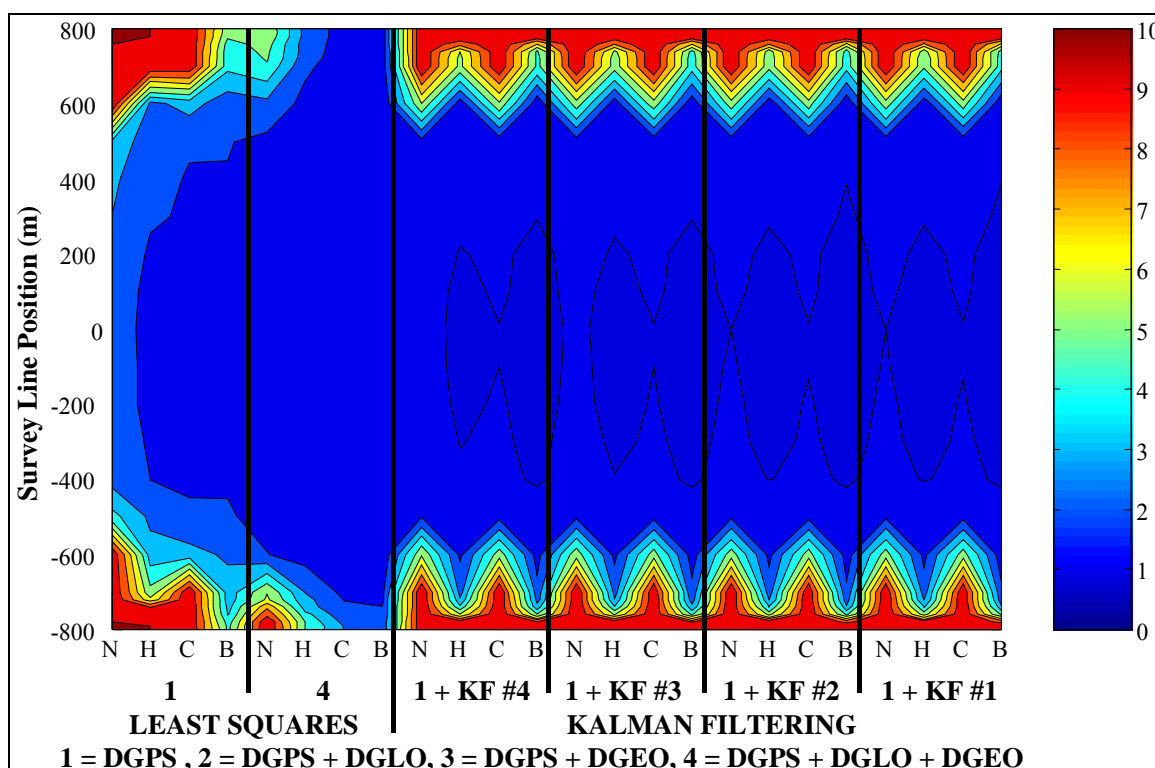


Figure 4-27 East / West Line - HDOP 95% - DGPS & All Kalman Filters

the difference in results. The addition of the Kalman filter slightly improves the availability of DGPS alone and DGPS with a height constraint.

Figure 4-28 now compares least squares with Kalman filter #4. Once the Kalman filter is augmented with at least one additional satellite system, the results are almost equivalent to the most augmented least squares case. When the most augmented Kalman filter case is examined, the 95% HDOP is less than 2.0 next to the cliff. The corresponding most augmented least squares case has a 95% HDOP less than 4.0. While a HDOP of 4.0 may meet some operational requirements the marine availability standard is 2.0. Thus the addition of the Kalman filter makes navigation available, even close to the cliff.

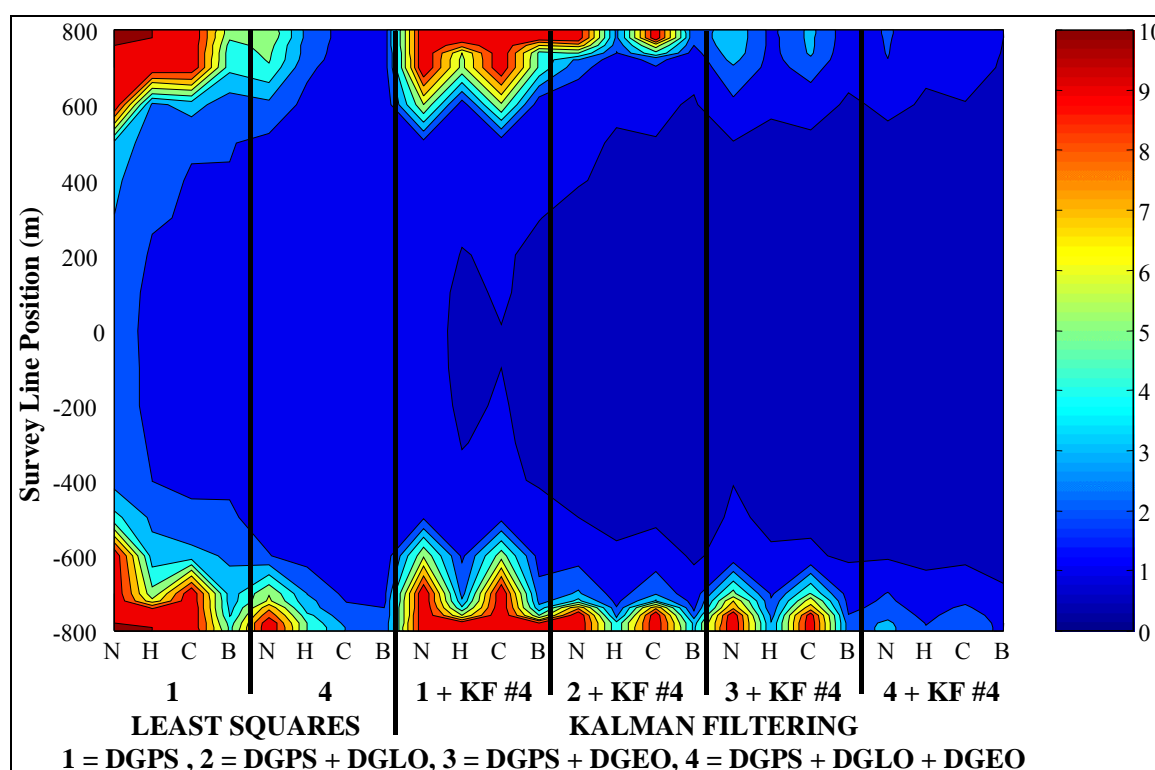


Figure 4-28 East / West Line - HDOP 95% - DGPS & Kalman Filter #4

The reliability results for the four Kalman filters were again almost identical to each other, therefore, only the reliability results for Kalman filter #4 are presented in Figure 4-29. In the most augmented least squares case the 95% MHE is less than 25 m next to

the cliff, and is less than 10 m when the launch is 100 m from the cliff wall. The Kalman filter only needs to augment DGPS with one additional satellite system and the constraints to exceed these results. The most augmented Kalman filter case has a 95% MHE of less than 10 m next to the cliff. The addition of the Kalman filter is almost equivalent to adding an additional satellite system. The most augmented Kalman filter case allows reliable positioning throughout the entire survey line. However, one word of caution, these results assumed that the blunder did not bias the filter prior to detection. The results may be different if a different blunder type (i.e. slow ramp) was simulated. For the “step” blunder simulated herein, the filter improves the availability and greatly enhances the reliability.

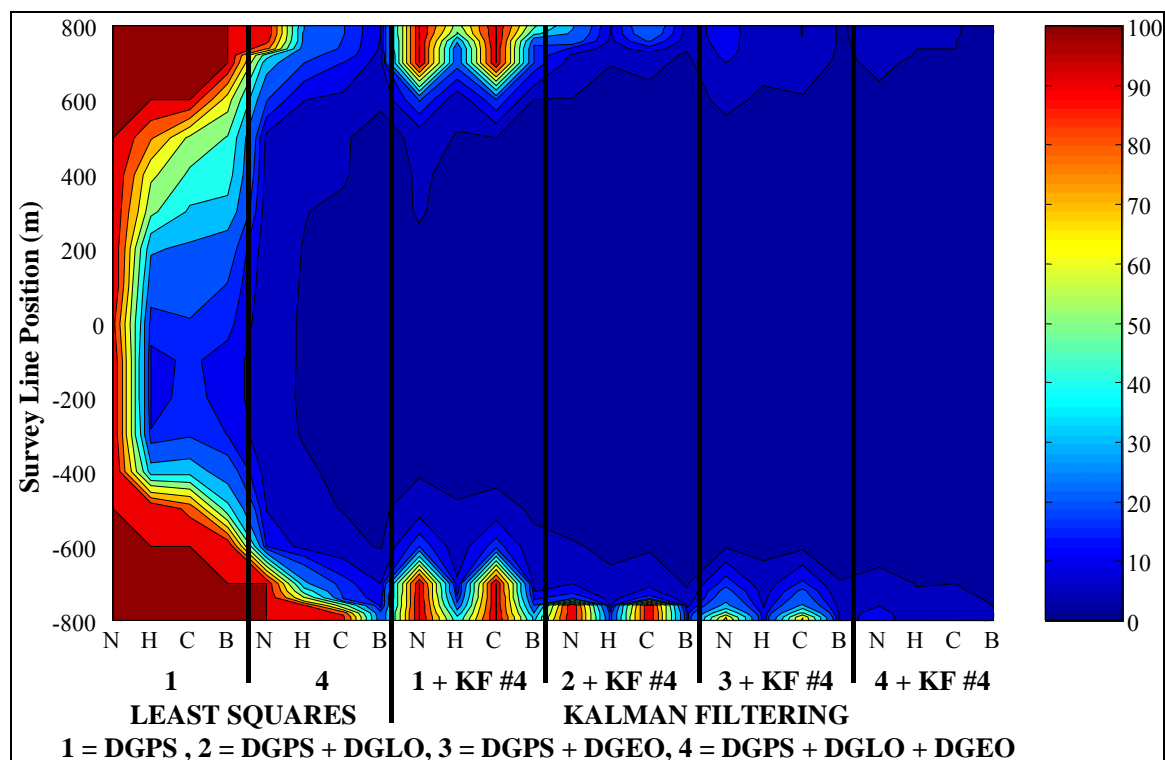


Figure 4-29 East / West Line - MHE 95% - DGPS & Kalman Filter #4

CHAPTER 5

STATIC DATA ANALYSIS

5.1 *Introduction*

Before the results from the DGPS signal simulator and the field campaign in Saanich Inlet, Vancouver Island are presented, the results from a one hour static test conducted on November 17, 1997 at the University of Calgary will be presented. This controlled environment will validate the processing software, DGPS augmentations, and the GPS GLONASS receiver used for the Saanich Inlet test.

The two Ashtech GG24™ receivers used during the Saanich Inlet test were installed on the roof of the engineering building at the University of Calgary. One hour of data was collected and processed using the University of Calgary's C³NAVIG²™ software package. At the time there were 25 healthy GPS satellites and 15 healthy GLONASS satellites. In order to validate the reliability improvement attained through augmentation, simulated pseudorange blunders were superimposed on each tracked GPS satellite (PRN # 1, 5, 7, 14, 15, 21, 25, 29, and 30), one at a time. Figure 5-1 shows the four ramping errors that were added to the data. The error was ramped at 0.5 m/s until it reached a maximum of 50 m, held at 50 m for 100 s and then ramped back down to zero at -0.5 m/s. Each blunder lasted 300 s, thus 1200 s of biased measurements were introduced to each satellite. The data was processed nine times, once for each satellite's blunder. The isotropic mask angle was varied from 5° to 20° in 5° increments. The following six positioning methods were employed:

- 1) DGPS alone
- 2) DGPS and a height constraint

- 3) DGPS and single point GLONASS
- 4) DGPS, single point GLONASS, and a height constraint
- 5) DGPS and DGLO
- 6) DGPS, DGLO, and a height constraint

C³NAVIG²TM was used with an epoch by epoch least squares reliability algorithm. The sum squared residuals (SSR) were tested using global α_g , β_g , and λ values consistent with the local $\alpha_1 = 0.1\%$, $\beta_1 = 10\%$, and $\delta_0 = 4.57$ values used in CHAPTER 4. Thus $\beta_g = \beta_1$, $\lambda = \delta_0^2$, and α_g varied with the epoch's redundancy. For each epoch the resulting HPE will be analysed as a measure of the augmentations reliability.

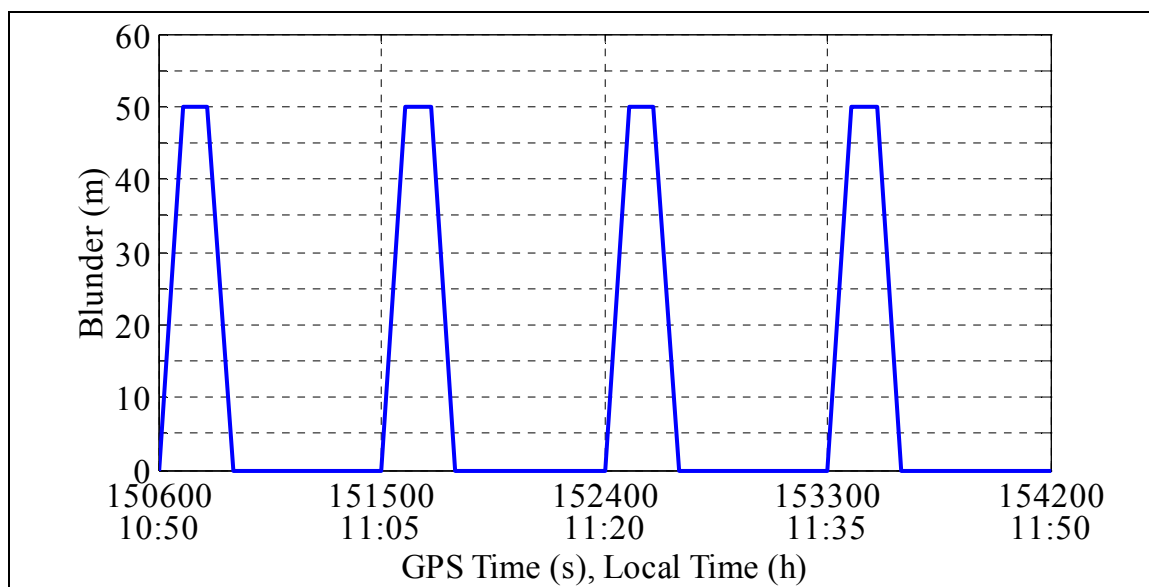


Figure 5-1 Blunder Introduced on Each GPS Satellite

5.2 Results

Figure 5-2 shows the HPE that occurred when the reliability checking was disabled using a 15° mask angle and the blunder was applied to PRN 1. Although the magnitude of the blunder was the same for the four ramps, the HPE varies due to the changing geometry. As expected, when DGPS is augmented the magnitude of the HPE is decreased. Even in the most augmented case (DGPS + DGLO + Height) the maximum HPE exceeded 25 m.

Although one would normally expect reliability checking to be enabled, many commercial marine DGPS receivers do not use any reliability checking. CHAPTER 6 addresses the reliability checking of marine receivers. Without reliability checking a blunder can play havoc with marine positioning.

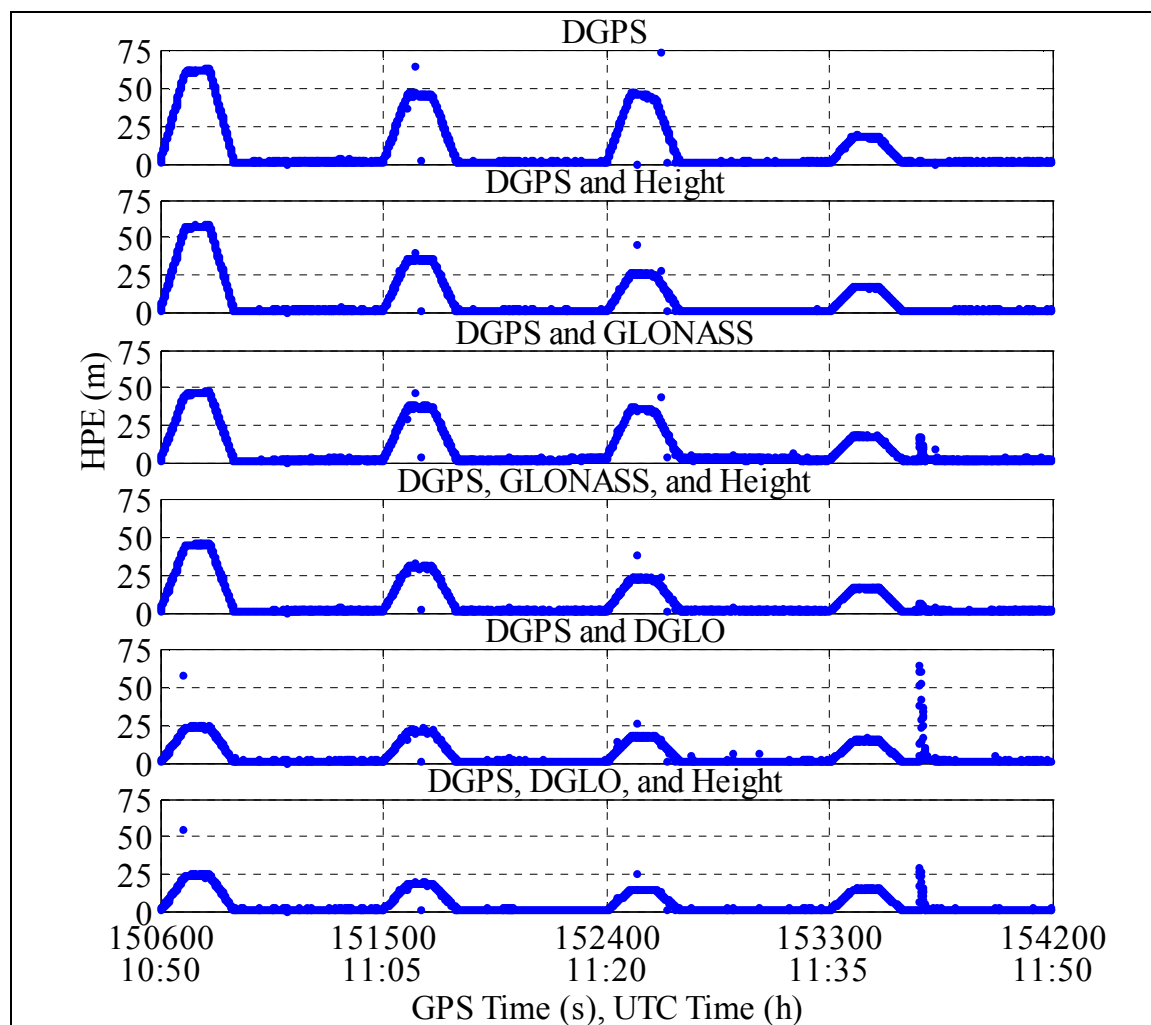


Figure 5-2 HPE - 15° Mask Angle - Ramp on PRN 1 Reliability Disabled

Figure 5-3 shows the results when the same data is analysed with reliability checking enabled. DGPS alone has difficulty detecting the first ramp, but the subsequent ramps are correctly detected and isolated. When single point GLONASS was added it greatly improved the performance during the first ramp however the blunder was undetected at

the beginning and end of the ramps. Once DGLO was added the ramping errors are caught almost immediately, and the impact on the HPE is negligible. For all of the methods, the performance in the latter three ramps is much better, which is consistent with the previous figure.

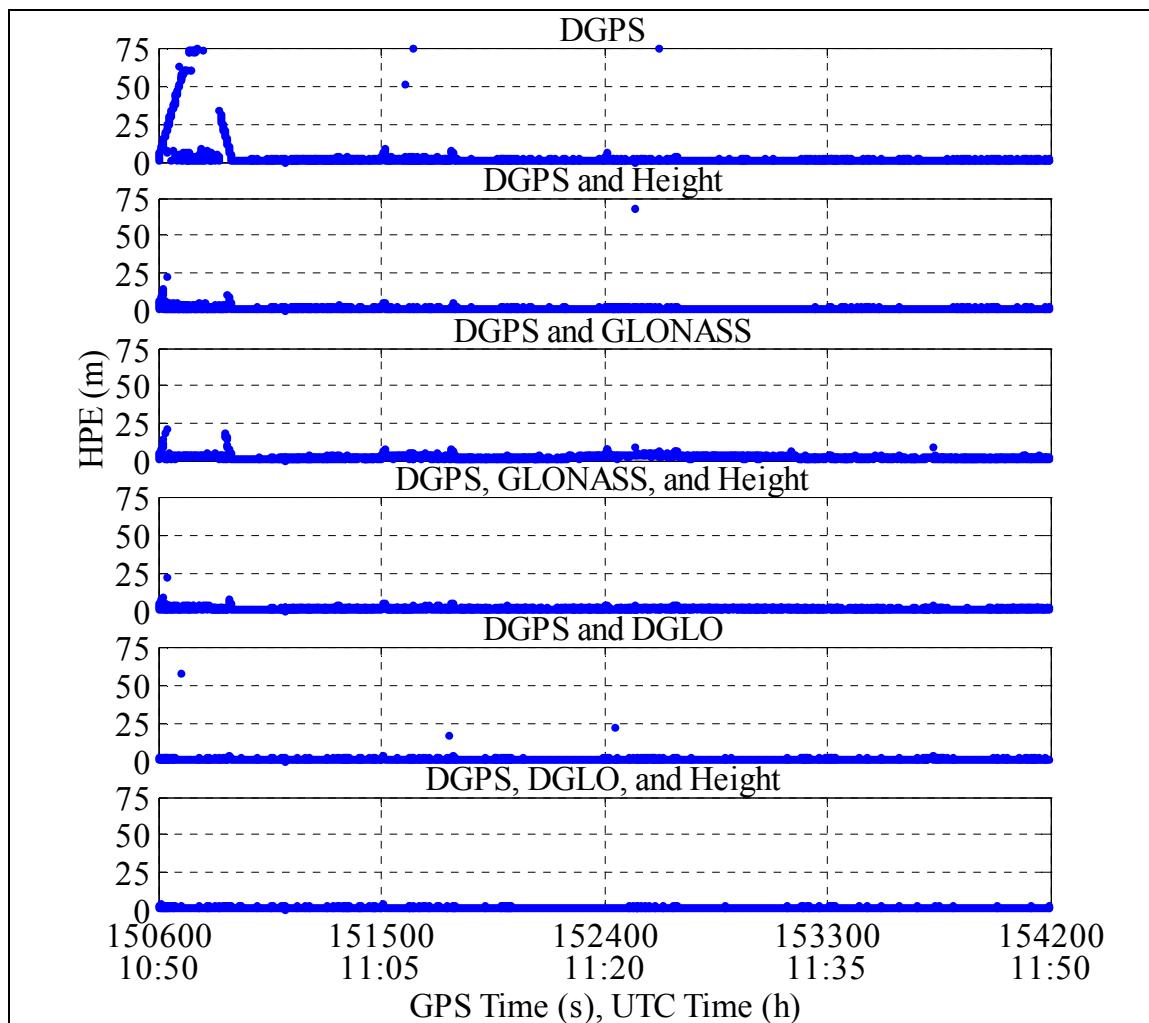


Figure 5-3 HPE - 15° Mask Angle - Ramp on PRN 1 Reliability Enabled

Figure 5-4 shows a close up of the first ramp to help emphasise the fault detection capabilities of the six positioning methods. Three things are evident from these graphs. First as DGPS is augmented the time taken to detect the error is shortened. Second, even before the error is detected, the magnitude of the HPE is reduced. Finally, since an epoch

by epoch reliability algorithm was implemented there are several spikes in the HPE indicating that the biased satellite could not be detected. Once DGLO is added the error is quickly detected as indicated in the figure.

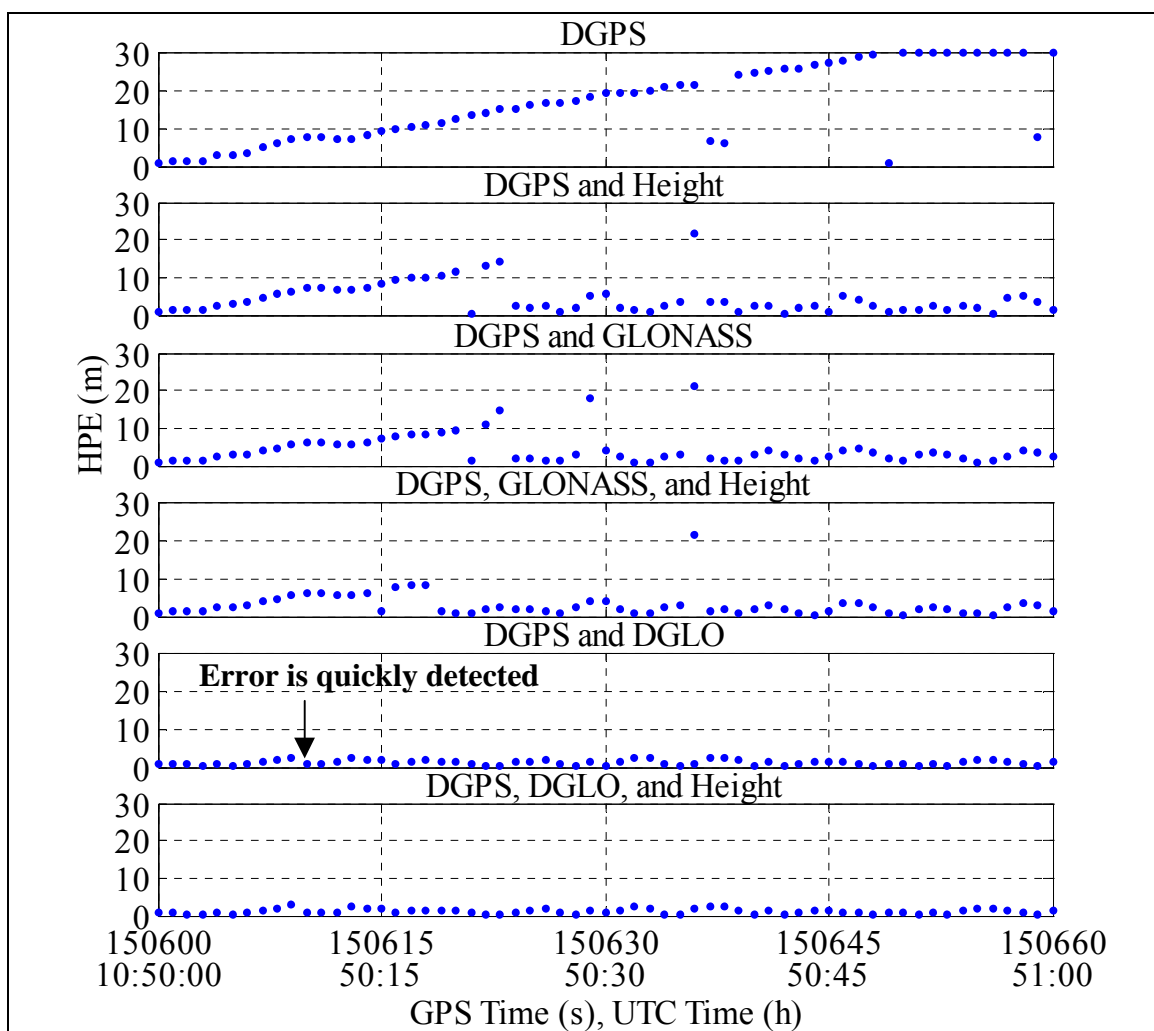


Figure 5-4 HPE - 15° Mask Angle - Ramp on PRN 1 Reliability Enabled

The previous results only reflect the ramp error on PRN 1 and a 15° mask angle. The other mask angles and GPS satellites were also analysed, but will not be presented individually. Figure 5-5 summarises the results for all of the mask angles, and all of the satellites during the first ramp. At the lower mask angles of 5° and 10° the improvement in HPE is not dramatic. Augmenting DGPS improves the reliability of the positions, but

not significantly. For instance the 95% HPE varies from 2.2 m to 1.4 m from the least to the most augmented case using a 10° mask angle. However, at the 15° mask angle the results are more significant. The DGPS 95% HPE is > 10 m while the DGPS with DGLO is 1.5 m. This follows the same trends that were seen in the simulation results, that is, the real benefit of the augmentations occur during high masking conditions. While augmenting with single point GLONASS improves the HPE, the height constraint outperforms it every time. It is really only once GLONASS is added in differential mode that it has a dramatic effect on the HPE. Therefore single point GLONASS will not be used as an augmentation in CHAPTER 7.

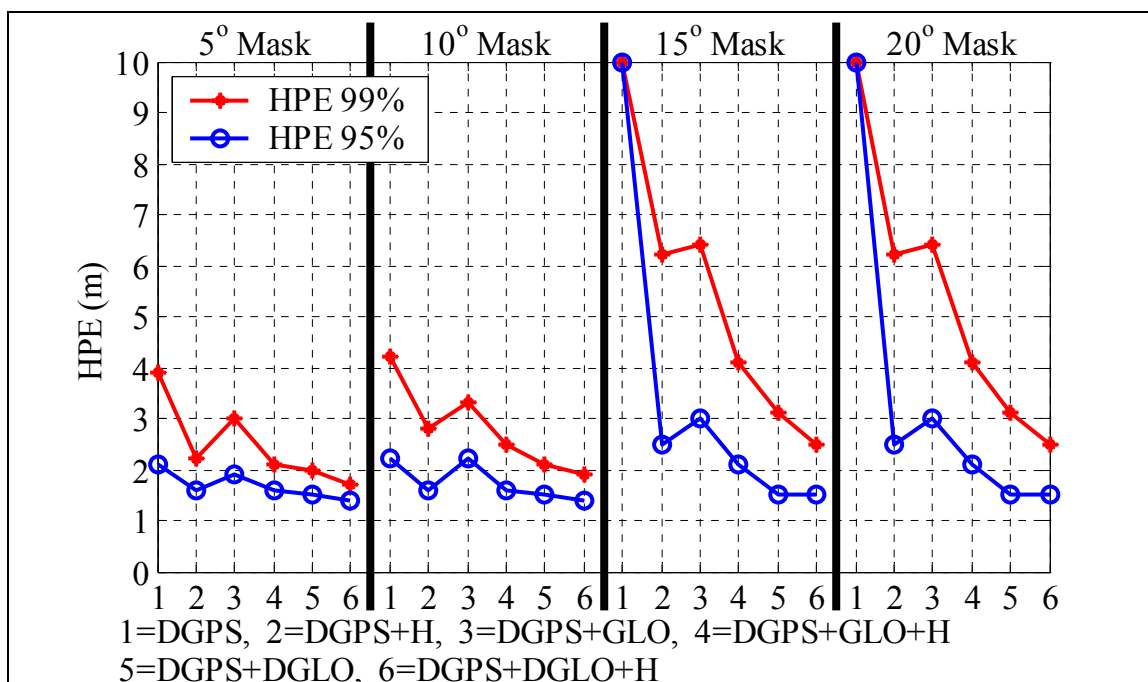


Figure 5-5 HPE - Four Mask Angles - Six Positioning Methods Reliability Enabled

This static test validates both the processing software and the Ashtech GG24™ receiver that will be used in CHAPTER 7.

CHAPTER 6

GPS SIGNAL SIMULATOR DATA ANALYSIS

6.1 Introduction

CHAPTER 4's software simulations illustrated the inherent danger when only precision is examined and reliability is ignored. The HPE results from CHAPTER 5 demonstrated how a simple reliability algorithm could detect a range error. The next question that needs to be answered is; Do DGPS user receivers employ a real time reliability algorithm? To answer this question four marine user DGPS receivers were tested using a Global Simulation Systems (GSS) DGPS signal simulator. The four receivers that were tested are as follows:

NovAtel OEM3: The NovAtel OEM3 is a dual frequency survey grade GPS receiver. It is regularly used in high accuracy applications, such as hydrographic surveying, but is not normally used for general navigation. It was included in this test as the control receiver. During the test the NovAtel was operated in narrow correlator mode.

CSI GBX-Pro: The CSI GBX-Pro is an integrated DGPS sensor, with a dual frequency CSI radiobeacon receiver integrated with an Ashtech G12™ GPS engine. The Ashtech G12™ engine is the GPS only equivalent to Ashtech's GG24™ GPS GLONASS receiver discussed in section 2.5.4. This receiver is used by professional navigators wanting superior performance from their navigation suite. During the test it was operated with its Edge™ correlator.

MX-9212: The MX-9212 is an older DGPS sensor manufactured by Magnavox in the early 90's. It was state of the art technology when it was first introduced and was

used as the reference station and integrity monitor during the CCG's DGPS system development. While this receiver has been replaced by newer Leica products (Magnavox was taken over by Leica), it was tested to gauge the difference between different generations of products. This receiver is assumed to employ a wide correlator.

Northstar 941: The Northstar 941 is an integrated DGPS navigation receiver, with a radiobeacon receiver and a CMC Allstar GPS engine. The unit contains a very user friendly interface and is often used for recreational boating, and commercial shipping. This receiver is assumed to employ a wide correlator.

The GPS simulation lasted 75 minutes with each user receiver following the trajectory shown in Figure 6-1. The test was run in differential mode with the real time corrections being transmitted by a CCG DGPS reference station. A fairly benign environment was simulated with SA and AS off, no satellite clock or ephemeris errors, and the sea state ranged from 0 to 3. During the straight portions of the trajectory the ship moved at a constant speed of 36 km/h except for the affects of the sea state model. The ship

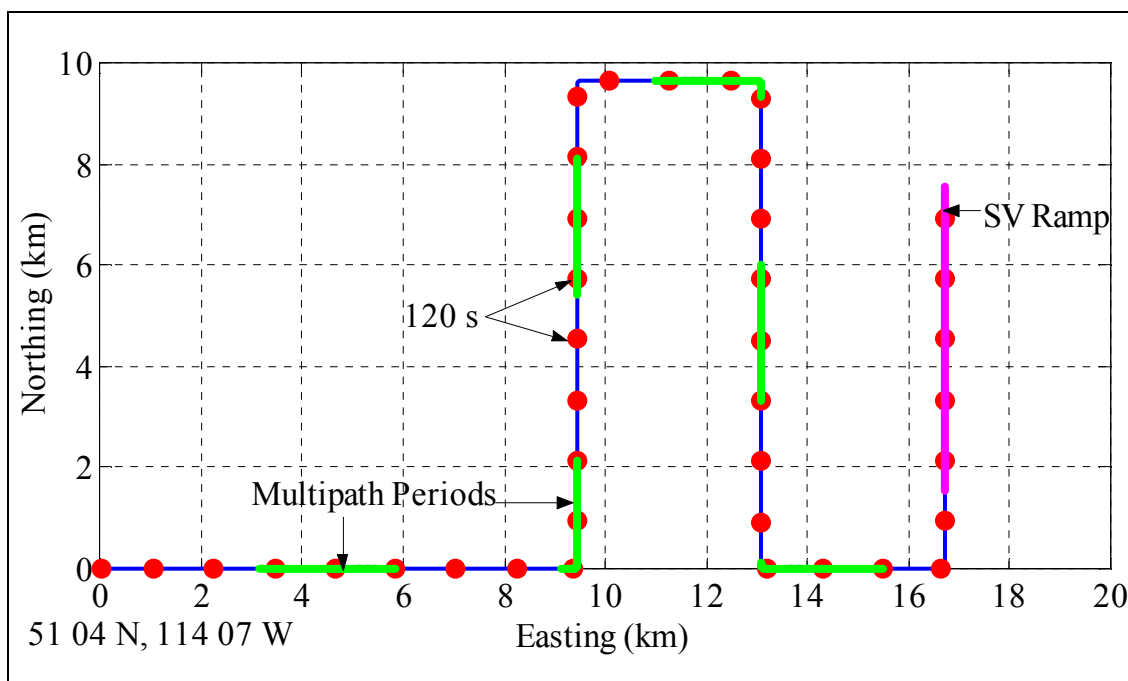


Figure 6-1 Ship Test Trajectory

decelerated into the turns and accelerated out of the turns. Figure 6-1 also shows where the six multipath periods were in the simulation. Just prior to the multipath being added to PRN 8, its signal was turned off for 30 seconds, thereby limiting the performance of carrier smoothing. During the last 10 minutes of the test a slow satellite clock ramp was added to PRN 8.

Figure 6-2 shows the number of visible satellites above a 5° mask angle, the resulting HDOP, and MHE ($\sigma^2 = 1 \text{ m}^2$ and $\delta_0 = 4.57$) for the simulation. This time period was chosen due to its high level of redundancy and low MHE. The user receivers will be able to easily detect the multipath blunders if they employ a real time reliability algorithm.

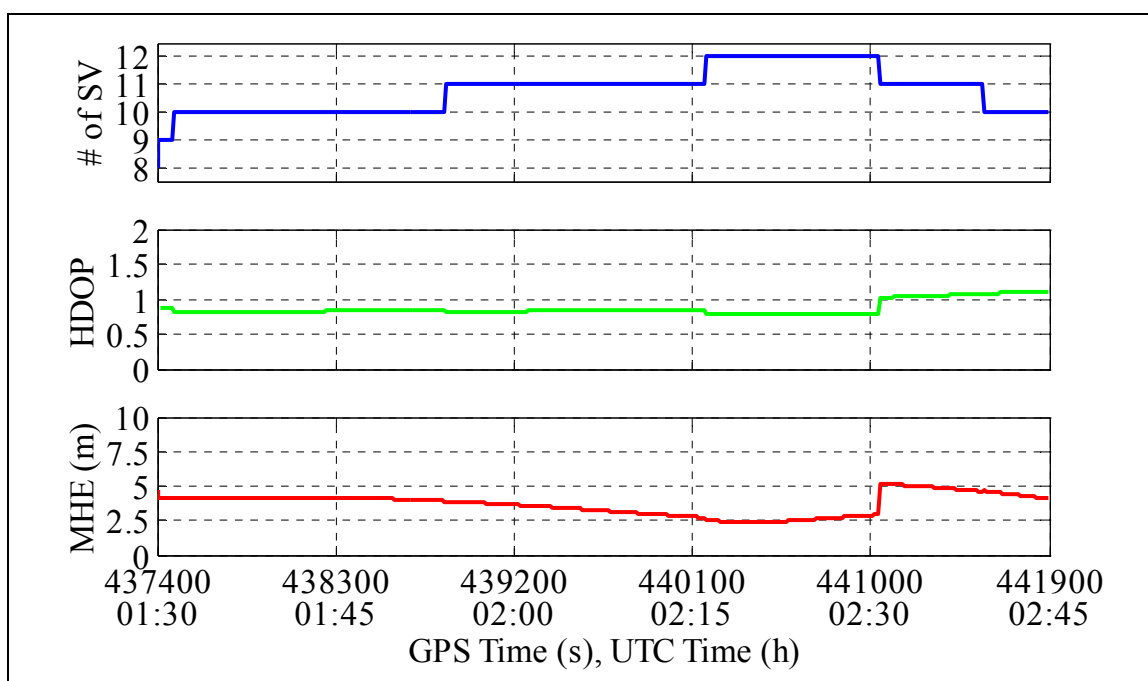


Figure 6-2 Number of SVs, HDOP, and MHE for the Simulation

Figure 6-3 plots the multipath delay and amplitude relative to PRN 8's direct signal. The delays were chosen to be integer wavelengths of the GPS L1 frequency, which maximises the multipath error. The amplitude was varied from -20 dB to 0 dB . In most cases the multipath signal will be weaker than the direct signal due to the reflection and

polarisation losses (see section 2.5.5.1 for more details), however, it is possible for the multipath signal to have the same power level if the direct signal is partially blocked.

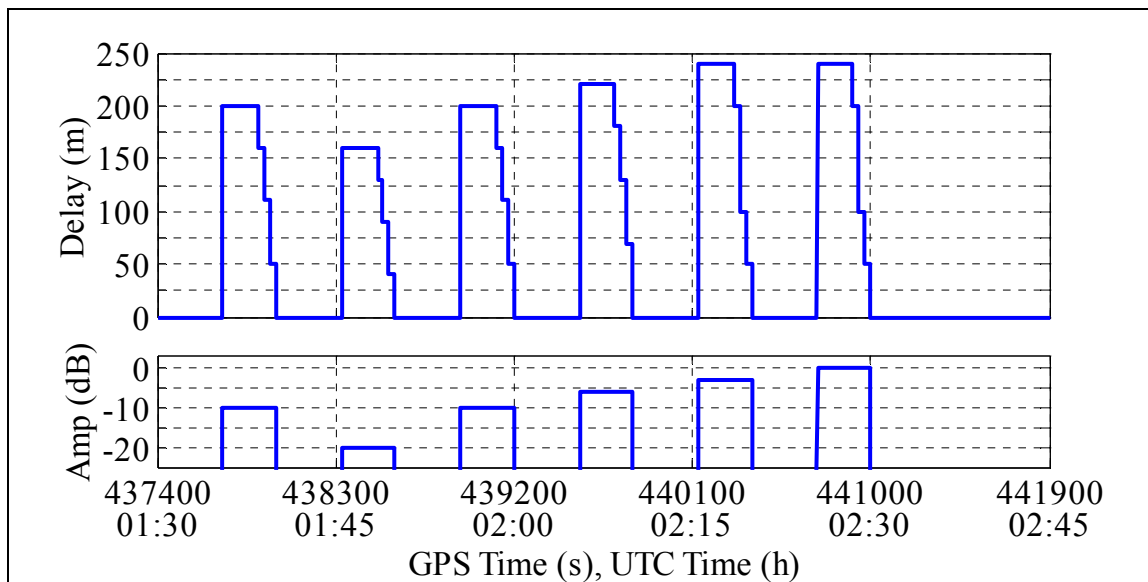


Figure 6-3 Multipath Signal Delay and Amplitude Added to PRN 8's Direct Signal

The range errors generated by this multipath signal for a wide and narrow correlators are plotted in Figure 6-4, assuming infinite bandwidth. The NovAtel OEM3 and the CSI

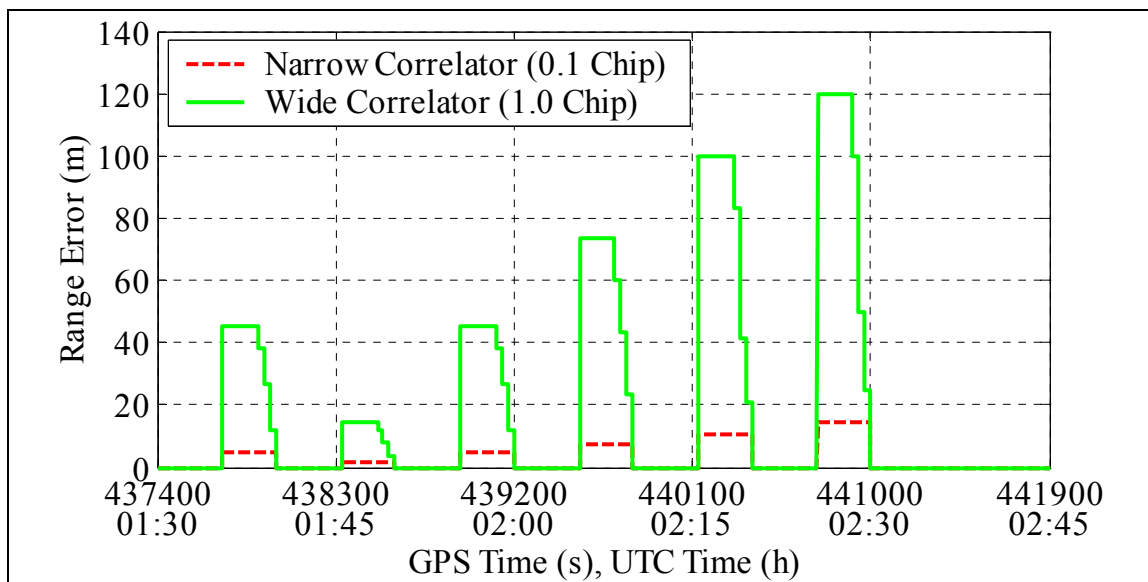


Figure 6-4 Multipath Range Error Added to PRN 8

GBX-Pro should have range errors close to that of the narrow correlator, while the Northstar 941 and the MX-9212 should be similar to the wide correlator.

6.2 *Least Squares Results*

Each receiver was subjected to the same multipath environment. The data was analysed in the following ways:

- 1) Receiver's Internally Computed DGPS Position
- 2) Post-Processed DGPS Position using Least Squares – Without Reliability Checking (No Rejection)
- 3) Post-Processed DGPS Position using Least Squares – With Reliability Checking (With Rejection)

First, the receiver's internally computed DGPS position was compared against the truth to determine if any of the receivers detected the large multipath blunder, or if they otherwise mitigated the affect of the blunder. Then the raw data was analysed using the University of Calgary's C³NAVIG²™ post processing software. The raw data was processed without reliability checking (No Rejection). Then re-processed using a simple reliability checking algorithm (With Rejection). The reliability algorithm tested the SSR using global α_g , β_g , and λ consistent with the local $\alpha_l = 0.1\%$, $\beta_l = 10\%$, and $\delta_o = 4.57$ used in CHAPTER 4. Thus $\beta_g = \beta_l$, $\lambda = \delta_o^2$, and α_g varied with the epoch's redundancy. If the SSR passed that epoch was considered free from blunders, and the position was plotted as a blue circle. If not subset testing was performed. SSR were computed and tested as described above, with one of the following results:

- 1) Only one subset passed, therefore the blunder was found and excluded. The position was plotted as a green circle.
- 2) More than one subset passed, therefore the blunder was detected but could not be positively identified. The subset whose position had the SSR was plotted as a red diamond.

- 3) No subsets passed, therefore the blunder was detected but could not be positively identified. Since no subsets passed the position is suspect and the subset with the minimum SSR was plotted as a circle with a black outline.
- 4) The SSR threshold was exceeded, but insufficient redundancy exists to test the subsets. The position is plotted as a black square.
- 5) The position solution is unique, therefore reliability testing cannot be performed. The position is plotted as a red square.

The multipath periods are shown in the forthcoming figures as alternating pairs of dashed lines, and are labelled as multipath period one (M1) to six (M6). The final dashed line in each figure indicates where the satellite clock ramping error begins (labelled ramp in the figures).

Figure 6-5 shows the results for the NovAtel OEM3. At the beginning of the test before multipath was even added, the NovAtel's internally computed position was in error by > 100 m. This was echoed in the raw data, as shown by the vertical line at the start of the

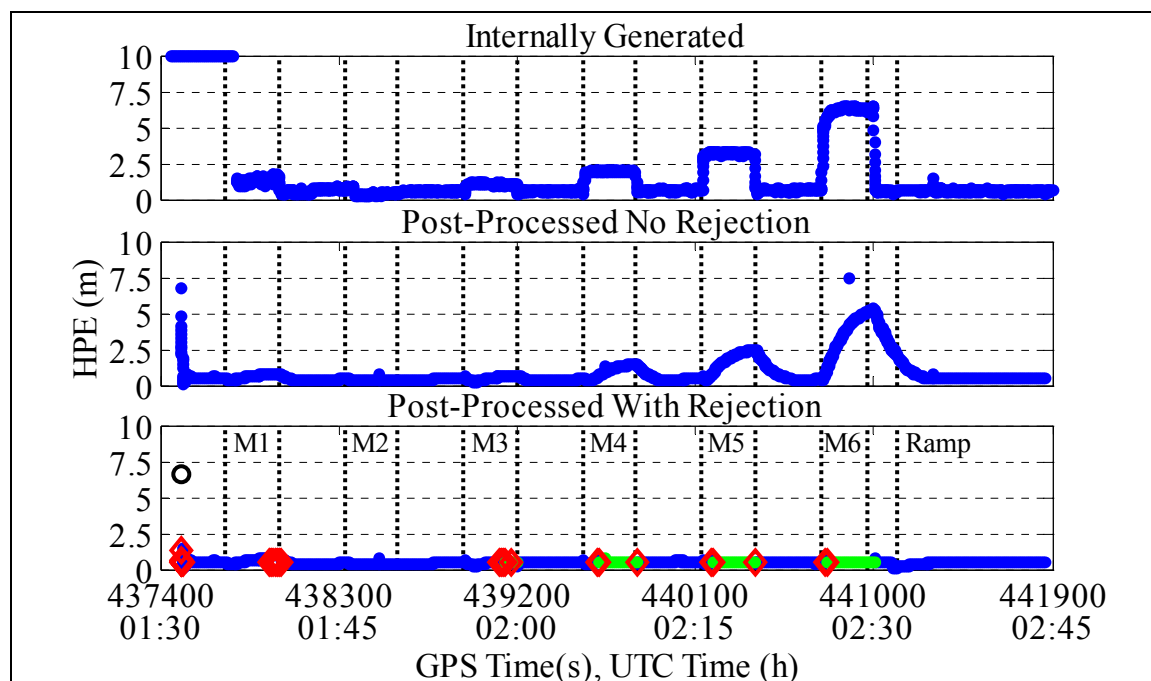


Figure 6-5 NovAtel OEM3 HPE for the Three Positioning Cases

test. Since the receiver operated correctly during the rest of the test, this initial period of instability was not included in the analysis. During the multipath periods the narrow correlator mitigated the affects of the multipath, with a maximum error of 7.5 m which occurred during the last multipath period. Similar results are obtained when the raw data is processed without using the reliability algorithm. Once the reliability algorithm is implemented, even these errors are successfully detected and removed. At the beginning and end of the multipath periods, the error is detected but often cannot be isolated.

The CSI GBX-Pro results, shown in Figure 6-6, are very similar to that of NovAtel OEM3. The Ashtech Edge™ correlator mitigates the multipath effects in the first five multipath periods. However, in the sixth period the receiver's internally generated position has a maximum error of 60.0 m. These results are echoed in the post processed results without reliability. Once the reliability algorithm is implemented the large errors are detected and removed, as shown in panel three of Figure 6-6. During the first and third multipath periods the multipath induced errors were large enough to be detected but

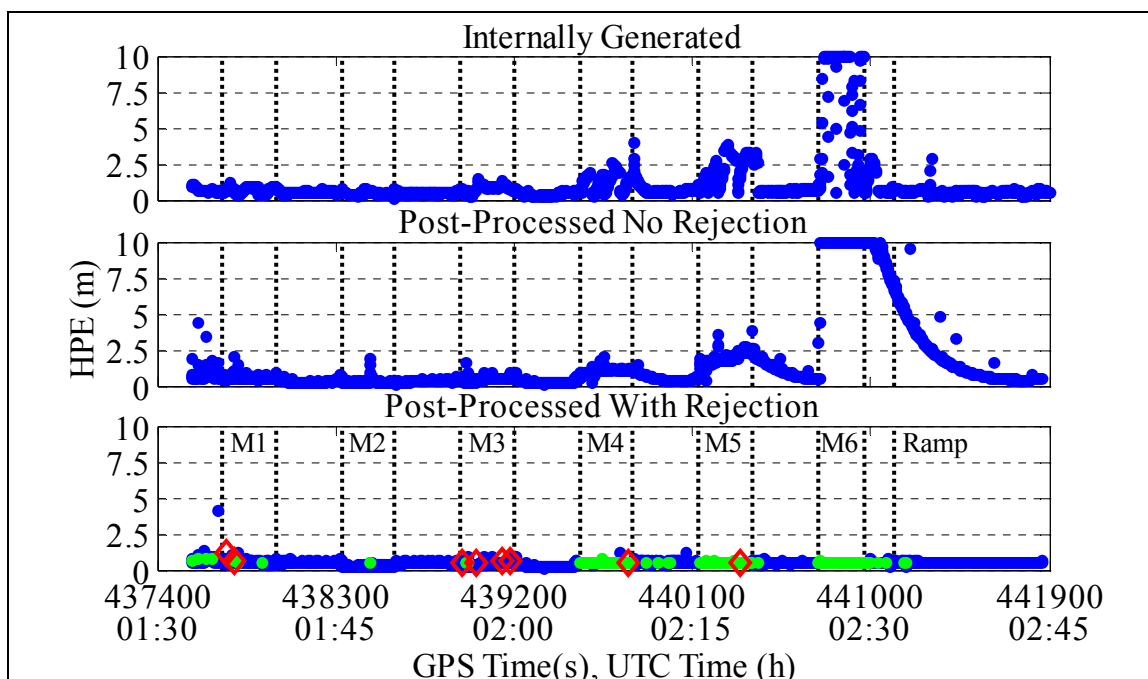


Figure 6-6 CSI GBX-Pro HPE for the Three Positioning Cases

could not be isolated as indicated by the numerous red diamonds. These results illustrate a very important point, even high quality receivers with high performance correlators are susceptible to blunders.

Figure 6-7 shows the results for the MX-9212. The MX-9212's hardware correlator cannot mitigate the multipath, and the resulting errors are an order of magnitude worse than either the NovAtel OEM3 or the CSI GBX-Pro (excluding period six). The internally generated position errors exceeded 10 m in five of the six periods, with a maximum HPE of 38.4 m. The slow decay of the position error even after the multipath has been turned off is due to the biasing of the carrier smoothing filters. However, once the reliability algorithm is activated, all of the multipath errors are detected and most are removed. During the first multipath ramp the reliability algorithm detected a problem but all of the resulting subsets failed (hence the large number of black circles). While this is not the optimum behaviour, it is infinitely better to detect the error than to blindly accept it. During the remaining multipath periods the errors are successfully detected and isolated.

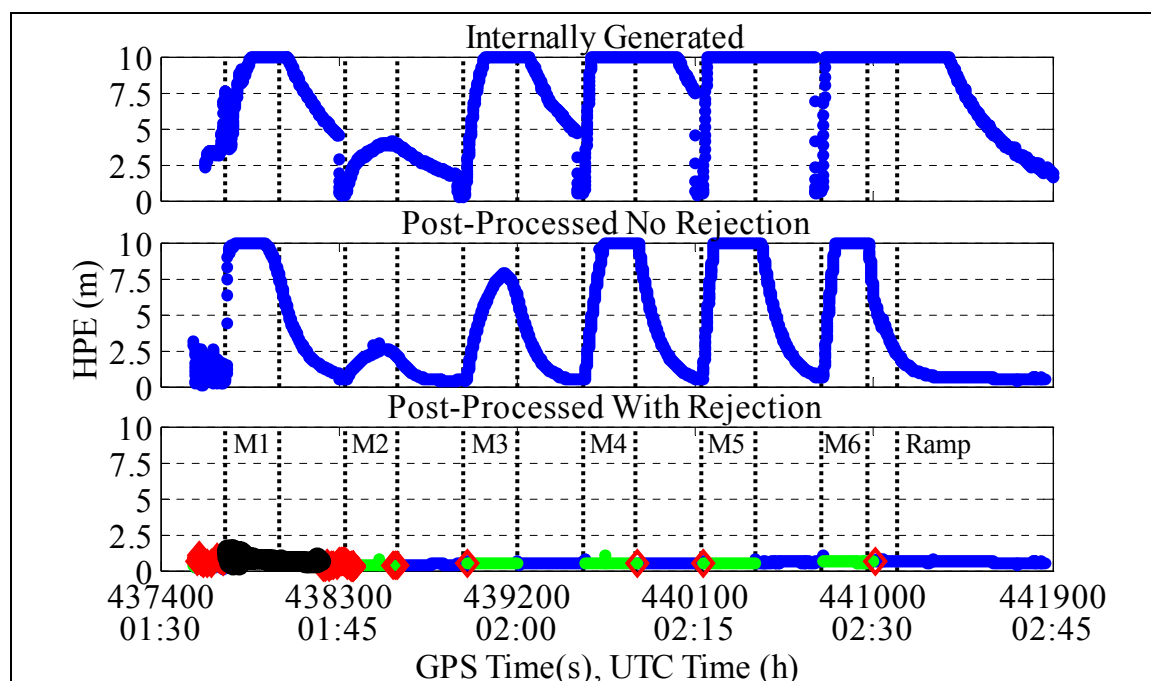


Figure 6-7 Magnavox MX-9212 HPE for the Three Positioning Cases

Since the Northstar 941 receiver does not output raw data, only the internally computed DGPS position was analysed as shown in Figure 6-8. The Northstar 941 only tracked PRN 8 (multipath contaminated satellite) during the first three multipath periods, thus only those results are presented. The position errors during the first three periods are comparable to that of the MX-9212. Thus even larger errors would be expected in the final three multipath ramps if the receiver had tracked PRN 8.

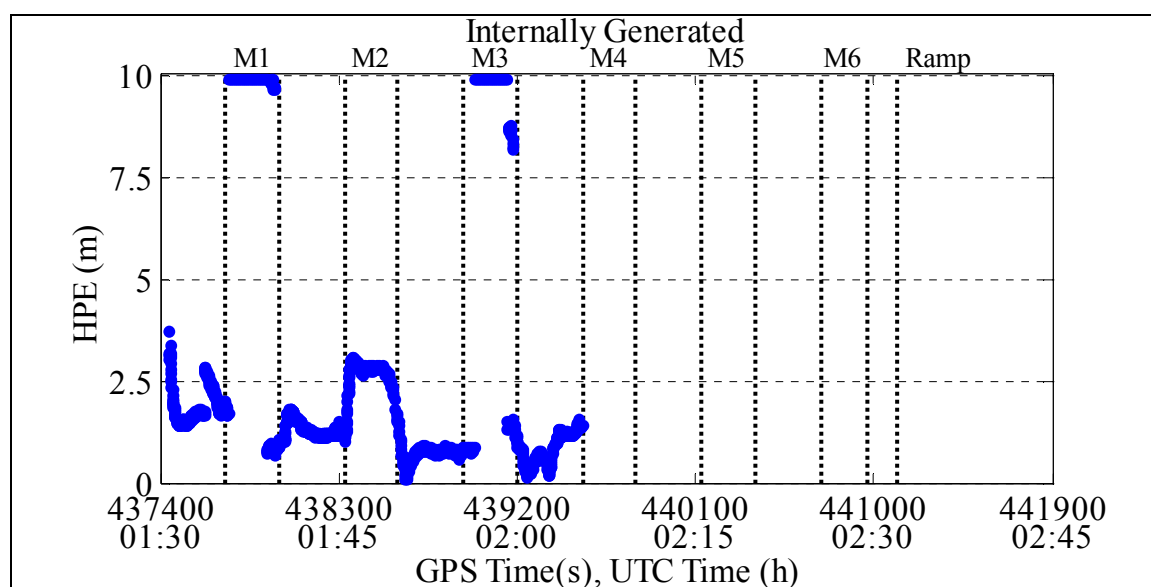


Figure 6-8 Northstar 941 HPE for the Internally Generated Position

Table 6-1 Maximum and RMS Errors (m) During the Multipath Periods

Receiver	Internal DGPS No Rejection		Post-Process No Rejection		Post-Process With Rejection	
	Max	RMS	Max	RMS	Max	RMS
NovAtel OEM3	6.5	3.0	7.4	1.7	0.8	0.5
CSI GBX-Pro	64.0	10.8	87.9	14.3	1.2	0.5
MX-9212	38.4	18.1	26.0	10.0	1.4	0.6
Northstar 941	18.5	9.8	n/a	n/a	n/a	n/a

None of the receivers employed an internal reliability algorithm. Once multipath was allowed to enter the position computation algorithm it played havoc with the results, as

illustrated by the post processing with no reliability positions, and the MX-9212 internally generated position. Table 6-1 summarises the maximum and RMS errors.

Implementing the simple reliability algorithm improves the position results by more than an order of magnitude. Caution must be exercised when interpreting these results, this does not mean that a reliability algorithm will be able to remove all multipath errors. The algorithm will be able to catch the large errors, if proper redundancy exists. To reliably operate during periods of low redundancy, hardware implementations such as choking antennas and high performance correlators must be used.

6.3 *Kalman Filtering Reliability Results*

A Kalman filter reliability algorithm will now be compared with the least squares algorithm from the last section. The three receivers that output raw data will be used for the comparison. The data will be presented with the

- 1) Post-Processed DGPS Position – Without Reliability Checking
- 2) Post-Processed DGPS Position – With Least Squares Reliability Checking
- 3) Post-Processed DGPS Position – With Kalman Filtering Reliability Checking

C³NAVG²™ modified with a Kalman filter was used for the analysis. Kalman filter #1 from Table 2-16 will be used in this analysis. In order to assess the relative improvement between the two positioning methods, the isotropic mask angle was varied from 5° to 25° in 5° increments. As stated above the least squares reliability algorithm tested the SSR. Similarly the Kalman Filtering reliability algorithm checked the SSI. The same markers are plotted as listed in the previous section.

All of the results for the three receivers for the five mask angles are included in Appendix G, only the 20° isotropic mask case will be presented here, followed by a summary of the overall isolation results.

The HPE results for the NovAtel OEM3 receiver with a 20° isotropic mask angle is shown in Figure 6-9. Without a reliability algorithm the HPE spiked to 13.4 m during the last multipath ramp. Once the least squares reliability algorithm is applied the multipath errors are detected during the last four multipath ramps, however, the blunder can only be isolated during the fourth ramp. The Kalman filter detects and isolates the blunder during the last four multipath ramps. Without reliability checking 572 position errors were greater than 2.5 m, least squares reliability checking reduced this to 56 and Kalman filtering reduced this to 5 positions.

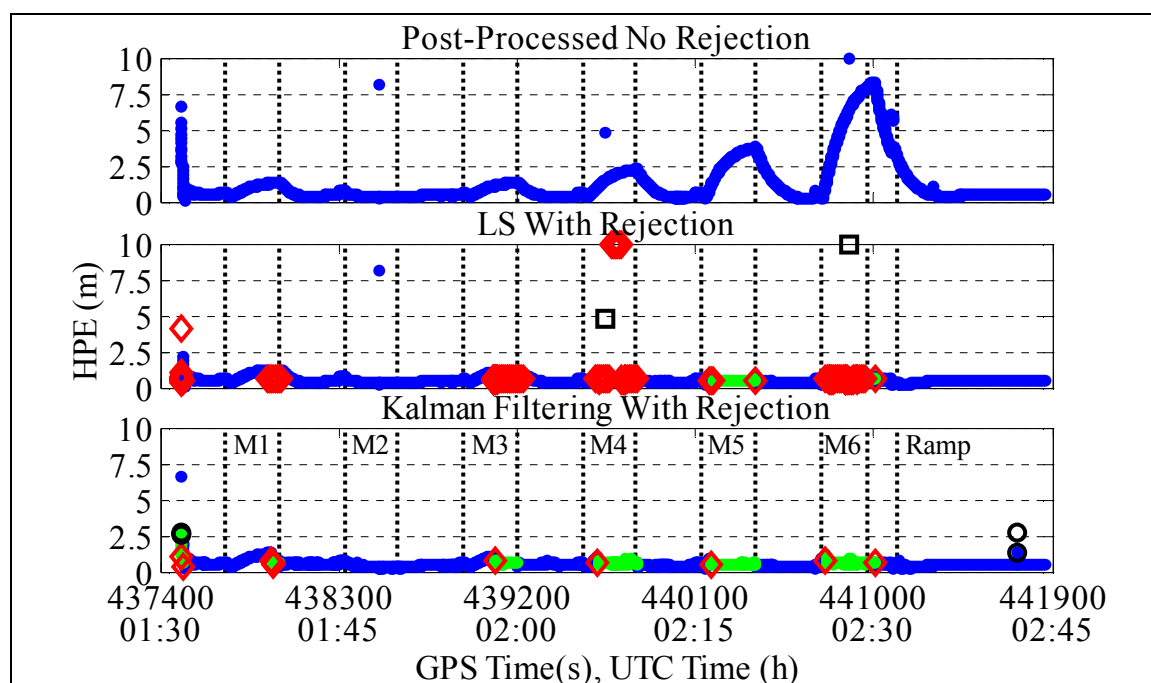


Figure 6-9 NovAtel OEM3 – 20° Mask Angle

The results for the CSI GBX-Pro (Figure 6-10) has the same trend as the NovAtel OEM3. The CSI GBX-Pro without reliability checking exhibits slightly higher noise than the NovAtel and with many position spikes in the 5-10 m range. The least squares reliability algorithm detects these spikes, however, their either isn't sufficient redundancy to perform subset testing (black square) or multiple subsets passed (red diamond). Once again the Kalman filter is able to isolate the errors and remove the position spikes.

Without reliability checking 454 position errors were greater than 2.5 m, least squares reliability checking reduced this to 40 and Kalman filtering reduced this to 0 positions.

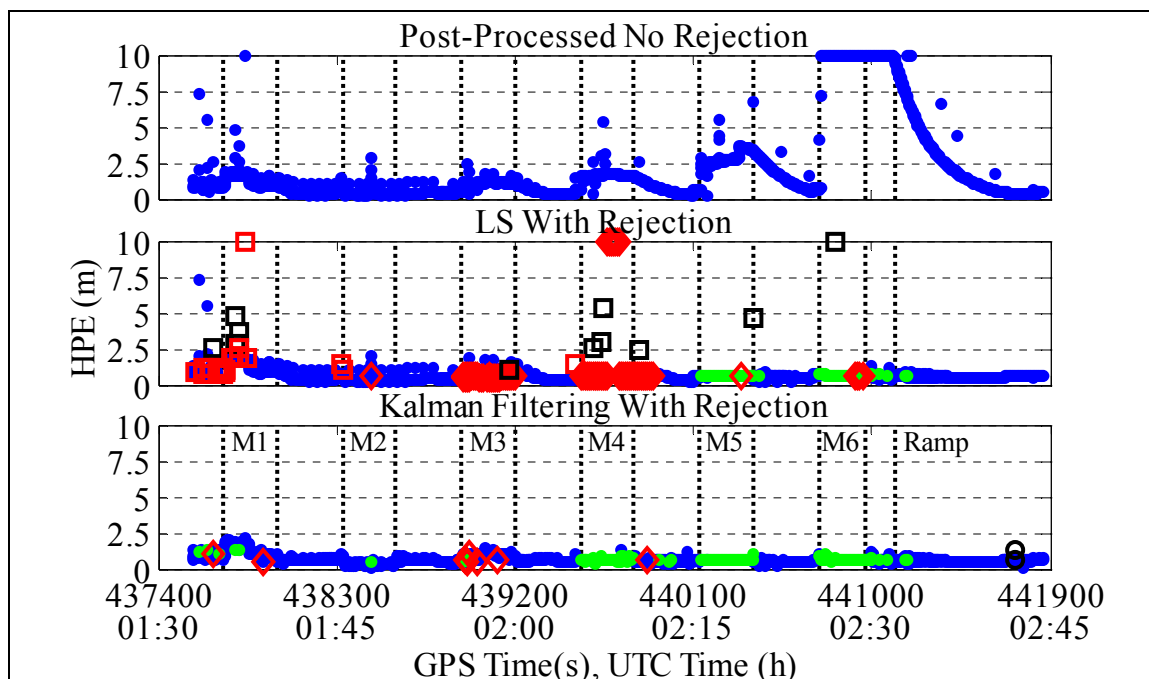


Figure 6-10 CSI GBX-Pro – 20° Mask Angle

The results for the MX-9212 with a 20° isotropic mask angle for the three positioning methods is shown in Figure 6-11. The differences between this receiver's results and that of the NovAtel and CSI are due to its wide correlator. The wide correlator's measurement noise is much higher than the other receivers and it is much more susceptible to multipath as shown by the position error being greater than 10 m in five of the six multipath periods. The least squares reliability algorithm detects the multipath errors but cannot isolate the blunders until the third multipath period, due to insufficient redundancy (note the numerous black squares during the first multipath period). The Kalman filter encounters the same problem during the first multipath period, however, by the second period the filter is able to detect and isolate the blunder. The filter also removes the least squares position spikes during the fourth and sixth multipath periods. Excluding the first multipath period without reliability checking there were 1837 position errors greater than

2.5 m, least squares checking reduced this to 142 and Kalman filtering further reduced it to 62 positions. Once again the filter is able to remove the position spikes.

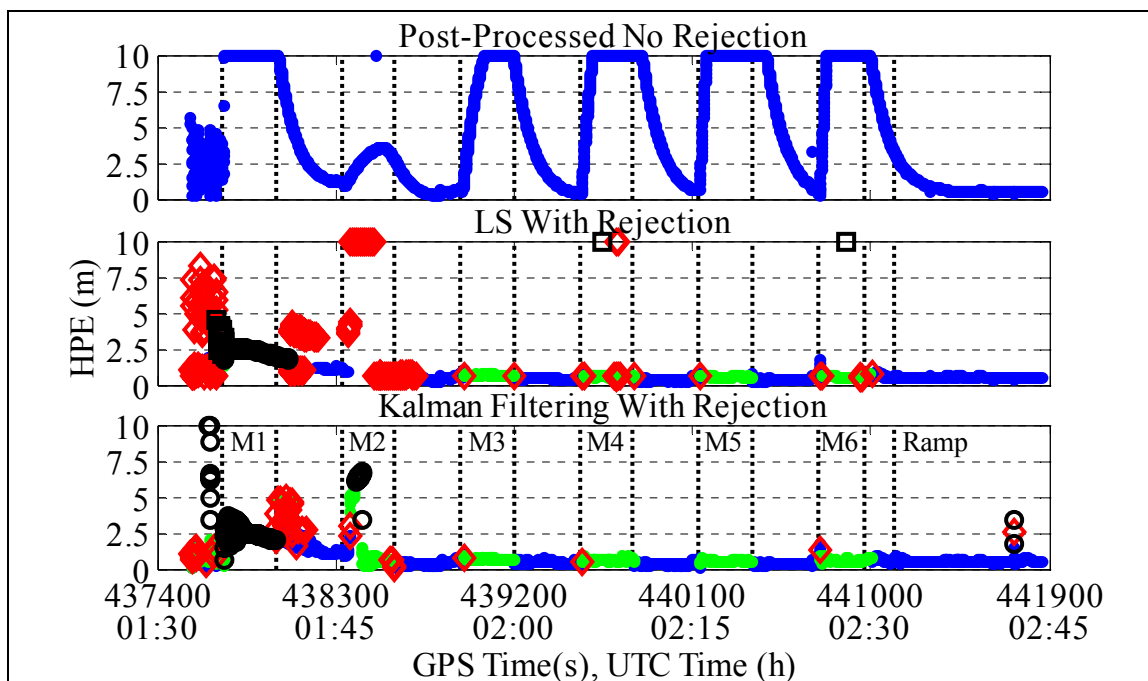


Figure 6-11 MX-9212 – 20° Mask Angle

The least squares' and Kalman filter's ability to isolate the multipath errors for the three receivers is shown in Figure 6-12. At the lower mask angles the two positioning methods are equivalent. However, as the mask angle increases the Kalman filter outperforms standard least squares by up to 30%. The higher mask angles reduce the least squares redundancy making it difficult to isolate the error. During these times the dynamic constraints provided by the Kalman filter allow it to isolate the error. Why are the isolation probabilities not 100%, and why does the MX-9212 outperform the newer receivers? The answer lies in the receiver's correlator, in the first three multipath periods the correlator for the NovAtel and CSI reduces the multipath error below the reliability detection point. This is not a problem since it has minimal effect on the position. The MX-9212 on the other hand lets the multipath bias its range measurement, which in turn gives the reliability algorithm the chance to isolate the blunder.

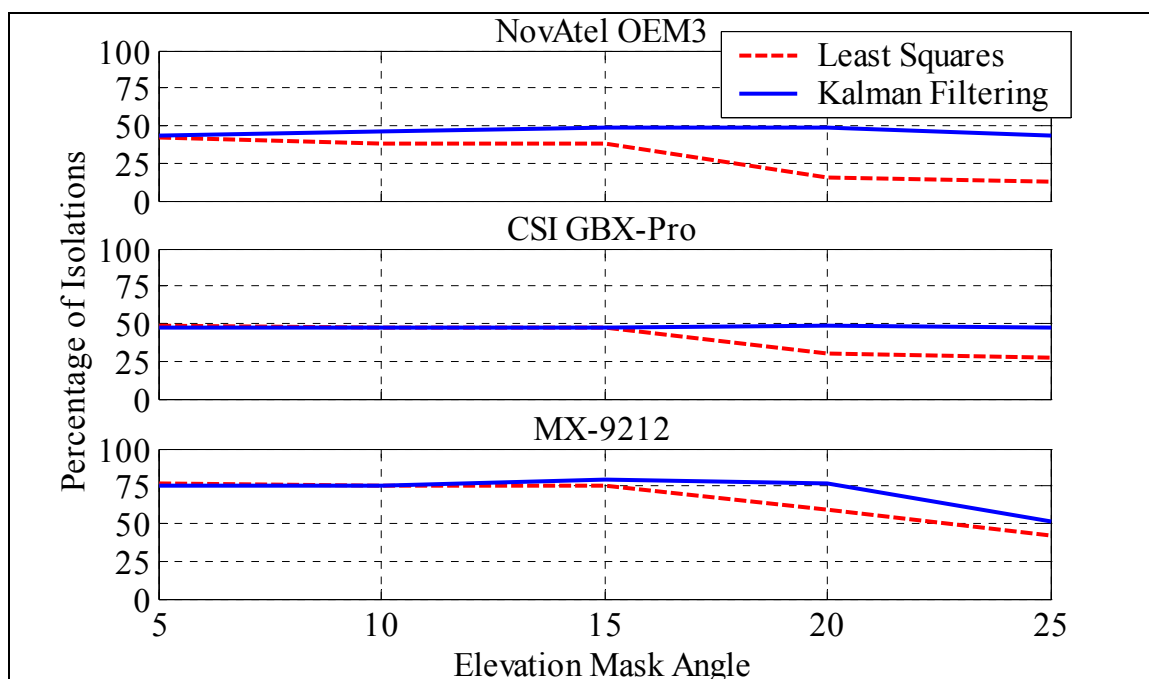


Figure 6-12 Isolation Probabilities During the Multipath Periods

These results are encouraging and discouraging at the same time. Applying reliability algorithms enables even older wide correlator receivers like the MX-9212 to navigate reliably. This is encouraging since the Northstar 941's results are very similar to the MX-9212. This means that user receivers such as the Northstar 941 could have their reliability dramatically improved through a firmware upgrade. The discouraging results come from the NovAtel and CSI results. These high performance receivers with the special hardware correlators (Narrow™ and Edge™) do not employ an internal reliability algorithm. Their special hardware correlators mitigate the multipath, which works well in most cases. However, when the larger errors occurred the receivers blindly accepted them, which is discouraging.

CHAPTER 7

VICTORIA DATA ANALYSIS

7.1 *Field Test Description*

A field test on a representative ship was required to validate the conclusions from CHAPTERS 4, 5, and 6. These chapters demonstrated the availability and reliability improvements attained through augmenting DGPS. The test was conducted on July 25, 1997 in Saanich Inlet, British Columbia, with the assistance of the Canadian Hydrographic Service (CHS) and the CCG. The test consisted of a 40 minute trial using the CCG Survey Launch the Raven (Figure 7-1) from the Institute of Ocean Sciences (IOS), Saanich Inlet, Vancouver Island. See Appendix H for additional pictures of the test set up.



Figure 7-1 CCG Survey Launch the Raven

Typical sets of North/South and East/West survey lines were observed, as shown in Figure 7-2. Two Ashtech GG24™ integrated GPS/GLONASS receivers were used for the test. One was installed at the IOS as the reference station and the other was used on the Raven. The distance between the two receivers was less than 15 km. The raw GPS and GLONASS code and carrier phase observables were processed using the University of Calgary's C³NAV2™ post processing software. The true trajectory was computed from the GPS carrier phase observables using the University of Calgary's FLYKIN™ software package. Due to the cliffs, GPS phase lock was often lost which precluded obtaining a fixed integer ambiguity solution. A float solution was used as the true trajectory instead, with a decimetre-level consistency between the forward and reverse solutions.

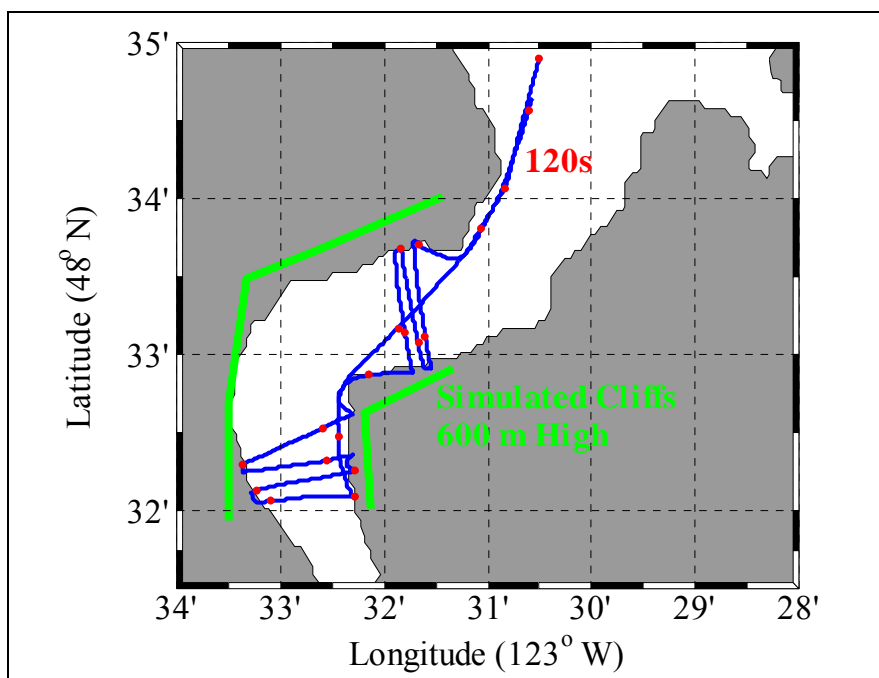


Figure 7-2 Field Test Trajectory in Saanich Inlet, Vancouver Island

Since augmenting GPS with single point GLONASS performed poorly during the simulations and static tests, this augmentation was not used for the field test. A clock constraint was implemented by connecting Rubidium frequency standards to the GG24™

receivers. A height constraint was implemented using tidal information. In total, the following eight positioning methods were analysed:

- 1) DGPS
- 2) DGPS + Height
- 3) DGPS + Clock
- 4) DGPS + Height + Clock
- 5) DGPS + DGLO
- 6) DGPS + DGLO + Height
- 7) DGPS + DGLO + Clock
- 8) DGPS + DGLO + Height + Clock

For each positioning method, the availability and reliability improvements were calculated. In addition to analysing the data using the masking conditions provided by the actual terrain as shown in Figure 7-3, 600 m high simulated cliffs were added to the trajectory and the data was reanalysed for this case. The location of the simulated cliffs are shown in Figure 7-2. Two environments were analysed, namely (i) the actual terrain and (ii) 600 m high simulated cliffs.

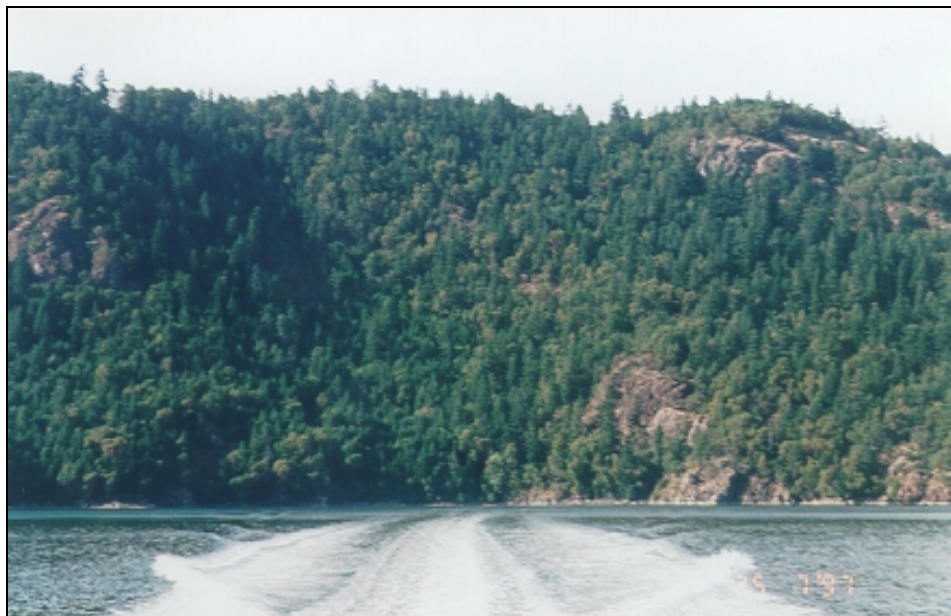


Figure 7-3 Cliffs in Saanich Inlet Taken During the Test

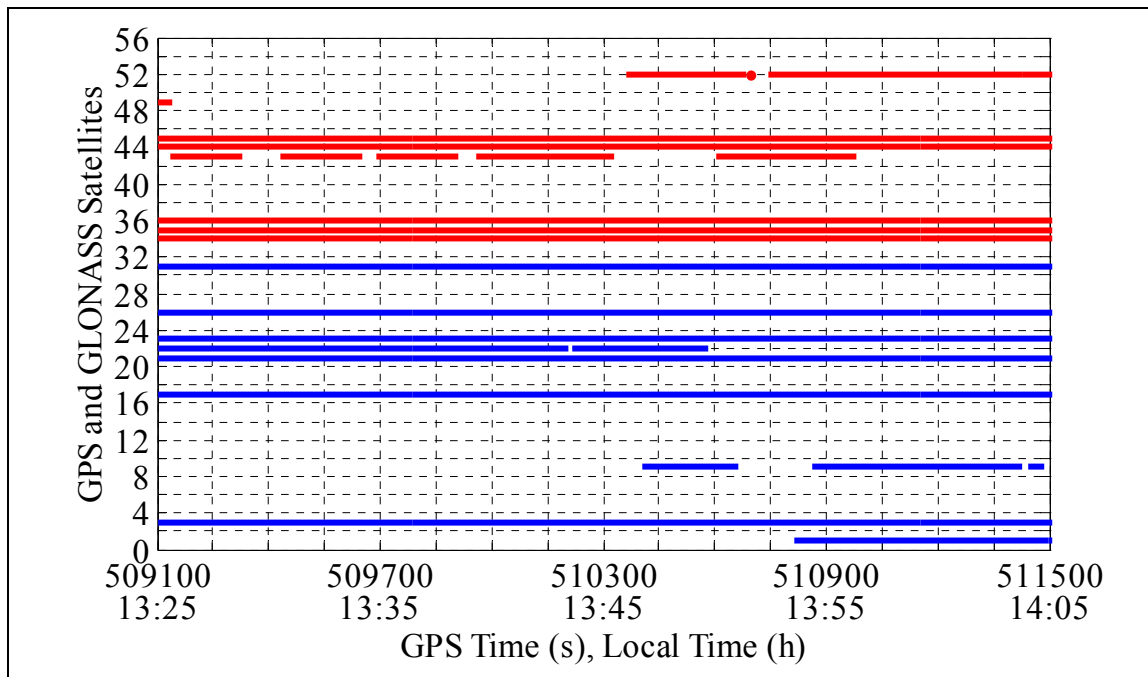


Figure 7-4 GPS and GLONASS Satellite Visibility at the RS During the Test

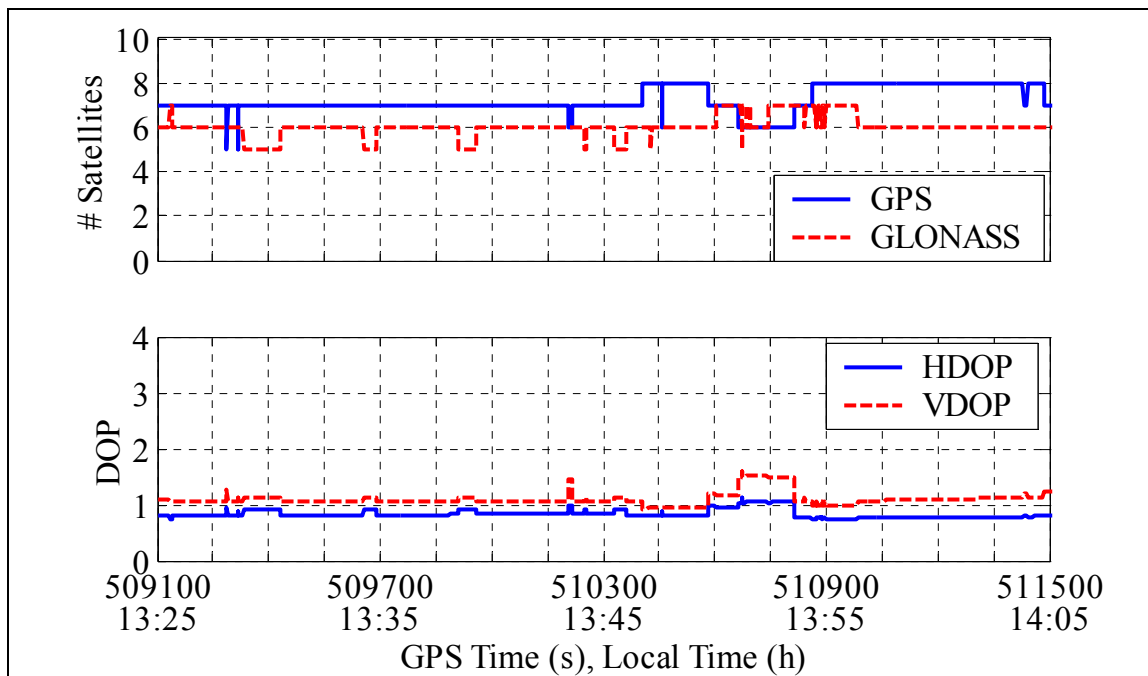


Figure 7-5 Number of Satellites and DOP at the Reference Station During the Test

In July 1997 there were 25 healthy GPS satellites and 15 healthy GLONASS in their respective constellations as shown in Figure 2-2 and Figure 2-4. During the test nine GPS satellites and eight GLONASS satellites were tracked by the reference station as shown in Figure 7-4. The GPS satellites are numbered from 1 to 32, and the GLONASS satellites from 33 to 56. Figure 7-5 plots the number of tracked satellites from each constellation and the resulting DOP values. The reference station tracked between 11 and 15 satellites during the test and the maximum DOPs were 1.1 and 1.6 for the HDOP and VDOP respectively. Thus any availability or reliability problems will be caused by the masking effects of the inlets.

The availability improvement was determined by comparing the resulting HDOP for each positioning method. There are a number of ways to present the different HDOPs. Plotting the HDOP vs. time for each positioning method shows all of the data, but doesn't capture the overall availability improvement. Quoting a single HDOP percentile shows the overall availability improvement, but only provides one point on the cumulative distribution function. Thus to show the entire picture, the cumulative probability distribution functions are used for each positioning method.

The reliability improvement is much harder to measure using real data. If a position is "reliable", it implies that there are no blunders in the observations. Thus to measure the reliability differences between the various methods, blunders were added to the observations. Each positioning method was processed separately and an attempt was made to detect the blunders and remove them from the position computation using the same least squares algorithm described in sections 5.1 and 6.2. The ramping blunder, shown in Figure 7-6 was added to each GPS satellite, (PRN # 3, 17, 21, 23, 26, and 31), one at a time. In total, two ramping blunders were added to each GPS satellite during the 40 minute test. The error was ramped up at a rate of 0.5 m/s until it reached a maximum of 50 m. It was then held constant at 50 m for 100 s and ramped back down to zero at a rate of -0.5 m/s. Each positioning method was processed using C³NAV²TM six times, once for each GPS biased satellite. Since there were 600 s of biased data for each satellite

and there were six satellites with blunders, there were 3600 s of biased data present for each positioning method. For each of these 3600 epochs, the HPE was calculated using the decimetre-level reference trajectory. The reliability improvement was determined by investigating the HPE cumulative distribution curves for each positioning method.

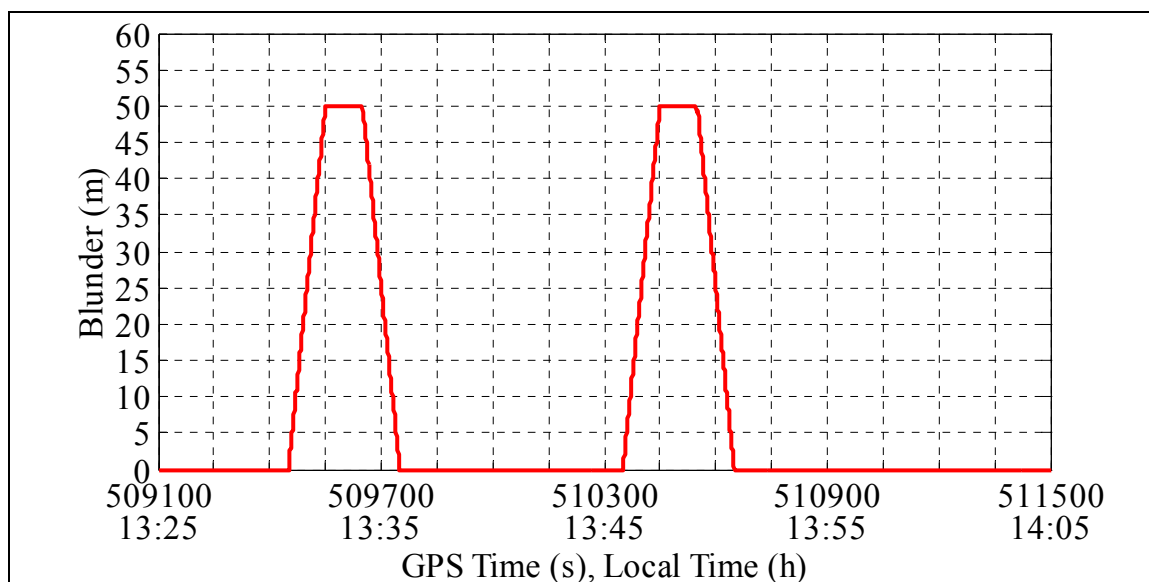


Figure 7-6 Blunder Added to GPS Satellites (PRN # 3, 17, 21, 23, 26, and 31)

7.2 Field Test Results

Both the availability and reliability results are presented using cumulative distribution curves for the eight positioning methods and the two terrain profiles (actual and simulated cliffs). The DGPS methods are plotted using dashed lines and the DGPS + DGLO are plotted using solid lines. The four constraint methods use the following markers:

- Star - no constraints
- Circle - height constraint
- X - clock constraint
- Triangle - both height and clock constraints

7.2.1 Availability Results

When the actual terrain is analysed, all the positioning methods tested have very good availability. The 95% HDOP for any one of the methods is better than 2.7, as shown in Figure 7-7. At the lower HDOP values, there are differences between the various methods, with the combined DGPS + DGLO method out performing the DGPS method, as expected. The height and clock constraints produce similar results regardless of the constellations used. The addition of both constraints results in only marginal improvement compared with a single constraint. While augmenting DGPS with DGLO or constraints improves availability, it does not produce significant availability improvements for the actual terrain case.

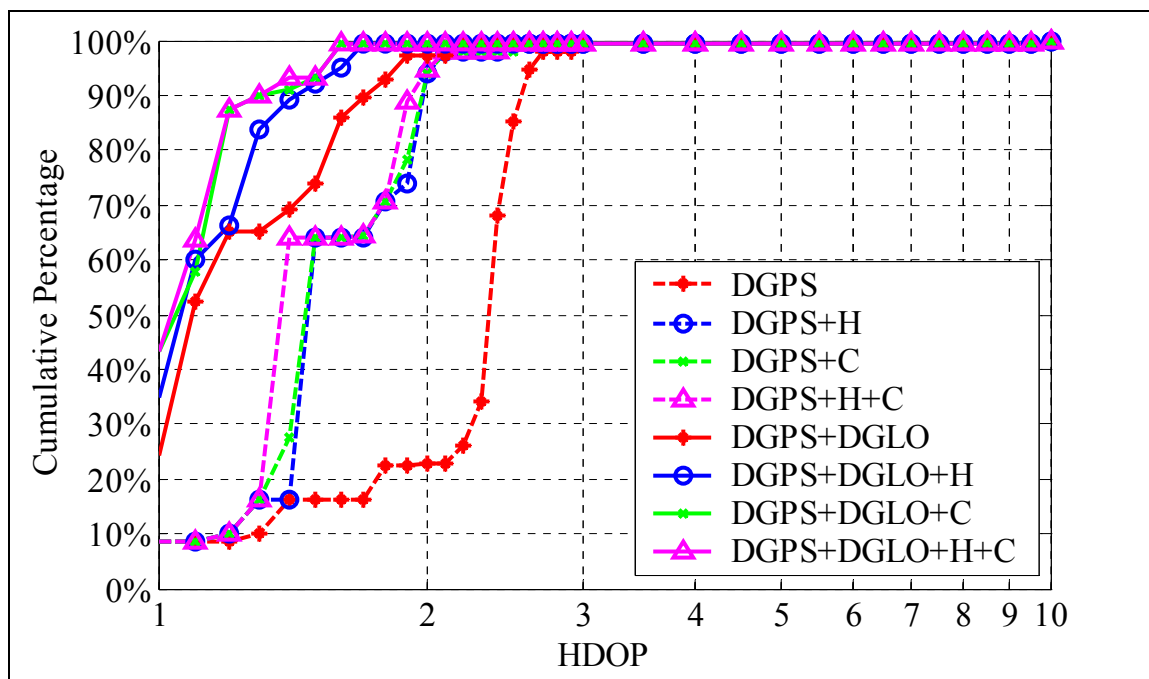


Figure 7-7 Actual Terrain – HDOP

However, when the 600 m simulated cliffs are introduced, there is a much greater separation between the various methods, as shown in Figure 7-8. DGPS alone has a very low availability, the 95% HDOP value being greater than 10. Augmenting DGPS with a single augmentation, either DGLO or a constraint, improves the availability, however, the

95% HDOP only improves to 3.5. Once DGLO and the constraints are combined, the 95% HDOP improves to 2.3. These results highlight an important fact, namely the real strength of augmentations in terms of availability occur during extreme masking conditions.

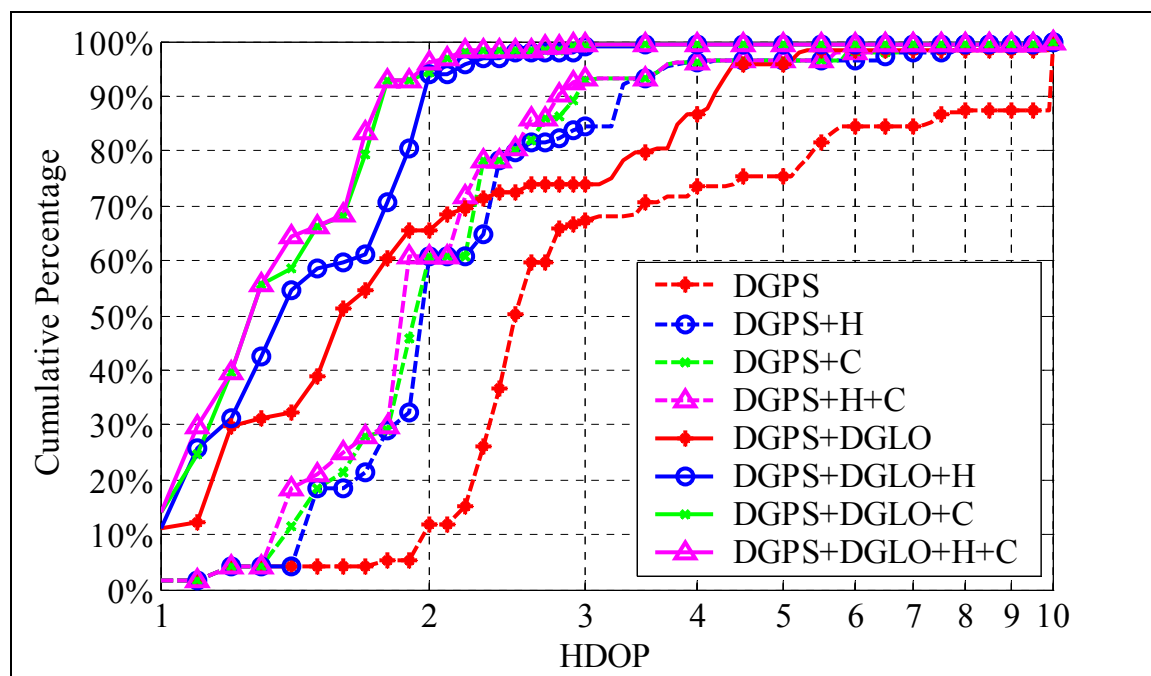


Figure 7-8 Simulated 600 m Cliffs – HDOP

7.2.2 Reliability Results

The reliability improvements for the actual terrain and the simulated cliffs are presented in Figure 7-9 and Figure 7-10, respectively. Unaided DGPS performs poorly in the actual terrain case; only 80% of the positions have a HPE less than 10 m. However, once a single augmentation is added, 95% of the positions have a HPE less than 1 m. While the DGLO method outperformed the unaided DGPS method, all of the augmentations performed very well. The blunders introduced are successfully detected.

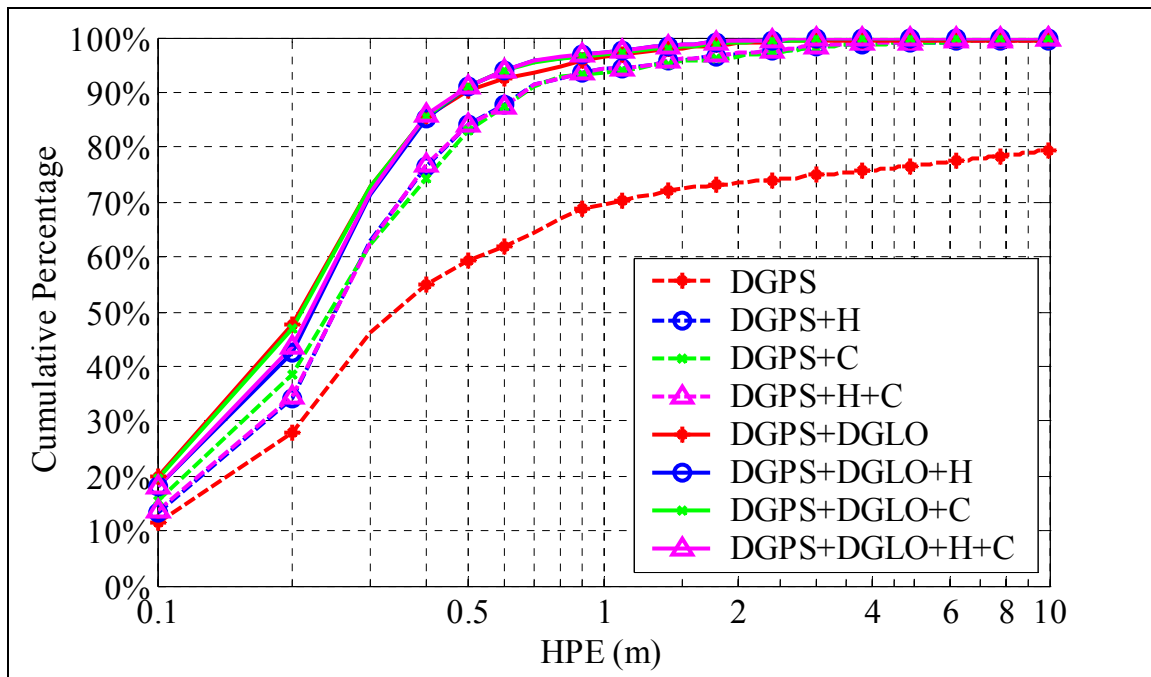


Figure 7-9 Actual Terrain - HPE 6 SVs During Ramps

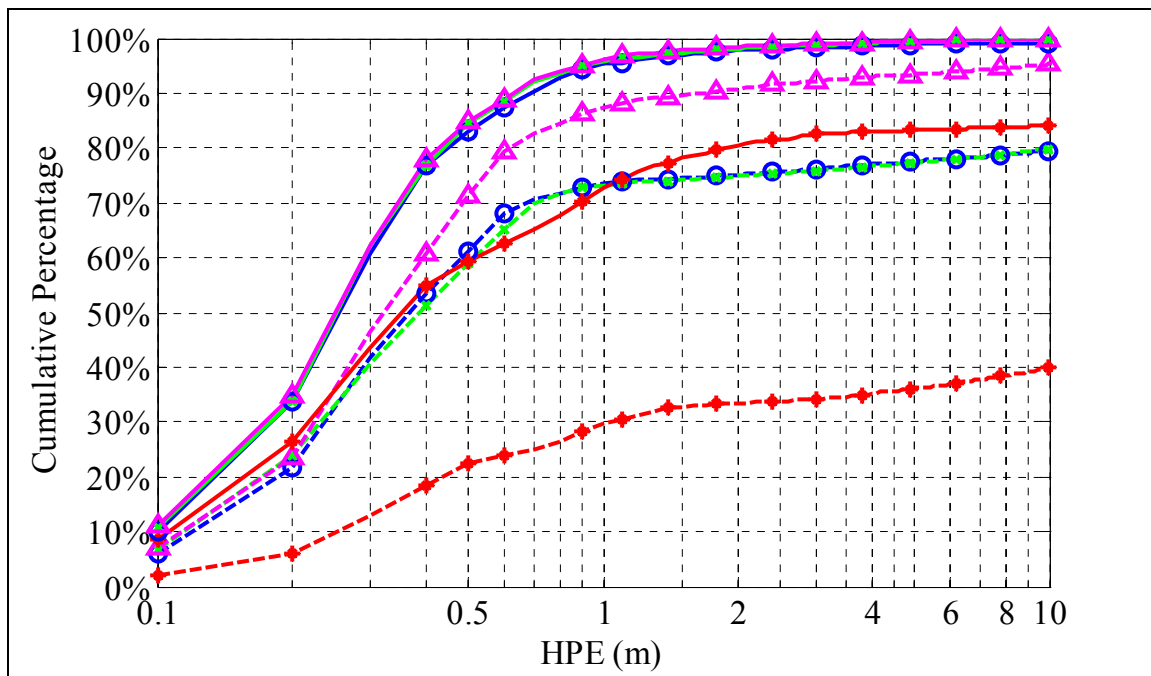


Figure 7-10 Simulated 600 m Cliffs - HPE 6 SVs During Ramps

As was the case with the availability analysis, the separation between the positioning methods increases once the simulated cliffs are added, as shown in Figure 7-10. In the case of unaided DGPS, only 40% of the positions have a HPE less than 10 m. When DGLO is added, the reliability of the positions is greatly improved, with 80% of the positions having a HPE less than 10 m. The 95% HPE improves to 1.0 m once DGLO and at least one constraint are added to DGPS. Even with the extreme masking conditions created by the simulated cliffs, reliable positions are still possible.

These results reconfirm the analysis presented in the previous chapters, that real time augmentations can dramatically improve the availability and reliability of the position.

CHAPTER 8

CONCLUSIONS AND RECOMMENDATIONS

8.1 *Conclusions*

Blunders in marine navigation can be caused by extreme ionospheric phenomenon and multipath. The ionospheric simulations demonstrated that SED can produce multiple simultaneous blunders. The multipath simulations demonstrated that the multipath error was extremely dependent on the simulated vessel and environment. The survey launch results did not show the large multipath spikes that were evident from the large ship. However, even when the spikes from the large ship were taken into account, the 99.9% values for the wide and narrow correlators were only 43 m and 11 m respectively. Assuming that any size blunder can occur is not a realistic assumption. The simulations also showed that the second largest simultaneous blunder was < 4 m (99.9% of the time). Thus if multiple blunders are going to be assumed the second blunder should be limited to the 4 m range.

Applying the multipath blunder limits to the reliability simulations significantly improved the reliability performance for the unaugmented cases. The highly augmented cases were only marginally improved, since they already had sufficient redundancy to detect the blunder. When the multiple blunders were limited, the results were only slightly worse than the limited single blunder, due to the size of the second limited blunder. For many applications making the assumption of one blunder may be acceptable.

The availability and reliability simulations demonstrated the tremendous improvements that can be obtained when DGPS is augmented with other satellite systems and

constraints. The most dramatic effects are seen in the moderate to extreme masking conditions. During all of the simulation scenarios as well as during the DGPS simulator tests, the high performance correlators consistently out performed the wide correlator due to their superior multipath rejection and measurement variance. In the simulation sections the high performance correlator acted like an augmentation unto itself.

The simulations demonstrated that DGPS will meet most availability and reliability requirements under benign masking conditions ($\leq 10^\circ$). Augmenting DGPS with constraints improved the availability for the 20° mask case, however even with constraints the availability is poor for the higher isotropic mask angles. DGPS requires additional satellite augmentations to meet the reliability targets for isotropic mask angles of 20° and above.

While augmenting DGPS with single point GLONASS improves the results, the improvements are marginal at best. This is due to the increase in the observation variance (from 1 m^2 to 64 m^2) and the lack of healthy GLONASS satellites. The small constellation makes it difficult for this augmentation to be effective.

Adding the current constellation of GLONASS satellites in differential mode improves the results, however the augmentation still suffers from the lack of healthy satellites. The GLO10 constellation that was simulated is truly a partial constellation. If GLONASS was maintained by the Russian Federation it would be beneficial to combine it with GPS. However, the future of GLONASS is uncertain given the slow decline in the number of healthy satellites and the birth of Galileo.

If GLONASS could ever reach FOC status again, its differential augmentation performance would be similar to that of Galileo. The Galileo constellations consistently out performed the full GLONASS constellation, because they were simulated with more satellites (six more for GAL30 and nine more for GAL24).

The differential GEO satellites gave very interesting results. By the very nature of GEO satellites they provide poorer coverage in the mid to high latitudes. Thus under the moderate to high masking conditions the GEO augmentation did not help the Northern locations. However, for lower latitudes it often dramatically improved the availability and reliability for specific locations.

Once one of the Galileo constellations is added to DGPS most of the availability and reliability requirements can be met for isotropic masking angles $\leq 30^\circ$. When extreme mask angles are encountered ($\geq 40^\circ$ isotropic and severe constricted waterways), DGPS must be augmented with Galileo as well as constraints. Even then the 95% MHE is in the 30 m range. In order to reliably work under these masking conditions planning must be performed.

The two Galileo constellations produced very similar world results for all but the extreme mask conditions. Under extreme mask conditions GAL30, the pure MEO constellation, moderated the results by reducing the maximum HDOPs and MHEs and increasing the minimum values. While GAL24 produces lower minimum values, the best overall performance was provided by the GAL30 constellation.

Augmenting DGPS with dynamic constraints through the use of a Kalman filter greatly improved the availability and reliability of the navigation solution. The hydrographic survey simulations demonstrated that adding a Kalman filter was equivalent to augmenting DGPS with an additional partial constellation such as DGEO or DGLO. However, the analysis assumed that the blunder did not bias the filter prior to detection. If the blunder was allowed to bias the filter, it would affect the reliability. The degree to which it would affect the reliability would be dependent on the specific blunder characteristics. While the most dramatic improvements are obtained during extreme masking conditions, a properly tuned filter will always improve the results.

While augmenting DGPS can improve its reliability performance, this is irrelevant if the marine user receivers do not implement a reliability algorithm. The receiver evaluation

demonstrated that many marine user receivers do not perform any reliability checking, which needlessly allows blunders (e.g. multipath) to corrupt the navigation solution. High performance correlators can mitigate this problem by reducing the magnitude of the multipath ranging error, however, without a reliability algorithm the navigation solution can still be corrupted. The CSI GBX-Pro with a high performance correlator allowed multipath to bias its position by 60 m. This is unacceptable for high end receivers. A simple reliability algorithm run in post processing detected and isolated most of the blunders. Thus good hardware is not enough, the navigation solution must be checked in software as well. Adding the Kalman filter to the test improved the blunder detection and isolation even further.

The static test and the field test on the survey launch confirmed that integrating DGPS with another satellite constellation can be easily done and dramatically improves the availability and reliability of the position solution. The least squares reliability algorithm was run in post mission and demonstrated that reliable navigation is achievable even under the demanding hydrographic surveying environment.

8.2 *Recommendations*

In order to improve the position's reliability the blunder characteristics must be well defined. Therefore further multipath data collection and analysis is recommended. Armed with this information a strategy for addressing multipath blunders can be developed. This may involve special user receivers, special installation instructions, and even operator training. Similar work must be done for the ionosphere. Since certain ionospheric events can cause large blunders, their signatures should be investigated. Being able to detect the problem is just as important, if not more important than isolating the problem.

Once this additional information on the error sources has been obtained the design of shipboard DGPS receivers must be reformed to address the potential blunders. As illustrated in CHAPTER 6 many survey and marine DGPS receivers do not employ a real time reliability algorithm. This is not acceptable. The standards governing shipboard

equipment should be changed to mandate the use of a real time reliability algorithm. This will begin to address the problem of unreliable navigation.

The question as to how to augment DGPS is difficult to answer. DGLO services are not available in North America and will probably not be available, if at all, for some time. That leaves single point GLONASS, which as the simulations showed is only marginally effective. Unless the GLONASS constellation is rejuvenated mariners will have to wait for Galileo.

The height, clock, and dynamic constraints all improved the availability and reliability of DGPS. Therefore they should be implemented whenever possible. Most users will not have access to a Rubidium clock. However, all marine users can implement a height constraint and dynamic constraints within a Kalman filter. These augmentations are not cost prohibitive and offer the user dramatic improvements in performance.

Other sensors should also be evaluated to determine their potential benefit in augmenting DGPS. This could include augmenting DGPS with a low cost inertial measurement unit (IMU). Their short term stability should definitely be a benefit during satellite blockages. These units should become economically feasible within the next 10 years.

APPENDIX A

ADDITIONAL GALILEO CONSTELLATIONS

A.1 Introduction

In Section 2.4 and Chapter 4 two Galileo constellations were introduced and simulated. During this research several additional constellations were analysed and interesting results were obtained when different satellite plane phasing was tested. The constellations given in Table A-1 are simulated in this appendix. Constellation 1 (C1) simulates 24 MEOs without any GEOs. Constellation 2 (C2) adds nine GEOs to (C1). Constellation 3 (C3) simulates the 30 MEO constellation. Constellation 4 (C4) uses the a previously proposed altitude for Galileo with the original GPS satellite. Constellation 5 (C5) uses the GPS altitude with the original GPS satellite configuration.

Table A-1 Different Satellite Constellations

Test #	MEO	GEO	Altitude	Walker Configuration
C1	24	0	24,126 km	24/3/2
C2	24	9	24,126 km	24/3/2
C3	30	0	24,126 km	30/3/2
C4	24	0	24,126 km	24/6/1
C5	24	0	20,181 km	24/6/1

A.2 Walker Constellation

Walker defined a general format for circular orbit satellite constellations with equal spacing. The constellation is defined as T/P/F, where T is the total number of satellites, P is the number of orbital planes and F gives the relative phasing between satellites in

adjacent planes. If a satellite in one plane is just crossing through the equatorial plane in the northern direction, the adjacent plane satellite is offset by an angle of $F \cdot 360^\circ / T$. (Walker, 1978). For example C1 with a Walker 24/3/2 configuration, has 24 satellites in three orbital planes with 30° phasing between planes.

A.3 Global Availability Results

Figure A-1 to Figure A-4 show the availability contour plots for the entire globe, for C1 to C4, using GGPLAN. The simulations were conducted over 24 hours at 60 second intervals with a 10° latitude spacing and a variable longitude spacing based on the latitude. Overall the results are good for the first three constellations, however, there is an obvious problem with C4 as shown in Figure A-4. The 95% HDOP is fine until $\pm 50^\circ$ latitude, and then is terrible. What is causing the problem?

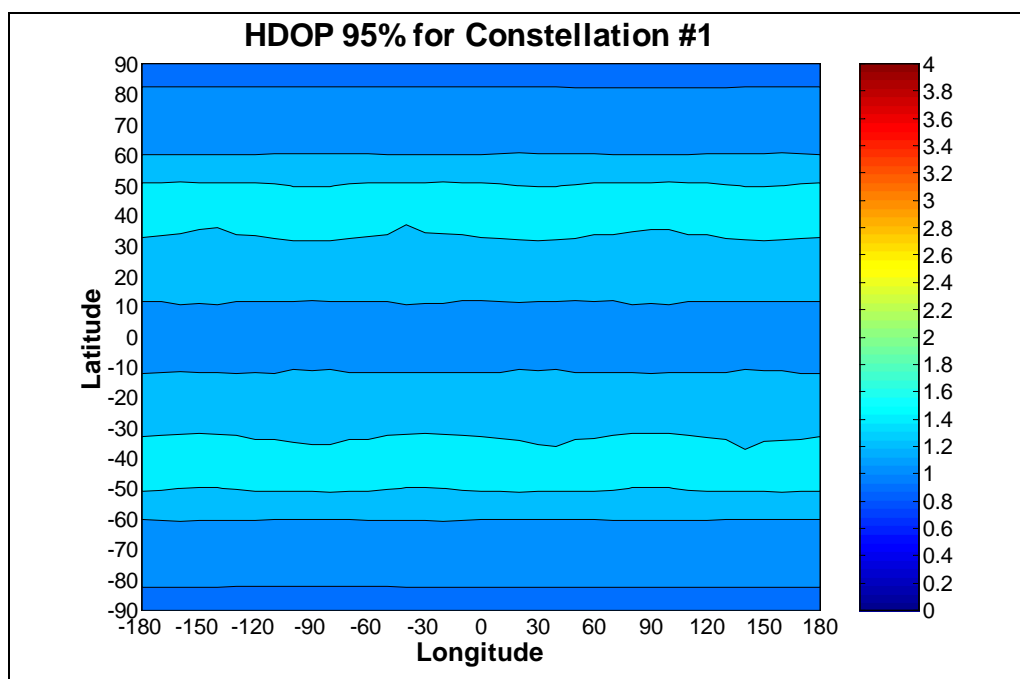


Figure A-1 HDOP 95% for the World using the Constellation #1.

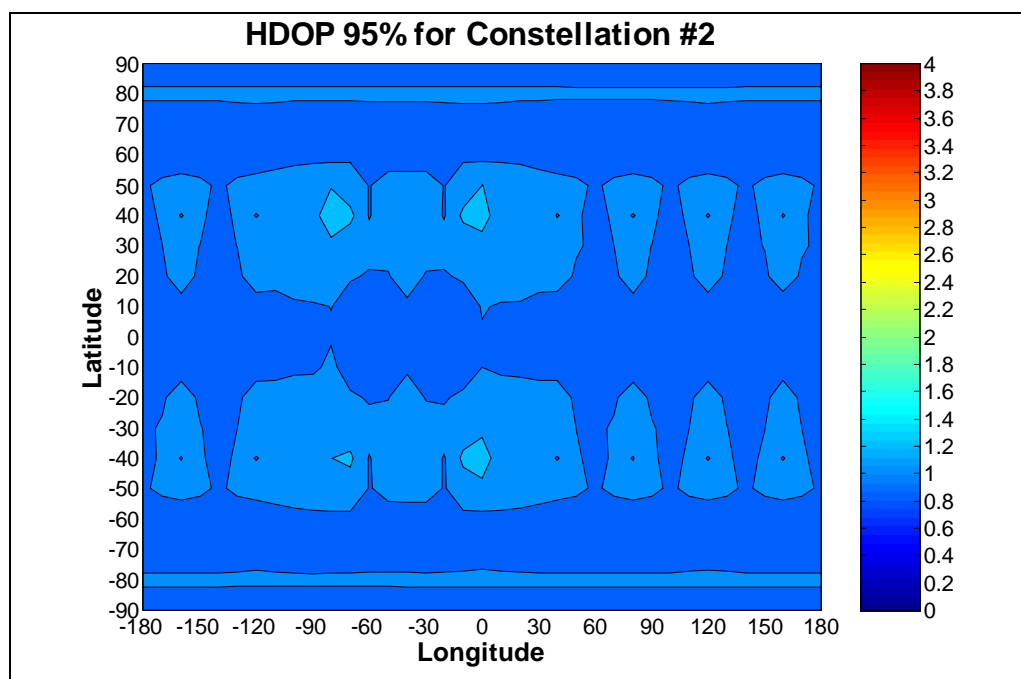


Figure A-2 HDOP 95% for the World using the Constellation #2.

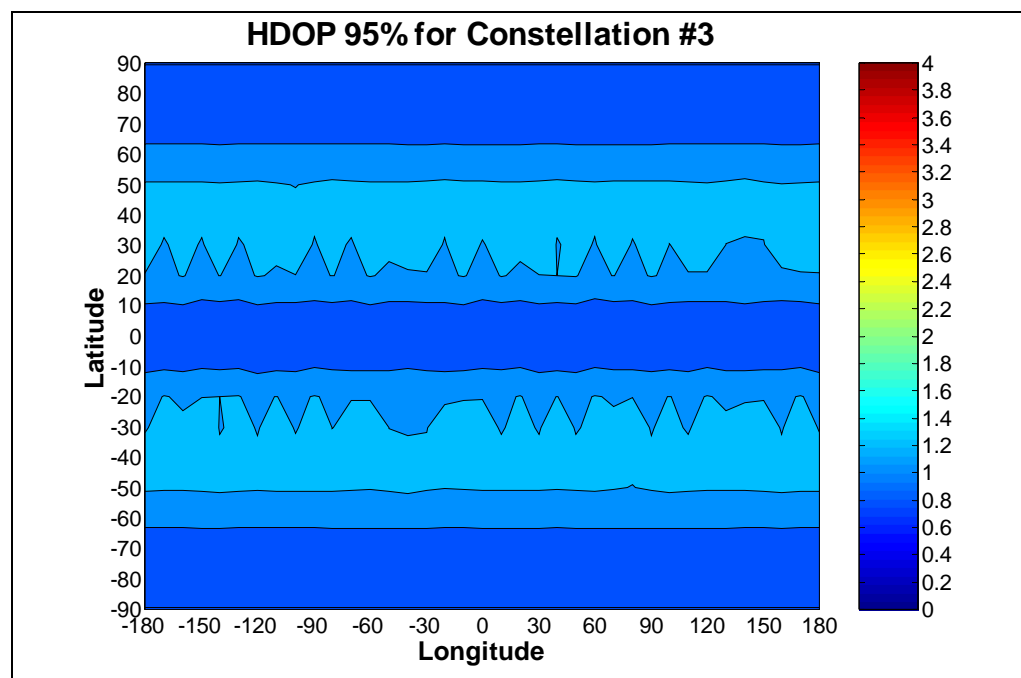


Figure A-3 HDOP 95% for the World using the Constellation #3.

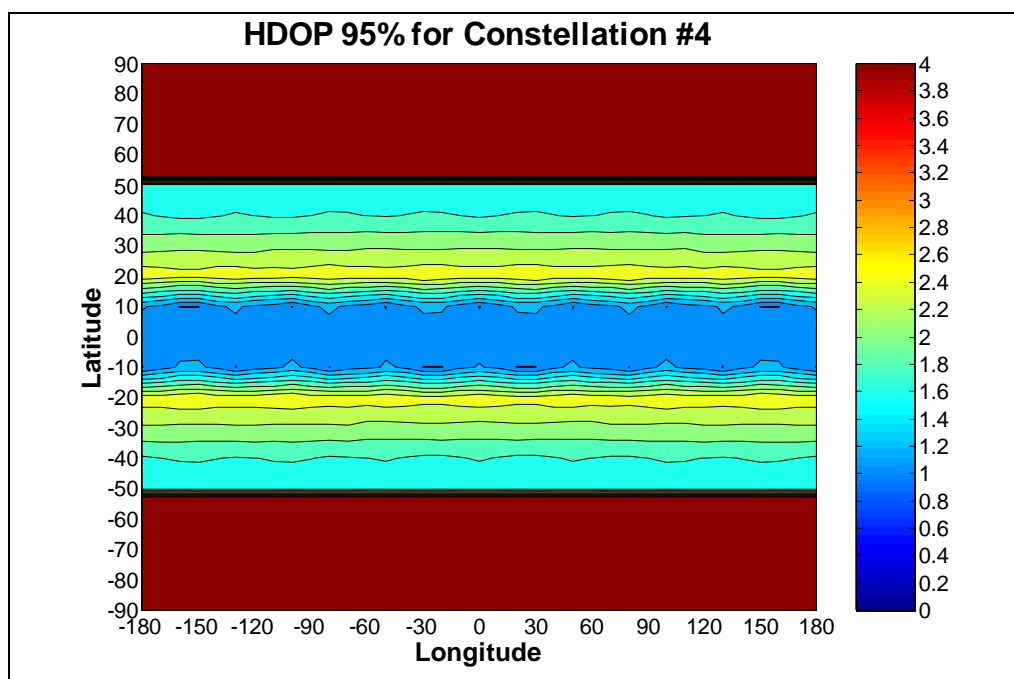


Figure A-4 HDOP 95% for the World using the Constellation #4.

A.3.1 C³NAV²™ Repeats the GGPLAN Analysis for 60° N, 120° W,

C³NAV²™ will be used to verify the output of GGPLAN. Since C³NAV²™ requires an ephemeris and observation file, C4's almanac was used to generate ephemerides and observations for a station at 60° N, 120° W. C³NAV²™ was then used to calculate the HDOP and the number of tracked satellites at that location. C³NAV²™ results are presented in Figure A-5 and GGPLAN's results are presented in Figure A-6. The figures are identical indicating that the problem is not within GGPLAN.

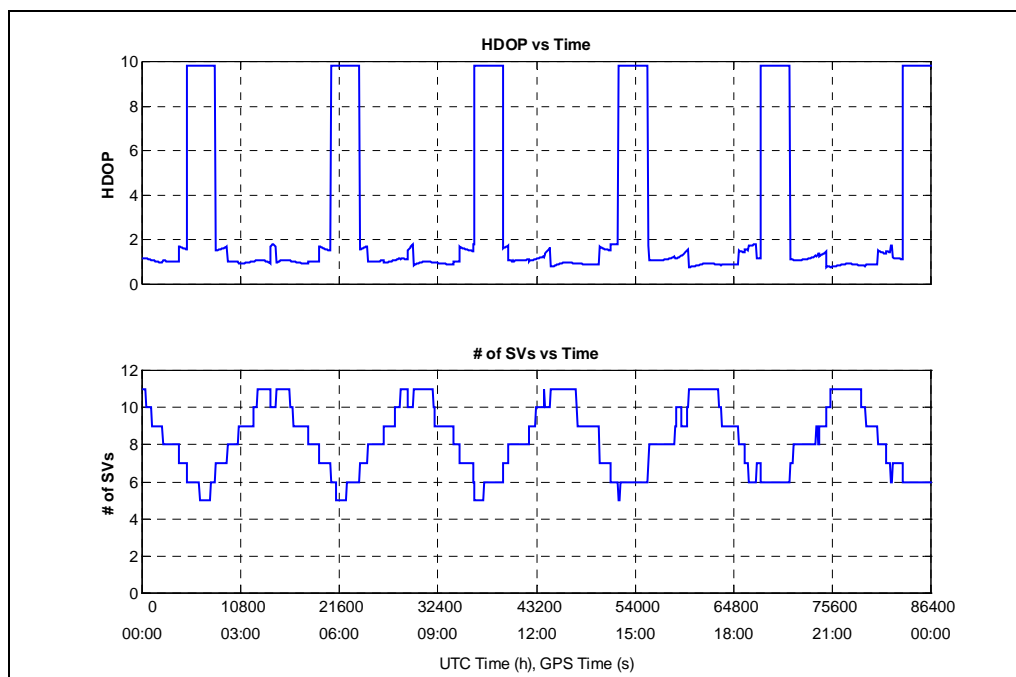


Figure A-5 HDOP and Number of Satellites Tracked for the Entire Test from C³NAVG²TM

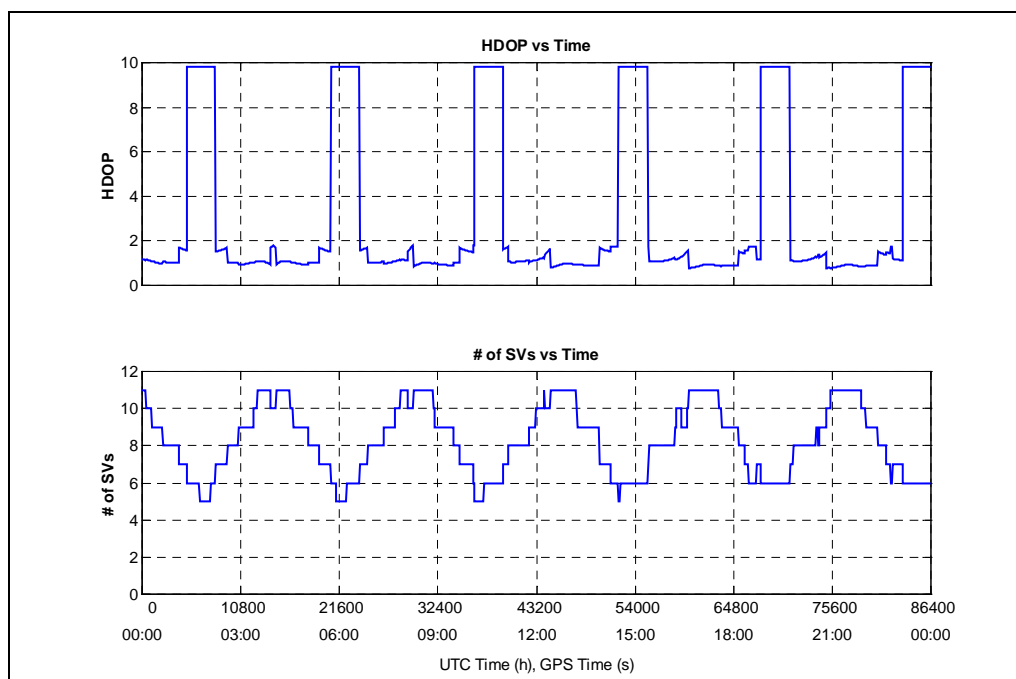


Figure A-6 HDOP and Number of Satellites Tracked for the Entire Test from GGPLAN

The next question that must be answered is. Why does the HDOP spike during the test?. In order to answer this question the first poor geometry period is examined 4860 - 8040 s. Figure A-7 and Figure A-8 show the satellite polar plot and the HDOP / Number of satellites respectively for the first poor geometry period. The HDOP jumps to > 10 as soon as PRN #11 is dropped and returns to normal once PRN #17 is acquired. The other satellites appear to be in a straight line, which would explain the poor geometry. The beginning of the first poor geometry period has been blown up in Figure A-9 and Figure A-10. Figure A-9 also contains the horizontal error ellipse. The semi-major axis of the ellipse is 42 with the semi-minor being 0.7. Thus since the visible satellites are essentially in a straight line the HDOP is extremely poor.

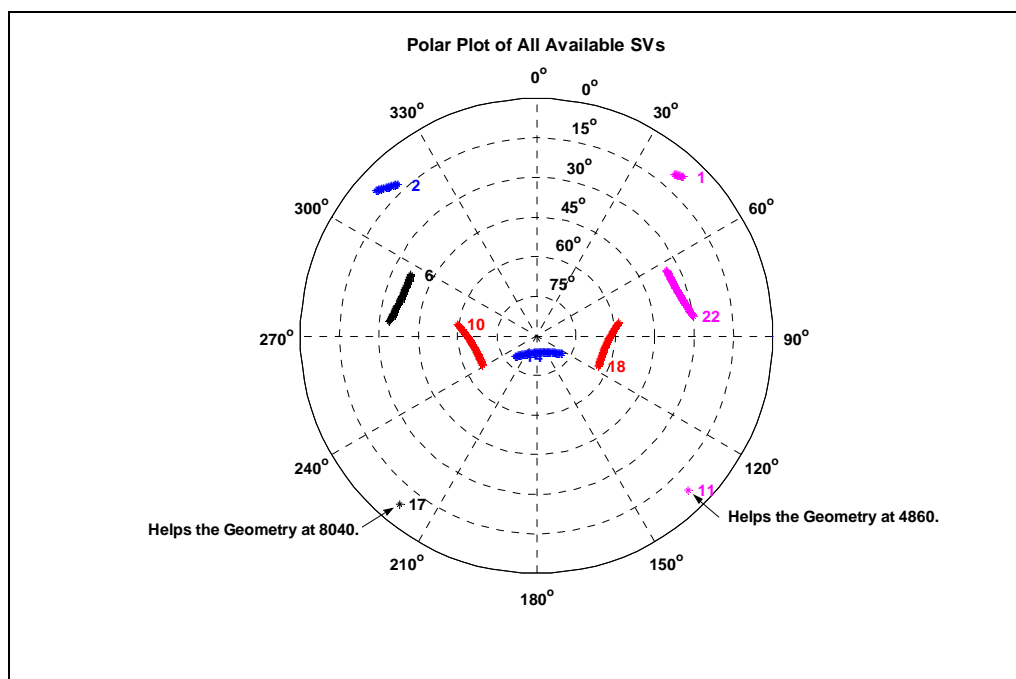


Figure A-7 Satellite Visibility for the First Poor Geometry Period from C³NAVG²™ (4860-8040)

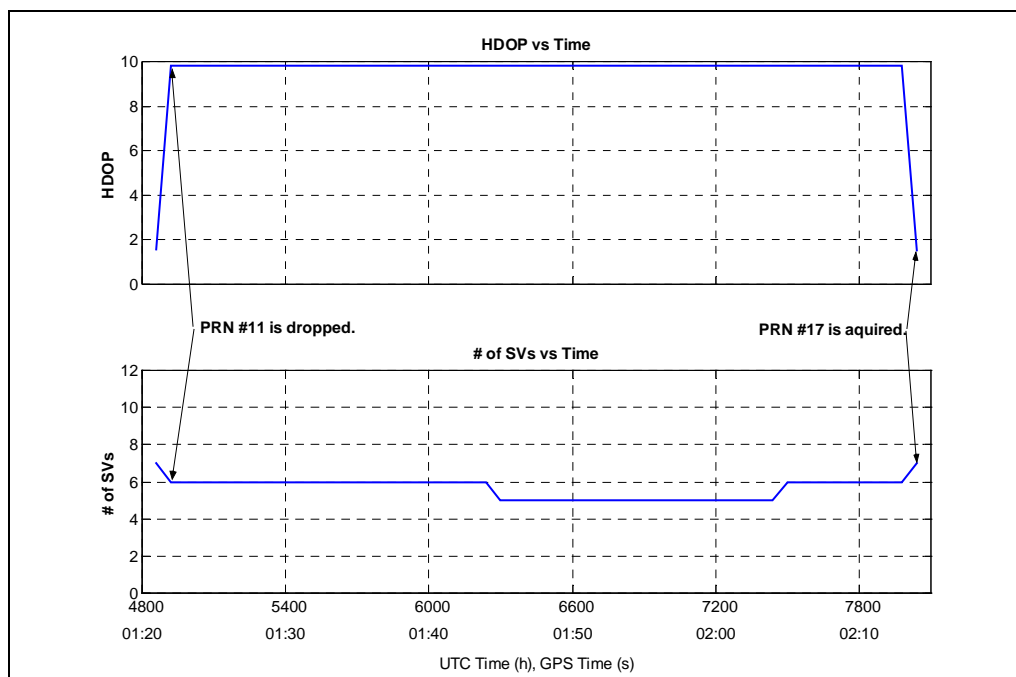


Figure A-8 HDOP and Number of Satellites Tracked: First Poor Geometry Period from C³NAV²™ (4860 - 8040)

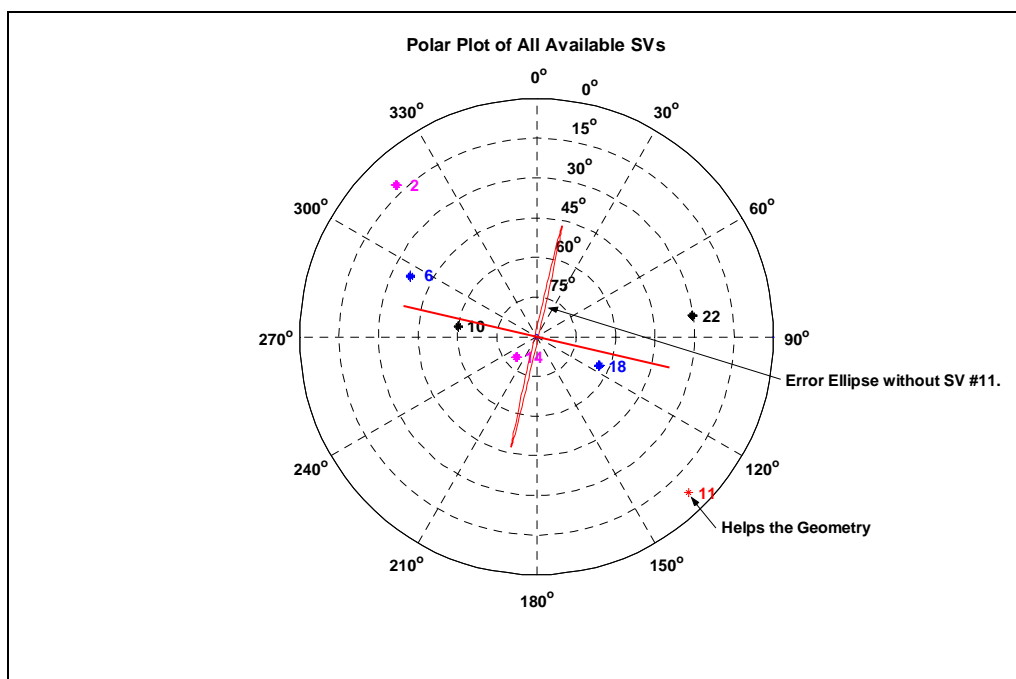


Figure A-9 Satellite Visibility for the Beginning of the First Poor Geometry Period from C³NAV²™ (4910 - 5000)

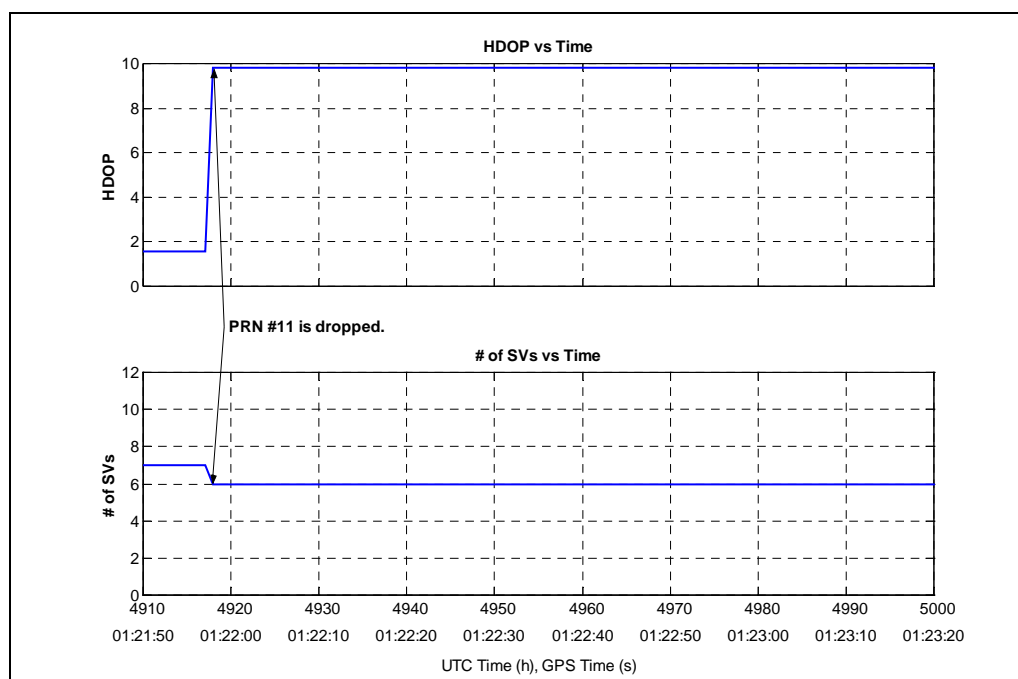


Figure A-10 HDOP and Number of Satellites Tracked for the Beginning of the First Poor Geometry Period from C³NAVG²™ (4910 - 5000)

The almanac used for the simulation must be wrong. The almanacs for the five constellations listed in Table A-1 were generated with Eastward phasing. The tests were redone with Westward phasing almanacs. Figure A-11 to Figure A-15 show the global results for the five constellations with westward phasing. The availability results for all of the constellations are as expected. The entire problem was caused by incorrect phasing of the satellites in their adjacent planes.

Figure A-16 shows the locations of the satellites within their orbital planes for eastward and westward phasing of the adjacent orbital planes. Both constellations seem normal, however, as illustrated above only westward phasing can be used.

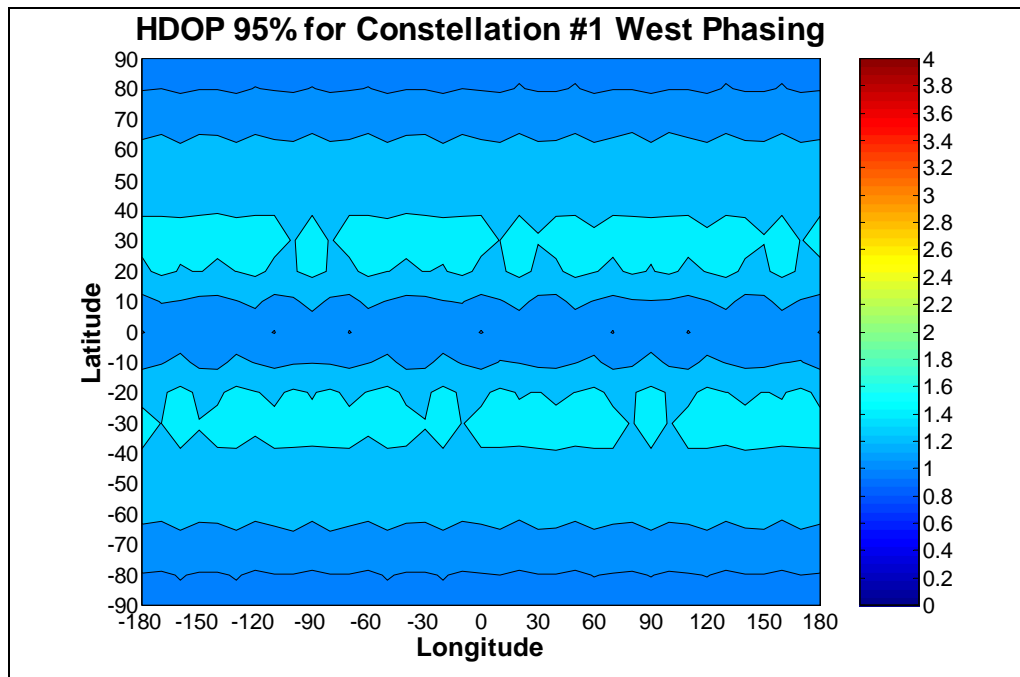


Figure A-11 HDOP 95% for the World using the Constellation #1 with Westward Phasing.

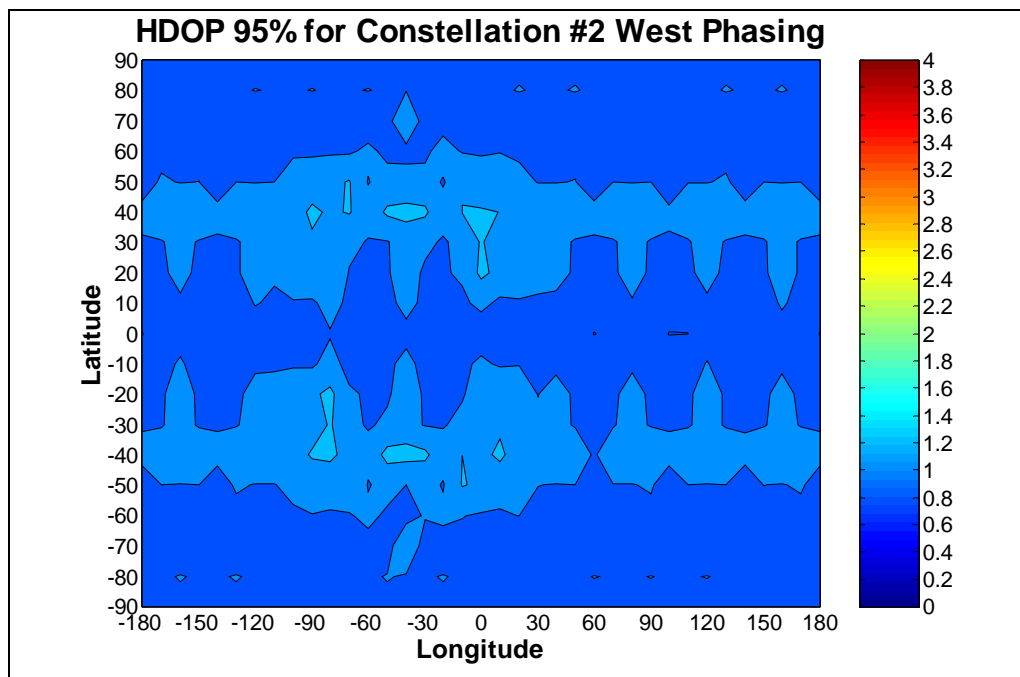


Figure A-12 HDOP 95% for the World using the Constellation #2 with Westward Phasing.

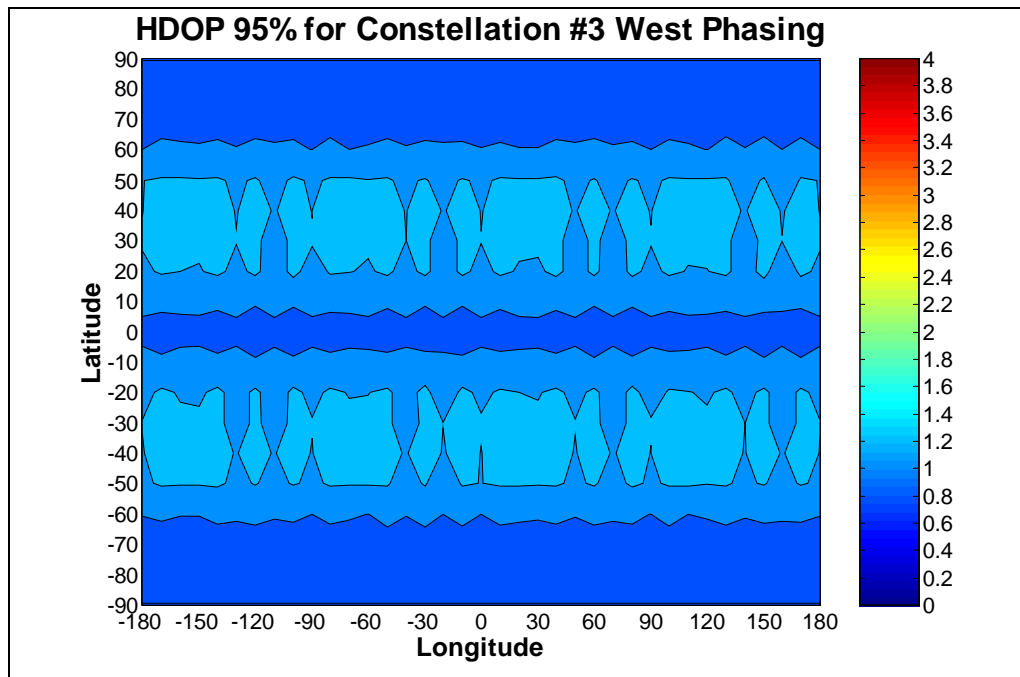


Figure A-13 HDOP 95% for the World using the Constellation #3 with Westward Phasing.

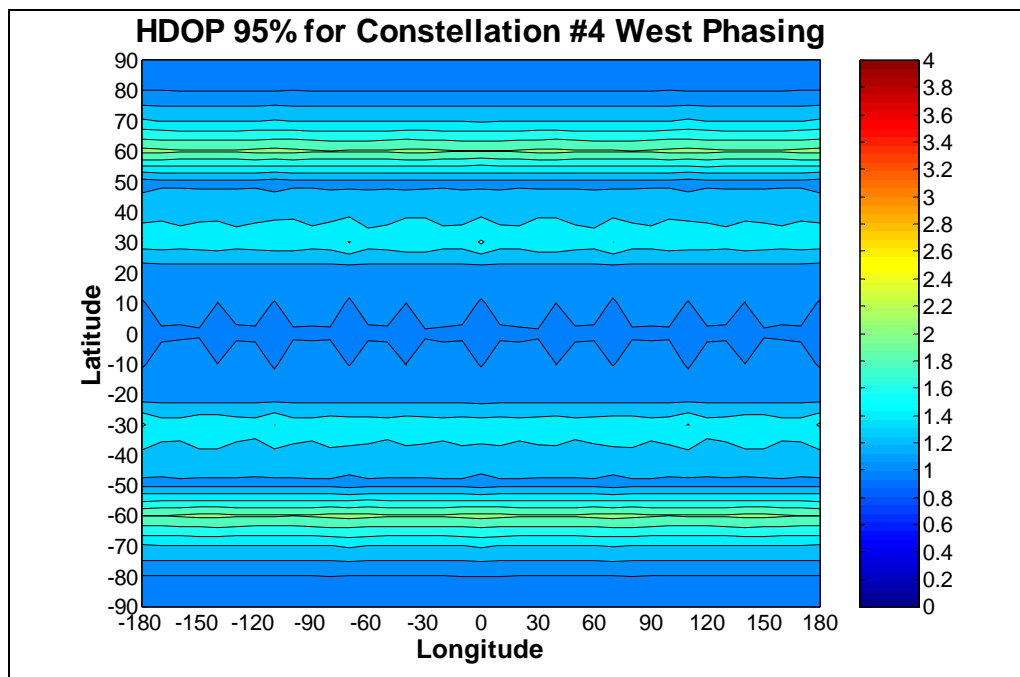


Figure A-14 HDOP 95% for the World using the Constellation #4 with Westward Phasing.

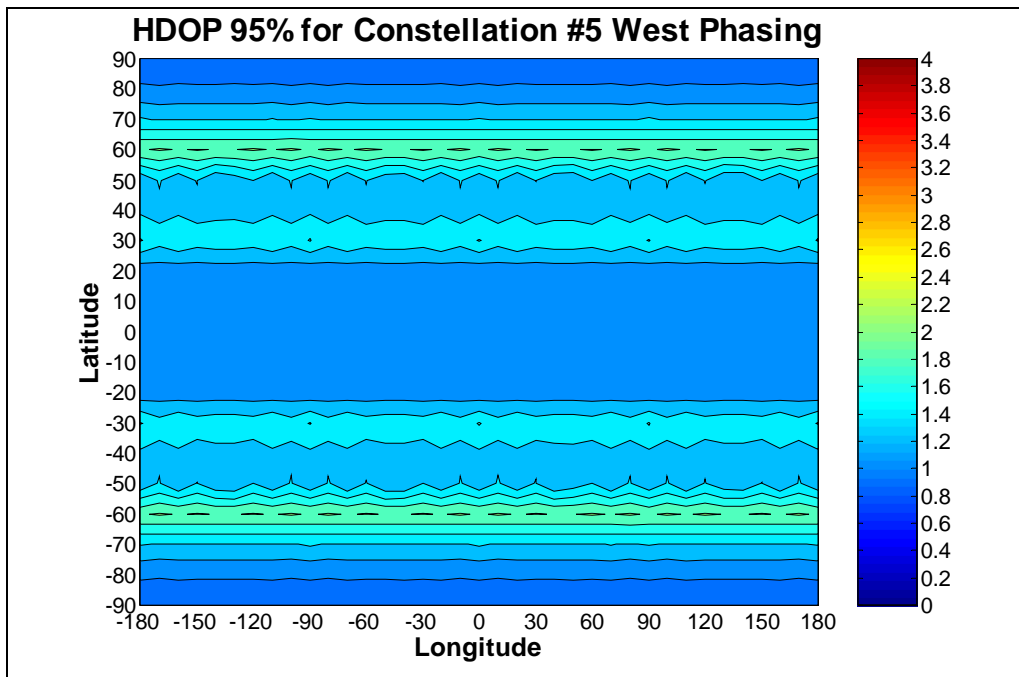


Figure A-15 HDOP 95% for the World using Constellation #5 with Westward Phasing.

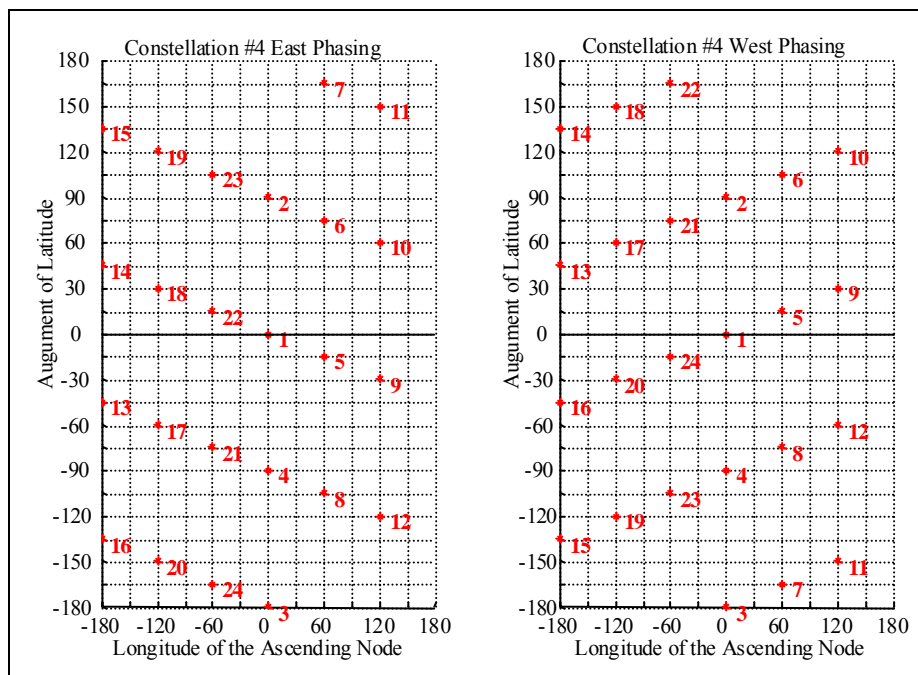


Figure A-16 Satellite Locations Within Their Orbital Planes for Different Orbital Plane Phasing of Constellation #4

APPENDIX B

MULTIPATH SIMULATION ANALYSIS PROGRAM FILE DESCRIPTIONS

This appendix provides sample option and reflector option files for the multipath simulation analysis program as well as descriptions of the input and output files.

B.1 Option File Description

A sample input file for the multipath simulation analysis program is as follows:

MULTIPATH SIMULATION ANALYSIS PROGRAM VERSION 3.0

```

START WEEK NUMBER           : 1023
START TIME (GPS SECONDS)    : 0.0
STOP WEEK NUMBER           : 1023
STOP TIME (GPS SECONDS)    : 86400.0
DATA INTERVAL (SECONDS)    : 5.0
MASK ANGLE (DEGREES)       : 5.0
ANTENNA GAIN PATTERN MODE  : INTERNAL
CORRELATOR SPACING CHIPS (E-P) : 0.50
DLL DISCRIMINATOR (COHERENT/DOT): DOT

REFLECTOR INPUT FILENAME   : e:\files\source\multisim\ver2\reflection.txt
OUTPUT FILENAME            : e:\junk\test2
SATELLITE POS (EPH/ALM)    : ALM
EPHEMERIS/ALMANAC FILE NAME : e:\files\almanac\yuma1023.txt

REFERENCE POSITION          PHI : 51 0 0.00
                           LAMBDA : -114 0 0.00
                           HEIGHT : 0.00
ANTENNA IN LOCAL GEODETIC (XYZ) : 1.000 0.000 17.000

```

Start and Stop Week: The start and stop week numbers must match the week numbers contained in the almanac.

Start and Stop Time: The start and stop times are the seconds into the specified week.

Data Interval: The data interval defines the time when the multipath errors are calculated for all visible satellites.

Mask Angle: A constant mask angle is used for the simulations.

Antenna Gain Pattern Mode: Antenna Gain pattern can be either none or internal. If none is selected then it is assumed that the receiving antenna is an omni-directional linearly polarised antenna. If internal is selected then the gain patterns for the right and left hand polarisation's as shown in Figure 2.42 will be employed.

Correlator Spacings: The correlator spacing between the early and prompt correlators is normally 0.5 and 0.05 for the wide and narrow correlators respectively. Which is 1.0 and 0.1 chips between the early and late correlators. Other correlator spacings can also be specified.

DLL Discriminator: The program has two built in discriminators. A coherent early minus late discriminator and a non-coherent dot product discriminator, infinite bandwidth is assumed.

Reflector Input Filename: The simulation program finds all of the valid reflection points from a defined area, composed of polygons. This is the filename for that input file.

Output Filename: The output filename is the root filename that will be used to create the following output files:

- 1) Output Results File
- 2) Output Summary File
- 3) Output Individual Satellite File

Satellite Pos: Specify whether to use the almanac or ephemeris to generate the satellites position. Currently only the almanac option is available.

Ephemeris/Almanac File Name: The name for the satellite position file.

Reference Position: The reference position in latitude, longitude, and height must be specified for the simulations. North, east and up are the positive directions. This defines the reference point for the simulations. The GPS antenna and the reflector input file positions are in local geodetic with reference to this position.

Antenna In Local Geodetic (XYZ): This is the GPS antenna's position in local geodetic (XYZ) in relation to the reference position defined above.

B.2 Reflector Input Filename Description

The reflector input file, defines the environment over which the multipath simulations will be conducted. The polygons defined within this file will be used to determine if there are any valid multipath reflection points for every satellite in view. The program can handle 50 separate polygons, each with a maximum of 10 vertices. Each polygon must be defined as follows:

```
REFLECTOR MODE           : PLANE
REFLECTOR MAGNITUDE      : 0.5
REFLECTOR PHASE          : 0.0
40.000000 10.000000 0.000000
40.000000 10.000000 10.000000
-40.000000 10.000000 10.000000
-40.000000 10.000000 0.000000
```

Reflector Mode: The reflecting surface can be either a fixed reflection, meaning that a reflection is forced from this point regardless of the geometry, or the reflector is a plane reflector defined by a set of vertices that are listed below.

Reflector Magnitude: This specifies the magnitude of the reflection coefficient for the given reflector. This is used to scale the magnitude of the reflected signal.

Reflector Phase: The resulting reflection phase shift in degrees. This is not currently used in the program.

Points: The last set of fields are the defining points in x, y, z local geodetic. If the reflector mode is fixed only the first point is read and this is the fixed reflection point. If the mode is plane, at least three points are required to define the polygon to a maximum of 10 points.

This set of four parameters is repeated for every polygon that makes up the multipath environment.

B.3 Output Summary File

The summary file named <output filename>.sum contains the specified options and reflection points. As well as error messages.

B.4 Output Results File

The output results file named <output filename>.out contains the following five parameters for each epoch:

- 4) Time in seconds into the week
- 5) Number of visible satellites for the epoch
- 6) The number of satellites that contained a code error greater than 1.0 m for that epoch
- 7) The maximum code error for that epoch
- 8) The second largest code error for that epoch

B.5 Output Individual Satellite File

The individual satellite files are named <output filename>.xxx where xxx is the satellite number zero padded (thus PRN 1 would be .001). The following parameters are output to the satellite's file:

- 9) Time in seconds into the week
- 10) The satellites PRN
- 11) The satellite's azimuth in degrees
- 12) The satellite's elevation in degrees
- 13) The multipath induced code error in meters
- 14) The multipath induced carrier phase code error in meters
- 15) The number of valid multipath reflection points that occurred for that satellite

APPENDIX C

ADDITIONAL MULTIPATH SIMULATIONS

C.1 Introduction

The multipath simulations presented in Chapter 3 attenuated all of the multipath signals by an additional 3 dB. This additional factor was intended to account for the simplifications made regarding the smoothness of the surface, and ignoring the Fresnel zone. To obtain a worst case estimate of the marine multipath errors, the simulations were re-run without the additional 3 dB factor.

C.2 Simulation Results

Figure C - 1 gives a summary of the marine multipath simulations. The statistics for the largest and second largest multipath errors for both the large ship and the survey launch are presented for the wide and narrow correlators. The top panel of the figure shows that the narrow correlator's maximum error exceeds that of the wide correlator by approximately 100 m. This seems counter intuitive, since the narrow correlator usually reduces the maximum multipath error. When the other percentiles (99.9%, 99% and 68%) are examined in both panels of the figure, the narrow correlator indeed shows superior performance. Is there a mistake in the simulations, or is this multipath error possible?

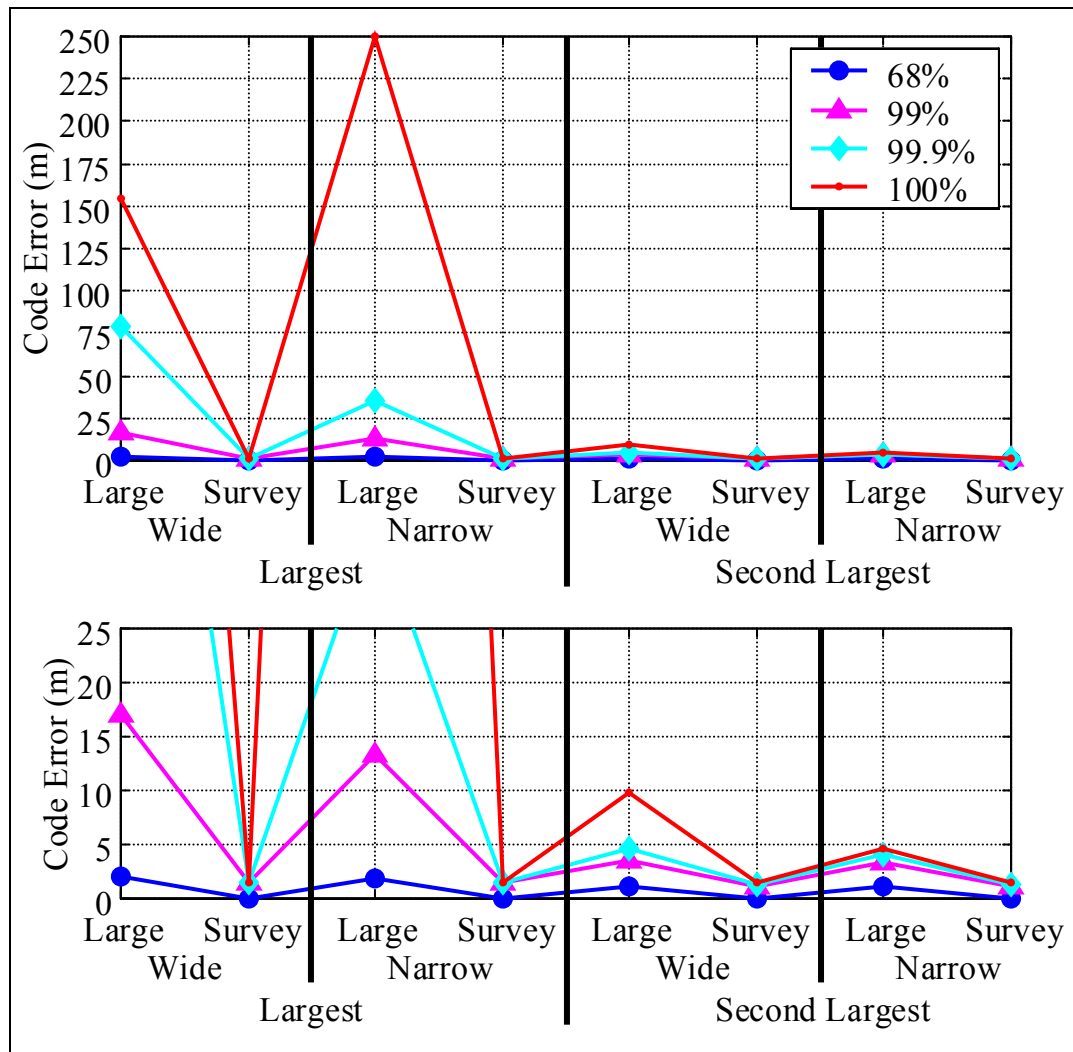


Figure C - 1 Multipath Simulation Summary Results Without the 3 dB Attenuation

Figure C - 2 shows the time series for the large ship's largest multipath error with an orientation of 60° for both the wide and narrow correlators. The anomalous result occurs just after 12:00 to both correlators. At first the narrow correlator minimises the error and then once the wide correlator has peaked at an error of 150 m the narrow correlator suddenly jumps to 250 m, and then snaps back down again. Figure C - 3 shows the range error for the period in question.

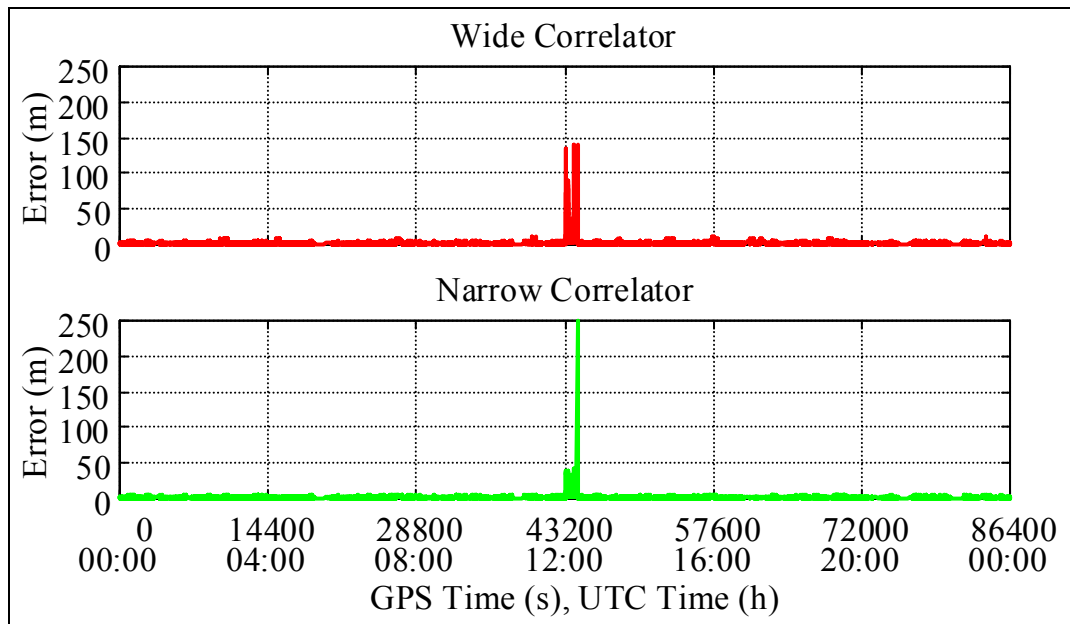


Figure C - 2 Large Ship, Largest Multipath Error, Ship Orientation 60°

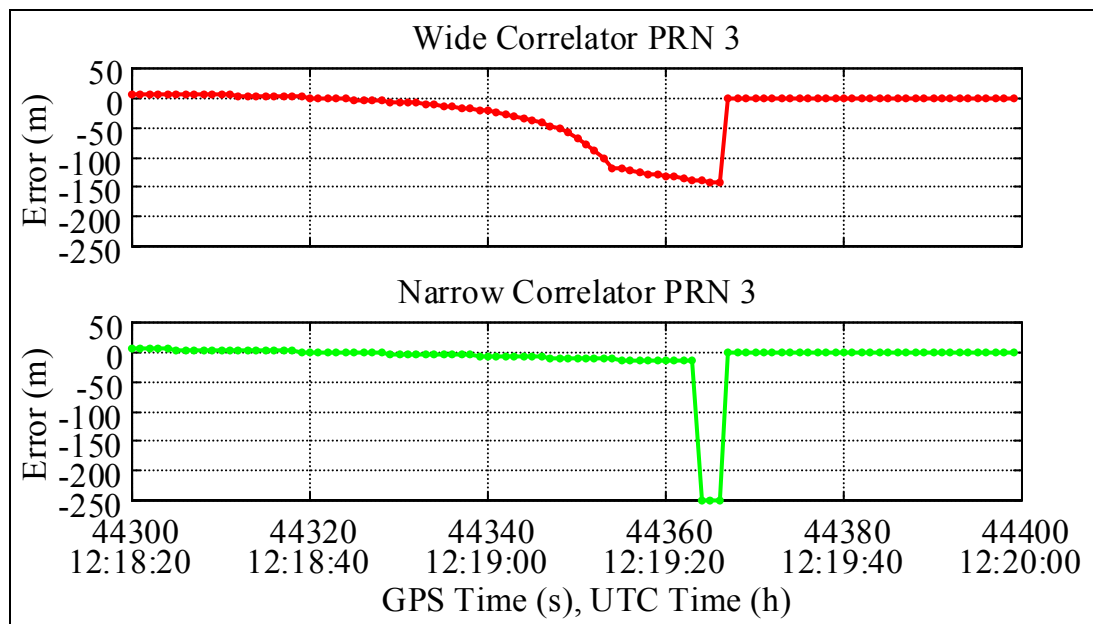


Figure C - 3 Large Ship, PRN 3's Code Multipath Error, Ship Orientation 60°

From Figure C - 3, the wide correlator's range error gradually changes from 7.8 m at 44300 to -142.4 m 66 seconds later. The next epoch one of the multipath reflections is blocked which causes the error to snap down to -1.1 m. The magnitudes and gradual

nature of the wide correlator error is believable. However, the narrow correlator shows a completely different behaviour. From 44300 to 44363 the ranging error gradually changed from 5.4 -14.5 m, however, the next epoch the error snaps down to -250 m, stays there for three seconds and then at 44367 when one of the multipath reflections is blocked the error snaps back to -1.0 m. While the snapping back to a small error after the removal of a multipath signal is expected, the drop from -14.5 to -250 m in one epoch is not expected nor believed. The narrow correlators ranging errors jumped from epoch 44363 to 44364, thus these two epochs will be examined in detail. The reflection parameters for the multipath signals during these two epochs are given in Table C - 1. Reflection #1 is from the main deck of the ship and reflection #2 is from the ship's mast.

Table C - 1 Reflection Parameters

Time	Reflection #1		Reflection #2	
	Magnitude	Delay	Magnitude	Delay
44363	0.3591	2.7399 m	0.7504	29.4104 m
44364	0.3589	2.7413 m	0.7503	29.4098 m

The DLL discriminator output for epochs 44363 to 44364 will be examined to determine if mathematically this multipath error could occur. Figure C - 4 shows the discriminator outputs for the two epochs. The x-axis shows the receiver's tracking point with the y-axis showing the corresponding discriminator output. The receiver's tracking point is updated via the following equation, where the DLL output in this simulation is from a dot product non-coherent discriminator:

$$\hat{\tau}_{i+1} = \hat{\tau}_i - \frac{\text{DLL Output}_i}{2} \quad (\text{C} - 1)$$

Figure C - 4 contains four panels, (a) / (b) correspond to epoch 44363 and (c) / (d) correspond to epoch 44364. The far right panels (b) / (d) are zoomed versions of the left side panels (a) / (c). The green dots in the figure show the update path for the DLL

discriminator for both epochs. The assumption is made that the receiver's initial tracking point is at point #1.

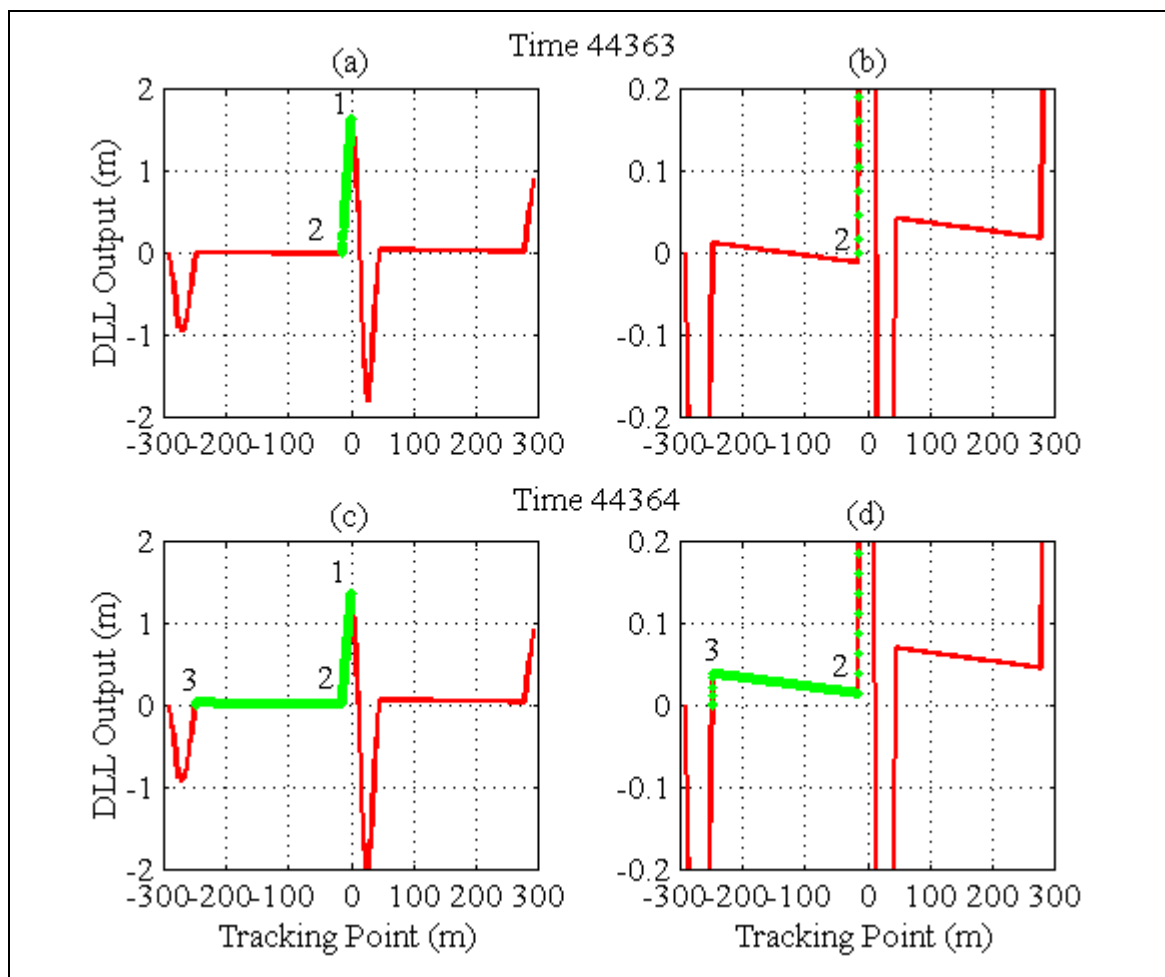


Figure C - 4 DLL Discriminator Output for Epochs 44363 and 44364

Examining the top two panels (a) / (b), the receiver starts at point #1 with a DLL output value of 1.4. Thus by applying (C - 1) the DLL tracking point will slowly move from point #1 to point #2 in approximately 104 iterations of the tracking loop. If the receiver was tracking the signal since 44300, the DLL would already be tracking at point #2. As shown in panel (b), point #2 is barely a zero crossing for the discriminator curve. At the next epoch (44364), point #2 is no longer a zero crossing. If the DLL starts at point #1, it will follow the green dots to point #2, and will continue to the zero crossing at point #3.

However, once point #2 is reached the DLL output will only be a few centimetres per update, therefore it will take approximately 18,000 updates for the tracking loop to reach the maximum possible error of -250 m.

Mathematically this 250 m error could occur, however, 18,000 updates is too long. In this marine multipath simulation, this large error only stayed for 3 seconds. Since most receivers use the a predetection integration time of 20 ms, and hence update their tracking loops at 50 Hz, there would only be 150 loop iterations for the error to grow. Table C - 2 shows the narrow correlator range error that would occur for various loop iterations, for the current multipath set-up. Thus the multipath conditions would have to persist for at least 60 seconds for the range error to grow to -39.1 m, after three seconds the error has only grown to -15.5 m.

Table C - 2 Narrow Correlator Errors for Various Loop Iterations

Time (s)	1	2	3	10	30	60	120	>360
Iterations	50	100	150	500	1500	3000	6000	>18,000
Error (m)	-14.8	-15.2	-15.5	-18.3	-26.3	-39.1	-67.9	-250

In addition to the huge number of iterations required to reach the maximum error, the receiver may loose lock before the maximum error is even reached. Figure C - 5 shows the autocorrelation triangles for the direct (green), multipath (red and magenta), and combined (black) signals for epoch 44364. The multipath signals are almost directly out of phase with the direct signal, which results in the combined signal having a maximum correlation value of only 0.08. The combined received power as calculated from the in-phase component and the quadra-phase components is plotted in Figure C - 6. The maximum combined received power is -20.2 dB below the direct signal alone. The minimum received power within ± 0.5 chips of 0 m delay is -33.1 dB. With 20-30 dB of attenuation the receiver is almost guaranteed to loose lock. Some receivers may still track the code for 0.5 to 1 second before declaring loss of lock. The exact receiver actions will depend on the receiver design. However, one can be assured that the receiver will not

track the attenuated signal for 360 seconds, which is the approximate time required to reach the maximum multipath error.

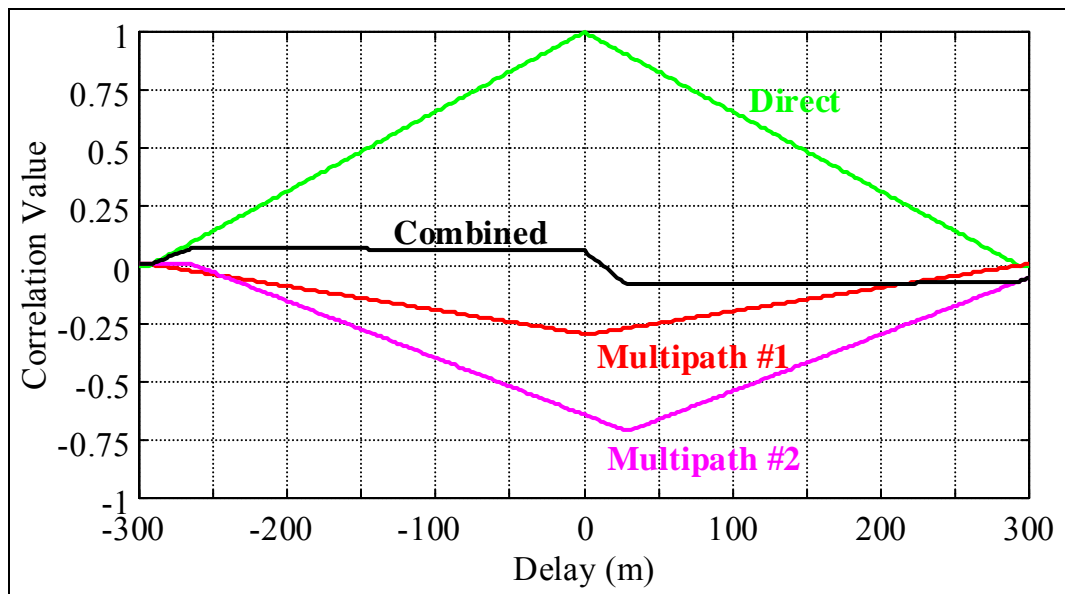


Figure C - 5 Autocorrelation Functions for Epoch 44364

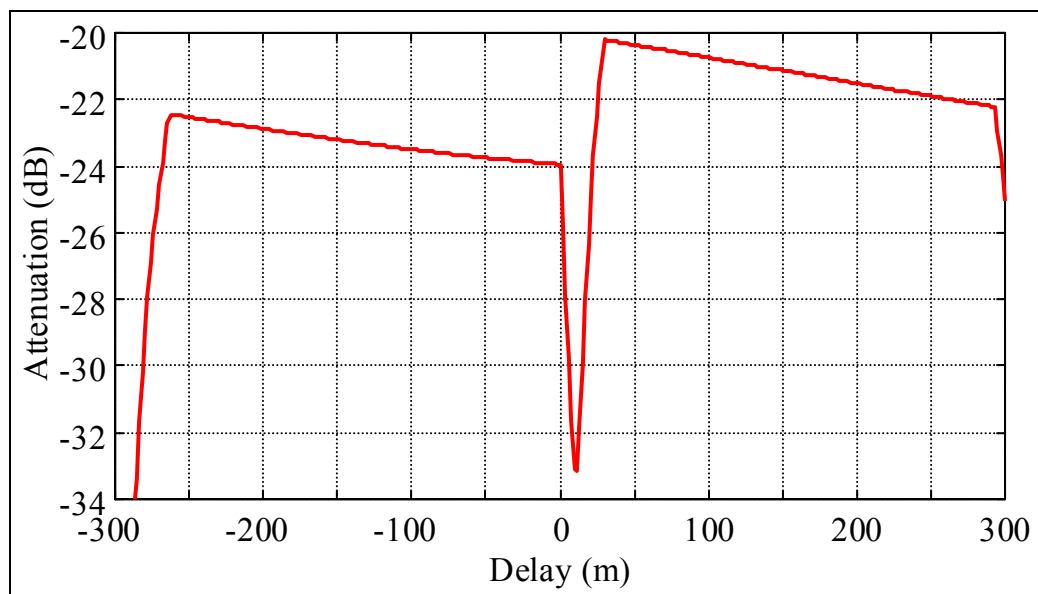


Figure C - 6 Power Loss due to Multipath Signals

C.3 Summary

While mathematically it is possible for the narrow correlator to have a tracking point that is in error by 250 m, it is not probable. First the multipath signals themselves must be of sufficient strength to almost completely cancel the direct signal, resulting in extremely distorted correlation and discriminator functions. Second the time required for the narrow correlator DLL to converge to the extreme tracking point exceeds 360 seconds. In the current simulation the multipath conditions only existed for three seconds. Finally even if the multipath conditions lasted for sufficient period of time, the receiver would probably loose lock on the signal, since the combined signal's power level is between 20-30 dB below that of the direct signal alone.

APPENDIX D

ADDITIONAL IONOSPHERIC SIMULATIONS

D.1 Introduction

The ionospheric simulation in section 2.5.3 assumed that the user was 5° north of the reference station. A second simulation was conducted with the user only 3° north of the reference station.

D.2 Simulation Results

Figure D - 1 contains the 95% differential misclosures for each simulation location and ionospheric profile. As expected from the previous simulations, the SED misclosures are the largest. The 95% peak is 25.0 m and it exceeds 10 m for 18° of latitude (35° N - 55° N). The maximum misclosure of 35.8 m occurred with the reference station at 47° N. The ionospheric trough also generates 95% misclosures exceeding 10 m, however, its 95% peak was 13.4 m approximately half of the SED value. In the 5° simulation the steep TEC gradient's maximum were minimal and they are even smaller for the shorter baseline. The steep TEC gradient's 95% maximum misclosure was only 1.8 m, and its overall maximum value was 2.7 m. These results are only slightly smaller than the 5° case.

Figure D - 2 takes each ionospheric profile and plots the 95% largest, second largest, and third largest simultaneous misclosure. Again the ionospheric trough and the storm enhanced density show three distinct lines for the three misclosures. These misclosure results are once again only slightly smaller than the 5° case.

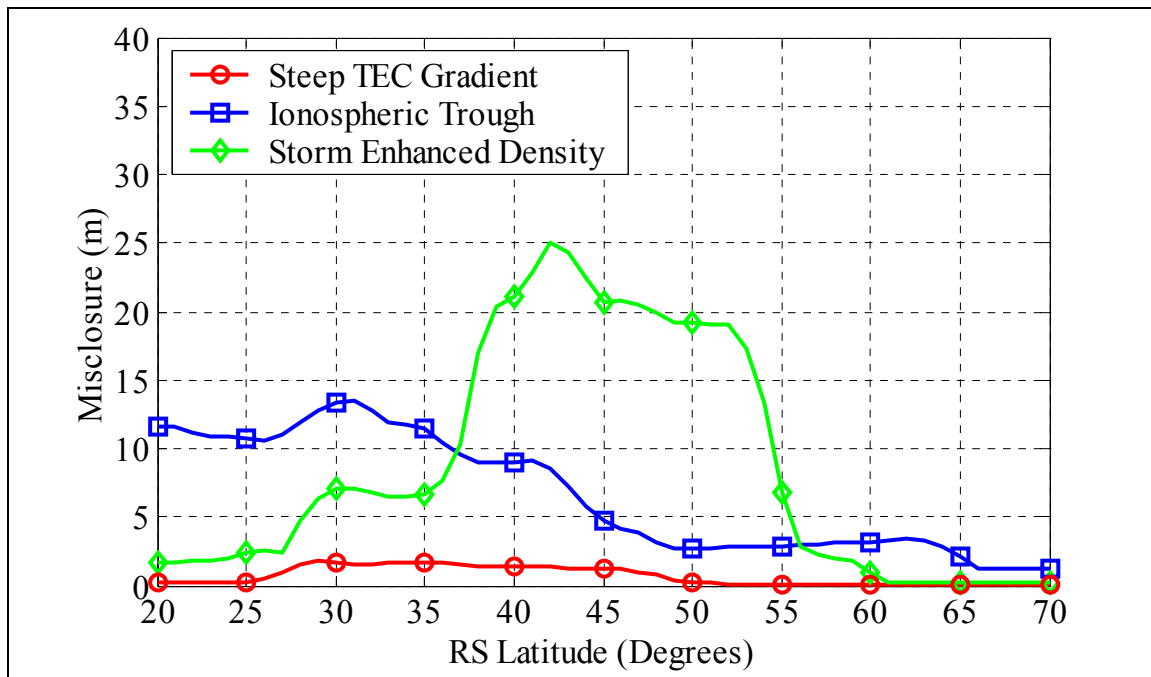


Figure D - 1 Satellite Misclosures (95%)

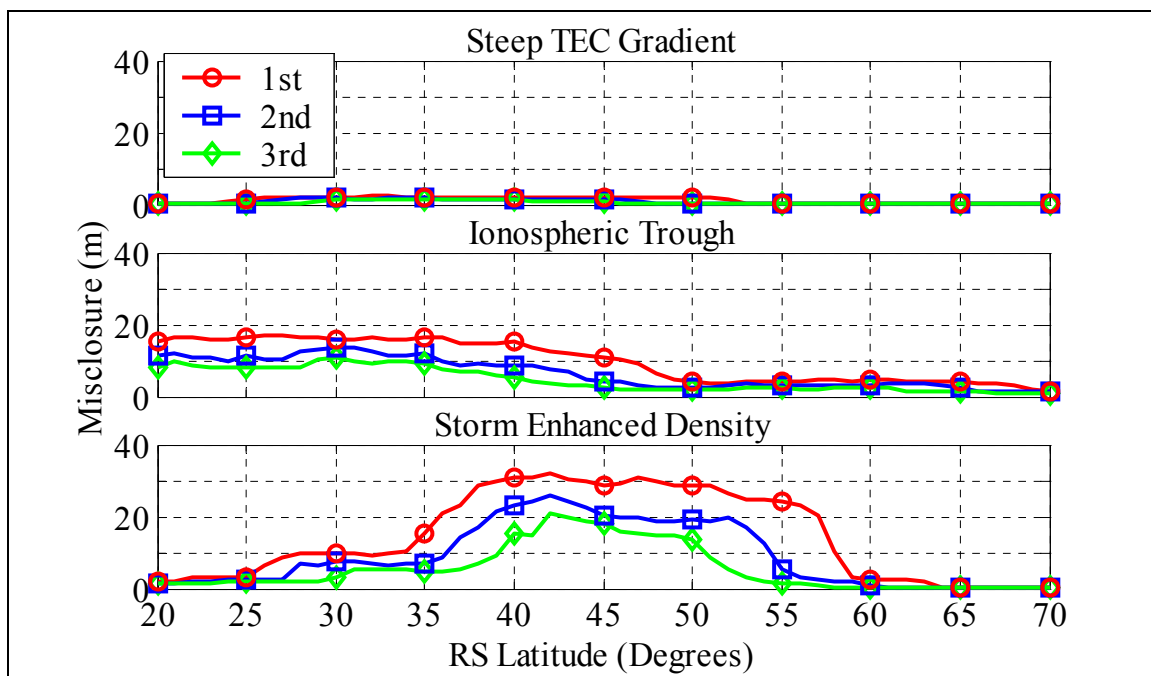


Figure D - 2 1st, 2nd, and 3rd Simultaneous Differential Satellite Misclosures (95%)

The misclosures were then propagated into the position domain. Figure D - 3 plots the 95% results for the HPE and VPE. The SED's maximum 95% HPE was 28.8 m and it exceeded 10 m for 19° of latitude. Although the baseline length was reduced by 40%, the resulting HPEs are still very large. The ionospheric trough is almost half of the SED values, with a maximum 95% HPE of 14.2 m. The ionospheric trough produced 95% HPEs exceeding 10 m for 13° of latitude.

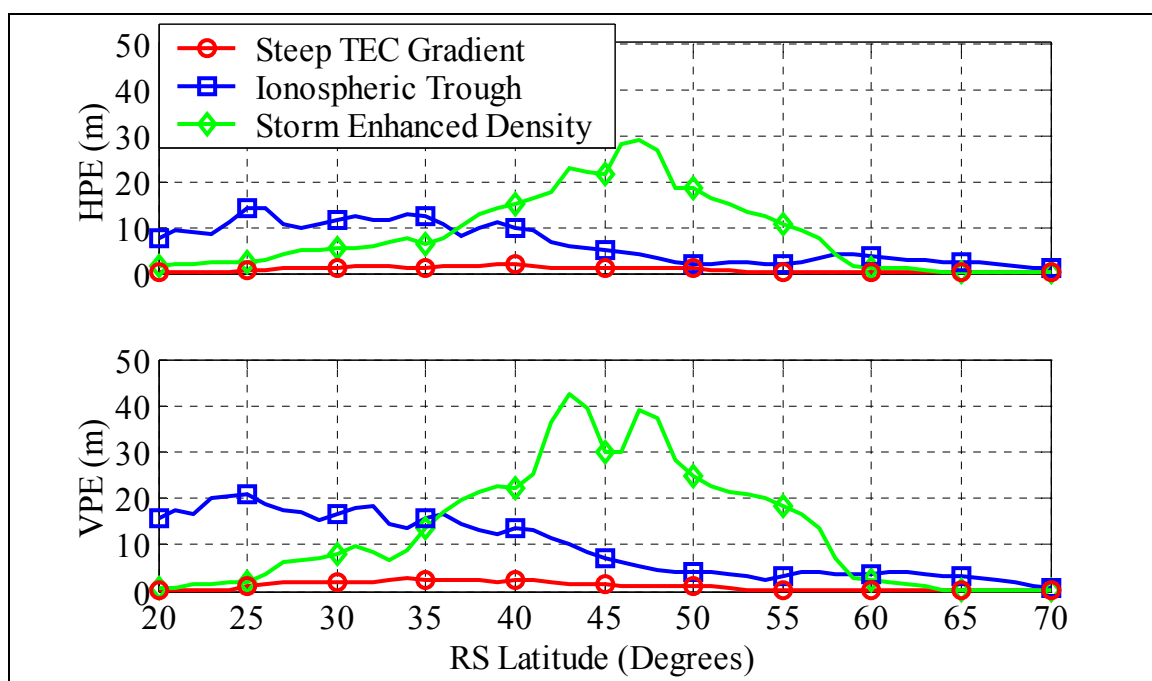


Figure D - 3 Position Errors

Thus reducing the baseline distance by 40% does not reduce the misclosures and the resulting position errors by the same amount for the SED. This stems from the nature of the SED. The SED is characterised by a spike in TEC several degrees wide. As long as only one of the ionospheric pierce points is on this spike, large misclosures and position errors will occur.

APPENDIX E

ADDITIONAL KALMAN FILTER DYNAMIC MODELS

E.1 Introduction

Three additional Kalman filter dynamic models are included in this appendix. The constant position, velocity, and acceleration models.

E.2 Constant Position Model

The constant position model, assumes that the user's position is slowly changing. Thus the velocity is modelled as white noise.

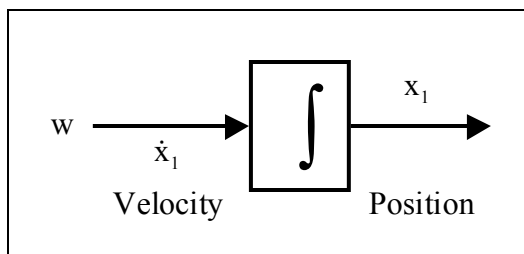


Figure E - 1 Constant Position State Diagram

$$\begin{aligned} [\dot{x}_1] &= [0] \cdot [x_1] + [S] \cdot w \\ \dot{x} &= F \cdot x + G \cdot w \end{aligned} \tag{E - 1}$$

The state transition matrix ϕ is the inverse Laplace transform of the resolution matrix:

$$\phi = L^{-1} \left((s \cdot I - F)^{-1} \right) \Big|_{t=\delta t} \tag{E - 2}$$

Substituting the value of F from equation (E - 1) into equation (E - 2) and performing the inverse Laplace transform results in the following state transition matrix:

$$\phi = 1 \quad (\text{E - 3})$$

Thus when the state transition matrix is used to propagate the states via $x_{n+1} = \phi \cdot x_n$ this expands to:

$$x_{n+1} = x_n \quad (\text{E - 4})$$

The process noise covariance matrix (Q_k) must be determined using:

$$Q_k = \int_{t_0}^t \phi(t-\tau) \cdot G(\tau) \cdot Q(\tau) \cdot G^T(\tau) \cdot \phi^T(t-\tau) \cdot d\tau \quad (\text{E - 5})$$

Substituting the expressions for G from equation (E - 1) and for ϕ from equation (E - 3) and I for Q into equation (E - 5) and simplifying, results in the following expression for Q_k :

$$Q_k = S^2 \cdot \delta t \quad (\text{E - 6})$$

E.3 Constant Velocity Model

The constant velocity, is just that, it assumes that the user's velocity is constant and only changes due to random white noise. This is most appropriate for low dynamic applications.

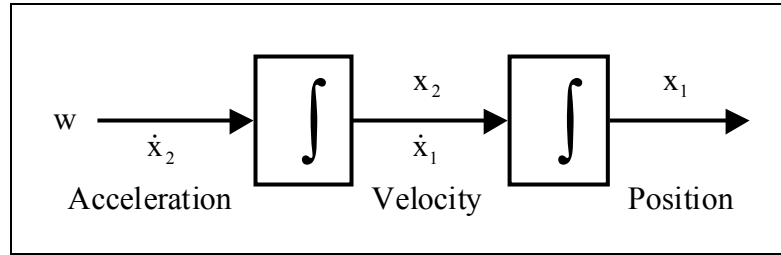


Figure E - 2 Constant Velocity State Diagram

$$\begin{bmatrix} \dot{x}_1 \\ \dot{x}_2 \end{bmatrix} = \begin{bmatrix} 0 & 1 \\ 0 & 0 \end{bmatrix} \cdot \begin{bmatrix} x_1 \\ x_2 \end{bmatrix} + \begin{bmatrix} 0 \\ S \end{bmatrix} \cdot w \quad (\text{E - 7})$$

$$\dot{x} = F \cdot x + G \cdot w$$

The state transition matrix ϕ is the inverse Laplace transform of the resolution matrix:

$$\phi = L^{-1} \left((s \cdot I - F)^{-1} \right) \Big|_{t=\delta t} \quad (\text{E - 8})$$

Substituting the value of F from equation (E - 7) into equation (E - 8) and performing the inverse Laplace transform results in the following state transition matrix:

$$\phi = \begin{bmatrix} 1 & \delta t \\ 0 & 1 \end{bmatrix} \quad (\text{E - 9})$$

Thus when the state transition matrix is used to propagate the states via $x_{n+1} = \phi \cdot x_n$ this expands to:

$$\begin{aligned} x_{n+1} &= x_n + \delta t \cdot \dot{x}_n \\ \dot{x}_{n+1} &= \dot{x}_n \end{aligned} \quad (\text{E - 10})$$

The process noise covariance matrix (Q_k) must be determined using:

$$Q_k = \int_{t_0}^t \phi(t-\tau) \cdot G(\tau) \cdot Q(\tau) \cdot G^T(\tau) \cdot \phi^T(t-\tau) \cdot d\tau \quad (\text{E - 11})$$

Substituting the expressions for G from equation (E - 7) and for ϕ from equation (E - 9) and I for Q into equation (E - 11) and simplifying, results in the following expression for Q_k :

$$Q_k = \begin{bmatrix} \frac{S^2 \cdot \delta t^3}{3} & \frac{S^2 \cdot \delta t^2}{2} \\ \frac{S^2 \cdot \delta t^2}{2} & S^2 \cdot \delta t \end{bmatrix} \quad (\text{E - 12})$$

E.4 Constant Acceleration Model

This assumes that the user is travelling with a constant acceleration, with the jerk showing up as white noise. Most commercial vehicles do not behave in this manner. Their accelerations are short duration, and they are closer to a constant velocity rather than a constant acceleration. However, the model is included for completeness.

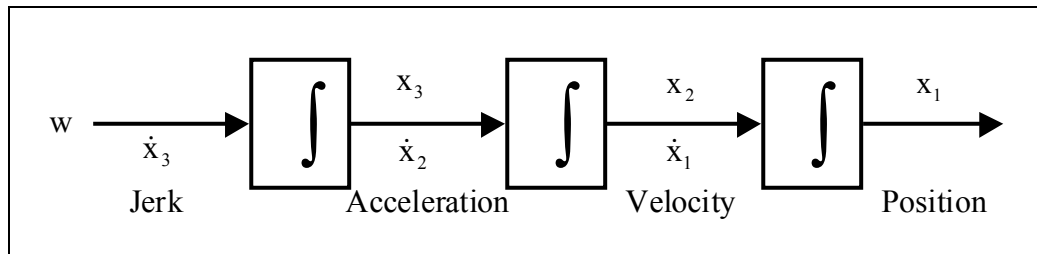


Figure E - 3 2 Constant Acceleration State Diagram

$$\begin{bmatrix} \dot{x}_1 \\ \dot{x}_2 \\ \dot{x}_3 \end{bmatrix} = \begin{bmatrix} 0 & 1 & 0 \\ 0 & 0 & 1 \\ 0 & 0 & 0 \end{bmatrix} \cdot \begin{bmatrix} x_1 \\ x_2 \\ x_3 \end{bmatrix} + \begin{bmatrix} 0 \\ 0 \\ S \end{bmatrix} \cdot w \quad (\text{E - 13})$$

$$\dot{x} = F \cdot x + G \cdot w$$

The state transition matrix ϕ is the inverse Laplace transform of the resolution matrix:

$$\phi = L^{-1} \left((s \cdot I - F)^{-1} \right) \Big|_{t=\delta t} \quad (\text{E - 14})$$

Substituting the value of F from equation (E - 13) into equation (E - 14) and performing the inverse Laplace transform results in the following state transition matrix:

$$\phi = \begin{bmatrix} 1 & \delta t & \frac{\delta t^2}{2} \\ 0 & 1 & \delta t \\ 0 & 0 & 1 \end{bmatrix} \quad (\text{E - 15})$$

Thus when the state transition matrix is used to propagate the states via $x_{n+1} = \phi \cdot x_n$ this expands to:

$$\begin{aligned} x_{n+1} &= x_n + \delta t \cdot \dot{x}_n + \frac{1}{2} \cdot \delta t^2 \cdot \ddot{x}_n \\ \dot{x}_{n+1} &= \dot{x}_n + \delta t \cdot \ddot{x}_n \\ \ddot{x}_{n+1} &= \ddot{x}_n \end{aligned} \quad (\text{E - 16})$$

The Process Noise covariance matrix Q_k must be determined using:

$$Q_k = \int_{t_0}^t \phi(t-\tau) \cdot G(\tau) \cdot Q(\tau) \cdot G^T(\tau) \cdot \phi^T(t-\tau) \cdot d\tau \quad (\text{E - 17})$$

Substituting the expressions for G from equation (E - 13) and for ϕ from equation (E - 15) and I for Q into equation (E - 17) and simplifying, results in the following expression for Q_k :

$$Q_k = \begin{bmatrix} \frac{S^2 \cdot \delta t^5}{20} & \frac{S^2 \cdot \delta t^4}{8} & \frac{S^2 \cdot \delta t^3}{6} \\ \frac{S^2 \cdot \delta t^4}{8} & \frac{S^2 \cdot \delta t^3}{3} & \frac{S^2 \cdot \delta t^2}{2} \\ \frac{S^2 \cdot \delta t^3}{6} & \frac{S^2 \cdot \delta t^2}{2} & S^2 \cdot \delta t \end{bmatrix} \quad (\text{E - 18})$$

APPENDIX F

PICTURES OF THE CANADIAN COAST GUARD SHIPS

F.1 Introduction

This appendix contains pictures of the CCG ships referenced and used in this thesis. The links to the ship's web pages have also been included.

F.2 The CCGS Martha L. Black

The CCGS Martha L. Black is a light icebreaker / major nav aids tender (buoy tender) built in 1986 by Versatile Pacific Shipyards, Vancouver, British Columbia. For information on the ship see the CCG web page

http://www.ccg-gcc.gc.ca/fleet/details_e.asp?name=MARTHA+L%2E+BLACK



Figure F - 1 Picture of CCGS Martha L. Black (CCG, 2002).

The CCGS Martha L. Black was used by the Canadian Coast Guard as a research platform to detect marine multipath (CCG, 2000 and Lachapelle et al., 2002a). The large simulated ship in CHAPTER 3 was loosely modelled on the CCGS Martha L. Black.

F.3 The CCGS F.C.G. Smith

The CCGS F.C.G. Smith is a multi-hulled survey and sounding vessel built in 1985 by Georgetown Shipyard, Georgetown, Prince Edward Island. For information on the ship, see the CCG web page

http://www.ccg-gcc.gc.ca/fleet/details_e.asp?name=F%2EC%2EG%2E+SMITH.



Figure F - 2 Picture of CCGS F.C.G. Smith (CCG, 2002).

Data from the CCGS F.C.G Smith was used to generate the Kalman filter parameters in section 2.8.

F.4 CCGS Tofino

The CCGS Tofino is a multi-task lifeboat built in 1970 by McKay Cormack Ltd, Victoria, British Columbia. For information on the ship, see the CCG web page http://www.ccg-gcc.gc.ca/fleet/details_e.asp?name=TOFINO.



Figure F - 3 Picture of CCGS Tofino (CCG, 2002).

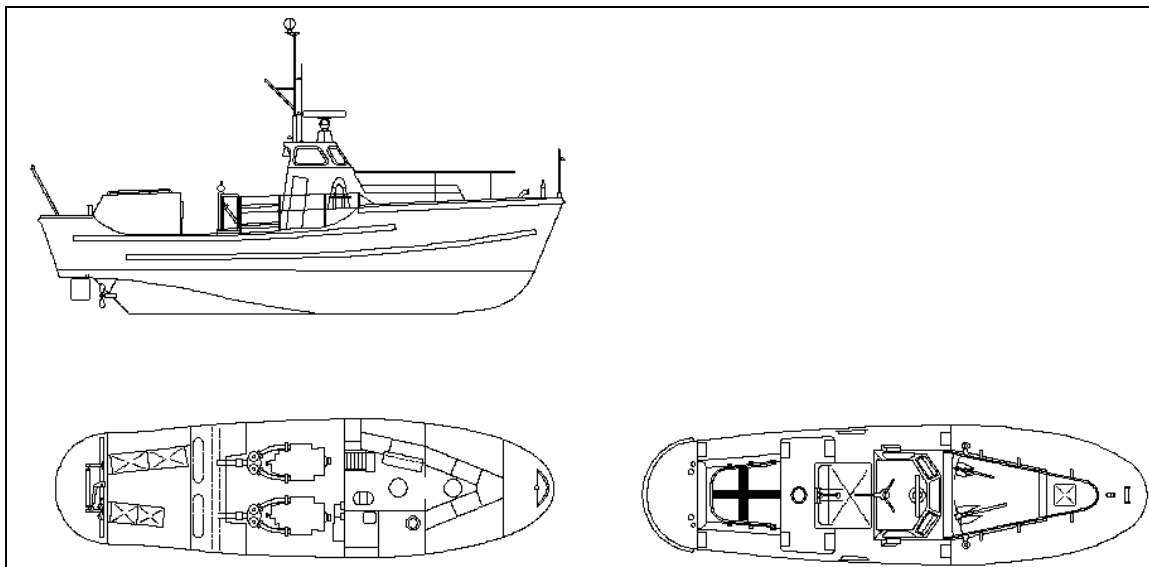


Figure F - 4 Engineering Drawings of the CCGS Tofino (CCG, 2002)

The survey launch simulated ship in CHAPTER 3 was based on the CCGS Tofino.

F.5 CCG Survey Launch the Raven

The Raven survey launch was the test platform for the Saanich Inlet test, described in CHAPTER 7.



Figure F - 5 Picture of the CCG Survey Launch Raven

APPENDIX G

ADDITIONAL RESULTS FROM THE DGPS SIGNAL SIMULATOR

G.1 Introduction

CHAPTER 6 only contains the results for the 20° mask angle for the three receivers. This appendix contains the results for all five mask angles.

G.2 NovAtel OEM3

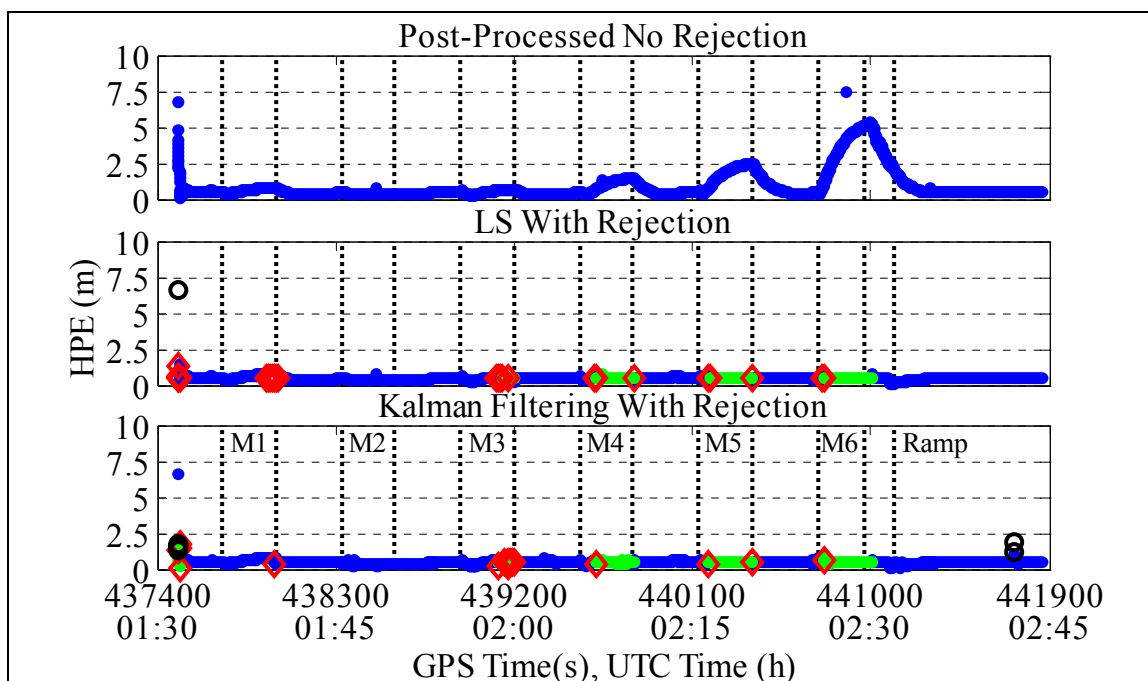


Figure G - 1 NovAtel OEM3, 5° Mask Angle, Carrier Smoothing

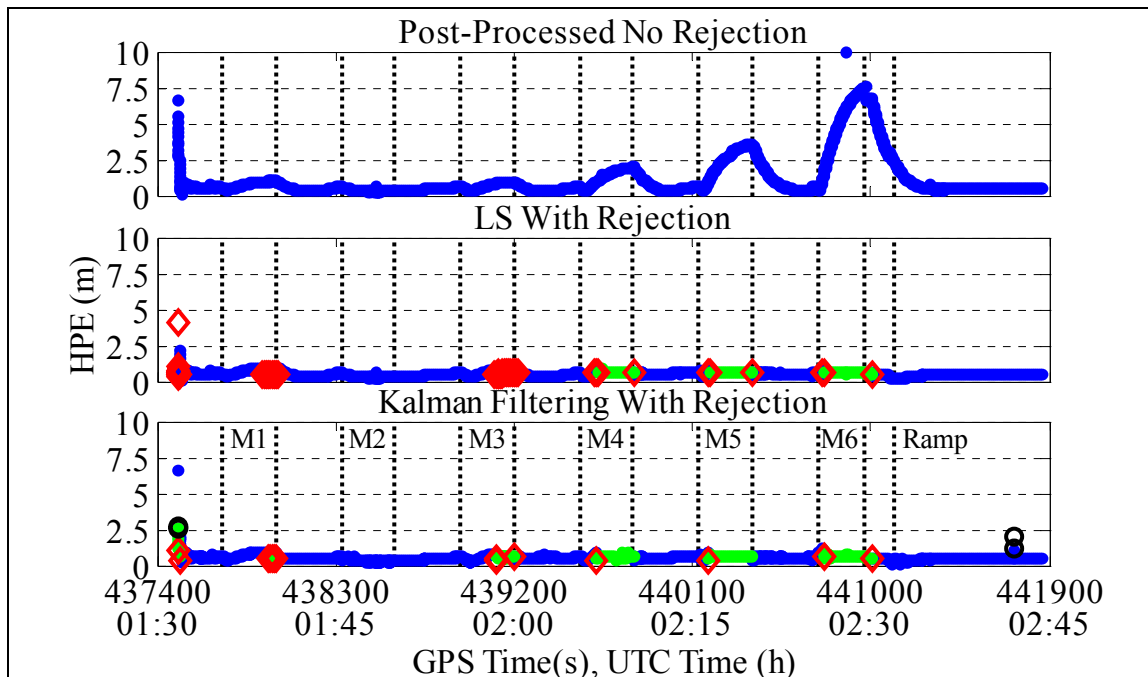


Figure G - 2 NovAtel OEM3, 10° Mask Angle, Carrier Smoothing

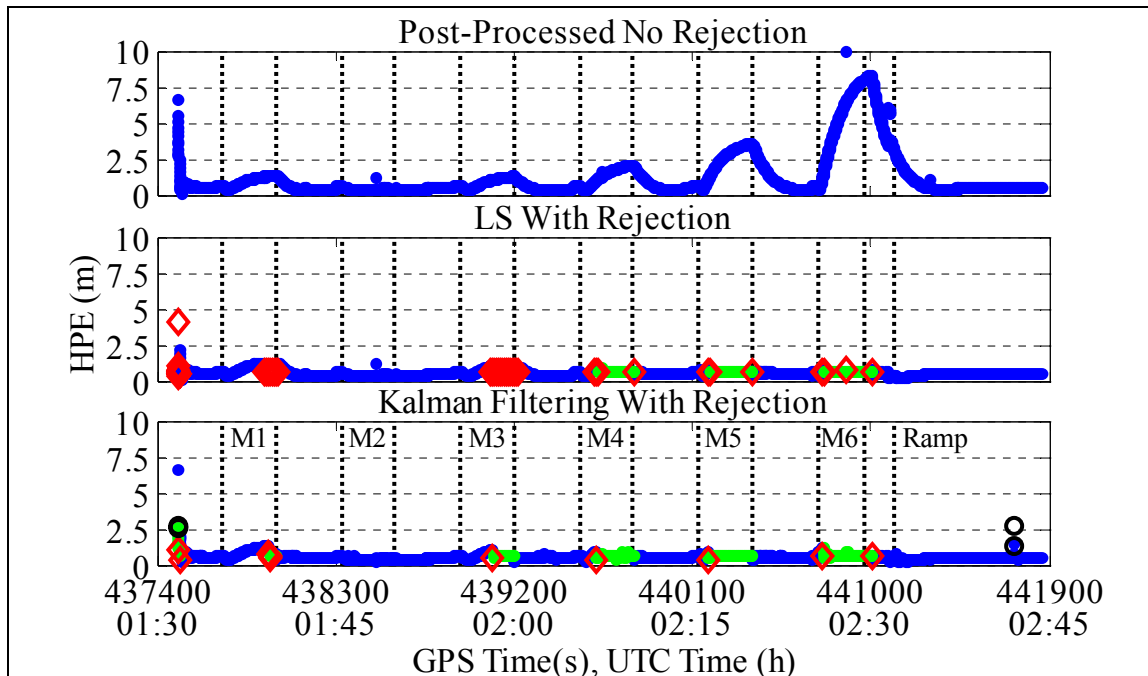


Figure G - 3 NovAtel OEM3, 15° Mask Angle, Carrier Smoothing

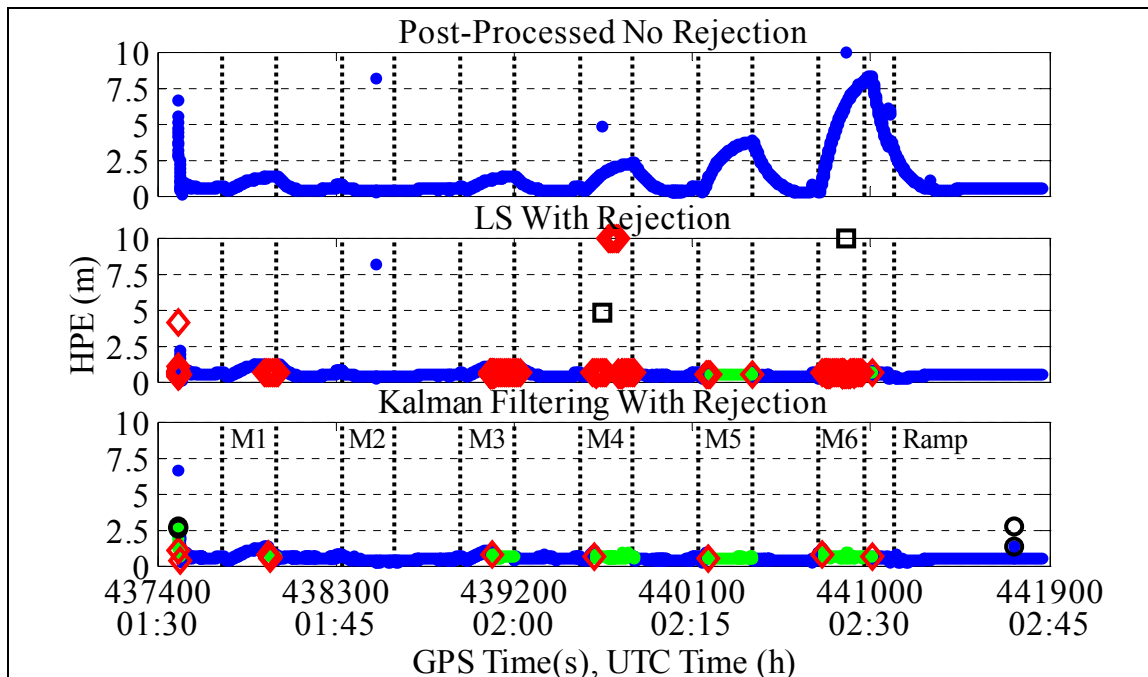


Figure G - 4 NovAtel OEM3, 20° Mask Angle, Carrier Smoothing

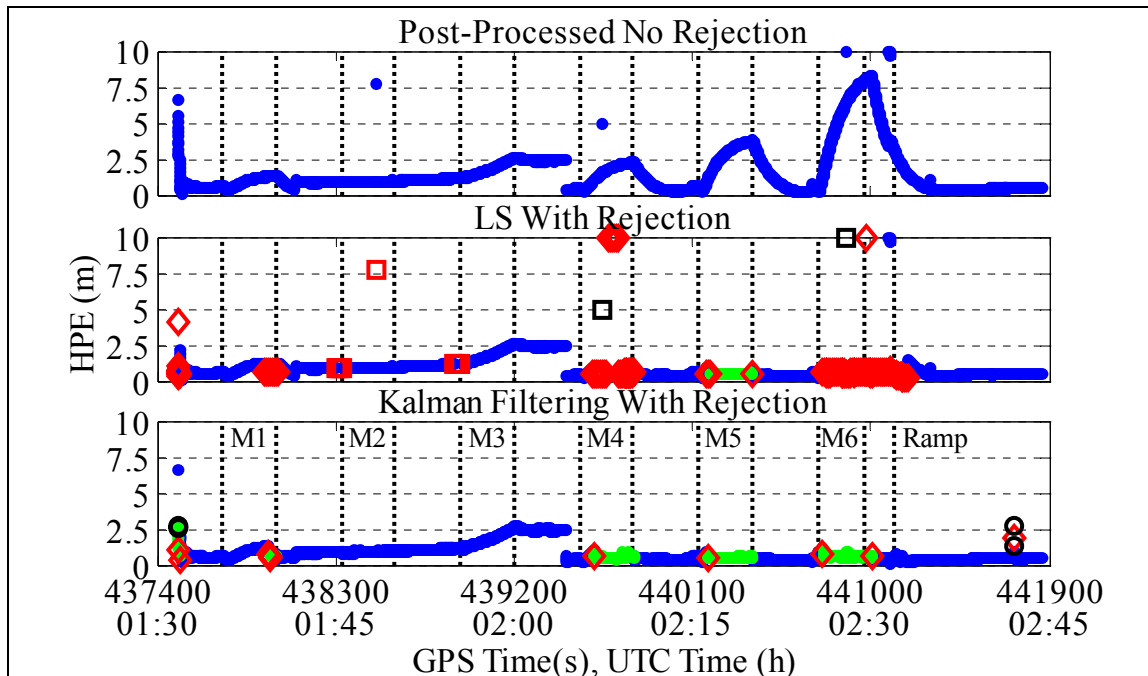


Figure G - 5 NovAtel OEM3, 25° Mask Angle, Carrier Smoothing

G.3 CSI GBX-Pro

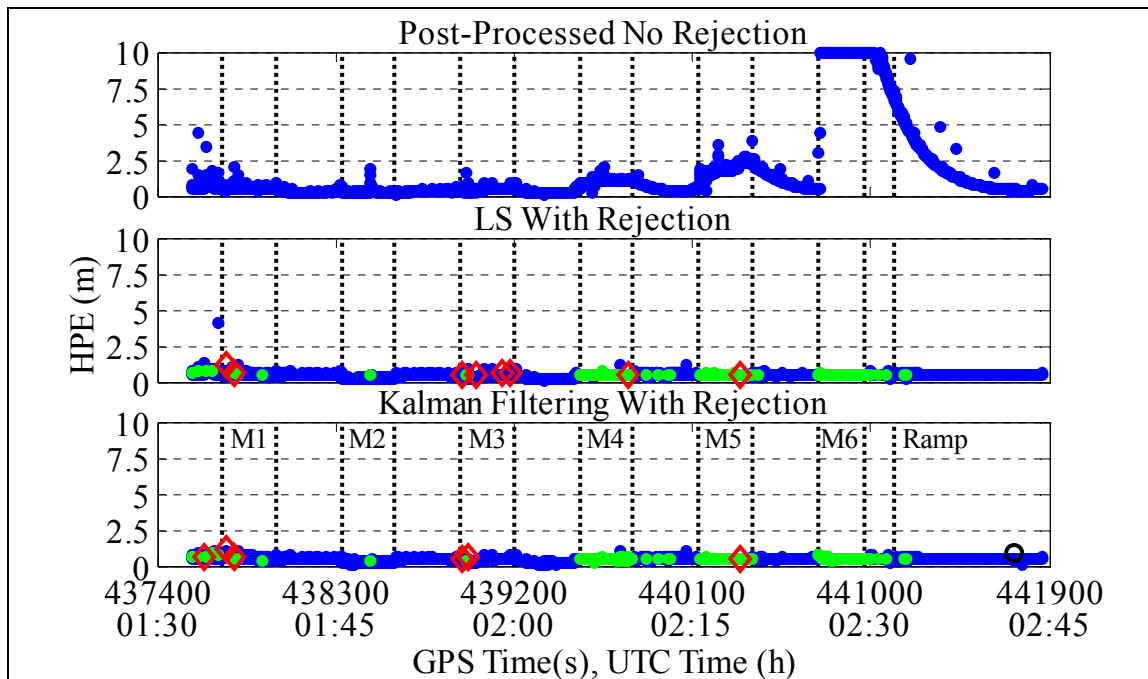


Figure G - 6 CSI GBX-Pro, 5° Mask Angle, Carrier Smoothing

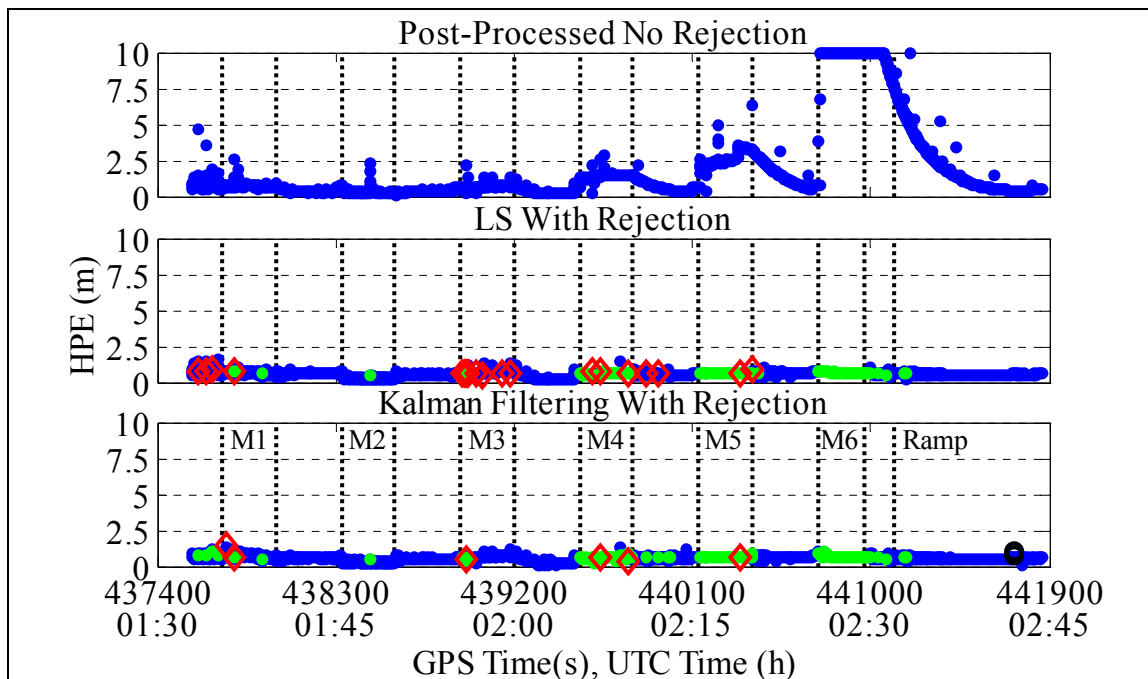


Figure G - 7 CSI GBX-Pro, 10° Mask Angle, Carrier Smoothing

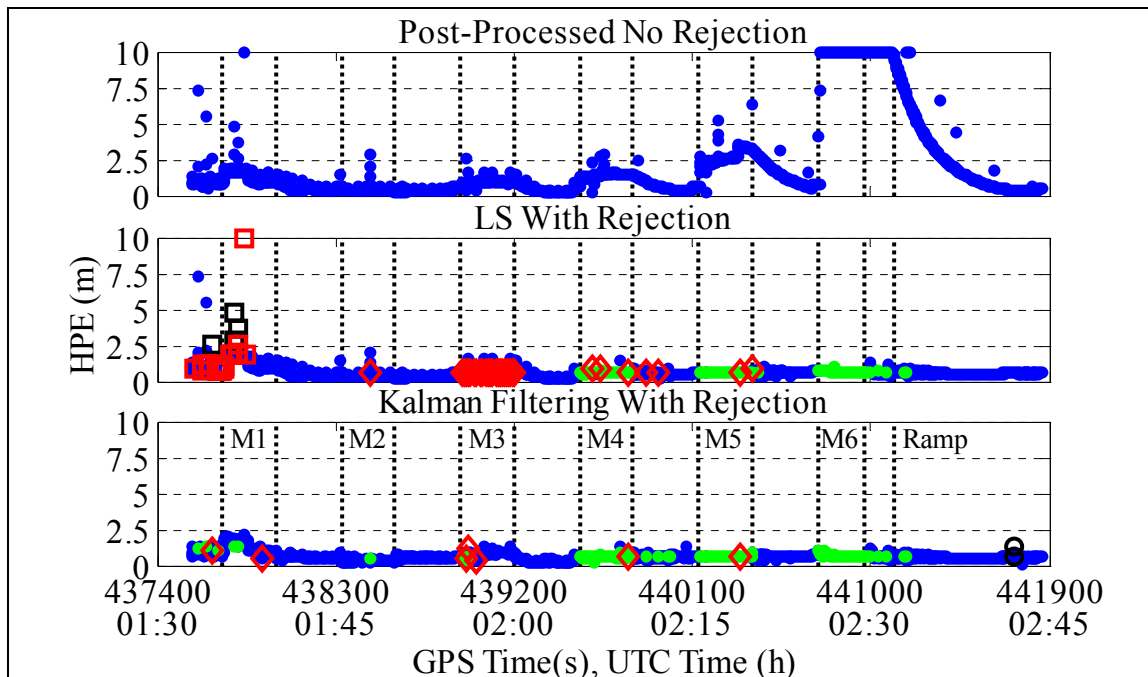


Figure G - 8 CSI GBX-Pro, 15° Mask Angle, Carrier Smoothing

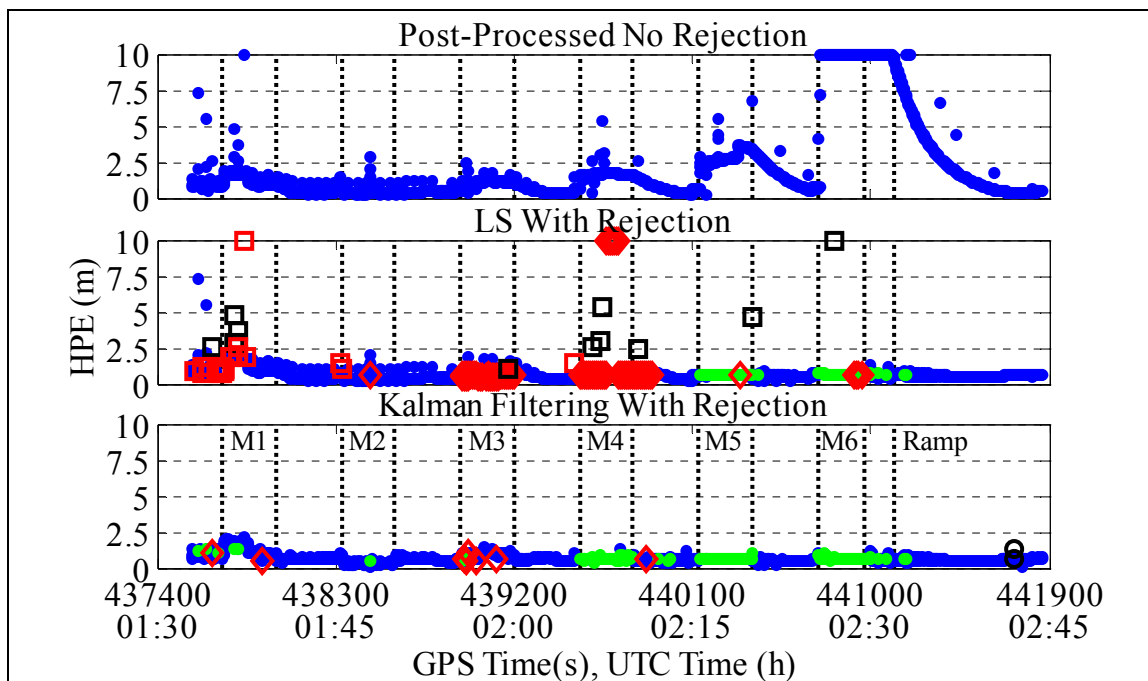


Figure G - 9 CSI GBX-Pro, 20° Mask Angle, Carrier Smoothing

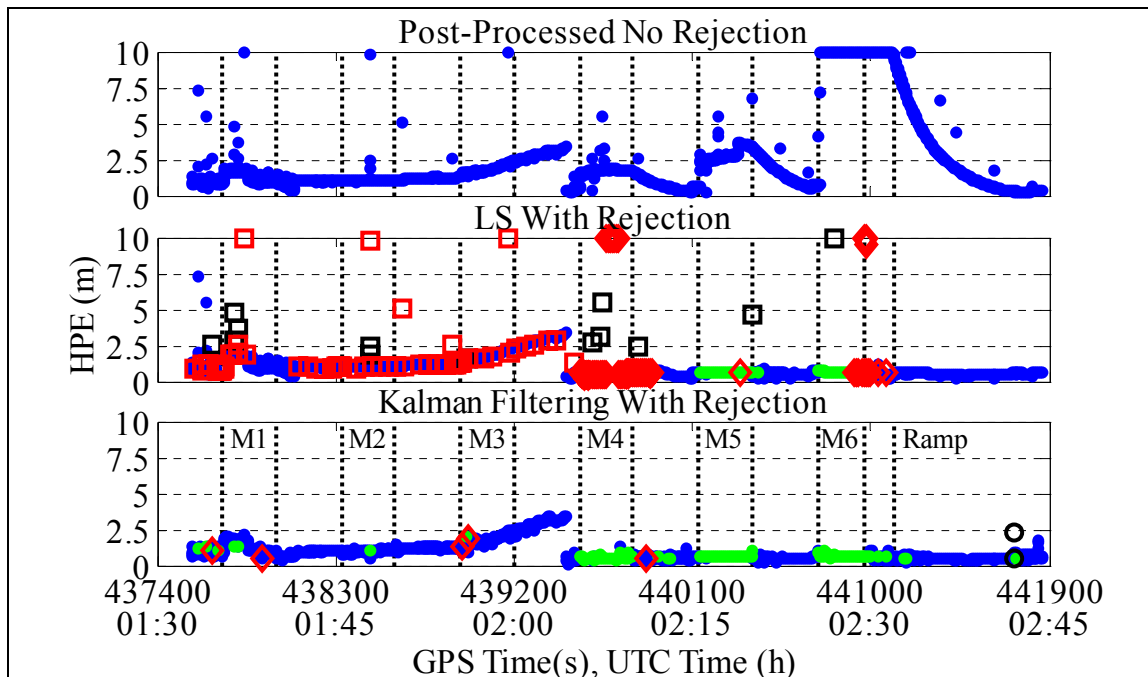


Figure G - 10 CSI GBX-Pro, 25° Mask Angle, Carrier Smoothing

G.4 MX-9212

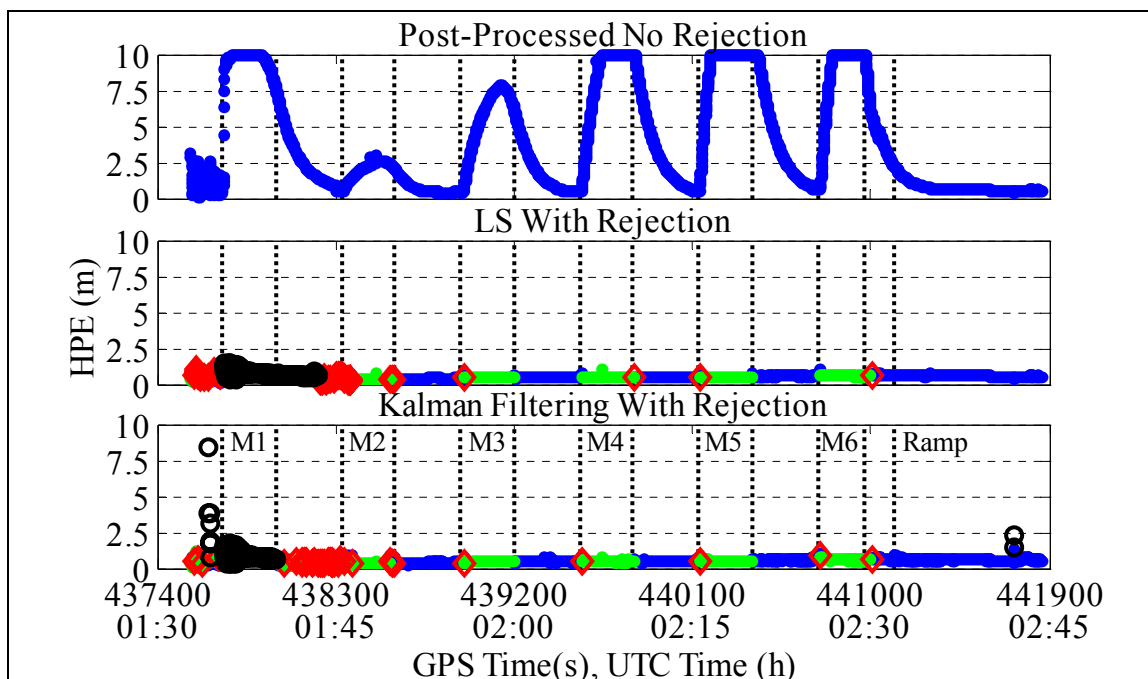
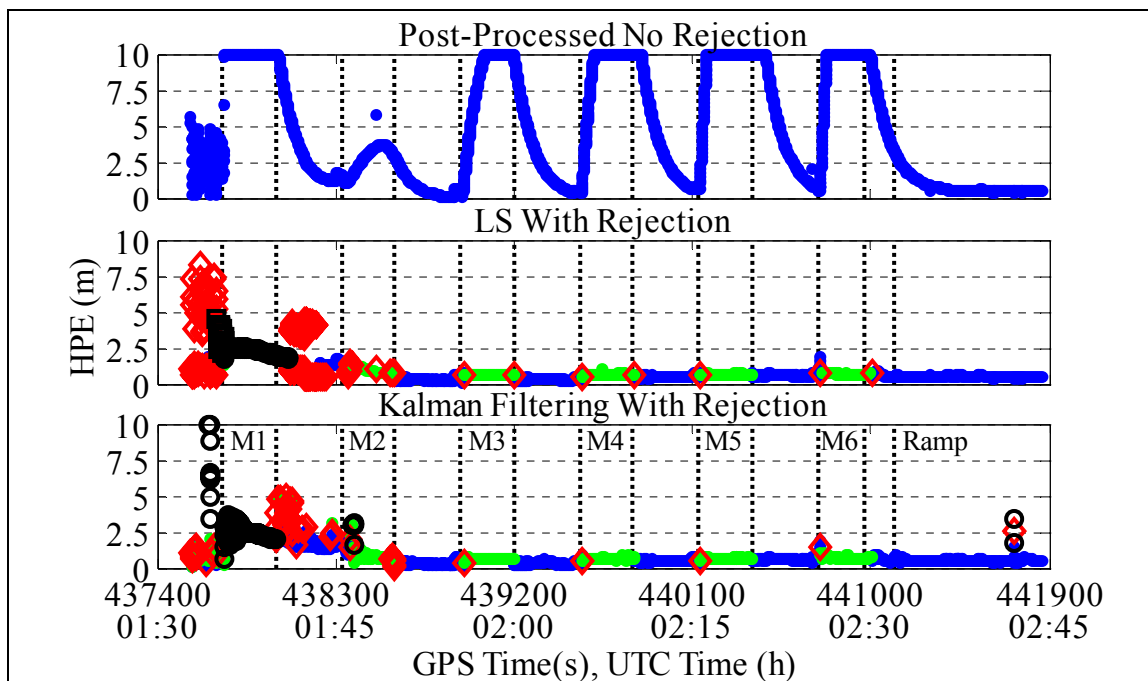
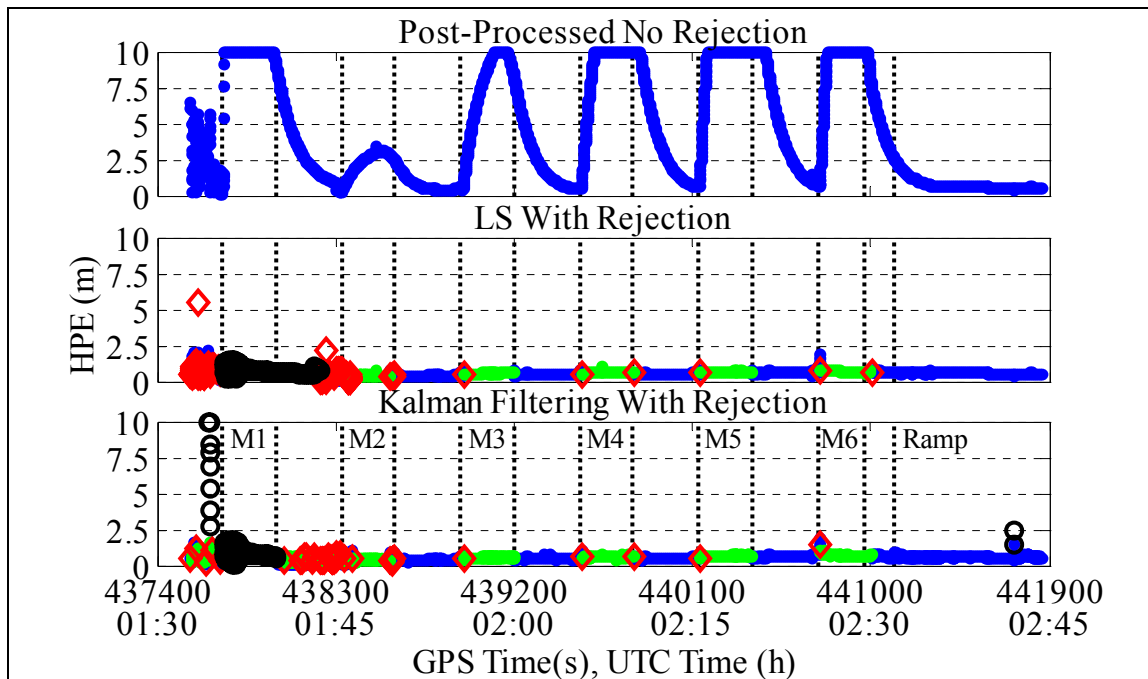


Figure G - 11 MX-9212, 5° Mask Angle, Carrier Smoothing



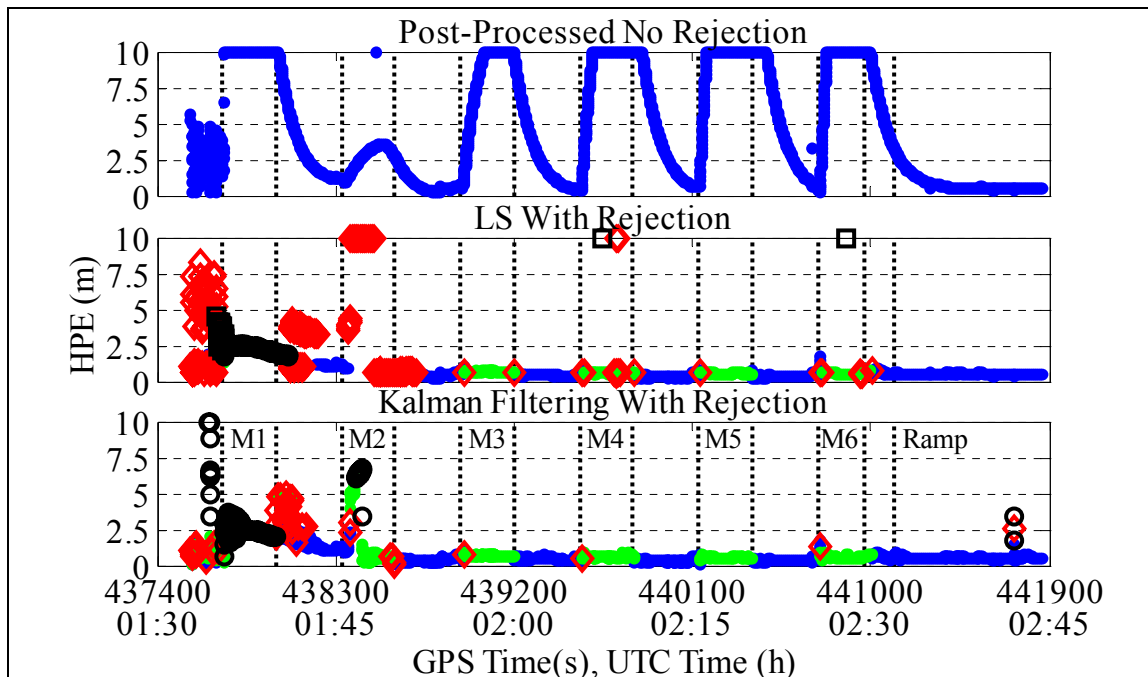


Figure G - 14 MX-9212, 20° Mask Angle, Carrier Smoothing

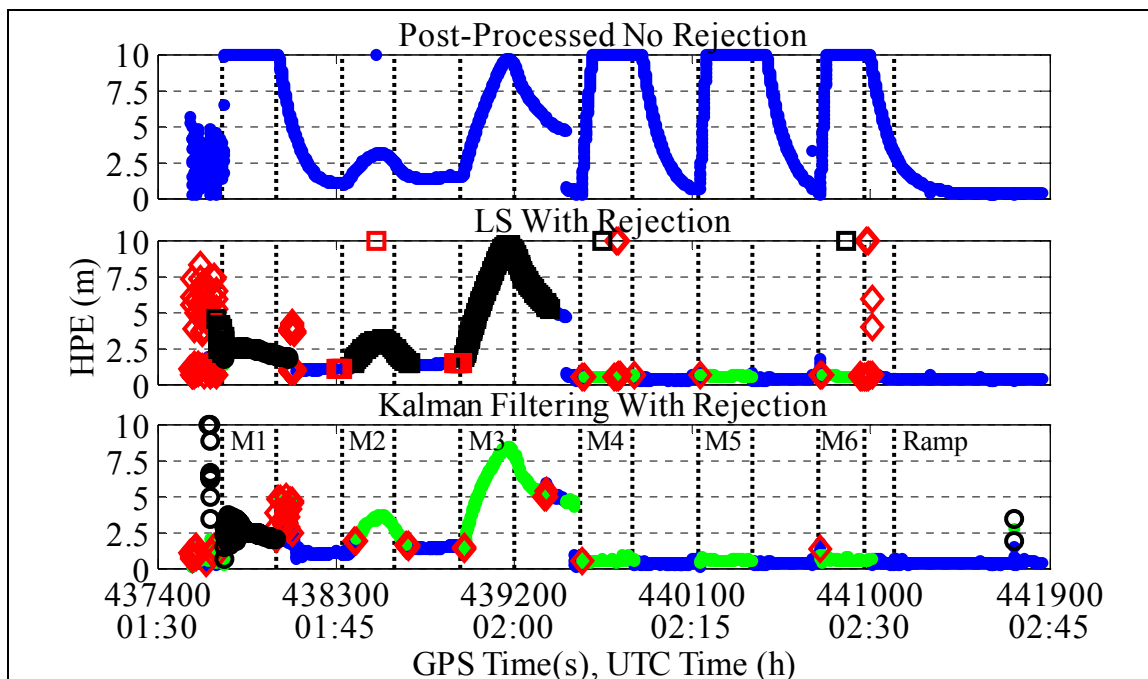


Figure G - 15 MX-9212, 25° Mask Angle, Carrier Smoothing

APPENDIX H

ADDITIONAL PICTURES OF SAANICH INLET TEST

H.1 Introduction

This appendix contains additional pictures of the Saanich Inlet, Vancouver Island test.

Figure H - 1 shows the location of the Ashtech GG24™ antenna on the Raven. The other three antennas were installed to collect data for other research.

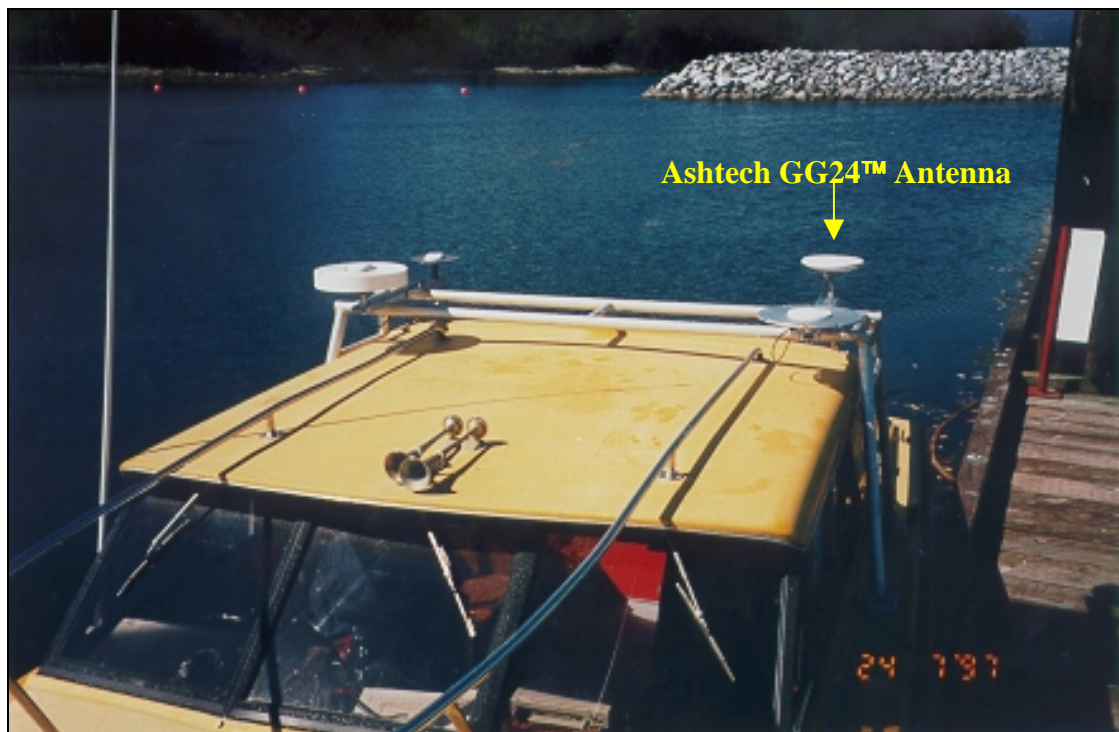


Figure H - 1 GPS Antenna Set up on the Raven

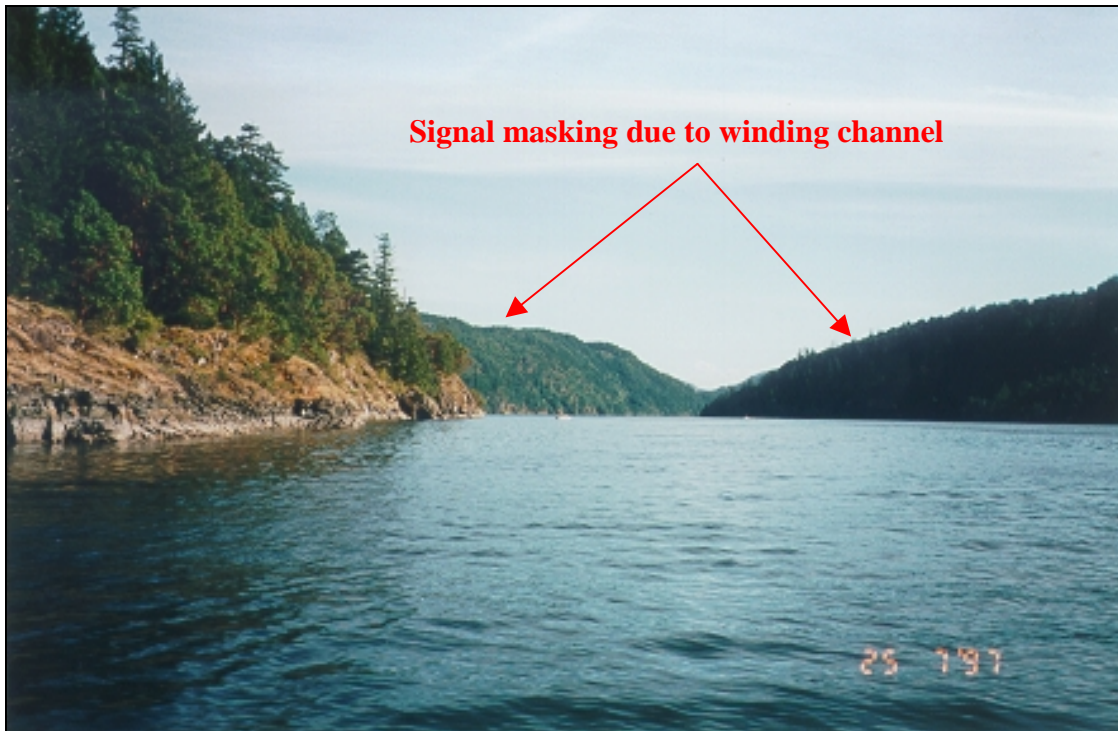


Figure H - 2 The Bends in Saanich Inlet



Figure H - 3 Touching the Shoreline at the End of the Survey Line

Figure H - 2 shows the bends in the channel and the masking that the winding channel produces. The wake in Figure H - 3 shows that the Raven almost touched the shoreline at the end of each survey line. Figure H - 4 shows the test set up on the Raven with the Rubidium clock, GPS receivers and logging computers.

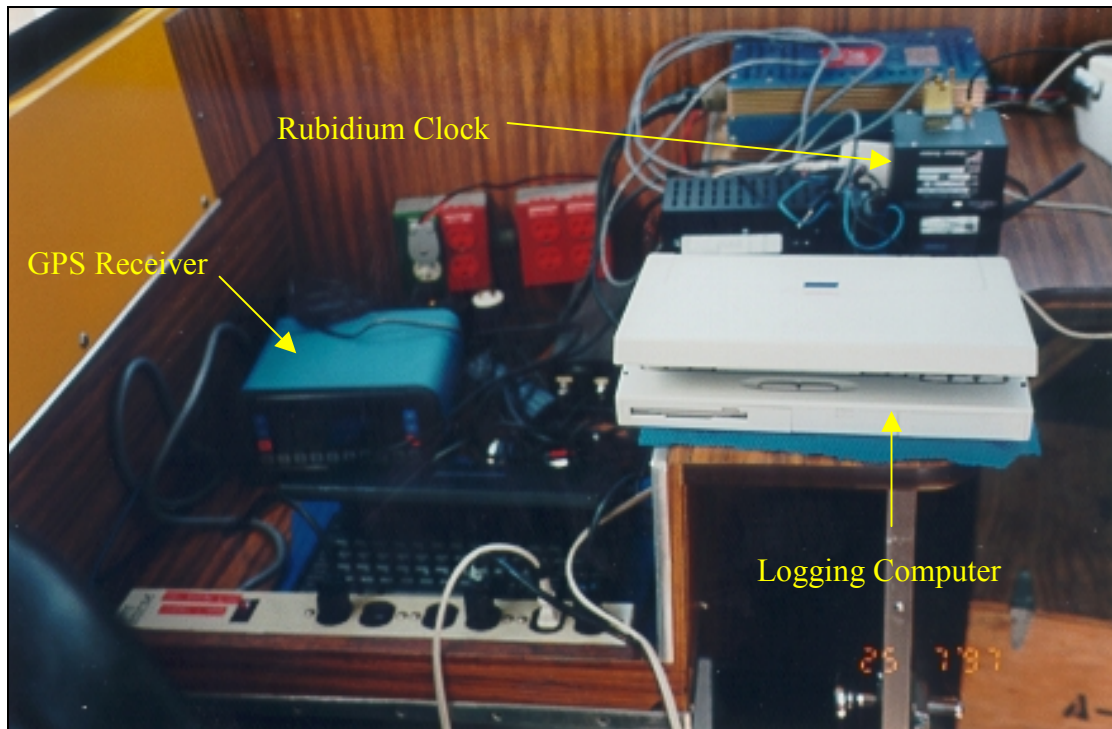


Figure H - 4 Test Set up on the Raven

REFERENCES

- Baarda, W., 1967, Statistical concepts in geodesy, Netherlands Geodetic Commission, Publications on Geodesy, New Series, Vol 2(4), Delft.
- Baarda, W., 1968, A testing procedure for use in geodetic networks, Netherlands Geodetic Commission, Publications on Geodesy, New Series, Vol 2(5), Delft.
- Bisnath, S., V. Mendes, and R. Langley, 1997, *Effects of Tropospheric Mapping Functions on Space Geodetic Data*, Presented at the 1997 IGS Analysis Centre Workshop, Pasadena, CA, 12-14 March, 1997.
- Braasch, M.S., 1995, *Multipath Effects*, Chapter 14 in *Global Positioning System: Theory and Applications Volume I*, ed. B. W. Parkinson and J. J. Spilker Jr., Volume 163 Progress in Astronautics and Aeronautics, American Institute of Aeronautics and Astronautics, Washington, DC, 1996.
- Breeuwer, Edward, 1991, *Modelling and Measuring GPS Multipath Effects*, Thesis A-285 Delft University of Technology, January, 1991.
- Brown R.G., and P. Hwang, 1997, *Introduction to Random Signals and Applied Kalman Filtering*, John Wiley & Sons, Inc, Toronto, 1997.
- Brunner, F., and M. Gu, 1991, An improved model for the dual frequency ionospheric correction of GPS observations, manuscripta geodaetica No. 16, Springer-Verlag, pp. 205-214, 1991.
- CCG, 1996, *Differential Global Positioning System (DGPS) Broadcast Standard For Marine Navigation*, Technical and Operational Services Directorate, Canadian Coast Guard, 1996.
- CCG, 2000, *Project Justification for Measuring the Multipath Error on CCG Ships*, Project # FQAL, Integrated Technical Support Directorate, Canadian Coast Guard, September, 2000.
- CCG, 2002, *Web Page www.ccg-gcc.gc.ca*, accessed on August 30, 2002.
- Collin, Robert E., 1985, *Antennas and Radiowave Propagation*, McGraw-Hill Book Company, Toronto, 1985.
- Cook G., 2001, *GLONASS: Still Out There*, Proceedings of ION GPS 2001, Salt Lake City, UT, September 11-14, 2001, pp. 68-74.
- CSI Wireless Inc., 2000, *Radiobeacon Listing*, Web Page <http://www.csi-dgps.com/csical/dgps/b-list.htm>, accessed on July 26, 2000.
- Davis, J. L., T. A. Herring, I. I. Shapiro, A. E. E. Rogers, and G. Elgered, 1985, *Geodesy by radio interferometry: Effects of atmospheric modelling errors on estimates of baseline length*, Radio Science, Vol. 20, No. 6, pp. 1593-1607, Nov.-Dec. 1985.

- DLR, 2002, *GLONASS Updated Information Service*, Web Page <http://www.kn.nz.dlr.de/>, accessed on May 22, 2002.
- Enge, P. and A.J. Van Dierendonck, 1995, *Wide Area Augmentation System*, Chapter 4 in *Global Positioning System: Theory and Applications Volume II*, ed. B. W. Parkinson and J. J. Spilker Jr., Volume 163 Progress in Astronautics and Aeronautics, American Institute of Aeronautics and Astronautics, Washington, DC, 1996.
- ESA, 2001, *Space serving European citizens*, European Space Agency press Release 65-2001, November 15, 2001.
- EUROPA, 2002a, *The Galileo Programme - Programme Phases*, Web Page http://www.europa.eu.int/comm/energy_transport/en/gal_how1_en.html, accessed on May 29, 2002.
- EUROPA, 2002b, *The Galileo Programme - Technical Features*, Web Page http://www.europa.eu.int/comm/energy_transport/en/gal_how_en.html, accessed on May 29, 2002.
- Fisheries and Oceans Canada, 2000, *Dhaliwal Declares New Coast Guard Satellite Navigation System Fully Operational*, NR-HQ-00-23E, May 25, 2000.
- Fontana, R., W. Cheung, and T. Stansell, 2001b, *The Modernized L2 Civil Signal Leaping Forward in the 21st Century*, GPS World, September 2001, pp. 28-34.
- Fontana, R., W. Cheung, P. Novak, and T. Stansell, 2001a, *The New L2 Civil Signal*, Proceedings of the ION GPS 2001, Salt Lake City, UT, September 11-14, 2001, pp. 617-631.
- Fortes L.P., 2002, *Optimising the Use of GPS Multi-Reference Stations for Kinematic Positioning*, Ph.D. thesis at the University of Calgary, UCGE Report No. 20158, April 2002.
- Fortes L.P., G. Lachapelle, M.E. Cannon, G. Marceau, S. Ryan, S. Wee and J. Raquet, 1999, *Testing of a Multi-Reference GPS Station Network for Precise 3D Positioning in the St. Lawrence Seaway*, Proceedings of the ION GPS 99 Conference, Nashville, TN, September 14-17, 1999, pp. 1259-1269.
- Foster, J.C., 2000, *Quantitative Investigation of Ionospheric Density Gradients at Mid Latitudes*, Proceedings of the ION NTM 2000 Conference, Anaheim, CA, January, 2000, pp. 447-453.
- Gallagher, F., 2002, *Single Frequency ionospheric Correction Parameters Anomaly*, Department of the Air Force, 50th Space Wing (AFSPC), 2 SOPS/DO, Memorandum for Record, June 6, 2002.
- Genesis Office, 2001a, *Decision on Galileo postponed, but Work Carrier On*, Galileo Newsletter, Number 17, December 2001, pp 1.

- Genesis Office, 2001b, *US Diplomatic Efforts against Galileo*, Galileo Newsletter, Number 17, December 2001, pp 2-3.
- Genesis Office, 2002a, *Galileo Takes Off!*, Galileo Newsletter, Number 19, March 2002, pp 1.
- Genesis Office, 2002b, *Galileo Signal-In-Space (SIS) Characteristics and Mapping to Frequencies*, Galileo Newsletter, Number 20, May 2002, pp 1-2.
- Griffiths, D., 1989, *Introduction to Electrodynamics*, Second Edition, Prentice Hall, Englewood Cliffs, New Jersey, 1989.
- Hargreaves, J.K., 1992, *The Solar-Terrestrial Environment*, Cambridge University Press, Cambridge, 1992.
- Hecht, E., 1990, *Optics Second Edition*, Addison-Wesley Publishing Company, Inc, Don Mills, Ontario, 1990.
- Hein, G., J. Godet, J. Issler, J. Martin, R. Lucas-Rodriguez, and T. Pratt, 2001, *The Galileo Frequency Structure and Signal Design*, Proceedings of the ION GPS 2001 Conference, Salt Lake City, UT, September 11-14, 2001, pp. 1273-1282.
- Hebert, J., J. Keith, S. Ryan, M. Szarmes, G. Lachapelle and M.E. Cannon, 1997, *DGPS Kinematic Carrier Phase Signal Simulation Analysis for Precise Aircraft Velocity Determination*, Proceedings of the ION AM 1997 Conference, Albuquerque, NM, July, 1997.
- Hopfield, H.S., 1969, *Two Quartic Tropospheric Refractivity Profile for Correcting Satellite Data*, Journal of Geophysical Research, April, 1969.
- IALA, 1999, *DGNSS Reference and Transmitting Stations in the Maritime Radionavigation (Radiobeacons) Band (283.5-315 kHz Region 1; 285-325 kHz Regions 2 and 3)*, List Of Radionavigation Services, Issue 7, August 1999.
- IGS, 2002, *IGS Products*, Web Page, <http://igsceb.jpl.nasa.gov/components/prods.html>, accessed on July 7, 2002.
- IHO, 1998, *IHO Standards for Hydrographic Surveys*, Special Publication No. 44, 4th edition, International Hydrographic Bureau, Monaco, April 1998.
- Jordan, E., and K. Balmain, 1968, *Electromagnetic Waves and Radiating Systems*, Second Edition, Prentice-Hall, Inc, Englewood Cliffs, New Jersey, 1968.
- Kaplan, Elliott D., 1996, *Understanding GPS Principles and Applications*, Artech House Mobile Communications Series, E. D. Kaplan Editor, Artech House, Boston, US, 1996.
- Kelly, R. J., 1998, *The Linear Model, RNP, and the Near-Optimum Fault Detection and Exclusion Algorithm*, Papers published in Navigation, Global Positioning System Vol. V, The Institute of Navigation, Alexandria, VA, pp. 227-259

- Klobuchar, J. A., 1996, *Ionospheric Effects on GPS*, Chapter 12 in *Global Positioning System: Theory and Applications Volume I*, ed. B. W. Parkinson and J. J. Spilker Jr., Volume 163 *Progress in Astronautics and Aeronautics*, American Institute of Aeronautics and Astronautics, Washington, DC, 1996.
- Klobuchar, J.A., P.H. Doherty, and M.B. El-Arini, 1995, *Potential Ionospheric Limitations to GPS Wide-Area Augmentation System (WAAS)*, *Navigation: Journal of the Institute of Navigation*, Vol. 42, No. 2, Summer 1995, pp. 353-370.
- Koch, K.R., 1999, *Parameter Estimation and Hypothesis Testing in Linear Models (2nd Edition)*, Springer-Verlag, New York, 1999.
- Kok J.J., 1984, *On Data Snooping and Multiple Outlier Testing*, NOAA Technical Report NOS NGS 30, National Geodetic Information Center, Rockville, MD, 1984.
- Krakiwsky, E.J., 1992, *The Method of Least Squares: A Synthesis of Advance*, Department of Geomatics Engineering, University of Calgary Lecture Notes #10003, March 1992.
- Krakiwsky, E.J., D.J. Szabo, P. Vaníček, and M.R. Craymer, 1999, *Development and testing of in-context confidence regions for geodetic survey networks*, Final contract report for Geodetic Survey Division of Geomatics Canada, by the Department of Geomatics Engineering, The University of Calgary, the Department of Geodesy and Geomatics Engineering, the University of New Brunswick, and the Geodetic Survey Division of Geomatics Canada. Department of Geodesy and Geomatics Engineering Technical Report No. 198, University of New Brunswick, Fredericton, New Brunswick, Canada, 24 pp.
- Kraus, J., and K. Carver, 1973, *Electromagnetics*, Second Edition, McGraw-Hill Book Company, Toronto, Canada, 1973.
- Lachapelle, G., 1997, *GPS Theory and Applications*, Lecture Notes for ENGO 625, Department of Geomatics Engineering, University of Calgary, Fall, 1997.
- Lachapelle, G., 1998, *Hydrography*, Lecture Notes #10016, Department of Geomatics Engineering, University of Calgary, September, 1998.
- Lachapelle, G., and S. Ryan, 2001, *Future Trends in Marine Navigation and Positioning Technology*, *Lighthouse*, No. 60 Fall / Winter 2001, pp 15-22.
- Lachapelle G., A. Bruton, J. Henriksen, M.E. Cannon, and C. McMillan, 1996, *Evaluation of High performance Multipath Reduction Technologies for Precise DGPS Shipborne Positioning*, *The Hydrographic Journal* No. 82, October 1996, pp. 11-17.
- Lachapelle, G., M. E. Cannon, L. P. Fortes, K. O'Keefe, and J. Sharma, 2000, *Testing of a Multi-Reference Station Approach for OTF Ambiguity Resolution in the St. Lawrence River*, Report for the Electronic Engineering Branch of the Canadian Coast Guard, March 31, 2000.

- Lachapelle, G., M. E. Cannon, L. P. Fortes, and J. Stephen, 1999, *Feasibility Study on the Use of a Multi-Reference Station Approach for OTF Ambiguity Resolution in a Constricted Waterway (St. Lawrence)*, Report for the Electronic Engineering Branch of the Canadian Coast Guard, April 30, 1999.
- Lachapelle, G., G. D. MacGougan, and L. K. Siu, 2002a, *CCG Shipboard Multipath Assessment CCGS Martha L. Black, Trois-Rivières, Québec*, Report for the Integrated Technical Support Directorate of the Canadian Coast Guard, July 8, 2002.
- Lachapelle, G., S. Ryan, M. Petovello and J. Stephen, 1997, *Augmentation of GPS/GLONASS For Vehicular Navigation Under Signal Masking*, Proceedings of the ION GPS 97 Conference, Kansas City, MO, September 16-19, 1997, pp 1511-1519.
- Lachapelle, G., S. Ryan, and C. Rizos, 2002b, *Servicing the GPS user*, Chapter 14 in Manual of Geospatial Science and Technology, ed. J. D. Bossler, Taylor & Francis, New York, NY, 2002.
- Spilker, J. J. Jr., 1994b, *Satellite Constellation and Geometric Dilution of Precision*, Chapter 5 in Global Positioning System: Theory and Applications Volume I, ed. B. W. Parkinson and J. J. Spilker Jr., Volume 163 Progress in Astronautics and Aeronautics, American Institute of Aeronautics and Astronautics, Washington, DC, 1996.
- LaMance, J., A. Brown, and J. Spalding, 1995, *Boosting Shipboard RAIM Availability*, Proceedings of the ION GPS 95 Conference, pp. 907-912.
- Langley, R., 2001, *PRN22 Anomaly*, e-mail to the CANSPACE list server on August 24, 2001.
- Leica, 2002, Personal conversations with the technical support personnel at Leica, 2002.
- Leick, A., 1995, *GPS Satellite Surveying (2nd Edition)*, John Wiley & Sons, Inc. 1995.
- Lu, G., and G. Lachapelle, 1992, *Statistical quality control for kinematic GPS positioning*, manuscripta geodaetica, Springer-Verlag, Vol. 17, pp. 270-281.
- Lucas, R. and D. Ludwig, 1999, *Galileo: System Requirements and Architectures*, Proceedings of the ION GPS 99 Conference, Nashville, TN, September 14-17, 1999, pp 2097-2101.
- Mendes, V.B., 1999, *Modelling the Neutral-Atmosphere Propagation Delay in Radiometric Space Techniques*, Ph.D. Dissertation, University of New Brunswick, Fredericton, Canada, 1999.
- Misra, P., R. Abbot, E. Gaposchkin, 1996, *Integrated Use of GPS and GLONASS: Transformation Between WGS 84 and PZ-90*, Proceedings of ION GPS 96, Kansas City, Missouri, September 17-20, 1996, pp. 307-314.

- Mitrikas, V., S. Revniviykh, and E. Bykhanov, 1998, *WGS84/PZ90 Transformation Parameters Determination Based On Laser And Ephemeris Long-Term GLONASS Orbital Data Processing*, Proceedings of ION GPS 98, Nashville, TN, September 15-18, 1998, pp. 1625-1635.
- Morley, T., 1997, *Augmentation of GPS with Pseudolites in a Marine Environment*, MSc Thesis, published as Report No. 20108, Department of Geomatics Engineering, The University of Calgary.
- Niell, A., 1996, *Global mapping functions for the atmosphere delay at radio wavelengths*, J. Geophys. Res., 100, 3227–3246, 1996.
- Niell, A., 2000, *Improved atmospheric mapping functions for VLBI and GPS*, Earth Planets Space, No. 52, pp 699-702, 2000.
- Office of Science and Technology Policy, 1996, *U.S. Global Positioning System Policy*, White House, March 29, 1996.
- Office of the Assistant Secretary of Defense, 1995, *Global Positioning System Fully Operational*, News Release (No. 384-95), July 17, 1995.
- Office of the Assistant Secretary of Transportation, 1998, *GPS to Provide two New Civilian Signals*, DOT 55-98, March 30, 1998.
- Office of the Assistant Secretary of Transportation, 1999, *Secretary Slater Officially Switches On Satellite Navigational and Positioning Systems*, CG 06-99, March 12, 1999.
- Office of the U.S. President's Press Secretary, 2000, *Statement by the President Regarding the United States' Decision to Stop Degrading Global Positioning System Accuracy*, May 1, 2000.
- Office of the U.S. Vice President, 1999, *Vice President Gore Announces New Global Positioning System Modernization Initiative*, January 25, 1999
- Parkinson, B. W. 1996, *Introduction and Heritage of NAVSTAR, the Global Positioning System*, Chapter 1 of *Global Positioning System: Theory and Applications*, B. W. Parkinson and J. J. Spilker Jr. Editors, Volume 163 Progress in Astronautics and Aeronautics, American Institute of Aeronautics and Astronautics, Washington, DC, 1996.
- Parkinson, B. W. and J. J. Spilker Jr., 1996, *Global Positioning System: Theory and Applications*, B. W. Parkinson and J. J. Spilker Jr. Editors, Volume 163 Progress in Astronautics and Aeronautics, American Institute of Aeronautics and Astronautics, Washington, DC, 1996.
- Raquet, J., 1998, *Development of a Method for Kinematic GPS Carrier-Phase Ambiguity Resolution Using Multiple Reference Receivers*, PhD Thesis, UCGE Report Number 20116, Department of Geomatics Engineering, The University of Calgary, 1998.

- Ray, Jayanta Kumar, 2000, *Mitigation of GPS Code and Carrier Phase Multipath Effects Using a Multi-Antenna System*, Ph.D. dissertation, University of Calgary, February, 2000.
- RTCA, 1998, *Minimum Operational Performance Standards for Global Positioning System / Wide Area Augmentation System Airborne Equipment*, RTCA/DO-229A, Developed by RTCA Special Committee NO. 159, June 8, 1998.
- RTCM, 1998, *RTCM Recommended Standards for Differential GNSS (Global Navigation Satellite Systems) Service*, Version 2.2, RTCM Paper 11-98/SC104-STD, Developed by RTCM Special Committee NO. 104, January 15, 1998.
- RTCM, 1999, *RTCM Recommended Standards for Differential NAVSTAR GPS Reference Stations and Integrity Monitors (RSIM)*, Future Version 1.1, RTCM Paper 64-99/SC104-X, Under Developed by RTCM Special Committee No. 104, August 16, 1999.
- Russian Federation Ministry of Defence, 2002, *Co-ordinated Scientific Information Centre*, Web Page <http://www.rssi.ru/SFCSIC/english.html>, access on May 22, 2002.
- Russian Federation Ministry of Defence, 1995, *Global Satellite Navigation System GLONASS Interface Control Document*, RTCA Paper No. 639-95/SC159-685 GNSSP/2-WP/66, November 14, 1995.
- Ryan, S., F. Forbes, and S. Wee, 1997, *Avoiding the Rocks - The Canadian Coast Guard Differential GPS System*, Proceedings of the KIS-97 Conference, Department of Geomatics Engineering, The University of Calgary, Banff June, 1997, pp 367-375.
- Saastamoinen, J., 1973, *Contribution to the Theory of Atmospheric Refraction*, Bulletin Géodésique, Vol 107, March 1973.
- Schüler, T, 2001, *On Ground-Based GPS Tropospheric Delay Estimation*, Dissertation angenommen durch: Universität der Bundeswehr München, Fakultät für Bauingenieur- und Vermessungswesen, February 1, 2001.
- Schwarz, K.P., M.E. Cannon, and R.V.C. Wong, 1989, *A comparison of GPS kinematic models for the determination of position and velocity along a trajectory*, manuscripta geodaetica, Springer-Verlag, vol. 14, pp. 345-353.
- Seeber, Günter, 1993, *Satellite Geodesy*, Walter de Gruyter, New York, 1993.
- Sensor Systems, 2002, *GPS S67-1575-Series*, Web Page <http://www.sensorantennas.com/pdf/pg28.pdf>, accessed on July 7, 2002.
- Skalski, H., 2001, *PRN-22 Review and Panel Discussion*, Presented at the 38th CGSIC Meeting, Salt Lake City, September 10, 2001.

- Skone, S., 1999, *Atmospheric Effects on Satellite Navigation Systems*, ENGG 699.56 Lecture Notes, Department of Geomatics Engineering, University of Calgary, September 1999.
- Skone, S., and M.E. Cannon, 1997, *Ionospheric Limitation and Specification in the Auroral Zone*, Proceedings of the ION GPS 97 Conference, Kansas City, MI, September, 1997, pp 187-197.
- Spalding, J.W., 1998, *Positioning United States Aids-to-Navigation Around The World*, Presented at the IALA Conference, June 1998.
- Spalding, J.W., and Frank van Diggelen, 1997, *Positioning United States Aids-to-Navigation Around The World*, Proceedings of the ION GPS 97 Conference, Kansas City, MO, September 16-19, 1997, pp 981-987.
- Spalding, J.W., S. Flynn, and Frank van Diggelen, 1993, *Servicing and Positioning Aids-to-Navigation with DGPS*, Proceedings of ION GPS 93, pp 669-675.
- Spilker, J. J. Jr., 1994a, *GPS Signal Structure and Theoretical Performance*, Chapter 3 in *Global Positioning System: Theory and Applications Volume I*, ed. B. W. Parkinson and J. J. Spilker Jr., Volume 163 Progress in Astronautics and Aeronautics, American Institute of Aeronautics and Astronautics, Washington, DC, 1996.
- Spilker, J. J. Jr., 1994b, *Satellite Constellation and Geometric Dilution of Precision*, Chapter 5 in *Global Positioning System: Theory and Applications Volume I*, ed. B. W. Parkinson and J. J. Spilker Jr., Volume 163 Progress in Astronautics and Aeronautics, American Institute of Aeronautics and Astronautics, Washington, DC, 1996.
- Spilker, J. J. Jr., 1994c, *Tropospheric Effects on GPS*, Chapter 13 in *Global Positioning System: Theory and Applications Volume I*, ed. B. W. Parkinson and J. J. Spilker Jr., Volume 163 Progress in Astronautics and Aeronautics, American Institute of Aeronautics and Astronautics, Washington, DC, 1996.
- Teunissen, P.J.G., 1990, *An integrity and quality control procedure for use in multi sensor integration*, Proceedings of the ION GPS 90 Conference, pp. 513-522.
- Teunissen, P.J.G., 1998, *Quality Control and GPS*, Chapter 7 in *GPS for Geodesy 2nd Edition*, ed. P.J.G. Teunissen and A. Kleusberg, Springer, New York, NY, 1998.
- Thayer, G. D., 1974, *An improved equation for the radio refractive index of air*, *Radio Science*, Vol. 9, pp. 803-807, 1974.
- Tranquilla, J.M., and J.P. Carr, 1990, *GPS Multipath Field Observations at Land and Water Sites*, *Navigation: Journal of the Institute of Navigation*, Vol. 37, No. 4, Winter 1990-91, pp. 393-414.

- Tytgat, L. and P. Campagne, 2001, *Galileo: Taking the Next Step*, Proceedings of the ION GPS 2001 Conference, Salt Lake City, UT, September 11-14, 2001, pp. 1255-1263.
- USCG, 1993, *Broadcast Standard for the USCG DGPS Navigation Service*, Report Number COMDTINST M16577.1, April 1993.
- U.S. Department of Defense, 1995, *Global Positioning System Standard Positioning Service Signal Specification*, second edition, June 2, 1995.
- U.S. Department of Defence, 1999, *Navstar GPS Space Segment / Navigation User Interfaces*, ICD-GPS-200c October 11, 1999.
- U.S. Department of Defense, 2001, *Global Positioning System Standard Positioning Service Performance Standard*, October, 2001.
- U.S. Department of Defence and U.S. Department of Transportation, 1999, *1999 Federal Radionavigation Plan*, Report Number DOD-4650.5/DOT-VNTSC-RSPA-98-1.
- Van Dierendonck, A. J., 1994, *Understanding GPS Receiver Terminology: A Tutorial on What Those Words Mean*, Proceedings of the KIS-94 Conference, Department of Geomatics Engineering, The University of Calgary, Banff June, 1994, pp 15-24.
- Van Dierendonck, A. J. and Chris Hegarty, 2000, *The New L5 Civil Signal*, GPS World, September 2000.
- Van Dierendonck, A.J., and M.S. Braasch, 1997, *Evaluation of GNSS Receiver Correlation Processing Techniques for Multipath and Noise Mitigation*, Proceedings of the ION NTM 97 Conference, Long Beach CA, January 1997, pp. 207-215.
- van Diggelen, F., A. Brown, and J. Spalding, 1993, *Test Results of a New DGPS RAIM Software Package*, Proceedings of ION AM 93, pp 641-646.
- van Nee R.D.J., 1995, *Multipath and Multi-Transmitter Interference in Spread-Spectrum Communication and Navigation Systems*, Delft University Press, 1995.
- Vaniček, P., and E.J. Krakiwsky, 1986, *Geodesy: The Concepts (2nd Edition)*, North-Holland, Amsterdam, 1986.
- Walker, J. G., 1978, *Satellite Patterns for Continuous Multiple Whole-Earth Coverage*, IEE Conference Publication No.: 160, pp 119-122, 1978.
- Wanninger, L., 1993, *Effects of the Equatorial Ionosphere on GPS*, GPS World, pp. 48-54, July, 1993.
- Ward, Phillip, 1996, *Satellite Signal Acquisition and Tracking*, Chapter 5 in *Understanding GPS Principles and Applications*, E. D. Kaplan Editor, Artech House, Boston, US, 1996.

- Weber, T., H. Trautenberg, and C. Schäfer, 2001, *Galileo system Architecture – Status and Concepts*, Proceedings of the ION GPS 2001 Conference, Salt Lake City, UT, September 11-14, 2001, pp. 1264-1272.
- Wolfrum, J., M. Healy, J.P. Provenzano, and T. Sassorossi, 1999, *Galileo - Europe's Contribution to the Next Generation of GNSS*, Proceedings of the ION GPS 99 Conference, Nashville, TN, September 14-17, 1999, pp 1381-1390.
- Woo, K.T., 1999, Optimum Semi-Codeless Carrier Phase Tracking of L2, Proceedings of the ION GPS 99 Conference, Nashville, TN, September 14-17, 1999, pp 289-305.